Implementation of a Virtual Reality Module for Gaining Surgical Access via Planned Oblique Lateral Lumbar Interbody Fusion

Khaled El-Monajjed

Department of Mechanical Engineering

McGill University, Montreal

December 2020

A thesis submitted to McGill University in partial fulfillment of the requirements of the degree of Doctor of Philosophy in Mechanical Engineering

DEDICATION

I dedicate this thesis to my parents, Marwa Al-Zaim and Afif El-Monajjed for their endless support and motivation. Mom and Dad, this is but a minute symbol of gratitude for the sacrifices you have made, the hardships you had to go through and the effort you made to seek a better future for us.

I also dedicate this to my wife and life partner, Fatima Bohsali, for never doubting me and always showing her support and endless love.

Finally, I dedicate this to my daughter Marwa El-Monajjed, who was born while I was working on my PhD, I love you, Dad. Never let anyone ever tell you that you cannot do something, be strong and stay true to yourself always.

Life is but a perfect simulator rendering at light speed, bound by the space-time continuum, governed by its flawless laws of physics, dispatching events based on our input as we consciously connect through our physical body peripheral, powered by energy while continuously monitored to conceive a set of metrics whose outcome concludes our void when idle.

CONTENTS

LIST OF TABLES

LIST OF FIGURES

LIST OF EQUATIONS

LIST OF SYMBOLS AND ABBREVIATIONS

2D	Two Dimension
3D	Three Dimension
a	Displacement Boundaries
ALF	Anterior Layer of the Thoracolumbar Fascia
ALIF	Anterior Lumbar Interbody Fusion
API	Application Programming Interface
ATP	Anterior-to-Posterior
AxiaLIF	Axial Lumbar Interbody Fusion
BMD	Bone Mineral Density
CAD	Computer Aided Design
CNS	Central Nervous System
CPU	Central Processing Unit
CSA	Cross-Sectional Area
cTrA	Common Tendon of the Transverse Abdominis
DH	Disc Height
DLIF	Direct Lumbar Interbody Fusion
DoF	Degree of Freedom
DoFF	Degree of Freedom Force
E	Young's Modulus of Elasticity
EMG	Electromyography
ENR	Exiting Nerve Root
EO	External Oblique

F	Force
FEA	Finite Element Analysis
FEM	Finite Element Model
FPS	Frames Per Second
FSU	Functional Spinal Unit
GHz	GigaHertz
GPU	Graphical Processing Unit
GUI	Graphical User Interface
HMD	Head Mounted Displays
IAP	Intra-Abdominal Pressure
IO	Internal Oblique
I/O	Input/Output
IVD	Intervertebral Disc
K	Bulk's Modulus
LBP	Low Back Pain
LIF	Lumbar Interbody Fusion
LIFT	Lumbar Interfascial Triangle
LLIF	Lateral Lumbar Interbody Fusion
LVD	Lower Vertebral Depth
LVW	Lower Vertebral Width
M	Moment
MI	Minimally Invasive
MIS	Minimally Invasive Surgery
MI-TLIF	Minimally Invasive Transforaminal Lumbar Interbody Fusion
MLF	Middle Layer of the Thoracolumbar Fascia
MRI	Magnetic Resonance Imaging
OLIF	Oblique Lumbar Interbody Fusion
OLLIF	Oblique Lateral Lumbar Interbody Fusion
PH	Pedicle Height
P_L	Left Paraspinal Compartmental Pressure
PLED	Percutaneous Lumbar Endoscopic Discectomy

PLF	Posterior Layer of the Thoracolumbar Fascia
PLIF	Posterior Lumbar Interbody Fusion
PMC	Paraspinal Muscle Compartment
PNS	Peripheral Nervous System
POD	Postoperative Dysesthesia
P_R	Right Paraspinal Compartmental Pressure
PW	Pedicle Width
RA	Rectus Abdominis
RAM	Random Access Memory
SAP	Superior Articular Process
SCD	Spinal Canal Depth
SCW	Spinal Canal Width
t	Time
T_{ALFL}	Reaction Force at Left Anterior Layer of Thoracolumbar Fascia
T_{ALFR}	Reaction Force at Right Anterior Layer of Thoracolumbar Fascia
T_C	T_{CL} or T_{CR} without any specification of direction
T_{CL}	Reaction Force at Left connection between TLF and Abdominal Wall
T_{CR}	Reaction Force at Right connection between TLF and Abdominal Wall
TF	Transversalis Fascia
TLED	Total Lagrangian Explicit Dynamic
TLF	Thoracolumbar Fascia
TLIF	Transforaminal Lumbar Interbody Fusion
TPL	Transverse Process Length
T_{PLF}	Reaction Force at Posterior Layer of Thoracolumbar Fascia
TrA	Transversus Abdominis
u	Position
UPE	Ultimate Percent Elongation
UTS	Ultimate Tensile Strength
UVD	Upper Vertebral Depth
UVW	Upper Vertebral Width
υ	Poisson Ratio

VBHa	Vertebral Body Height Anterior
VBHp	Vertebral Body Height Posterior
VR	Virtual Reality
VRS	Virtual Reality Simulator
w(x)	Distributed Lateral Resistance
XLIF	Extreme Lumbar Interbody Fusion
τ	Torque
θ	Angle

ABSTRACT

Low Back Pain is currently one of the leading causes of disability worldwide. This usually initiates at the working age of young adults as acute low back pain and depending on several factors may, later, develop into chronic low back pain. While most cases of low back pain are eventually solved by nonsurgical management, those who show no sign of improvement ultimately undergo invasive surgery. Spinal Lumbar Interbody Fusion (LIF) surgeries have become well established given the progressive increase in surgical experience and knowledge. Oblique Lateral LIF (OLLIF) is one of the most recent surgical procedures which has shown advantages by leveraging entry via the silent intervertebral anatomical window; the Kambin's Triangle. Recent advancements in access instrumentation and internal medical imaging have given rise to the development of numerous Minimally Invasive Surgical (MIS) techniques. However, conducting a MIS has its challenges, such as having a minimal internal view which risks sensitive tissues and demands an adequate level of surgical experience. Thus, Virtual Reality (VR) medical simulators have risen as a solution.

The development of an anatomically accurate model marked the initiation of the set objectives. Initially, the model was utilized to extract reaction forces via offline FEM simulations to serve as boundary conditions for the initial state of the VR model. While the general VR development pipeline was later modified to ensure a performant real-time simulation, the studies conducted provided insightful knowledge on the force transmission within the spinal tissue involved within the scope of the surgery. The virtual model was, then, geometrically prepared for its incorporation into the VR scene followed by an assessment that confirmed the accuracy of the models. In addition to the geometrical preparations, the morphology of the various components invested within the model were compared in an anthropometric study to Caucasian morphological data. A cadaveric test benchtop frame was, then, constructed to fit a custom-made tensile testing machine suitable for carrying the cadaveric torso specimens. A set of procedures

were developed which identified tasks capable of extracting a full set of experimental data suitable for haptic rendering. Upon acquiring two male cadaveric torsos, the experiments were successfully conducted. The main observation that no visual access is available in the access gaining module of the OLLIF procedure presented an opportunity to integrate the haptic data without communication with the VR scene. Thus, the haptic device was configured to operate on an independent thread by calibrating the haptic device with the physical interface adopted in the simulator. The implemented algorithm was well suited for the purpose of the simulator developed specifically because it required the incorporation of muscle and disc tissue only.

The results conceived herein were embedded into a constructed VR scene. Gameplay and event-listeners were programmed into the VR scene providing the basic architecture required to operate the simulator. Additionally, further aiding tools, such as fluoroscopy, were included to provide the user with options based on their needs. Finally, a set of real-time and post-completion metrics were included in the scene to provide user-specific assessments on the performance of the simulation run.

RÉSUMÉ

La lombalgie est actuellement l'une des principales causes d'invalidité dans le monde. Cela commence généralement à l'âge de travailler chez des jeunes adultes en tant que lombalgie aiguë et, en fonction de plusieurs facteurs, peut, plus tard, se transformer en lombalgie chronique. Alors que la plupart des cas de lombalgie sont finalement résolus par une prise en charge non chirurgicale, ceux qui ne montrent aucun signe d'amélioration subissent finalement une chirurgie invasive. Les chirurgies de fusion intersomatique lombaire (FIL) sont bien établies compte tenu de l'augmentation progressive de l'expérience et des connaissances chirurgicales. Oblique Lateral LIF (OLLIF) est l'une des procédures chirurgicales les plus récentes qui a montré des avantages en tirant parti de l'entrée via la fenêtre anatomique intervertébrale, le triangle de Kambin. Les progrès récents dans l'instrumentation d'accès et l'imagerie médicale interne ont donné lieu au développement de nombreuses techniques de chirurgie mini-invasive (MIS). Cependant, la réalisation d'un MIS a ses défis, comme avoir une vue interne minimale qui met en danger les tissus sensibles et exige un niveau adéquat d'expérience chirurgicale. Ainsi, les simulateurs médicaux de réalité virtuelle (RV) sont devenus une solution.

Le développement d'un modèle anatomiquement précis a marqué le début des objectifs fixés. Initialement, le modèle a été utilisé pour extraire les forces de réaction via des simulations FEM hors ligne afin de servir de conditions aux limites pour l'état initial du modèle VR. Alors que le pipeline de développement VR général a été modifié par la suite pour assurer un Simulation performante en temps réel, les études menées ont fourni des connaissances approfondies sur la transmission de force au sein du tissu rachidien impliqué dans le cadre de la chirurgie. Le modèle virtuel a ensuite été préparé géométriquement pour son incorporation dans la scène VR suivie d'une évaluation qui a confirmé la précision des modèles. Outre les

préparations géométriques, la morphologie des différents composants investis dans le modèle a été comparée dans une étude anthropométrique à des données morphologiques caucasiennes. Un cadre de banc d'essai cadavérique a alors été construit pour s'adapter à un essai via machine de traction sur mesure adaptée au transport des spécimens de torse cadavérique. Un ensemble de procédures a été développé qui a identifié des tâches capables d'extraire un ensemble complet de données expérimentales adaptées au rendu haptique. Lors de l'acquisition de deux torses de cadavres masculins, les expériences ont été menées avec succès. La principale observation selon laquelle aucun accès visuel n'est disponible dans le module d'accès de la procédure OLLIF a présenté une opportunité d'intégrer les données haptiques sans communication avec la scène VR. Ainsi, le dispositif haptique a été configuré pour fonctionner à un fil indépendant en calibrant le dispositif haptique avec l'interface physique adoptée dans le simulateur. L'algorithme mis en œuvre était bien adapté aux fins du simulateur développé spécifiquement car il ne nécessitait que l'incorporation de tissu musculaire et discal.

Les résultats conçus ici ont été intégrés dans une scène VR construite. Le *gameplay* et les écouteurs d'événements ont été programmés dans la scène VR fournissant l'architecture de base requise pour faire fonctionner le simulateur. En outre, d'autres outils d'aide, tels que la fluoroscopie, ont été inclus pour fournir à l'utilisateur des options en fonction de ses besoins. Enfin, un ensemble de métriques en temps réel et après achèvement ont été inclus dans la scène pour fournir des évaluations spécifiques à l'utilisateur sur les performances de l'exécution de la simulation.

ACKNOWLEDGEMENTS

It is my utmost pleasure to extend my most sincere appreciation to my research director and mentor Professor Mark Driscoll for his tremendous guidance, support, understanding, patience and motivation throughout my entire doctoral degree. Learning from Professor Driscoll's vast academic and industrial experience as well as his exceptional communication skills have been and will always be my foundation tackling future endeavors. Words truly undermine my blissful experience with Professor Driscoll.

In addition, I would like to thank Professor Rosaire Mongrain and Professor Mathias Legrand for never hesitating to discuss and help guide my research project.

This research project was a result of a team effort provided by the Musculoskeletal Biomechanics Research Lab group who have supported me in times of need especially Dr. Brahim Brahmi, Ibrahim El-Bojairami, Sneha Patel, Trevor Cotter and Dr. Rodrigo Navarro.

I would also like to extend my appreciation to the project's partners CAE Healthcare and Depuy Synthes who have supported the progress of this project during its development. In addition, I would like to thank the Natural Science and Engineering Research Council of Canada, the Mechanical Engineering Department and MEDTEQ for their financial support. Moreover, I would like to thank Professor Yvan Petit and Elisabeth Laroche at Ecole de Technologie Supérieure at Universite du Quebec for their support in providing their technical services and facilities when conducting the experiments.

I would also like to extend my thanks to my mother and father who have believed in me and my capabilities without hesitation supporting my decision to pursue a PhD. I would also like to extend my thanks to my brother, Belal, who stands as my backbone and support and my sister, Sarah, who has continuously supported me during the hard times. Finally, it goes without saying that this would not have been possible without the support from my life partner, Fatima. The sacrifices she has done and support she has given me are what has made this possible.

AUTHORS CONTRIBUTION

I, Khaled El-Monajjed, hereby certify that I am the primary author of all the manuscripts and chapters within this dissertation. Under the supervision of Professor Mark Driscoll, I designed and conducted the 2D and 3D Finite Element Studies to address the undermentioned hypotheses realizing one possible use case of offline models to prepare the initial state of virtual models prior to real-time operation. Furthermore, I designed the geometrical preparation workflow and selected the applicable software required to achieve the graphical models of the simulator. This is in addition to the anthropometric study conducted to define scaling factors for possible variation. Furthermore, I designed and conducted the experiments necessary to achieve the data required for haptic integration as well as the benchtop required to carry the cadavers. Moreover, I realized the possible independent development of the haptic thread and developed the algorithm necessary to achieve force feedback. Finally, I programmed all the scripts specific to the gameplay and operation of the access gaining module within the simulator.

ORIGINAL CONTRIBUTION

The study reported within this thesis consists of novel architecture and ideas to construct a spinal lumbar interbody fusion simulator. In specific, the study consisted of the following contributions to knowledge:

1. First 2-Dimensional and 3-Dimensional Finite Element Analysis which incorporated the Thoracolumbar Fascia, lumbar vertebra, intervertebral disc, intramuscular pressure and Intra-abdominal Pressure to investigate the variation of the forces within the thoracolumbar fascia in different postures;
2. Development of a workflow for the construction of stable geometric tessellations suitable for real-time simulations and offline analyses;
3. Extracted the force profiles along the axial, radial and tangential directions of the probe used to gain access to the disc when interacting with the muscle, nerve and disc tissue of the Oblique Lateral Lumbar Interbody Fusion surgery from two fresh frozen cadavers;
4. Development of a force model algorithm that directly utilized the force profiles suitable for real-time rendering on an independent thread;
5. Full scale development of a VR simulator for the access gaining module of a spinal lumbar interbody fusion surgery.

INTRODUCTION

Low Back Pain (LBP) often begins at the working age. While most experience Acute LBP that usually resolves after a short period of time, many move on to Chronic LBP. After non-invasive treatments show little improvement, patients are usually referred to undergo surgical interventions, namely spinal fusion surgeries. With the technological advancements, surgical procedures have become less invasive with the introduction of Minimally Invasive (MI) methods. As such, MI spinal fusion surgeries have become widely spread and have been conducted countless times. Of the numerous spinal fusion surgeries, the recent Oblique Lateral Lumbar Interbody Fusion (OLLIF) has shown superior outcomes in comparison to the previously developed procedures. The OLLIF procedure leverages the anatomical window roughly located between the transverse processes of two consecutive vertebra, namely Kambin's Triangle. Consequently, the surgeon traverses a 10–15 mm incision applied to the skin and the Thoracolumbar Fascia (TLF) while puncturing through the paraspinal muscles, utilizing a 4 mm probe, to approach the intervertebral disc while ensuring minimal collision with the nerve. This is ensured via the assistance of further surgical tools including neuromonitoring and fluoroscopic imagery. The initial stage, namely the Access Gaining stage, of the surgery includes the achievement of a trajectory along a probe spanning from the outer skin to the disc. Subsequently, the puncture is dilated by traversing the probe with dilating tools. This, then, creates a passage to conduct the following stages including discectomy, laminectomy and cage insertion. Such continuous advancements and mastery of the procedural techniques require consistent training. While these techniques have shown considerable advantages, surgeons must possess sound skills including anatomical, procedural, mitigative and adaptive knowledge for a successful surgery. The time constraints imposed on medical practitioners, requiring them to achieve adequate knowledge through experience, poses a challenge. Hence, virtual reality simulators, which have

previously demonstrated beneficial outcomes on learning curves in fields such as aerospace, devise feasible solutions for the systematic development of surgical experience.

In such a case, the development of a high-fidelity medical simulator may fill that void righteously on the condition that it provides an immersive and realistic experience. As such, this requires the development a VR model that accurately captures the anatomy of the tissue at hand, along with auditory feedback, haptic feedback, scene events and metrics.

The general objective of this doctoral project is to develop a VR module employed for medical training on the access gaining stage of the OLLIF procedure. To achieve this endeavor, anatomical and mechanical characterization of spinal tissue, as well as, spinal fusion surgeries, VR-based medical simulators and real-time numerical techniques were methodically reviewed.

This dissertation is composed of eight chapters as shown in Figure 0-1. Relevant literature was first reviewed (Chapter 1), followed by the research objectives and corresponding hypotheses (Chapter 2). The necessary components constructed to work towards building the simulator were, then, detailed. Consequently, three scientific manuscripts in Chapter 3, 4 and 5 were conceived. Chapter 6 details the development of the VR simulator. The explored themes were bound under a general discussion in Chapter 7 and Chapter 8 ends this dissertation with a conclusions and perspectives.

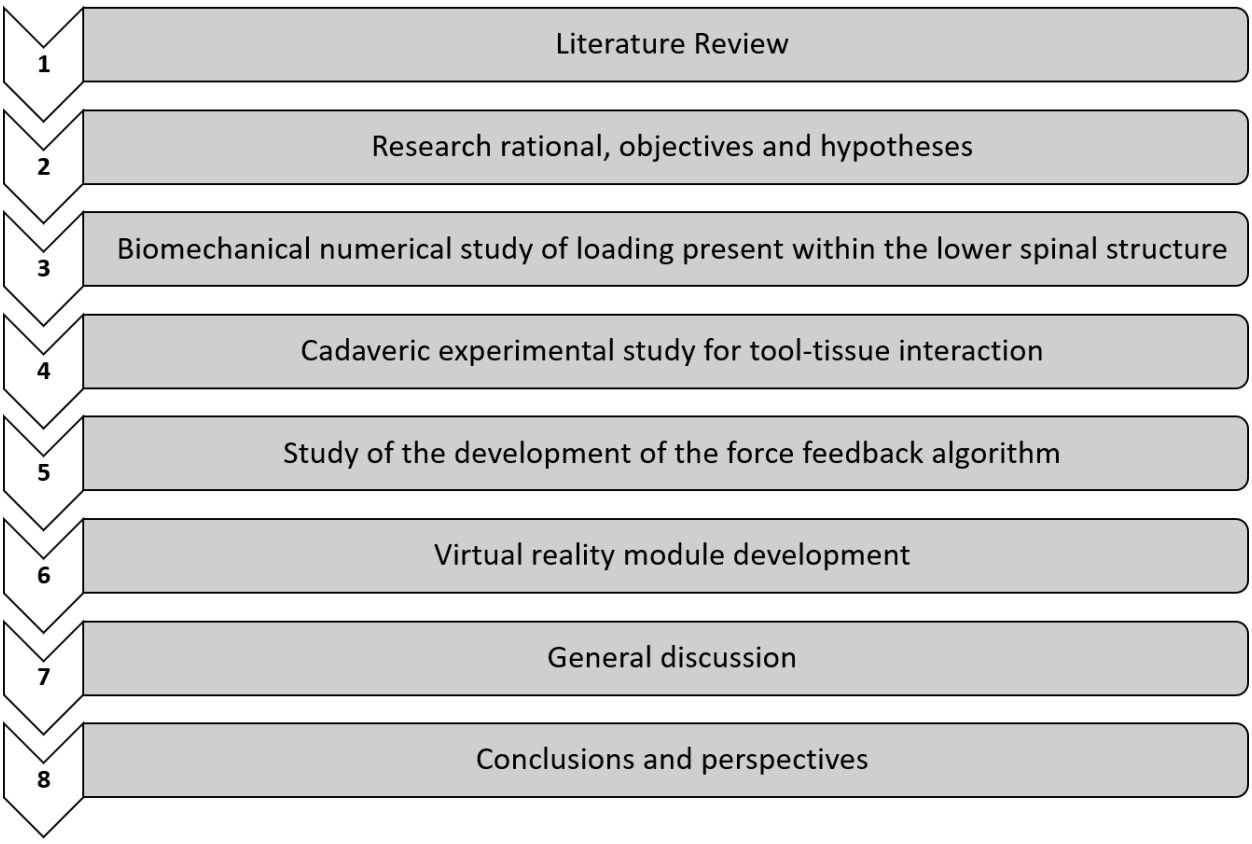

Figure 0-1: List of chapters

1

LITERATURE REVIEW

1.1. MUSCULOSKELETAL ANATOMY, BIOMECHANISMS, MECHANICAL CHARACTARISTICS AND ITS VARIATION IN SPINAL DISORDERS

On January 7th, 2015, Igor Zaripov set a new world record for pulling a 13 ton bus using only his teeth [1]. On July 9th, 2016, powerlifter Eddie Hall deadlifted a total weight of 500 kg to set a new world record while only weighing 186 kg (i.e. 2.6 times his body weight) [2]. Whether it was for breaking world records or carrying light loads, the human musculoskeletal system presents itself as a natural prodigy. Generally, the musculoskeletal system comprises a spinal structure that sustains the stabilization of the human posture under static and dynamic conditions. Operating within its structural limits, its neural, active and passive subsystems ensure the continuous stabilization of the spinal system while protecting the relatively softer tissues such as the spinal cord and nerve roots.

Panjabi et al. [3] conceptualized the musculoskeletal system as composed of three main subsystems, namely, the *passive*, *active* and *neural* and *feedback* subsystems. The *passive* subsystem within the torso region includes the vertebrae, intervertebral discs, spinal ligaments, facet articulations, joint capsules and thoracolumbar fascia. The *active* subsystem consists of the tendons and muscles surrounding the spinal column and engulfing the abdominal cavity. While the *neural* and *feedback* subsystem consists of neural transducers embedded within the active and passive tissue connected to the neural control systems. These subsystems operate in harmony to ensure the aforementioned functions are efficiently achieved.

1.1.1. VERTEBRA

The spinal column is composed of 24 vertebrae and is divided into three major parts each with a distinct curvature. Table 1.1 below describes the different regions and the most prominent features of each region.

Table 1.1: Spinal Vertebra Features

Spinal Regions	*Number*	*Curvature*	*Special Features*
Cervical	7	Concave	• First two vertebrae (Atlas & Axis) provide the pivoting motion of the head and have no vertebral body. • C_3 to C_7 are distinguished with a longer lateral length compared to the anterior-posterior length and a relatively straight spinous process. • C_3 to C_7 have a unique structure namely the Transverse Foramen; a passage for the vertebral veins, arteries and nerves. • Smallest and Lightest Vertebrae • Facet joints are oriented towards the coronal plane
Thoracic	12	Convex (Kyphosis)	• Spinous Processes of T_1-T_{12} are highly steeped inferiorly. • Costal Facets where the head of the ribs are joined (i.e. also known as Demifacets) • Facet joints have an intermedial orientation
Lumbar	5	Concave (Lordosis)	• Larger-sized vertebra due to increase in weight load bearing • Short, thick Pedicles • Laminae are flat hatchet-shaped spinous process • Triangular-shaped vertebral foramen • Facet joints are oriented towards the sagittal plane
Sacral	5-6 Fused	Convex	• Triangular shaped bone situated between the hipbones of the pelvis. • Supports and translates the weight of the body bridging to the lower body through the pelvis • Facet Joints face posterolaterally in the superior portion and anterolaterally in the inferior portion
Coccygeal	3-5 Fused	Convex	• Designates the end of the vertebral column • Serves as a connecting site for muscles of the pelvic floor as well as the Sacrotuberous and Sacrospinous ligaments • Provides a stabilizing and supporting function while sitting. • Facet Joints (or the Coccygela Cornua) orient caudally and articulate with the sacrum

In general, a vertebra consists of a main *Vertebral Body* connected to a *Neural Arch* through two bridges known as *Pedicles* to form a hollow canal through which the spinal cord rests, namely the *Vertebral Foramen*. The Neural Arch comprises two sets of *Superior Articular Facets* and *Inferior Articular Facets* which contact adjacent vertebra above and below it, respectively. Connecting the Superior and Inferior Articular Facet is the *Pars Interarticularis*. The Arch extends posteriorly through the *Lamina* region to end at the *Spinous Process* and laterally to a *Transverse Process* at each side. The vertebral body is composed of two main regions namely, the outer *Cortical Rim* and the inner cellular *Cancellous* structured from a network of vertical and horizontal narrow bone struts oriented towards the axial line of loading

called *trabeculae*. Superior and Inferior surfaces of the vertebral body are covered by bony endplates known as *Epiphyseal Plates*. Figure 1–1 depicts the anatomy of a lumbar vertebra.

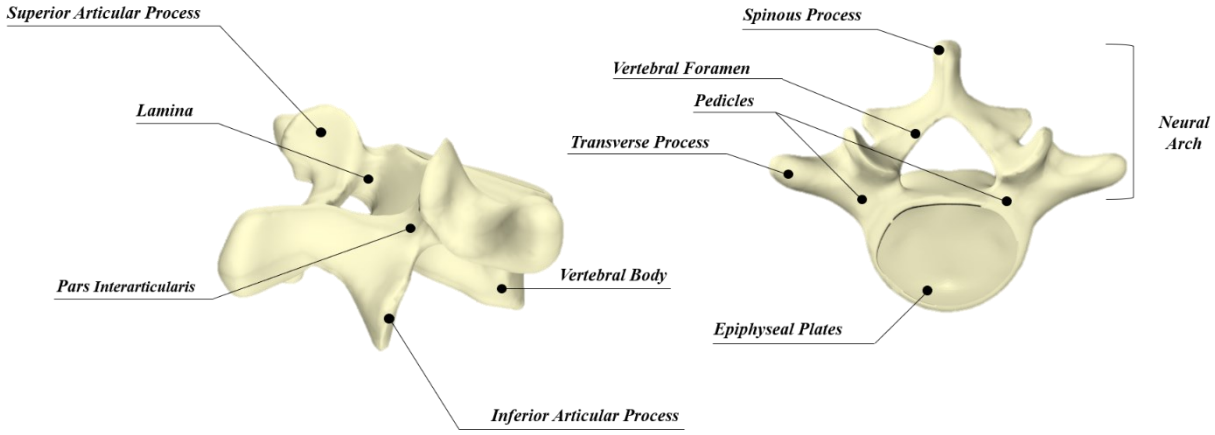

Figure 1-1: Anatomical Description of Lumbar Vertebrae

A vertebra is an irregular multiphase composite bone that is composed of water (15–25%), a stiff brittle mineral-based inorganic phase (i.e. 33–43%) and soft deformable collagenous organic phase (32–44%) on the microscopic level forming a complex structure to achieve a stiff lightweight mechanical support [4]. Minerals give the bones its rigidity and collagen proteins provide strength and elasticity. Generally, vertebral bones are mainly divided into two structures: the dense compact cortical bone and the cellular cancellous bone. Mechanical tests conducted on cortical and cancellous bone material have shown that both elements exhibit viscoelastic behavior whereby the damping factor is dependent on the water content as observed in creep and stress relaxation tests (i.e. material dependent on strain rate such that a higher strain rate produces higher elastic modulus) [5]. Nevertheless, due to the complexity in quantification and modeling of the viscoelastic behavior on the macroscopic scale, it is usually assumed that at small strains, the behavior of both bone elements is linearly elastic [6]. The material behavior is, thus, defined by a Modulus of Elasticity (**E**) quantity and Poisson Ratio ($\boldsymbol{\nu}$) defined along orthogonal directions. While the proper assignment of material behavior is a controversial issue within the FE society, the validity of choice depends on the scope of the study. Tables 1.2 and 1.3 summarize cortical and cancellous material behavior and their accompanying mechanical properties compiled and based on previous studies and book chapters [7-9].

Table 1.2: Biomechanical Properties of Vertebral Cortical Bone

Vertebral Cortical Bone				
Material Model	E [MPa]	ν	G [MPa]	Reference
Linear Elastic Isotropic	5000	0.30	-	Goel et al. [10], Shirazi-Adl et al. [11], Zander et al. [12]
Linear Elastic Isotropic	5000	0.20	-	De Visser et al. [13]
Linear Elastic Isotropic	10000	0.30	-	Argoubi and Shirazi-Adl [14], Kumaresan [15], Rohlmann et al. [16]
Linear Elastic Isotropic	11300	0.20	-	Little et al. [17]
Linear Elastic Isotropic	12000	0.30	4615 (Shirazi-Adl et al. [11])	Tadano et al. [18] , Chosa et al. [19], Herkowitz et al. [20], Fantirossi et al. [21], Shirazi-Adl et al. [11], Lavaste et al. [22], Goel et al. [10], Park et al. [23], Wang et al. [24], Kiapour et al. [25], Baroud et al. [26], Zhong et al. [27], Ruberté et al. [28], Kurutz and Oroszváry [29], Goto et. al [30], Lafage et al. [31], Ivanov et al. [32], Cassidy et al. [33], Bellini et al. [34]
Linear Elastic Transversly Isotropic	11300 13800 19400	0.274 0.237 0.237	-	Yoon et al. [35]
Linear Elastic Transversly Isotropic	11300 11300 22000	0.48 0.20 0.20	3800 5400 5400	Lu et al. [36], Schmidt et al. [37], Chen et al. [38]
Linear Elastic Transversly Isotropic	8000 8000 12000	0.40 0.23 0.35	2857 3200 3200	Noailly et al. [39], Malandrino et al. [40]
Linear Elastic Transversly Isotropic	8000 8000 12000	0.40 0.35 0.30	-	Ayturk et al. [41]
Linear Elastic Transversly Isotropic	2000 - 8000 2000 - 8000 8000 - 14000	0.30	-	Sylvestre et al. [42]
Poroelastic	10000	0.30	-	Ferguson et al. [43]

Table 1.3*: Biomechanical Properties of Vertebral Cancellous Bone*

Vertebral Cancellous Bone				
Material Model	E [MPa]	ν	G [MPa]	Reference
Linear Elastic Isotropic	10	0.20	-	Shirazi-Adl et al. [11], Cassidy et al. [33], Lu et al.[36], Goel et al. [10], Wang et al. [24], Chen et al.[38], Zhong et al. [27], Ruberté et al. [28]
Linear Elastic Isotropic	50 74 81 140 100 100 150 500 750	0.20 0.20 0.20 0.20 0.29 0.30 0.30 0.20 0.20	-	Rohlmann et al. [16], De Visser et al. [13], Baroud et al. [26], Little et al. [17], Zhang et al. [44], Lavaste et al. [22], Kurutz and Oroszváry [29], Rohlmann et al. [16], Zander et al. [12]
Poroelastic	100	0.20	-	Argoubi and Shirazi-Adl [14], Williams et al. [45], Goto et al. [30], Lafage et al. [31], Park et al. [23]
Linear Elastic Transversly Isotropic	200 140	0.45 0.315	-	Rohlmann et al. [16]
Linear Elastic Transversly Isotropic	140 140 250	0.45 0.176 0.315	48 77 77	Noailly et al. [39], Malandrino et al. [40]
Linear Elastic Transversly Isotropic	140 140 200	0.45 0.32 0.32	48.3	Lu et al. [36]
Linear Elastic Transversly Isotropic	112 112 340	0.3 0.1 0.1	52 53 53	Bellini et al. [34], Fantigrossi et al. [21]
Linear Elastic Transversly Isotropic	2000 - 8000 2000 - 8000 375 - 2000	0.30	-	Schmidt et al. [37]

Variation among the biomechanical properties of vertebra may be a result of differences within the bone density of the cancellous vertebral body [46], spinal level variation [47], shear strength of the endplate [48] as well as the material properties of the posterior elements. In fact, the latter is often assigned a different properties specifically, $\mathbf{E}$ = 3.5 GPa and $\boldsymbol{\nu}$ = 0.25, respectively [12, 21, 23, 25, 34, 37, 38, 45]. It is worthy to note that contrary to the published data of cortical and trabecular macroscopic structural mechanical properties, Bayraktar et al. [49] have observed that the elastic modulus of cortical tissue (19.9 ± 1.8 GPa) is only 25% more than trabecular tissue (18 ± 2.8 GPa). Cortical bone apparent densities measure between 0.1 – 0.3

g/cm^3 [53]. However, cancellous bone was found to vary between 1.4–2 g/cm^3. Helgason et al. conducted an extensive study which described the mathematical relationships between bone density and mechanical properties [54]. Additionally, vertebral body heights were previously measured to be 30.7 ±2.1 mm, 29.6 ±1.9 mm and 26.7 ±1.9 mm posteriorly and 30.6 ±1.8 mm, 31.0 ±2.1 mm and 31.5 ±2.1 mm anteriorly for L_3, L_4 and L_5 male subjects, respectively [55].

Epiphyseal plates, also known as growth plates or simply endplates, are situated between the vertebral body and intervertebral discs within the spinal vertebrae. It is within these plates that the human vertebrae grow in height since childhood by the mechanism of endochondral ossification [56]. This region is specifically unique with its suggested functional ability to store nutrition given the high vacuole and lipid content most abundant with Type II Collagen [57]. MRI scanning has shown this region to be highly innervated even exceeding that of intervertebral discs [58]. In general, endplates are composed of hyaline cartilage weakly bonded with the cortical bone with a typical thickness of 0.8 mm decreasing towards its central region (i.e. 0.2 mm). According to their micro-CT images, Zehra et al. observed that endplates are 14% thicker superiorly, on average, compared to their inferior position [59]. In contrast, Palepu et al. observed that both endplates had a concave form thickened at its center. Furthermore, they noticed that average endplate thickness was highest in the inferior plates compared to the superior plates. The reported thickness showed an increasing thickness value of 0.2 mm, 0.3 mm, 0.35 mm, 0.37 mm and 0.4 mm across L_1, L_2, L_3, L_4 and L_5 vertebra, respectively measured at the center [60]. The endplate's porosity was shown to be strongly correlated with its reported average thickness. Furthermore, they noticed that the average thickness of the endplates showed no significant change with age in contrast to the reported thinning of endplates accompanied with vertebral trabecular bone deterioration [52]. Table 1.4 provides an overview of the common material properties adopted by the different components of the epiphyseal plates.

Table 1.4: Biomechanical Properties of Vertebral Epiphyseal

Vertebral Epiphyseal Plates					
Structure	Material Model	E [MPa]	ν	G [MPa]	Reference
Cartilaginous Layer	Linear Elastic Isotropic	24	0.4	-	Wang et al. [24]
	Linear Elastic Isotropic	23.8 - 25	0.3 – 0.4	-	Benzel et al. [61]
Bony Layer	Linear Elastic Isotropic	5000	0.4	-	Ni et al. [62]
	Linear Elastic Isotropic	500 - 12000	0.3 – 0.4	-	Benzel et al.[61]
	Linear Elastic Transversly Isotropic	2000 - 8000 2000 - 8000 375 - 2000	0.30	-	Schmidt et al. [37]

Testing of the vertebra in its aggregate form (i.e. without anatomical decomposition) under low strain limits has previously shown to achieve an Ultimate Tensile Strength (UTS) of 3.5 MPa, Ultimate Percentage Elongation (UPE) of 0.8% and Elastic Modulus (E) of 410 MPa [63].

1.1.2 INTERVERTEBRAL DISCS

Alternating between each pair of adjacent vertebrae is a hydrated cartilaginous Intervertebral Disc (IVD) that exhibits large deformations (i.e. up to 35% in compression anteriorly and 60% extension posteriorly [64]) and provides flexibility. In general, an Intervertebral Disc is composed of three main structures, an inner gelatinous tissue termed the *Nucleus Pulposus* (NP) (77% water, 4% Collagen, 14% Proteoglycans) surrounded by thick outer ring of fibrous cartilage termed the *Annulus Fibrosus* (AF) (70% water, 15% Collagen, 5% Proteoglycans [65]) and covered inferiorly and superiorly by the two cartilaginous sections of the *Endplates*. The three components combined form the largest avascular part in the adult human body. The Nucleus Pulposus is a sphere-like semi-fluid incompressible tissue composed of water, fibrillar collagens and aggrecan as well as other minor components such as glycoproteins

(e.g. elastin and fibronectin). The NP's location is usually more posterior than anterior within the AF but may vary according to posture. The Annulus Fibrosus consists of a series of 15–25 concentric collagenous *lamella* (Figure 1–2). Each Lamellae is about 0.14–0.52 mm thickness and is composed of parallel collagen fibers oriented at 30° (to the disc's horizontal plane) and is embedded within a ground substance. Moreover, the Collagen fibers are arranged loosely in the innermost lamellae of the AF and arranged in a herringbone pattern in the outermost 1–2 layers providing further strength. Lamellae are usually characterized as ligamentous attachments to the external rim of the vertebra, and the *capsular* portion of the AF encompassing the NP. The total ring structure contains between 20–62 circumferential collagen fibers with an inter-bundle (i.e. ground substance or gelatinous phase) distance of 0.22 mm. The morphometry of the IVD varies along the span of the spine. Among other features, Pooni et al. reported on the variations of the height and cross-sectional area along the vertebral column. In specific, they noted that the least disc height was measured at T_4–T_5 with a larger increase caudally than cranially. Moreover, the disc areas increased linearly from the cervical to the lumbar spine [66]. Nevertheless, there is no clear separation in the boundary between the NP and the AF as it is estimated that the NP occupies 25-50% of the of the sagittal cross-area of the disc [54], often assumed to be 0.707 times the disc radius [64]. In measuring the dimensions of intervertebral discs of normal subjects, Mirab et al. reported a mean anterior discal height of 15.21 ±1.24 mm, 18.41 ±1.49 mm and 18.71 ±1.61 mm for the L_3/S_1 intermediate FSU levels. The discal heights decreased to measure 9.08 ±1.22 mm, 10.14 ±1.01 mm and 8.51 ±1.08 mm for the same respective levels posteriorly. Anterior-posterior lengths measured 32.86 ±2.44 mm, 33.08 ±2.37 mm and 31.33 ±2.55 mm for the respective levels. Finally, transversal discs measured 52.59 ±1.69 mm, 55.12 ±1.69 mm and 52.87 ±2.14 mm for each of the L_3/S_1 segmental levels [67]. However, the authors did not report on the precision of their instrumentation including the resolution of the captured images and technique of digitized measurements that may explain the high precision of their reported values

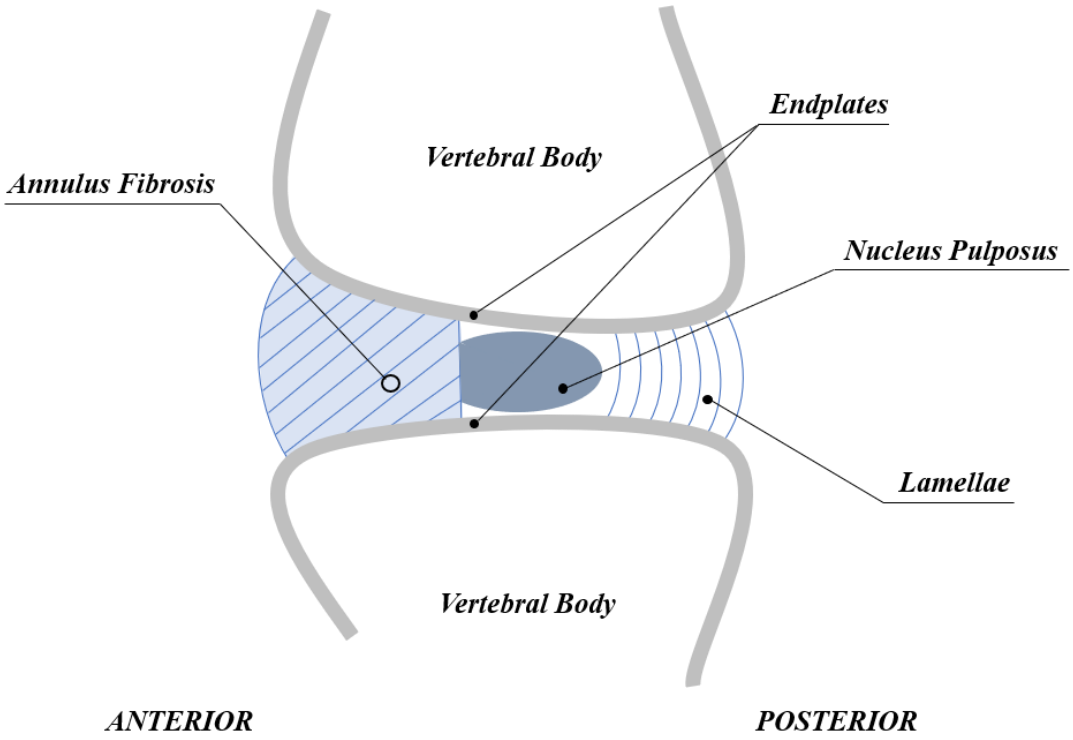

Figure 1-2: Depiction of Intervertebral Disc

Given the anatomy of the IVD described above (Figure 1–2), a typical healthy IVD exhibits a viscoelastic response. Mechanical Modelling of IVDs vary among the numerical studies found in literature. This depends on a number of factors including the aim, scope and desired output defined within the study. Schmit et al. categorized IVD modeling techniques into three classes namely (1) elastic, (2) multi-phasic transient and (3) transport model [68]. Basic Elastostatic models assume that the AF adopts linear orthotropic properties and the NP acts as an ideal fluid. This, however, has been suggested to have a limiting effect on the actual behavior of the AF which would otherwise be described as nonhomogeneous nonlinear anisotropic. The latter is due to the observed stiffness effects as a result of the resistance by collagen fibers which tends to invalidate the linear assumption of disc stiffness [69, 70]. While basic Elastostatic models provide information about the load-displacement, axis of rotation, compression preload, stress/strain fields and material/structural properties, material non-linearity plays a greater role in flexural and torsional loadings [68]. Elastodynamic models predict the free-vibration, forced-vibration, impact loading and damping behavior of the IVD. However, a multi-phasic transient model may more accurately represent the IVD which displays global creep/relaxation response,

swelling/osmolality and endplate interactions. Keller et al. [71], for instance, defined a three parameter model to describe the viscoelastic behavior of IVDs for all spinal segments using the Kelvin model in series with a spring. As such, they reported a good correlation between the experimental and analytical results (< 1%). Studies investigating the viscoelastic behavior suggest that the mechanics of axial disc displacement are highly time-dependent such that the rate and duration of loading impacts the recovery response [45]. This gave rise to the more advanced Transport Models of IVDs representing the IVD as bi-phasic, i.e. incompressible porous solid fully saturated with incompressible fluid phase. Additionally, it has been represented as tri-phasic which incorporates the chemical mechanics in addition to the bi-phasic characteristics. The latter model aims to better understand the fluid flow within the solid-fluid interaction that impacts disc's response by leveraging the fluid pressurization and collagen stiffening effects [68].

Typical FE models differentiate the properties of an IVD by defining three main components, namely, the *Nucleus Pulposus*, *Fibers of the Annulus* forming a collagenous matrix embedded in the *Ground Substance* of the Annulus Bulk. Tables 1.5 and 1.6 provide a list of material properties and models adopted by previous authors. Hyperelastic models may be used for a more accurate modelling of the IVD. In such a case, the ground substance would be represented by hyperelastic models and the fibers would adopt a non-linear tension-only behavior with alternating diagonal patterns.

Table 1.5: Biomechanical Properties of Nucleus Pulposus

Nucleus Pulposus			
Material Model	E [MPa]	ν	Reference
Fluid-Like solid, linear elastic, isotropic	1	0.499	Shirazi-Adl et al. [11], Goel et al. [10], Zhong et al. [27], Zhang et al. [44], Ruberté et al. [28], Kurutz and Oroszváry [29], Bellini et al. [34], De Visser et. al. [13], Fantigossi et al. [21], Ivanov et al. [32]
	2	0.499	Sylvestre et al. [42]
	4	0.499	Lavaste et al. [22], Goel et al. [10], Lafage et al. [31]
	10	0.4	Chen et al. [38]
Incompressible Fluid	-	-	Lu et al. [36], Little et al. [17], Rohlmann et al. [16], Kiapour and Goel et al. [25]
Incompressible Fluid-Filled Cavity	-	-	Park et al. [23], Schmidt et al. [37], Rohlmann et al. [12]
Quasi incompressible	-	-	Rohlmann et al. [72]
Hyperelastic, neo-Hookean	-	-	Moramarco et al. [73]
Mooney-Rivlin, incompressible	-	-	Noailly et al. [39], Baroud et al. [26], Schmidt et al. [68]
Poroelastic	varied	0.17	Malandrino et al. [40]
	1	0.45	Williams et al. [45]
	1.5	0.1	Argoubi and Shirazi-Adl [14]
	1.5	0.17	Ferguson et al. [43]
Viscoelastic Solid	2	0.49	Wang et al. [24]
Osmoviscoelastic	0.15	0.17	Schroeder et al. [74]

Table 1.6: Biomechanical Properties of Annulus Fibrosus

Annulus Fibrosus					
Material Model	Ground Substance		Fibers		Reference
	E [MPa]	ν	E [MPa]	ν	
Linear elastic, isotropic matrix, tension only elastic fibers	4	0.4	500	-	Lu et al. [36]
	4	0.45	500	0.3	Fagan et al. [75]
	4	0.45	400 / 500 / 300	0.3	Kurutz et al. [29]
	4.2	0.45	450	-	Zhong et al. [27]
	4.2	0.45	450	0.3	Shirazi – Adl et al. [11]
	4.2	0.45	175	-	Chen et al. [38]
	4.2	0.45	360 / 420 / 485 / 550	0.3	Denoziere et al. [76]
	2	0.45	500	-	Lavaste et al. [22], Goel et al. [10]
	8	0.45	360 / 420 / 485 / 500	-	Baroud et al. [26]
	4.2	0.45	Non-Linear	-	Goto et al. [30]
	4.2	0.45	500	-	Zhang et al. [44]
Hyperelastic matrix, nonlinear outwards stiffening fibers	3.15	0.45	-	-	Ruberté et al. [28]
	3.15	0.45	-	-	Noailly et al. [39]
	3.15	0.45	-	-	Moramarco et al. [73]
Hyperelastic matrix, nonlinear (14 layers, 8 layers)	Hyperelastic NeoHookean $c_1 = 0.3448$ $c_2 = 0.3$		-	-	Rohlmann et al. [72], Goel et al. [10]
Hyperelastic matrix, nonlinear (16 layers)	Hyperelastic Mooney-Rivlin $c_1 = 0.56$ $c_2 = 0.14$		-	-	Schmidt et al. [68]
Hyperelastic matrix, nonlinear	Hyperelastic Yeoh $c_{10} = 0.0146$ $c_{20} = 0.0189$ $c_{30} = 0.041$		Non-linear, 2 families of fibers $A_3 = 0.03$ (MPa), $B_3 = 120$		Puttlitz et al. [41]
Hyperelastic matrix, linear elastic tension only fibers	Hyperelastic Mooney-Rivlin $c_1 = 0.7$ $c_2 = 0.2$		500	0.3	Little et al. [17]
Viscoelastic matrix, nonlinear elastic fibers	8	0.45	-	-	Wang et al. [24]
Poroelastic matrix, linear elastic fibers	2.5	0.17	60	0.33	Ferguson et al. [43]
Poroelastic matrix, nonlinear elastic fibers	2.5	0.4	-	-	Williams et al. [45]
	2.5	0.1			Argoubi et al. [14]

1.1.3. MUSCLES

In-vivo studies of the spinal system have estimated normal spinal loadings reaching up to 1500 N. Under the control of the passive subsystem alone, the spinal column behaves similar to an inverted pendulum, as described by Panjabi [3]. As such, the muscles have been previously shown to play a role in spinal buckling prevention [77]. Mcgill et al. studied the coordination in muscle activation to maintain the stability of the spine and the resulting instability from the loss of normal motor patterns [78-80]. Hence, this realizes the presence of a counter-support beyond the passive elements alone to maintain an erected spine dynamically supported. This may be achieved via the active musculature and controlled by the high innervation that transduces activation into signals communicated with the nervous systems.

A total of 700 muscles have been currently identified within the human body varying according to type between skeletal, smooth and cardiac. Smooth muscle cells, as the nomenclature suggests, lack striations and sarcomeres. As such, a smooth fiber has a spindle shape with a single nucleus and a fibral diameter of 3–8 μm spanning 200 μm long. These are smaller and shorter than skeletal muscle fibers measuring 10–100 μm in diameter with lengths up to 600 mm (e.g. Sartorius muscle [81]). However, cardiac muscle fibers measure 10–20 μm in diameter and 50–100 μm in length [82].

Skeletal muscles form the largest tissue set in the body characterized by high plasticity and the ability to vary their mass and strength considerably [83]. As the name suggests, Skeletal muscles are voluntary muscles identified by their direct attachment to the skeletal system. Such muscles vary in speed of contraction, fiber arrangement and size. Fiber arrangements vary between parallel (fusiform) and slanted (unipennate, bipinnate and multipinnate) depending on the average fiber angle relative to the axis of the force generation of the muscle, namely the Pennation angle. Herman et al. provided a lengthy review of muscle fiber arrangement, microscopic and macroscopic perspectives of the muscle constitution and force muscle generated as a function of their length and contraction speed [63]. In general, fiber length plays a role in the muscle function such that longer fibered muscles produce forces over greater ranges of lengths. This is based on the fact that a higher number of sarcomeres are embedded within the muscle fiber bundles. In contrast, shorter fiber muscles have a lower number of sarcomeres but are able to produce forces at higher relative velocities [84].

The muscles of the back are categorized into three groups; intrinsic or deep muscles that connect to vertebral column, intermediate muscles that help with the thoracic cage movement and superficial muscles that control neck and shoulder movements. Most commonly, intrinsic muscles are often considered the only true back muscles dominated by the *erector spinae* (*ES*), a group of interlocked muscles that span from the skull to the sacrum [85]. The erector spinae mainly control the forward flexion of the thorax which are embedded within the thoracolumbar fascia. To the author's knowledge, Macintosh and Bogduk [86] were the first to report a comprehensive descriptive anatomy of the lumbar erector spinae while Delp et al. [87] provided the first anatomical measurements of these muscles. This muscle set is mainly formed of the *Spinalis* spanning along the T_{11}–L_2 spinous processes which connects to the thoracic vertebrae and blends with the longissimus thoracis laterally. The largest of the erector spinae group are the *Longissimus* that originate at the transverse processes of the inferior vertebral levels in the form of five bands from the lumbar transverse processes to attach to the iliac crest. Finally, the last of the ES muscle group set, namely *Iliocostalis,* are normally narrow with fusiform fibers. The Iliocostalis Lumborum originates at the medial-dorsal end of the iliac crest and inserts into the L_1–L_4 lumbar transverse processes and thoracolumbar fascia along four broad bands. Anterior to the erector spinae, a deeper and shorter muscle, namely *multifidus* (*MF*), lies in association with the spinous and transverse processes. This muscle consists of numerous bands that originate from each vertebral spinous process and lamina to reach two to four segments below. Ward et al. [88] analyzed the constitution of the multifidus muscle to observe three major design factors suitable for stabilizing the spine. First, they observed that the multifidus was composed of highly pennate fibers extending only 20% of its actual length. Second, their mechanical testing revealed that its fibers are twice as stiff as limb muscle tissue. Third, the shorter sarcomeres of the multifidus during extension may realize a higher muscle strength especially in rotational maneuvers. Dispersed between the vertebral protrusions are even smaller muscles; *rotators*, *interspinales* and *intertransversarii*. Spanning along the length of the spine, the words "cervicis", "thoracis" and "lumborum" are commonly augmented to the latter muscles.

Table 1.7: Physiological Cross Sectional Area (PCSA) of reported left, right and average Erector Spinae

Muscle	Erector Spinae PCSA (cm^2)		
	Erector Spinae Left	**Erector Spinae Right**	**Erector Spinae Average**
Maki et al. [89]	21.885	21.429	21.66
Sugawara et al. [90]	12.0	11.1	11.5
Jorgensen et al. [91]	-	22.0	-
Shin et al. [92]	-	-	21.45
Schweitzer et al. [93]	-	-	11.6
Bogduk et al. [86]	-	-	16.5
Reid and Costigan [94]	16.02	15.73	15.9
Tracy et al. [95]	-	-	20.0
Chaffin et al. [96]	18.0	18.1	18.05
Tsuang et al. [97]	16.55	16.375	16.46

Table 1.7 reports measured values of the Physiological Cross-Sectional Areas (PCSA) of left, right and average erector spinae muscles from previous reported publications. Average measured values of previous reports have shown that the erector spinae cross-sectional areas at normal postures measured 26.0, 19.6, 8.3 cm^2 at the L_3/L_4, L_4/L_5 and L_5/S_1 spinal levels, respectively for 26 male adults over the range of 17 to 56 years with a mean age of 29 years [98]. Additionally, the Multifidus has been previously measured to have a mean PCSA of 23.9 ±8.4 cm^2 [87].

Further extrinsic spinal muscles play a role in postural spinal stabilization. One of the latter muscles includes the Quadratus Lumborum which assists in lateral bending. PCSA measurements of the Quadratus Lumborum measured a mean of 4.7, 7.1, 7.5 cm^2 at L_3/L_4, L_4/L_5 and L_5/S_1 spinal levels. [98].

Marked as the largest muscle in the cross-section of the lower lumbar vertebra, the Psoas Major has been suggested to aid the spine during lateral flexion by generating increased compressive forces [99]. Yet, recent studies have shown that the muscle's primary function is to

permit hip flexion [100]. PCSA measurements of the Psoas Major muscle recorded 14.8, 17.4 and 14.9 cm^2 at the L_3/L_4, L_4/L_5 and L_5/S_1 spinal levels, respectively [95].

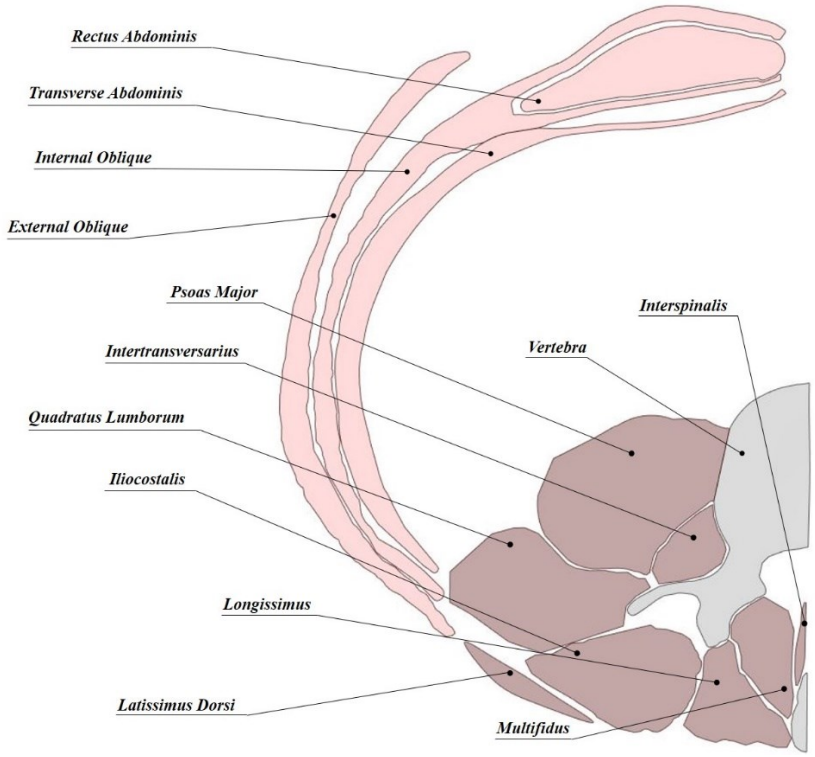

Figure 1-3: Muscle Cross-section at L4 level depicting the location of the abdominal muscles (in light red) and the spinal muscles (in dark red)

Lying lateral to the Quadratus Lumborum muscle are a set of abdominal muscles, namely, *Transverse Abdominis* (*TrA*), *External Oblique* (*EO*), *Internal Oblique* (*IO*) and *Rectus Abdominis* (*RA*) listed in increasing order of thickness [101] (Figure 1–3). These anterolateral muscles have been shown to play a role in the stability of the spine in different functional activities [102]. With the angular variation of their fiber arrangements, the composite mechanism of the muscles tightly bind together and upon contraction pressurize the abdominal cavity [84]. The Transversus Abdominis defines the deepest lateral muscle originating from the lumbar vertebra and iliac crest to line interiorly by the *Transversalis Fascia*, an endo-abdominal fascial layer covering the entire abdominal cavity.

Several methods to represent the force–velocity relations of a muscle have been proposed following *in vivo* experimentation. Most notably, the Hill relation has been shown to possess several advantages such as its applicability for several types of muscle for skeletal muscles in the

relaxed state [103]. Schleifenbaum et al. conducted tensile tests on the femoral muscles attached and observed mean failure loads of 26.7 ±8.8 N with an elongation of 94.8 ±36.2 % [104]. Hansen et al. provided an extensive review of the cross-sectional areas and force resultants measured at the different spinal levels [105]. Table 1.8 lists the passive mechanical properties of muscle tissue for various species.

Table 1.8: Biomechanical Properties of Passive Relaxed Muscular Tissue

Passive Mechanical Properties of Muscle Tissue			
Material Model	E [MPa]	ν	Reference
Linear Elastic, Non-Homogenous, Bulk Muscle, Human	1.2	0.45	Metan et al. [106]
	480	-	Buchanan et al. [107]
	$E_{MULTIFIDUS}$ = 0.03687		Ward et al. [88]
	$E_{RECTUS\ ABDOMINIS}$ = 0.52		Deekan et al. [108]
	$E_{TRANSVERSUS\ ABDOMINIS}$ = 1.03		
	0.4	-	Taylor et al. [109]
Linear Elastic, Indentation, Bulk Muscle, Human	0.08	-	Pailler et al. [110]
	0.06	-	Steege et al. [111]
	0.0062	-	Krouskop et al. [112]
	0.05 – 0.145	-	Reynolds [113]
	0.021 – 0.13	-	Mak et al. [114]
Linear Elastic, Fiber Bundle, Human	$E_{MULTIFIDUS}$ = 0.09134	-	Ward et al. [115]
	$E_{LONGISSIMUS}$ = 0.06285		
	$E_{ILIOCOSTALIS}$ = 0.05883		
	0.0436 – 0.0335	-	Noonan et al. [116]
Linear Elastic, Bulk Muscle, Rat, Cat or Rabbit	0.05 – 0.35	-	Close et al. [117], Hawkins et al. [118], Herzog et al. [119]
2-parameter Viscoelastic Model, Fiber, Porcine	5 Hz: 8.5 kN/m 30 Hz: 347 kN/m	-	Aimedieu et al. [120]

Silver-Thorn et al. [121] reported bulk soft tissue relaxations after indenting muscle tissue at a speed of 5 mm/s to observe a 55–95 % force relaxation on average. Taylor et al. measured, in experimenting with porcine muscle, an apparent toughness of a muscle layer as 2.49 kJ/m^2 and a fracture stress of 0.15 MPa [109].

Tendons extend from muscle peripherals and adhere with bone structures to form a precise dense connective tissue assembly to resist movement and damage [93]. Tendon cellular structures consist of protein collagen (mainly type I collagen with 60% -85% [122]) fiber embedded in a 55–70% water composition within a proteoglycan extracellular matrix. This cell-

matrix composition of tendons is similar to that of ligaments in terms of cell type, vascular and innervation sources. However, the cellular structure of tendons contains much less amount of elastin than collagen [122]. Researchers have realized that the collagen fibrils are the smallest functional bearing unit of the tendon and it is that cross-linking between in collagen that is believed to be a major source of the mechanical properties of the tendon [123]. Tendons are characterized by their capability to recoil after the stretching force is removed as a result of "crimps" found within the tendon fibrils. In specific, when it is stretched, these crimp zones are reduced followed by recoil of tendon fibrils upon force removal. A highly compliant tendon results with a change in the tendon's strain response with an extension beyond its normal length causing a loss of joint position control. Moreover, the elongation present in tendons allows the muscle to shorten further which, in turn, allows the sarcomere to shorten further for a given contractile force. This elevates the operative mechanism of the muscle force effects [124]. Mechanical properties of tendons have been previously observed to be ~1.2 GPa for the Transversus Abdominis tendon with a mechanical hysteresis of 5–25% reaching up to loads of 530N [125]. Typical tendon dimensions of the spinal muscles measure thicknesses ranging from 0.32–0.86 mm with lengths of 19.23–44.14 mm [126].

1.1.4. THORACOLUMBAR FASCIA

In accordance with active muscle contraction, stabilizing muscular strength requires the assistance of a set of load-reducing mechanisms when substantial external loads are to be lifted [127]. Among other tissue, this has been suggested to be the result of mechanisms set forth by a complex aponeurotic fascia surrounding the torso, namely the Thoracolumbar Fascia (TLF). Willard et al. [128] defined the TLF as a connective tissue composed of "irregular collagen fibers" that wraps muscle tissue and resists tensional forces. Anatomically, the TLF is a "girdling structure of aponeurotic and fascial layers" that separates the paraspinal muscles from posterolateral abdominal muscles. The TLF, also termed axial or appendicular fascia, is the second of four-fascia located in the deep region surrounding the musculoskeletal system [129]. In specific, it is a relatively thicker and denser fascia that can be divided into two formations based on location: (1) Axial Investing Fascia (also composed of Epaxial Fascia and Hypaxial Fascia) and (2) Appendicular Investing Fascia [130]. The two fascial components lie within the erector spinae complex along the thoracic and lumbar regions of the spine. Specifically, the

Epaxial Fascia and Hypaxial Fascia fuse at the Lateral Raphe to conceive one large cylinder investing the muscles of the Thoracoabdominopelvic and two longitudinal cylinders on each of the two sides of the spinous process of the vertebrae [131]. Anatomically, the TLF covers the extensor muscles in the thoracic regions and extends to attach to the thoracic vertebrae posteriorly and the ribs laterally within the medial region. Its fiber arrangement defines an angle of 20–40° sloping in the craniolateral-to-caudomedial direction [128]. It then splits into three layers, Anterior (*ALF*), Middle (*MLF*) and Posterior (*PLF*), covering the Psoas Major, Quadratus Lumborum and Erector Spinae with the Multifidus in the lumbar region, respectively (Figure 1–4).

In general, the thickness of the aponeurosis was previously measured to be 0.52–0.55 mm in the lumbar region but becomes significantly thinner in the thoracic region [132]. The MLF, situated between the Quadratus Lumborum and the Erector Spinae, yielded an approximate thickness of 0.11–1.34 mm and reduces to 0.62 mm at the transverse process connection. This was observed to be greater than the reported thickness of the PLF near the spinous process of 0.56 mm in one study [132]. Willard et al. observed that the PLF conceives three sublayers comprising a superficial layer with a thickness of 75 μm increasing to 152 μm at the intermediate layer to reach 450 μm for the deep layer of the PLF (i.e. to measure a total of 0.68 mm) [128]. In comparison, the ALF thickness has been reported to range between 0.06–0.14 mm with a mean value of 0.1 mm [132].

The junction of the hypaxial muscles (i.e. EO, IO, TrA) and epaxial muscles (i.e. ES, MF) is achieved via the *Lateral Raphe* (*LR*). According to Bogduk & Macintosh, the LR represents a thickened complex of dense connective tissue set along the iliac crest and extends towards the 12th rib [133]. This intersection joins the paraspinal muscle sheaths with the TrA and IO muscle sheath to form a dense junction [134]. Furthermore, this forms a triangular-shaped structure at the LR termed Lumbar Interfascial Triangle (LIFT), also called the *Common Tendon of Transversus Abdominis* (*cTrA*).

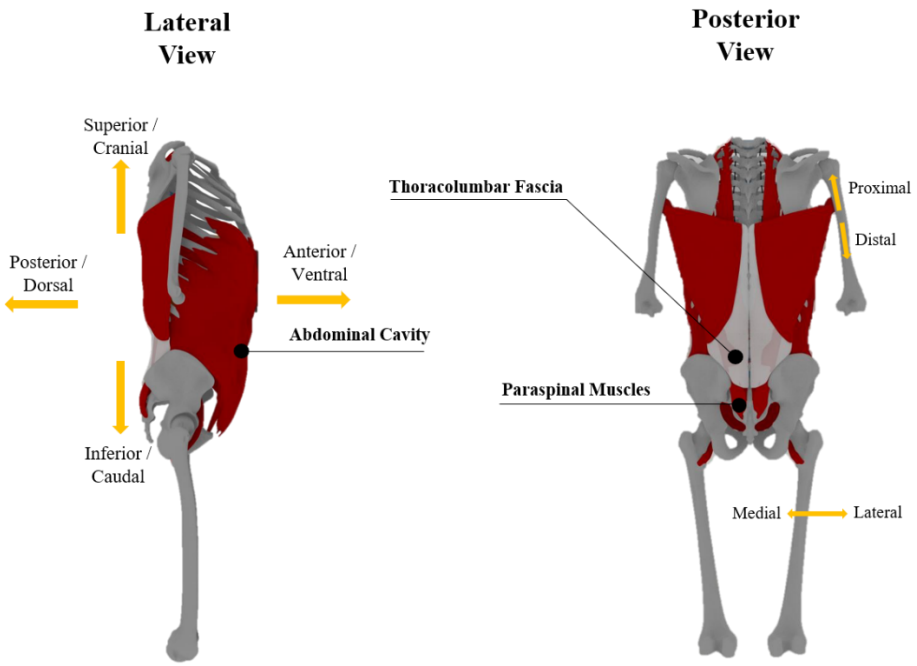

Figure 1-4: Thoracolumbar Fascia and Abdominal Cavity locations

Specifically, two models emerge in research when depicting the TLF which include the two-layered model and three-layered model [135]. Willard et al. conducted a review differentiating the main anatomical differences [128]. In both models, the Paraspinal Muscles are contained in a sealed compartment differing only by the inclusion of the ALF. This is mostly due to the fact that the ALF's structure is relatively thin and may not transmit tension from the abdominal muscles to the TLF [90]. Thus, researchers were mainly concerned with the structure and mechanism of the PLF and MLF and considered the ALF as part of the *Transversalis Fascia* (*TF*) [136].

Willard argued that the TLF connectivity provides central support to the spine [137]. Vleeming and Stoeckart showed particular interest in the PLF attesting its importance in transferring forces between the spine, pelvis and lower limbs promoting coordinated activities (e.g. walking and running) [138]. Barker et al. argued that the strength of the MLF has been underestimated and that it can uphold force transfer of strong TrA contractions which plays a large role in lumbar segmental control [139]. A recent study by Vleeming examined the coupled mechanism of Paraspinal and Deep Abdominal Muscles when noticing a "point of equal tension" between the muscles by force transfer through both the middle (MLF) and posterior layers (PLF)

of the TLF [140]. This agrees with Fairbank et al. and Gracovetsky's suggested role of TLF which realizes that any muscle or group of muscles that subject the TLF to lateral tension can provide an extensor moment [141]. Garfin et al. observed a loss of 15% in muscle strength when examining the role of the fascia in maintaining muscle pressure and tension [142]. Furthermore, Gracovetsky et al. observed a 30% increase in TLF length when the spine is fully flexed [127]. A series of experiments by Tesh et al. showed that the TLF had a less-than-expected role in sustaining lateral forces and performed tensile tests on TLF specimens to conclude that the PLF can withhold up to 335 N [102]. This value was later considered to be an underestimate, whereby Adams and Dolan's calculation signified that the tensile loading capability of the TLF could exceed 1 kN [143]. They consequently suggested that Tesh's observations could be the result of testing cadaver models in full flexion state with arms positioned behind the head. Moreover, they realized that the TLF is arranged in a way such that it is mechanically strongest in a straight posture as it acts on straightening the lumbar lordosis.

Few studies have been conducted to characterize the mechanical properties of the fascia layers. Yahia et al. conducted tensile tests on TLF cadaveric specimens and achieved stress-strain graphs with a strain of 11.43% including viscoelastic characterizations of the TLF showing a 3 N reduction in ~100 s [144]. In other fascia studies, the Transversalis Fascia was previously defined as having a young's modulus of 3 MPa [108] and ranging between 1–27 MPa [145]. The Fascia Lata, for instance, measured a young's modulus of 3.2–41.9 MPa and 71.6–275.9 MPa in the transverse and longitudinal directions, respectively [146]. This was previously measured to be 397.5 MPa by Butler et al. [147].

The anatomical position of the TLF suggests that it may indeed generate a reasonably large extensor moment with low compressive forces on the spine with the aid of abdominal muscles. This motivated the further understanding of the TLF mechanism in relation to the abdominal muscles, specifically, to recognize the mechanism of tensioning TLF [140]. In theory, the Abdominal Cavity and Thoracolumbar Fascia also act as compensatory stabilizers of the Lumbar Spine in Patients with Low Back Pain (LBP). Fairbank et al. [148] observed abnormal elevations of *Intra-Abdominal pressures* (*IAP*) during lift movements in patients experiencing LBP. This stimulated researchers to investigate the role of IAP in spinal stability.

1.1.5. ABDOMINAL CAVITY

The abdominal cavity lies deep to the thin interlining of the Transversalis Fascia and anterior along the posterior wall of the retro-peritoneal fascia. The abdominal cavity is the largest enclosed cavity in the human body bounded cranially by the diaphragm and caudally by the pelvic cavity. The abdominal cavity houses numerous vital organs including the stomach, liver, gallbladder, spleen, pancreas, small and large intestines, etc. The transverse area of the peritoneal cavity has been previously measured to be in the range of 144.4 cm^2 at the L_4/L_5 level [149]. According to a cadaveric study conducted by McGill et al., a transverse cross-section at the L_4/L_5 level showed that among 13 subjects, the length between the anterior layer of the trunk to the disc centroid was estimated to be 57.2 ±5.2 % of the total trunk depth [99]. Furthermore, previous measurements of the abdominopelvic cavity recorded mean areas of 94 and 103 cm^2 [150].

In association with active abdominal muscular contraction, the abdominal pressure, namely *Intra-Abdominal Pressure* (*IAP*) was observed to dynamically change in different maneuvers and was previously suggested to play a role in spinal stability [151]. Initially, researchers were met with the challenge of properly measuring the IAP. Specifically, the low fluid content that transmits the IAP resulted with difficulties in measuring animal IAP using open-ended catheters [152]. Advanced measurements later used air-filled balloons placed in the abdomen using catheters which were connected to manometers [153]. This introduced the definition of the resting abdomen as positive with a magnitude of 5–7 mmHg [154]. Advancements in technology have later allowed researchers to realize that IAP could be measured through natural orifices (e.g. vaginal fornices and rectum) or through miniature radio-pill transmitters. Hence, the literature contains a large variation of the reported normal and abnormal IAP depending on the method adopted for measurement. De Keulenaer et al. conducted a review to describe a normal intra-abdominal pressure and the effect of positioning and body mass on IAP [155]. They concluded that a normal IAP magnitude ranges between 5–7 mmHg. In morbidly obese subjects, this may increase up to 9–14 mmHg. These were achieved via measuring the IAP through the bladder in a supine position. However, orienting the patient's bed to an angle of 30–45° resulted with an average IAP of 4–9 mmHg. Fletcher et al. conducted a similar study to investigate whether prone positioning results with a raised IAP, which may result with adverse physiological effects. They observed that IAP in the supine position resulted

with 14.5 mmHg while the mean IAP in the prone position was defined at 10.3 mmHg to reach 8.4 mmHg after a 5-hour bed rest [156].

1.1.6. PERIPHERAL NERVES

The third main subsystem described by Panjabi [3] is the neural and feedback system, composed of the *central (CNS)* and *peripheral (PNS)* nervous system. The central nervous system includes the brain and spinal cord. The peripheral nervous system refers to the supplementary nervous system acting as a relay between the CNS and the different body organs. In specific, this includes the somatic nerves, autonomic nerves, sensory and autonomic ganglia with their corresponding tissue elements [157]. The nerve is a cable-like structure formed of a bundle of nerve fibers, namely *axons*, and is composed of *neurons* on its cellular level. These cells have special properties to send signals in the form of electrochemical waves with neurotransmitters at the junction of neurons, namely *synapses* for communication.

The complex nervous architecture forms a plexus at the lumbosacral level, *lumbosacral plexus*. Payne provides a lengthy review of the different nerve connectivity and nomenclature of the lumbosacral plexus [158]. At the L_4–L_5 spinal level, the exiting nerve beneath the L_4 superior articular process divides anteriorly and posteriorly. The anterior nerves include the *Accessory Obturator Nerve* and the *Obturator Nerve*. Furthermore, the posterior nerve consists of a subdivision that extends to the *Femoral Nerve*, branches out to the psoas and iliacus muscles and extends towards the *Lumbosacral Trunk*. At the root of the nerve, extensions for the Gray Rami Communicantes exist. Exiting nerve roots from the lumbar FSUs extend to form the Lumbar Plexus and are enclosed within an osseoligamentous space which is exposed to dynamic stretches and strain [158].

The exact mechanism behind nerve tissue injury causes, contributions and severity of its pathologies remains enigmatic. While compression is the most common injury mechanism associated with nerves, specifically the exiting nerves, inflammation and nerve tethering have been believed to be common causes related with pain. Hence, the effect of mechanically inducing force on nerve responses are necessary for clinical assessment. Beel et al. conducted tensile tests on mice dorsal nerve roots at a low strain rate (i.e. 1 mm/s) measuring a maximum stress of 306 kPa and a fracture stress of 302 kPa [159]. Sunderland et al. observed that the nerve strain-rate is time-dependent. However, this varies based on the nerve's diameter and histology.

In specific, they exhibit a higher mean maximum stress (624.9 kPa) and mean Modulus of Elasticity (E) (2.9 MPa) at higher strain rates of 15 mm/s [160]. Furthermore, the specimens recorded a mean reduced relaxation of 9–12% [161]. Similar to most soft tissue, nerve roots exhibit an initial toe region (i.e. nerve elongates without being stretched) then an elastic region and is followed by rupture directly beyond the proportional limit [162]. Moreover, Singh et al. observed that the thinner roots (i.e. higher lumbar roots) are more susceptible to injury than thicker roots (i.e. lower lumbar roots) [160]. Table 1.9 depicts the biomechanical properties of nerve roots found in the literature.

Table 1.9: Biomechanical Properties of Nerve Roots

Passive Mechanical Properties of Nerve Tissue					
Material Model	**E [MPa]**	**Ultimate Strain [%]**	**Max Stress [MPa]**	**Rate [mm/s]**	**Reference**
Linear Elastic, Mice	1.2	46	0.302	1	Beel et al. [159]
Visco-Elastic, Mice	1.3 2.9	29.5	0.257 0.624	0.01 15	Singh et al. [160]
Linear Elastic, Human	-	-	3.9 – 29.4	1.27	Sunderland and Bradley [163]
	1.71	15 (elastic limit) 28 (failure)	-	0.17	Kwan et al. [164]
	-	18	13		Herman et al. [63]

1.1.7. SPINAL STABILITY AND LOADING

The standalone vertebral column is inherently unstable [165]. *In-vitro* experimentation has revealed that the standalone thoracolumbar spine (T_1-L_5) buckles under a caudo-cranial force just above 20 N [166] and the Lumbar spine (L_1-L_5) under a load of 90 N [77]. However, an *in vivo* spine experiences up to three times the body weight in the standing position [167]. In fact, these loads may be increased up to 6000 N in excessive daily activities and 18000 N when powerlifting [168]. This stirred a high interest for researchers to better understand the stabilizing mechanism of the human spine.

The ability for the musculoskeletal system to carry out its functions may depend on its state of stability. In the case of the musculoskeletal system, this is interpreted as Spinal Stability. However, there is little consensus among researchers on the exact definition of stability, admitting a challenge when attempting to quantify it [169]. McGill et al. conceived the foundation of stability to be based on potential energy [79]. In specific, they defined stability

such that regardless if the system “is in equilibrium (static) or changing with time (dynamic)”, they “must give a small perturbation and observe the new behavior. If the new behavior is approximately the same as the old, qualitatively speaking, the system is stable. If the changed behavior becomes indistinguishable from the old behavior, returning to its original position or trajectory after a sufficiently long time, the system is asymptotically stable”. Moreover, they defined a system as unstable “if the disturbed behavior differs significantly from the old behavior”. Panjabi defined stability from the basis of the three subsystems that compose the musculoskeletal system [3]. Furthermore, White and Panjabi defined instability as “the loss of the ability of the spine under physiologic loads to maintain relationships between vertebrae in such a way that there is neither damage nor subsequent irritation to the spinal cord or nerve roots, and, in addition, there is no development of incapacitating deformity or pain due to structural changes” [170]. Moreover, the American Academy of Orthopedic Surgeons defined stability as the “capacity of the vertebrae to remain cohesive and to preserve the normal displacements in all physiological body movements [171]. Yet, the exact definition of “normal physiological movements” remains debatable with the challenge in correlating standard references with clinical and radiological findings [172].

In FE studies, a preload, namely the follower load, is applied along the vertebral surfaces following their orientations. In fact, Patwardhan et al. observed that a compressive load of 100 N resulted with an increase in the spinal load-bearing capacity up to 1200 N without damage or instability [173]. Zahari et al. investigated the variational effects of the follower loads when applied to finite element models [174] by specifying a set of pure moment loads of 7.5 Nm and 1.5 Nm in flexion and extension, respectively, with a 400 N compressive preload. They observed insignificant moments with inaccurate follower loads. Preloading in spine models has been previously observed to stiffen the IVD [65]. This was also observed in the lumbar facet joints whereby the facet force and contact area pressure increased [175]. Guo and Fan realized that the increase of follower load results with a decrease in vibrational effects and an increase in the dynamic response [176]. Kim et al. investigated the origin of the follower load which they observed is a result of the compressive forces generated by the back muscles in harmony with the activation of trunk muscles [177]. Han et al. optimized their ligamentous spine model which consisted of 232 spinal muscles to achieve an optimum compressive follower load that ranged from 496 N at the L_2–L_3 level to 627 N at L_5–S_1 level [178]. Pitzen et al. validated their FE

model with 12 cadaveric specimens of the L_3–L_4 SFU which exhibited an axial loading compression of 600 N, torsional loading of 25 Nm and shearing load of 250 N [179]. The varying spinal loads based on different daily activities were assessed by Rohlmann et al. who adhered a telemetered vertebral body replacement to measure loads in vivo [180]. The highest resultant force they measured was 1650 N when lifting a crate of 10.8 kg from the ground. The maximum bending moment measured was 6.2 Nm during an upper body flexion and the maximum torsional moment was measured during the "tying shoes" activity measuring 3.5 Nm. Shear forces were maximum in the anterior direction during upper body flexion (130 N), maximum in the lateral and posterior direction when the arm was raised with a weight in hand recording 230 N and 212 N, respectively. Moreover, NP pressurizations were measured to vary from 0.4 MPa when lying to 1.5 MPa when standing and sitting to reach 2.3 MPa when lifting [181]. If the spine is viewed as a cantilevered beam pivoted at the hip, the forces measured at the lower end of the back greatly exceed intervertebral disc tolerances which has led to the conclusion that additional support mechanisms must be present [182].

Seemingly, the first to invoke the concept that IAP assists in spinal unloading was Sir Arthur Keith, in 1923, who suggested that pressurizing the abdominal cavity in association with abdominal muscles induces a stiff cylindrical compartment (raised up to 100–150 mmHg) [183]. Nevertheless, the earliest theory was postulated by Bartelink who believed that the raised IAP due to abdominal muscle contraction created a balloon-like structure in the abdomen that results with an extensor moment [184]. He noted that a power-lifter carrying an 890 N load may exhibit a lumbosacral discal stress of 8900 N while an intervertebral disc fails at 1500–6200 N. Morris et al. built on Bartelink's calculations and recorded an IAP peak pressure of 200 mmHg which, in turn, reduces the force on the lumbosacral disc by 30% [182]. Termed the balloon theory, this provided the basis for future researchers to understand IAP mechanism and is considered the most widely accepted model for lifting even though the load reduction was not sufficient in the study [185]. Davis et al. realized that the increase in IAP during lifting occurs abruptly (i.e. 200 mmHg), but for a brief amount of time (i.e. 0–5 s) then plateaus at lower levels (i.e. 60 mmHg) during the remainder of the lift [186]. The peak pressure, which he termed "snatch pressure", was observed to depend on the speed of the lifting mechanism. The longer the lift was, the lower the snatch pressure recorded until it became negligible for durations longer than 600 ms. Studies have shown that, indeed, there is a correlation between the snatch pressure and lever moment on

the lumbar spine. However, Farfan et al. had opposing views and strongly suggested that pressures in the cavity cannot rise above aortic blood pressure (i.e. 120 mmHg) and, if it does, cannot suffice to avoid vertebral failure by not sufficiently opposing compressive forces [187]. This was, later, disproved by recording pressures up to 360 mmHg with vigorous exertions in the cavity and 200 mmHg during defecation [188]. Even though, it was believed that Valsalva maneuvers increase IAP, Nachemson et al. observed an increase in intra-discal pressure only during upright positions but a decrease if the subject is in a 30° forward bend [169]. Arjmand et al. showed that IAP upraise is the result of co-activation of abdominal muscle co-activation [189]. Heyman used the Plastic theory to show that the geometrical shape of the spine adopting the lumbar lordosis, in specific, along with IAP are necessary for the overall stability. They suggested that the IAP serves as a force reducing mechanism on both concave and convex arching of the Lumbar spine in different maneuvers [190]. The balloon theory was questioned on several aspects and proved inconsistent and limited by several authors which gave rise to other theories regarding the mechanism of the IAP. McGill et al. proposed that the IAP induced provides a rather resistive type of support by limiting intervertebral rotation and translation [191]. They then realized that its main role is providing additional stiffness to the trunk when combined with a co-activation of abdominal and back muscles [192].

Gracovetsky et al. investigated the ligamentous system in combination with the TLF and suggested that its mechanical properties may allow it to store sufficient tension to permit the spine to overcome the exceeded forces imposed on the muscles [193]. He proposed that the co-activation of the back muscles and abdominal muscles allows a transfer of tensile forces through the TLF and gives rise to IAP to provide anti-flexion moments. Essentially, this would provide an unloading effect on the spine which they termed “the hydraulic amplifier mechanism”. The exact mechanism of the IAP remains unclear and conflicting theories have risen in the past suggesting a need for further studies to test the different claims [194]. Recent understandings of the IAP have led to the concept of abdominal compliance (i.e. ease of which abdominal expansion can occur) which may be an indicator of pathologies [195]. This facilitated interest in realizing the IAP as a potential load-reducing mechanism.

The literature suggests numerous hypothetical concepts of spinal stability mechanisms that comprises the augmentation of the different body systems. It is evident, also, that there is a

great deal of variability in the biomechanical characteristics reported. This is expected given the inherent variation in anatomical features between human bodies.

1.1.8. Mechanical Variations of Tissue in Spinal Disorders

Low Back Pain (LBP) has been previously shown to be strongly associated with abnormalities within the musculoskeletal system in the body [196]. Young athletes with LBP, for instance, have exhibited abnormal and asymmetrical spinal motions [197]. Nevertheless, recent studies have reported that patients with LBP have lower segmental motions [198]. Posner et al. [199] reported a set of proposed thresholds that may suggest clinical instability for ROM including upper threshold values for flexion-extension of 15° for L_1–L_4 levels, 20° for L_4/L_5 and 25° for L_5/S_1 and an anterior translation of 4.5 mm which were later confirmed by Panjabi et al. [200]. Hence, it has been considered that any segmental deviation from the normal ROM may likely insinuate a disorder regardless of the direction.

Given the high nerve density in endplates, it has been suggested that vertebral endplates may play a role in LBP. In fact, nerve densities increased by more than 75% in endplates with LBP compared to normal endplates and has been observed to be even more innervated than intervertebral discs [58]. Permeability has been shown to increase by 50–130 % and thickness decreased by 20–50 % with advancing disc degeneration [201]. This was observed to mostly develop at the mid region whereby the epiphyseal plates become softer and more permeable [202]. In contrast, other studies have shown that endplate changes are mostly a normal consequence of age with no significant correlation to CLBP [203].

Patients with low back pain have shown variation in thickness, activity and recruitment of the Transversus Abdominis (TrA) and lumbar multifidus. Hides et al. investigated the cross-sectional area (CSA) of the multifidus and realized a decreased CSA in the muscle for patients with LBP [204]. Muscle atrophy was measured by localizing the spinal level at which the patient feels pain compared with its respective pair whereby the mean difference was 24.03%. He et al. conducted a review of the literature and realized an association between the CSA of the paraspinal musculature. They reported an increased presence of fat within the paraspinal muscles [205]. However, this decrease in size of the multifidus was suggested to be localized [206]. In terms of muscle recruitment and activity, studies have shown little-to-no difference for the internal and external oblique muscles but realized less TrA activity when testing EMG activity

[207]. The increase in muscle activity, tone and stiffness of the muscle is believed to compensate for the poor ligamentous integrity [208]. Non-invasive measurements of mean muscle stiffnesses using the myotonometer (i.e. a patented electronic tissue compliance meter) for patients with CLBP ranged between 299.67 N/m and 315.07 N/m and 316.80 N/m and 328.47 N/m, 267.60 N/m and 281.40 N/m for the L_3, L_4 and L_5 levels, respectively [209].

In a study conducted by Hodges et al. to investigate changes in mechanical properties of the trunk, the trunk stiffness was estimated to be greater in LBP patients when responding to anterior stimulation while damping decreased when stimulated in anterior and posterior directions when compared with healthy control groups. They suggested that the increase in trunk stiffness in LBP cases was most likely due to total muscle activation and control [210]. Similarly, Silfies et al. noticed that chronic low back pain groups demonstrated higher activation levels of the abdominal muscles than the normal control group [211]. Fairbank et al. observed that patients with LBP always experienced higher recordings of intra-abdominal pressure when lifting when compared with normal patients (up to a ~40% difference) [212]. In fact, previous suggestions related the possibility of using intra-abdominal pressure to quantify spinal stresses [213]. This is mainly the result of the increased intra-abdominal pressure in patients with LBP. Consequentially, elevated IAP has been observed to further affect normal patterns such as different breathing patterns [214] and induce pelvic girdle pain [150].

In degenerated discs, aging results with discal height loss beyond the normal values due to reduced hydration capacity along with fibrotic presence in the NP. This is accompanied with increased lesions across the anterior and posterior layers of the AF [215]. Inoue et al. conducted an in-depth analysis of the biomechanics of the IVD and its resulting instability [216]. In a comprehensive study of the effect of disc degeneration on its mechanical properties, Yi et al. noticed an increase in the compressive modulus of elasticity from 3.4–4.2 to 5.5–6.0 MPa for normal and severe cases of degenerated discs without affecting the Poisson ratio. Elastic anisotropy has been observed to be preserved during the advancement of degeneration which increases significantly in degenerated discs as a result of the loss of fibrous order. The elastic modulus was recorded as 5.68 MPa initially and increased to 29.10 MPa in the linear region for degenerated discs [217]. The NP modulus of elasticity increased from 0.9–1.2 in normal cases up to 1.0–1.7 in severe LBP cases with a decrease of the Poisson Ratio from 0.49 to 0.3–0.35 [218]. This is believed to be the result of the observed decrease in the proteoglycan and collagen

composition and its transition into a more fibrotic tissue [219] which tends to dehydrate the NP. Previous finite element studies analyzed the effect of degenerated discs by simply eliminating the incompressibility of the NP without inducing any morphological changes to the disc. Similarly, Kim et al. maintained the geometrical aspects of the degenerated disc similar to a normal disc but removed the hydrostatic pressure in the NP and increased the AF stiffness [220].

As a result of disc height loss, apophyseal joints adjacent to the discs may be also be subject to abnormal loads which may advance to osteoarthritis [221]. Given the morphological changes of the discal height, the loss of tension on the ligamentum flavum may result with a bulge towards the spinal canal due to the loss of elasticity [222]. MRI images showed a larger thickness of the Ligamentum Flavum near degenerated discs (3.17 mm) in comparison to normal discs (2.91 mm) [223]. Park et al. studied the effects accompanying discal degeneration progression to observe decreased FSU flexion-extension and lateral bending while increased intradiscal pressure in flexion-extension and facet joint forces at lateral bending and axial rotations [23]. Rohlmann et al. constructed and simulated an L_3/L_4 FSU to study the influence of degenerated discs by varying the discal height and NP bulk modulus according to degeneration progression defined by their grades. The grades defined healthy, mild, moderate and severe grade of degenerated discs with a 0%, 20%, 40% and 60% decrease in height, respectively. They observed that the mild case resulted with a 1.9°(± 2.5°) difference in intersegmental rotations which decreased with increasing degeneration grade. Furthermore, intradiscal pressures were lower while facet joints and outer annular layers showed higher stresses [16]. Nevertheless, the disc is not the only soft tissue to undergo remodeling in LBP patients.

Degenerative changes can also cause nerve root impingement in the neural foramen. Previous investigations on the morphological changes of vertebral orifices, particularly the pedicle to articular process distance and the posteroinferior distance of the upper vertebra to articular process suggest that the diminished length is most likely to compress or irritate the exiting nerve root [224].

1.2. MINIMALLY INVASIVE SURGERY

1.2.1. OVERVIEW OF LOW BACK PAIN

The distinction between pain and disability is clearly identified in the medical field. While disability is the inability of one to perform everyday activities [225], pain, as defined by the International Association for the Study of Pain, is an unpleasant emotional or sensory experience associated with actual or potential tissue damage [226]. In his book, Dr. Waddell explains that pain is rather a warning and settles on the definition that Low Back Pain as a whole is a symptom[1] regardless of the cause and condition [227]. The complication in the fact that pain is subjective appears in clinical assessment and patient communication. It is customary in clinical science to address Low Back Pain that has no specific cause as Non-Specific LBP which accounts for 90% of all patients with LBP [228].

LBP is divided into four categories depending on the time lapse of the pain. Given that medicine is a pragmatic affair, there are partial mismatches on the exact numeration between sources [226]. An accepted categorization for LBP can be set as follows:

- Acute LBP (ALBP): less than 6 weeks
- Sub-Acute LBP (SLBP): between 6-12 weeks
- Chronic LBP (CLBP): more than 12 weeks[2]
- Recurrent LBP[3] (RLBP): after recovery from an episode, patient has LBP at some time in the future [229].

CLBP may originate from injury, disease or elevated pressure on different structures of the body [230]. After a series of diagnosis, causes of CLBP may be the result of a malignancy, Vertebral Infection, Cauda Equina Syndrome, Vertebral Compression Fracture, Ankylosing Spondylitis, Progressive/ Neurologic deficits, Herniated Discs, Spinal Stenosis [231]. Casazza

[1] It is customary in the medical field that the difference between a symptom and a disease is that the former does not have a clear etiology.

[2] While clinicians usually define periods to distinguish between ALBP and specify its transformation to CLBP, some authors prefer to avoid the closed time criterion underlying the definition that CLBP is regarded as a disease.

[3] The definition of recurrent back pain is used in different manners among researchers and clinicians. Refer to the study by Stanton et al. for further information [11]. While this is rather a condition, specifying RLBP as a type is due to the fact that some people suffer from such episodes, while others experience it only once.

explains that most cases of ALBP are unknown and cannot be attributed with a specific cause but there are possible cases that should rather be considered and divides them into three major categories [232]:

1. Intrinsic Spine: Compression fracture resulting from trauma, Herniated Nucleus Pulposus, Lumbar Strains, Spinal Stenosis, Spondylolisthesis, Spondylolysis
2. Systematic: Connective Tissue Disease, Inflammatory Spondyloarthropathy, Malignancy, Vertebral Diskitis/Osteomyelitis
3. Referred: Abdominal Aortic Aneurysm, Gastrointestinal Conditions, Herpes Zoster, Pelvic Conditions, Retroperitoneal Conditions.

Pain is the result of nociceptors (i.e. specialized peripheral sensory neurons) transducing signals to the central nervous system as a result of stimuli. CLBP occurs when the noxious stimulus persists resulting with processes in the central and peripheral sensitization which converts ALBP to CLBP. In specific, sensitization is the increase in the excitability of neurons which transforms normal inputs into abnormal responses [233]. Anatomically, joints, discs and bone are richly innervated by A-delta fibers that have a strong contribution to the central sensitization upon continuous stimulation. In addition to the muscle, ligament and tendon functioning as load bearers, fascial tissues act as elastic springs with load bearing functions during oscillatory movements and are densely innervated by myelinated nerve ending. Thus, micro tearing and/or inflammation of the TLF could be a direct source of musculoskeletal pain causing LBP indirectly [234]. This perspective links the generated sensations of pain in the lower back region to specific anatomical regions of the musculoskeletal system due to mechanical instabilities. Non-Specific Low Back Pain in this case is usually termed Mechanical LBP and is considered to be the most difficult to identify with physical examination. Hall explains that LBP which has been cleared of any non-mechanical causes has a certain set of patterns that are common among all patients and categorizes the observation of mechanical LBP into four distinct patterns: two back-dominant patterns and two leg-dominant patterns [235]. Table 1.10 describes the categorization of the different pathologies described in non-specific mechanical LBP compiled from different sources [236, 237].

Table 1.10: Categorization of Non-specific Mechanical Low Back Pain

Diagnosis	Clinical Prevalence Percentage	Pain Trigger	Effect	Mechanism/Cause
Lumbosacral muscle and tendon strain / ligament sprain	70	General Movement, weightlifting, rotation, twisting	Lower ROM, local muscle tenderness	Abrupt traumatic incident
Lumbar Spondylosis	10	Extension or rotation	New bone formation, i.e. osteophyte growth over degenerated disc	Repetitive minor trauma, Age
Disc Herniation	5 – 10	Pivotal motions, weightlifting,	Loss of strength or reflexes, sciatica/radiculopathy	L5 or S1 nerve at L4 – L5, L5 – S1 levels, Annulus bulge/ rupture
Spondylolysis	< 5	Lumbar extension	No symptoms/ mild in children to low back pain in older population	L5 pars interarticularis fracture or defect or repeated injuries
Vertebral Compression Fracture	4	flexion	Chronic localized pain and functional impairment	Increased age, history of trauma, osteoporosis
Spondylolisthesis	3 – 4	Activities cause pain to radiate to buttocks or posterior pain with numbness	Spinal misalignment	L5, relative displacement of vertebra to one another
Spinal Stenosis	3	Standing or walking	Sensory loss, cramping or weakness in the legs with balance problems	Narrowing of spinal canal causing compression of spinal cord

Once the examination excludes the presence of any red flags (e.g. cancer, fracture, inflammatory arthritis, etc.) and is not categorized as either of the latter causes, MRI scans can attribute the cause to Degenerated Disc Disease (DDD) or, in other terms, Intervertebral disc degeneration (IDD). DDD is usually a natural consequence of age but also depends on biochemical factors [228]. It is worthy to note that genetic factors plays a significant role given the 50 – 70% variability observed in degeneration between patients [238]. In fact, DDD has been deemed as the most common cause of CLBP [229] in the form of Sciatica and Radicular Pain which can lead to Spinal Stenosis (i.e. narrowing of spinal nerve canals) on the long term [227]. In general, DDD alters the alterations in the disc's volume, shape, structure and composition of water content, proteoglycans and collagen. The main structural effect tends to be the loss of swelling ability and, thus, the loss of the NP volume as well as the formation of tears and fissures in the AF. Moreover, it alters the IVD's mechanical properties which affect the integrity of the spine in maintaining stability and adversely impacts the biomechanical function of other spinal

structures. This could result with implications on the IVD's height, hence leading to spinal stenosis, and structural alterations usually portrayed in the form of protrusion and/or prolapse (i.e. bulging) of the Annulus Fibrosis and/or herniation (i.e. rupture), whereby the nucleus penetrates the annulus shell [228]. The resulting diminished mobility and pain elevation necessitates a proper procedure whereby direct intervention relieves the patient. With the progression of disc degeneration, morphological features of the disc become more apparent and Magnetic Resonance Imaging (MRI) is employed to evaluate the ranking of the disc status. One of the more adopted classification grading scales is the Pfirrmann which adopts a 5-point grade scale whereby Grade I denotes a normal disc and Grade V designates a fully collapsed disc [239].

Treatments for LBP are perceived as more of diagnostics conducted on the patient to specify as accurately as possible a conceivable "interventional management" of pain. Clinicians agree that the goals of treatment for ALBP are to relieve the patient from the displeasing sensation of pain, improve the ability to re-function normally, reduce time spent off work and educate the patient of proper practices. Even though knowledge of the mechanism is prevalent, the treatment remains rather challenging [240]. The latter is a consequence of the ambiguity arising from LBP. Clinicians depend on a flowing diagnostic approach to LBP that aims to narrow down possible treatments. Moreover, it allows clinicians to rule out "Red Flags" that usually require a promptly aggressive diagnosis such as trauma due to injury causing fracture, major progressive neural deficiency, urinary retention, bladder or bowel incontinence, Saddle Anastasia, loss of anal sphincter tone, suspected spinal infection or a history in bone cancer [232]. Nasser explains [241] that the first step in the diagnostic is series of structured questioning to understand the history, environment, habits, life-style and working conditions. The clinician then conducts a physical examination in various positions in an attempt to localize the pain. It is recommended mostly that radiological examinations would only be requested if physical examination and history show a need for it [230]. Hence, doctors would rather refrain from referring patients to conduct any laboratory or imaging examinations. The clinician is then recommended by these guidelines to specify a certain treatment for the patient after the first or second visit depending on the diagnosis. Treatments can initially begin with drug therapy which includes non-steroids anti-inflammatory drugs (NSAIDS), Opioids, muscle sedatives/relaxants and Analgesics (i.e. Tramadol). At times, tricyclic antidepressants are prescribed for treatment of

neuropathic pain. If the clinician is able to specify the exact pain region, therapeutic injections could be used with minimal effects which includes trigger-point injections, selective joint injections and epidural injections with steroids. In other cases when LBP is not complicated, physical modalities including therapeutic heat, cryotherapy, electrotherapy and traction could be used given that the patient is showing progress. Evidently, most cases of LBP will eventually be solved by nonsurgical management [242]. Should the patients show no signs of improvement over a prolonged period of time, the clinician refers him to a specialist who would, depending on the state of pain level and general health state, recommend invasive surgery. Yet, even then, surgical indications for CLBP remain ill-defined [243].

1.2.2. Surgical Interventions via Lumbar Interbody Fusion

As the highest recorded diagnosis of LBP for patients above 65 years in the human population [244] and most common cause of LBP in athletes [245], treatments for DDD have widely emerged in efforts to moderate pain, increase function and minimize healthcare utilization [246]. When conservative measures and nonpharmacological therapies fail to reduce the pain, the patient is often referred to surgical options. While intermediate options, including arthroplasty, non-fusion stabilization [247] and interspinous implants [248], have proved to be successful, long-term results are still unknown [227]. Thus, often, lumbar interbody fusion (LIF) is the treatment of symptomatic lumbar DDD, along with trauma, infection and spinal disorders, when conservative measurements have failed.

The logic of the surgery is that the fusion of two vertebrae together will restrict localized relative motion, which, in turn, inhibits excessive motion and will alleviate the pain [227]. This is achieved by the placement of an implant (usually a cage or spacer with structural graft) within the intervertebral space (i.e. intervertebral disc) to decompress exiting nerve roots and, later, allow the vertebrae to fuse through the natural growth of bone. While spinal surgeries directly decompress the pain on the nerve, the natural fusion of the vertebra results with direct reduction in spinal flexibility which would otherwise be conceived via the discs. Furthermore, spinal surgeries accompany surgical risks, similar to any surgery, which may include anesthesia complications, blood clots (i.e. Thrombophlebitis), post operational lung complications, infection, hardware fracture, implant migrations, intraoperation spinal cord injury, persistence of pain, sexual dysfunction, transitional syndrome and improper vertebral fusion [249-251].

In the 15th and 16th century, spinal anatomy and biomechanical mechanisms began emerging [252]. This led to the development of a few external spinal devices that would aid spinal stability at the time. However, it was not until the 19th that foundational concepts and practical methods for surgical techniques were laid. This stems from the discovery of general anesthesia (1846), antisepsis (1867) and the development of x-ray imagery that allowed for an internal view of the body (1895) [253-255]. The need for usage of spinal surgeries rose from the wide spread of tuberculosis (incidence of 900 deaths per 100,000) in the 18th and 19th century accompanying spinal tuberculosis (Pott's Disease) which often led to bone destruction, kyphosis and vertebral collapse whereby medical practitioners realized the ineffective usage of external devices at the time [256]. The alternative developments for spinal stabilization initiated with the cervical spine then made its way towards the lumbar spine. The first case of a documented instrumented spinal fusion surgery was described by the Austrian surgeon Hadra in 1891 [257] who utilized a posterior invasive approach to reduce a suspected dislocation at the sixth cervical vertebra by binding the adjacent spinous processes of the segmental vertebra using a silver wire. The patient improved for a short while after which symptoms returned which after a re-operation was observed to be due to the loosening of the wire. This has since evolved to become a treatment option for symptomatic spinal instability, spinal stenosis, spondylolisthesis and degenerative scoliosis. Campell described trisacral fusion whereby an autograft from the iliac crest to the L5 transverse process was injected to obtain lumbar sacral fusion [258]. Simultaneously, Hibbs continued the adoption of the wiring technique for Pott's Disease and improved it by using larger areas for inducing spinal fusion and bone grafting for general spinal diseases [259]. However, corrosive issues with the wires utilized led to frequent failures before fusion was attained. Orthopedic surgeon King adopted Hibb's method but exchanged the wiring with facet screws to achieve better results in the late 1940s [260]. At the same time, Burns conducted the first anterior lumbar interbody fusion approach (i.e. ALIF) to treat spondylolisthesis for a 14-year-old boy by incising the posterior peritoneum after packing the intestines and drilling the fifth vertebra to embed an autograft from the boy's tibia to achieve a walk pain-free result after strict bed rest measures [261]. The discovery of disc herniations resulted with a rapid increase of spinal fusion surgeries leading to widespread in spinal interbody fusion surgeries but without any specific preferred techniques. Later in 1944, Briggs and Milligan described a posterior approach (PLIF) that results with improved rates by completely

exposing the spine posteriorly followed by the removal of the spinal processes as small chips along with the lamina and facet joints to obtain a complete visual access to the disc. The disc would then be removed and replaced by a round bone [262]. Later improvements included the use of autograft from several bone locations (as opposed to using the tibia only) by Cloward (1953) [263], development and adoption of Harrington rods (1962), further development and adoption of the pedicle screws (1988) and the development then adoption of cages (instead of prior use of bone peg) [264]. Alternative techniques to the PLIF and ALIF were later developed such as the transforaminal interbody fusion (TLIF) by Harms and Rolinger (1982) which advances at a more lateral approach to the disc space reducing the amount of nerve root retraction [265].

While surgical experience and knowledge significantly increased the successful adoption and clinical outcomes of such techniques, technological advancements in access instrumentation and internal imaging served as a catalyst for the development of less invasive techniques in surgical operations, namely minimally invasive surgeries (MIS). This is the result of the large incision sizes (~70–150 mm) that disrupt and damage the muscular and ligamentous disruption. Moreover, the usage of self-retaining retractors in open spinal surgeries tend to lead to a higher interoperative blood loss and possible irreversible tendon damage at attachment sites with the spinous processes. Furthermore, open surgeries have reported higher post-operative pain, increased post-operation medicinal usage, late ambulation and higher hospitalization time which would be mitigated by adopting MI techniques [266, 267]. Modern MI spinal surgeries were first introduced in the 1990s with the development of tubular refractors for lumbar access to report the first micro-endoscopic discectomy (i.e. insertion of a long thin flexible tube with a miniature camera placed at the tip to examine the disc) [268]. This has led to the adoption of MI surgeries for the treatment of various spinal pathologies including DDD, disc herniation, deformity, scoliosis, infection, tumor and instability. Traditional open surgical procedures, such as the PLIF, access the disc through the intertransverse region which requires an extensive stripping of the paraspinal muscles up to the transverse processes. This results with significant destruction, post-operative atrophy and scarring of the multifidus which has been associated with post-operative morbidity [269]. Hence, MI surgeries utilize tubular dilators that gradually expand punctured holes to exploit the transverse processes and intertransverse space [267]. Moreover, open lumbar fusion surgeries require the dissection of various muscular tissues to expose entry points for a

proper lateral-to-medial fixation of pedicle screws. However, percutaneous pedicle screw fixations employed in MI surgeries mitigate the risk of muscular denervation, facet capsular disruption, damage to proximal facet joints and the weakening of ligamentous structure that may lead to prolonged operative-induced pain and morbidity.

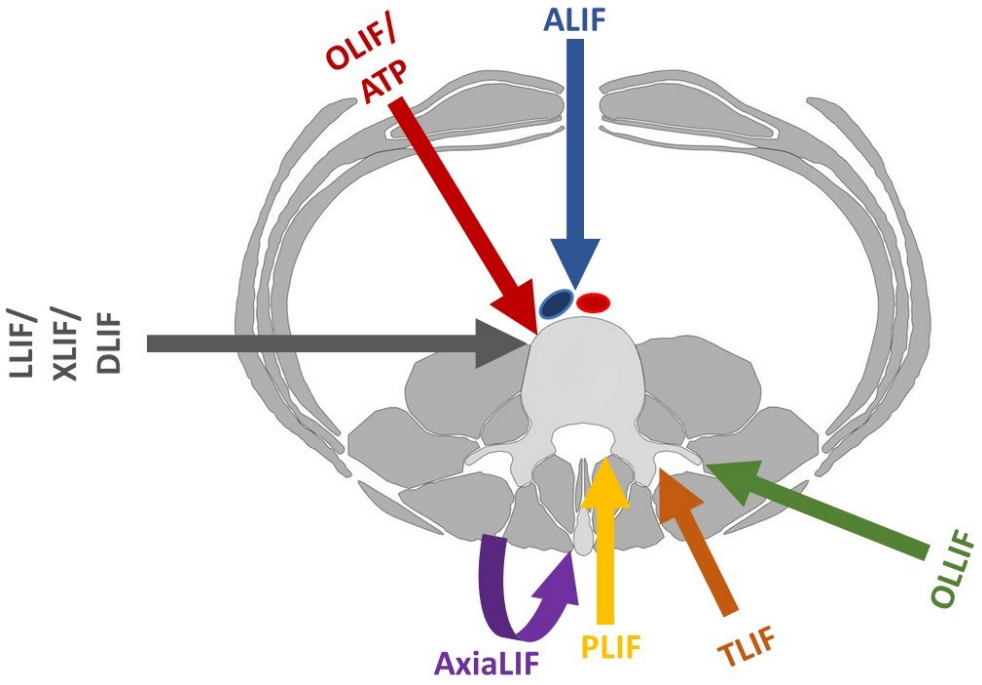

Figure 1-5: Depiction showing Lumbar Interbody Fusion (LIF) Types

LIF procedures are usually categorized according to the entry path adopted when performing the surgery. The popular LIF procedures include Anterior (ALIF), Posterior (PLIF), open Transforaminal (TLIF), Oblique Anterior to Psoas (OLIF/ATP or OALIF), Lateral/Extreme Lateral/Direct Lateral (LLIF/XLIF/DLIF), Axial (AxiaLIF), Minimally Invasive Transforaminal (MI-TLIF) and Oblique Lateral (OLLIF) Lumbar Interbody Fusion. Figure 1–5 depicts the difference in the access point of entry among the latter listed LIF surgical techniques. Generally, gaining access in the ALIF is achieved, as described by Mobbs et al., by placing the patient in a supine position and approaching anteriorly between the umbilicus and the symphysis pubis exposing the entire ventral surface of the disc such that an incision is applied on the midline section along the spinal levels of interest with a dissection of the skin and underlying soft tissue using a diathermy. The retroperitoneal corridor may then be accessed by dividing the exposed Linea Alba using a monopolar diathermy. In this case, tissue forceps are often employed to

elevate and retract the rectus abdominis muscle layers. A blunt dissection to the retroperitoneum exposes the inferior epigastric vessels which are then retracted with the psoas major muscle and genitofemoral nerves. Further retraction of the right and left common iliac artery and vein vessels conceives an access maintaining a full reveal of the discal space [270]. In PLIF procedures, the patient is placed in a prone position and a 70–150 mm incision depending on the desired exposure to the levels of interest is applied on the axial midline of the spine, as described by Mobbs et al. The surgeon then retracts the erector spinae until the bilateral facet joints are accessed. Surgeons may, then, add initial posterior fixation to expand the intervertebral space. Laminotomy is then performed medial to the facet and the dura retracted to expose a corridor to the disc space. TLIF procedures follow similar steps to the PLIF but with a direct and unilateral access to the intervertebral foraminal space reducing the direct dissection by exposing the neural foramen on one side only (i.e. the side that is consistent with the patient's symptoms). Posterior spinal elements are exposed using a standard subperiosteal dissection tool. A unilateral exposure reduces the risk of damage on the nerve root, dura and ligamentum flavum [271]. Hence, access to the disc in the TLIF procedure is achieved via one or both of unilateral laminectomy and inferior facetectomy facilitating bone graft [272]. This procedure was, later, adopted with the technological advancements in medical devices as a minimally invasive surgery. While maintaining the same access location, a small incision on the skin and the fascia is performed instead of a full open access. A tubular retractor system is then introduced with fluoroscopic aid to the facet joint. Dilating tubes of increasing diameter would then be employed to bluntly spread the muscles and port would be docked on the pars interarticularis of interest [273]. The following steps of the LIF procedure including facetectomy and discectomy would be performed using a microscopic camera introduced through the port [274]. LLIF procedures access the disc space from a direct lateral approach through the retroperitoneal trans-psoas tunnel using a minimally invasive approach. The patient is positioned laterally, at a true 90° angle, on the side that is deemed easier to access by the surgeon. The alignment is then confirmed by AP fluoroscopic imagery. Marking on the patient's skin for defining the point of entry is, then, performed using a k-wire and lateral AP imagery. Atraumatic tissue dilators and an expandable retractor are then passed through an incision performed on the mark after a second incision is conceived. The second incision of about 20 mm is performed so that the surgeon inserts the index finger between the erector spinae and the oblique abdominis (i.e. external and internal) to navigate the dilator

inserted within the first incision towards the psoas muscle. The procedure is conducted in this manner to ensure that the intra-abdominal contents are intact. This is followed by the insertion of increasing dilator sizes for blunt dissection while ensuring minimal damage to the psoas. Furthermore, electromyographic (EMG) monitoring is utilized on the dilator to ensure that the nerves of the lumbar plexus are outside the access tunnel. Ozgur et al. recommended that a threshold of 10 mA indicates a safe zone within the vicinity of the nerves [275]. Dissection using the dilator with the EMG-based electrode tip continues through the psoas until the disc is reached at which AP fluoroscopy confirms contact to finally expose the discal region. Similarly, the OLIF procedure follows the same procedure to gain access to the disc but is attained at the region defined between the Anterior-To-Psoas (ATP). This derived technique sustains a safe access allowing it to be conducted without the use of neuromonitoring since the dilator is inserted within the abdominal muscle layers reaching towards the disc, as described by Ohtori et al. The retroperitoneal space is, then, accessed by blunt dissection to mobilize the peritoneal region anteriorly and the psoas muscle posteriorly [276]. The AxiaLIF is a minimally invasive surgery that defines a different access location following a presacral anatomical entrance defined through a paracoccygeal incision but utilizes the same principles as the previous LIF procedures. In specific, the patient is placed in prone position and a 20 mm longitudinal incision at the level of paracoccygeal notch and a blunt cannulated dissector is advanced through the presacral space then anchored onto the sacrum. A stout guide is, then, passed through the dissector into the sacrum and advanced into the disc space to define a trajectory for dilator insertion.

In general, there is no clear definitive evidence, clinically, prioritizing one over all the others, some approaches possess advantages and disadvantages that are applicable depending on patient size, anatomy, spinal level access point and surgeon preference [271, 277]. However, clinical trials and previous adoptions of the different LIF techniques have recorded various advantages and disadvantages when adopting one technique over the other. Nevertheless, new techniques have emerged which leverage specific anatomical regions in the aim of reducing the size of the access pathway to the disc. Table 1.11 lists the different advantages and disadvantages of each of the latter list of LIFs [242].

Table 1.11: Comparison of LIF Surgeries

LIF Type	Advantages	Disadvantages	References
ALIF	• Complete exposure of the ventral surface of the disc • High fusion rates • Good radiological outcomes • Good restoration of discal height and lordosis • Little to no risk to dura, spinal canal and neural foramina	• Abdominal and vascular complications • Suitable only for L4/L5 and L5/S1 levels • Requires both a spinal and vascular surgeon to be present • Risk of vascular and visceral injuries as well as retrograde ejaculation	[270, 278-281]
PLIF	• Traditional lumbar approach whereby surgeons have been well trained on • Clear visualization of the nerve roots without compromising blood support to graft • Adequate interbody height restoration • Allows for a potential 360° fusion through single incision	• Paraspinal musculature disruption • Significant paraspinal iatrogenic injury with prolonged muscle retraction delaying mobilization and recovery • Difficulty in endplate preparation in comparison with ALIF • Risk of nerve root retraction may cause fibrosis and chronic radiculopathy	[271, 280]
TLIF	• Preserved ligamentous structure when compared to PLIF • Reduction of access-associated muscle injury • Less bleeding • Improved postoperative recovery • Ability to achieve circumferential fusion without neurological function or a need for sequential operations	• Significant paraspinal iatrogenic injury with the prolonged muscle retraction • Endplate preparation is more challenging than ALIF	[271, 272, 280]
MI-TLIF	• Significantly diminished tissue trauma • Minimally Invasive • Lower hospital time • Reduced peri and post-surgical pain • Faster healing rates • Significant reduction in blood loss compared with TLIF (reportedly, five-fold reduction)	• Risk of neurological injury • Risk of cerebrospinal fluid leakage • Increase technical challenge in performing LIF by surgeon • Smaller visualization in comparison to the open TLIF • Outcomes are just as good as an open TLIF	[274, 282, 283]

LLIF/DLIF/XLIF	• Use of monitoring aids with a decrease in the nerve injuries • Significant elevation in recovery times • Less post-operative pain • Reliable and reproducible results especially for sagittal and coronal deformity correction such as lumbar degenerative scoliosis • Does not require laminectomy, facetectomy or posterior spinal muscle damage	• Not suitable for L5/S1 level • Increase of risk due to lumbar plexus anatomical curvature • Risk of Bowel injury • Risk of CO_2 insufflation may result with lower cardiac output leading to elevated vascular and arterial pressures • Risk of major vessel injuries • High risk of injury if used without posterior aid	[275, 279, 280]
OLIF/ATP	• Minimally Invasive • Does not require laminectomy, facetectomy or posterior spinal muscle damage • No dissection to psoas muscle necessary in comparison with XLIF • Has same advantages as XLIF	• Risk of sympathetic dysfunction • Risk of vascular injury	[276, 284, 285]
AxiaLIF	• Minimally Invasive • Avoids critical neurovascular and spinal structures	• Risk of pseudarthrosis • Risk of Rectal Injury • Risk of transient nerve irritation • Risk of intrapelvic hematoma	[242, 286]

1.2.3. OBLIQUE LATERAL LUMBAR INTERBODY FUSION

Oblique Lateral Lumbar Interbody Fusion (OLLIF) is a relatively new technique that provides a solution to the latter complications, recording even faster surgery times and less complicated procedural tasks when compared to previous surgical techniques [287]. In comparison to the MI-TLIF procedure, OLLIF requires less laminectomy and facetectomy. In general, the operation follows the same route of LIF operations with the three major steps, Access Gain, Discectomy and Cage Insertion. The variation is specifically highlighted with the access route through Kambin's Triangle. With the aid of electrophysiological monitoring and bilateral fluoroscopy, OLLIF allows access to the IVD using Kambin's triangle through a 10–15 mm incision eliminating the need for direct visualization. In fact, this anatomical window has been previously utilized as corridor access for nerve root steroid injections [288] and radiographic purposes [289]. The triangle is defined by the existing nerve (as the hypotenuse), the superior endplate of the caudal vertebra at the base (12–18 mm) and the superior articular

process at its height (10–12 mm). Previous cadaveric studies have estimated that the triangle possesses an approximate area of 60, 71.5, 93.5 and 108 mm^2 for L_1/L_2, L_2/L_3, L_3/L_4 and L_4/L_5 spinal levels, respectively [290]. Hardenbrook et al. further studied the anatomical triangle's safety zone by removing the superior facet from 8 fresh frozen female cadavers and measured higher averaged areas of 115, 120, 119 and 116 mm^2 for the successive L_1/L_5 intersegmental levels, respectively [291]. While these areas provide a wide safety region for potential LIF surgeries, Ozer et al. reported on the large variations that exist within Kambin's Triangle and suggested that partial superior facetectomy may mitigate the risk of injury to the exiting nerve root [292]. Figure 1–6 depicts the Kambin's Triangle location on the spinal functional unit and the corresponding inferior and superior articular process.

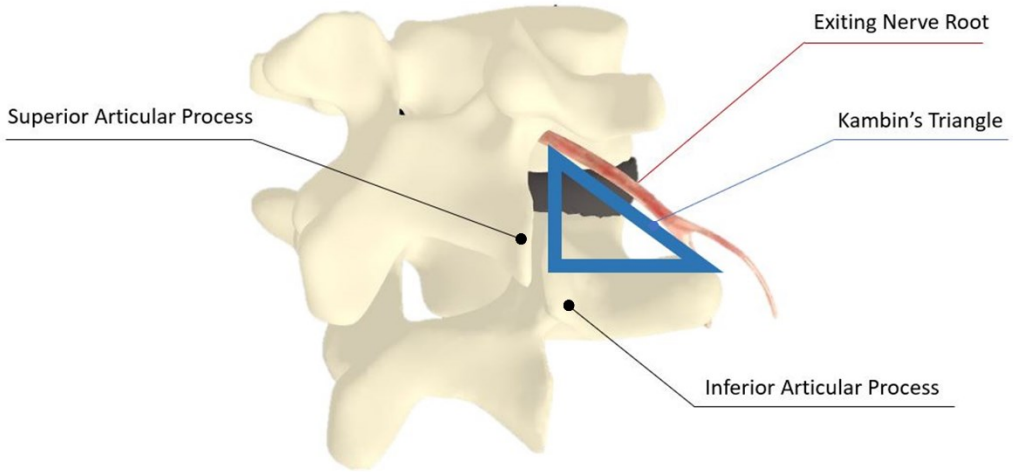

Figure 1-6: Depiction of a spinal functional unit showing the Kambin's Triangle anatomical feature bound by the exiting nerve root on the hypotenuse and the superior and inferior articular processes

Estimating the location of the Kambin's triangle defines the first step to achieving access to the IVD for an OLLIF surgery. Abbasi et al. provided a detailed description of the surgical procedure [277]. In general, the patient is placed in a prone position and tilted away from the surgeon by 3–5° until the completion of the cage insertion whereby the patient is returned to a full prone position. Fluoroscopy is then set up such that the disc needs to be visible and spinous

process centered at the midline of the pedicles. To define the point of entry, the surgeon measures the depth and width of the intervertebral disc using a lateral and A-P fluoroscopic view and marks the measurements on the skin of the patient's side to conceive a 45° angle of entry. Along the measured lines, a 10–13 cm point from the midline (i.e. the line drawn along the spinous processes) designates the entry point for the spinal levels of interest. A 10–15 mm incision is performed on the skin, underlying fatty layer and the posterior thoracolumbar fascia. Guided by fluoroscopy, the surgeon defines the angle of insertion using a long slender electrode whereby the probe punctures through the muscle layers traversing the retroperitoneal space. Electrophysiological monitoring stimulates the electrode probe at sensitivity rate of 3 mA as the probe progresses through the muscular tissue to ensure that the nerve root is not contacted. Upon achievement of the disc, further nerve stimulation ensures a safe access. A sleeve is, then, passed onto the electrode and a K-wire pierces through the disc to its midline. Fluoroscopic imagery may confirm the position at this point. A dilator is then entered on top of the K-wire inserting approximately 0.5 cm in the lateral view. Dilators of increasing diameters are, then, advanced on top of one another sequentially while gently dilating the tissue. Finally, an access portal sleeves the outer most dilator and is secured in position and locked. The dilator assembly is removed from the access portal resulting with an access tunnel spanning from the outer skin to the disc within the posterior muscles. Facetectomy (i.e. removal of superior and inferior facets) are then performed along with Discectomy (i.e. removal of the internal intervertebral disc tissue). The third stage includes the cage placement and fixation within the discal space and bone graft to aid with spinal fusion. The cage is then expanded to decompress the nerve roots. Finally, posterior pedicle screw fixations are advanced within the incision and are stimulated up to 30 mA to ensure no neural structures are in contact.

Abbasi et al. conducted 69 consecutive surgeries on 128 levels and noticed a mean time of 69 minutes (compared to 135 minutes in TLIF surgeries) for the entire surgery and a blood loss of 29 ml (compared with 355 ml in TLIF surgeries) [277]. Furthermore, they conducted an economic study and observed reduced surgical expenses down to approximately $5,273 in OLLIF surgeries compared to $11,264 for TLIF surgeries. This difference is also observed for inpatient cost (OLLIF $5,712 vs. TLIF $9,271), hospital costs due to the reduced resource consumption as well as surgical and post-surgical hospitalization time [293].

While the OLLIF technique may be conducted for the L_1/L_4 full spinal segmental levels with ease, the obstruction of the ribs inhibits its use for thoracic vertebra. Moreover, reaching the L_5/S_1 may be obstructed by sacral ala and iliac crest sometimes preventing its employment. However, MIS operations for spinal fusion remain technically demanding and suffer practical limitations in certain cases due to the relatively smaller visual access [17]. Insufficient data exists on the actual outcome of the OLLIF surgery on a large scale. In such a case, previous studies on surgical interventions that utilize a similar general procedure may provide insightful perspectives on the possible risks. In fact, exiting nerve root injury has been previously marked as the most devastating complication of Transforaminal Percutaneous Endoscopic Lumbar Discectomy (PLED); a surgical intervention targeting disc herniations through Kambin's Triangle [294]. Choi et al. evaluated the clinical-radiological features on 233 patients treated with PLED for disc herniation and reported on 20 patients exhibiting postoperative root-related dysesthesias. Sairyo et al. investigated an initial 100 cases of PLED under local anesthesia and realized 2 patients suffered from leg pain and dysesthesia 2 days after the surgery but the pain disappeared within 3 months. Hence, they suggested modifications to the technique of access gaining whereby the guide needle touches the caudal pedicle. This is done prior to entering Kambin's Triangle to avoid contacting the nerve which they termed the "walking technique" [295]. Reported studies on the complications of MI surgeries have questioned the advantages of laparoscopic over open techniques. In perspective, mastering operations with laparoscopic tools have been previously noted to be considerably challenging, specifically, if not utilized on a regular basis [275]. For instance, depth perception as a result of the usage of a two-dimensional video imaging is compromised. As such, the need for readily available and reliable VR medical simulators rises.

1.3. VIRTUAL REALITY-BASED SURGICAL SIMULATORS

It is necessary to realize that the development of virtual reality-based medical simulators encompasses various scientific fields. The embodied components stem from virtual reality, medical surgery and simulators. These include concepts from computer vision, linear mathematics, control systems, optics, computer science including graphical programming, surgical practices, educational techniques, material sciences, philosophy, etc. For an effective development of a surgical simulator, a proper understanding of simulators and virtual reality

should be attained. Hence, the subsequent review lightly touches on various parts of the above to conceive an understanding to the proper level. However, this is not meant to establish an exhaustive overview of each of the sections mentioned above. Thus, the content will initially differentiate between virtual reality and surgical simulators in the history and definition sections but will be combined together in subsequent sections to investigate VR surgical simulators specifically.

1.3.1. HISTORY

Mentions of medical simulators date back to over 2,600 years ago, as early as surgery was recorded. Uncoincidentally, the term simulation was first described when leaf and clay models were utilized to simulate the very first recorded operation, namely a forehead flap nasal reconstruction in India in 600 B.C. [296]. Sushruta Samhita described over 120 surgical instruments and 300 operations including the use of cadavers and synthetic models for practice prior to surgery. In his description, technical skills were experimented using worm-eaten wood and vegetables (i.e. watermelons, gourds and cucumbers) [297]. Interestingly enough, the use of oranges and bananas continue to be a practice maintained by medical students for suture training today [298]. Throughout history, medical simulators incorporated the use wooden benchtop models, live animals and human cadavers. In fact, Ambroise Paré [1510- 1590], arguably one of the fathers of surgery, was known to take embalmed cadavers home with him to practice on surgical techniques [299]. Similarly, cadavers continue to be used today since its adoption by the British Royal College, but the costs incurred of setting up and running the training modes sustain a burden on the educational bodies [300]. However, Cruelty to Animals Acts passed around the world in the late 1800s forbade the use of live animals for surgical training.

The first modern skills “simulator” was conceived in 1928 by Edwin Link who created a pilot training system that consisted of a pilot seat capable of maneuvering in pitch, roll, yaw and climb orientations. The link trainer reportedly taught six army members initially, but accommodated training for more than 6,000 army by the end of WWII [301]. One of the earliest modern medical training simulators was constructed by Madame du Coudray consisting of a fetal model and a human pelvis bone to train midwives in the eighteenth-century in France [302]. In more modern times, recordings of simulators appeared widespread such as the Resusci Annie, basically a training mannequin for teaching basic life support in 1960 after a girl drowned in the

Seine River in Paris inspired by Asmund S. Laerdal, a toy maker [303]. This made way to develop more complex simulators in the late 1960s such as the Sim One built by Abrahamson and Denson which simulated breathing, heart rate, blood pressure and consisted of eyes and a mouth that dynamically moved for an immersive experience [298]. High-fidelity training would not be revisited until the 1980s which gave rise to two notable simulators, namely the Comprehensive Anesthetic Simulation Environment (CASE) and Gainesville Anesthetic Simulator (GAS). CASE adopted team-based realistic environment concepts from aviation training models for crisis management and incorporated it into the anesthetic's curriculum. High-fidelity simulators have witnessed a steady rise in adopting simulators within curriculums since the construction of these two simulators. Patient-based simulations began to rise, later, in 1970 with the first computer-based simulator for clinical encounters in the Massachusetts General Hospital giving access to Ohio State University and University of Illinois. By 1973, University of Wisconsin developed its own computer-based simulator which became a basis for computerized examinations which, later, developed the concept of Objective Structured Clinical Examinations (OSCE). Using OSCEs, the training institution simulated a standardized situation and recorded the performance of students in terms of competence and confidence. Simulated patients have also taken the role of both students and trainees as they help students overcome sensitive topics and examinations such as cervical smear and vaginal examinations whereby Gynecology Training Associates permit the utilization of their own bodies as educational tools [304]. However, all the previous training simulators resulted with a certain amount of constrains from a financial and logistical point of view. Hence, the rise of virtual reality systems that combine simulation, immersion and interaction stirred great interest.

Many consider that the birth of virtual reality is owed to Sensorama, a single user console invented by Morton Heilig, a cinematographer, in 1955 before building the actual prototype in 1962 [305]. Interestingly enough, it included a stereoscopic display, stereo speakers and a tilting chair designed to engage the senses as much as possible for an immersive experience by the user. The Sensorama was designed to provide a multi-sensory, immersive experience for users to simulate riding a motorcycle in vast highways. Features included fans to simulate wind, a stereoscopic display showing the road, odor emitters to provide aromas similar to what a motorcycle rider would smell, a stereo-sound system and a movable chair with functionality to trigger the various stimuli at appropriate timings during the simulator. Despite it being entirely

mechanical with no digital computational features, the Sensorama led to Heilig's patent which is considered the first design of a Head-Mounted Display (HMD) [306]. The innovative system included a 3D photographic wide-angle view, an embedded stereo system and an "odor" generator; a portable version of the Sensorama, however, the design was not implemented. In 1961, two employees of Philco Corporation built the first HMD, namely Headsight, using a single cathode-ray tube (CRT) screen strapped to a helmet with a magnetic tracking system for graphical feedback supplied from a CCTV system located in dangerous areas. This was developed during the time that algorithms and systems were developed for rendering graphical data on display screens. Inevitably, the two fields collided, and the first computer-based HMD was constructed by Ivan Sutherland, namely the Ultimate Displa which was connected to a mechanical tracking system rigged to a railway system in the ceiling. This opportunity quickly received funding and applications in military helicopters. This later made way for innovations that improved each of its earlier generation. In 1990, Delp et al. developed the first VR-based surgical simulator that teaches lower limb reconstruction surgery which reached the widespread commercial market [307]. However, their system stirred concerns about their efficacy which were later put to rest after Seymour et al. demonstrated the significant reduction of procedure times to perform cholecystectomy (~ 30%) and were evidently five times less likely to injure the gall bladder after using a VR medical simulator [308].

The adoption of simulators for medical training purposes began receiving interest specifically with the Calmanization of general surgery which renovated the medical professional requirements together with the European Working Time Directive, whereby working hours reduced from 30,000 to 6,000 in promoting to a Senior House Officer and a Consultant [309]. Similarly, in 2003, the ACGME passed a regulation that required new surgeons to become proficient in shortened period of time [310]. One year later, in 2004, the Federal Food and Drug Administration (FDA) approved the introduction of carotid stent procedure into their training programs [311]. For the first time ever, medical students had to prove themselves using a competency-based task to be granted approval to perform a real surgery.

1.3.2. DEFINITION

Simulation is defined as "a technique to replace or amplify real experiences with guided experiences, often immersive in nature, that evoke or replicate substantial aspects of the real

world in a fully interactive manner" [312]. A simulator is a device or model that is employed to simulate or imitate a real-life scenario for a specific purpose [313]. Surgical simulators, such as humans, cadavers, live animals, benchtop models and virtual reality (VR) are all examples of constructed simulators to recreate surgical simulations for trainees to develop, practice and/or hone surgical skills.

The term virtual reality has been presented in the popular press to manifest similar to a mobile or television. As such, it wraps around a particular set of hardware, including computers, head-mounted displays, headphones and motion-sensing gloves. This alters the general notion and conceptual locus of virtual reality to be technological instead of experiential. The term was first adopted by Jaron Lanier, chief executive officer of VPL Research Inc., a manufacturer of gloves, goggles and other VR products in 1989 [314]. While this term serves as a marketing tool for product manufacturers, its definition does not suffice to be deemed acceptable for communication researchers and policy makers. In specific, this definition necessitates the requirement of presence of a minimal corpus of hardware for a system to be called VR. Moreover, there is no conceptual unit of analysis for VR such as the identification of a "single virtual reality". Finally, the lack of theoretical dimensions across a well-defined spectrum adds a challenging level to relevance and comparability. Hence, previous definitions of virtual reality were conceived with the realms of "presence"; the sense of being in an environment. This definition aided by the distal attribution feature conceives the notion of telepresence. As such, virtual reality would be defined without reference to a particular hardware setup but rather the extent one can experience a mediated environment as opposed to reality whereby one would experience a natural immediate environment [315]. Steuer analyzed the definition of virtual reality extensively and defined two major dimensions at which communication technologies vary including vividness (i.e. representational richness of the mediated environment as defined by the method of information presentation to the senses) and interactivity (i.e. extent to which participants can manipulate and vary the form and content of a mediated environment in real-time). These two concepts are measured in terms of breadth and depth for vividness while speed, range and mapping for the interactivity [316]. Webster's New Universal Unabridged Dictionary (1989) defines virtual as "being in essence or effect, but not in fact" and reality as "the state or quality of being real". Key elements of a virtual reality experience include the virtual world, immersion, sensory feedback and interactivity [317]. Various authors have found that a

philosophical approach to the definition of the virtual reality may work best whereby idealism and imperialism are employed for the definition of experience if virtual reality is defined as "a new way of gaining experience in cyberspace" [318]. Other definitions based on technology include "a natural interaction technology" [319], "a means of interaction by which people can manipulate and interact with complex data using computers" [320] and defining virtual reality as a participant-centered closed system implemented through computers and exploits the human/machine interaction with perceptual system [321]. It is evident that defining virtual reality can prove to be a difficult task due to the lack of a standard definition. By some school of thought, it is said to an oxymoron referred to as a "reality that does not exist" [322]. Perhaps Zhuang et al. defines it most accurately as a "high end Human-Machine interface that combines technologies such as computer graphics, image processing, pattern recognition, artificial intelligence, networking, sound, systems and others to produce computer simulation and interaction which gives the feeling of being present through multiple synthetic feedback sent to sensorial channels like virtual, aural, haptic and others" [323]. Variations of Virtual Reality include Virtual Environment, Artificial Reality, Virtual Worlds, Artificial Worlds, Cyberspace, Telepresence, real-time simulation. Burdea et al. raised the concept of "3 I"s of virtual reality; interaction, immersion, and imagination [324]. Hence, virtual reality systems cover a wide range of technologies that vary based on their level of immersion.

It is worthy to note that this is different from Augmented Reality (AR) whereby AR is a relatively new and quickly expanding type of technology that combines real-world physical objects with virtually-created objects (i.e. a user would experience overlapping virtual and real objects combined through a transparent screen). Sherman and Craig expand this definition to explain that AR would also incorporate technologies that would see virtual objects with one eye and real objects with the other eye [317]. Krevelen and Poleman present an extensive survey of AR in terms of technology, applications, limitations and notes of overlap in various aspects between the two types to the extent that AR and VR may both be considered under the parent category, namely Mixed Reality [325]. However, this notion has been further recently updated to recognize the presence of Extended Reality (XR) which acts as an umbrella that incorporates MR, VR and AR.

To understand how a person interacts with an immersive virtual reality environment, it is necessary to understand how perception is achieved and its engagement to the real world. In

general, perception can be defined as the process by which a person harvests data through their senses then compiles and interprets that information to conceive a state of awareness of the surrounding [326]. This is predominantly achieved via our five main senses, that work collectively to acquire data in real-time permitting us to build sufficient knowledge either consciously or unconsciously. In addition to external perceptions, internalized receptors conceive further perception of our presence within an environment and have shown to play a significant role in the virtual reality experience [327]. This includes vestibular sense which is derived from the inner ear which ensures or sustainability to balance. This has been suggested to be susceptible to error when conflict arises due to the misalignment of information with vision or aurora resulting with a "sensory conflict" that may lead to dizziness, vertigo or nausea in extreme cases [328]. Proprioception further provides the human with the spatial realization of the relative limb and body locations (i.e. position) derived from mechanoreceptors [329]. This is different from Kinesthesia which designates the perceptive sensation of joint motion or acceleration [330]. Interception is the perception of sensations from inside the body and includes the perception of physical sensations related to the internal organs such as the heartbeat, respiration, satiety as well as autonomic nervous system activity related to emotions. In specific, interceptive awareness is the process of making an unconscious inner sensation to become conscious [331].

1.3.3. System Types and Components

Virtual reality systems do not require a specific set of input or output devices to display a virtual reality environment from a conceptual basis. Muhanna et al. describe five key elements of any virtual reality experience [332]. These are a virtual world (i.e. space generated by a computer whereby a user interacts with virtual 2D or 3D graphical representations, i.e. avatar), immersion (i.e. capability of the participant to disconnect from the physical environment around them and connecting to the virtual space), feedback (i.e. sensory feedback such as movement of head, if using a head mounted display, corresponds to a direct movement of the view within the virtual world with no delays), interactivity (i.e. the capability of manipulating the virtual environment) and participants (i.e. the users themselves).

Heim explains that the basic virtual reality systems may be described as screen-based, pointer-driven and presented by 3D graphics [333]. Basic VR systems that may provide a virtual experience are divided into hand-based (such as cell phones, Personal Digital Assistants (PDA),

ultra-mobile computers and portable game consoles) and monitor-based (desktop computers displaying 3D graphics on monitors). Enhanced virtual systems incorporate more hardware and, thus, designate a higher level of immersion. These types have been categorized into partial (e.g. projectors that display virtual worlds on large screens such as the IDAV Tiled Powerwall which do not incorporate goggles but include connected glove input) and fully immersive systems (e.g. head mounted displays or helmet that provide a binocular view with a large field of view mounting two screen displays for each eye that tracks the head's location). The last group proposed in the taxonomy is the room-based system (e.g. full-flight simulators [334] or Cave Automated Virtual Environments (CAVE) [332]).

A virtual reality-based system consists of interactive output devices (i.e. wired HMD, mobile HMD, haptic devices or multisensory devices including tactile or olfactory generating feedback such as body worn devices), input devices (i.e. controllers, navigation devices, body trackers and gesture trackers), a virtual environment manufacturing system and the information software [335, 336] that allows the detection of the participant's action and instantaneously renders a corresponding effect such that a full interaction in real-time is possible. The power of interaction translates into captivity power such that the user feels immersed in the system defining the role of user experience. Finally, the integration of virtual reality into various applications such as education requires the developers to employ imagination in activating the different features of the system to ensure the environment constructed is as close to reality as possible. Furthermore, Burdea et al. introduced five classical components of any VR system as it interacts with a user based on tasks as depicted in Figure 1–7. Specifically, *input devices* capture, track and trigger signal input data from the user to the VR environment, communicated via a *hardware interface* which carries the *VR Engine* that leverages the use of various embedded and/or integrated *software and databases* for digital computation to render data back to be sensed by the user. There are two types of input devices, manual operation and automatic tracking. Manual Operation input-type devices include general (such as Keyboard, Mouse, Joystick, etc.) or customized instruments. Automatic tracking types includes Head (e.g. accelerometer, gyroscope), Hands (e.g. Data gloves, gyroscope), Eyes (e.g. camera, IR sensor), Body (e.g. IR sensor, depth camera), Voice (e.g. microphone) and Position (e.g. magnetic/optical/mechanics sensors). Position trackers have been mostly utilized for acquiring input values sampling head and hand positions, for instance, at rates of 20–120 Hz compiled in data structures formed of six

numbers representing three-dimensional (3D) translation and rotational transformations in the form of absolute or relative. Absolute trackers include the Polhemus Patriot/Fastrack (Polhemus, USA), AmfiTrack (Amfitech., Denmark) or DriveBAY and TrakStar (Northern Digital Inc., USA). Tracking balls or joysticks that measure displacements (or forces) by the user with respect to a fixed coordinate system such as the CLS-E Force Feedback Joystick (Brunner Elektronik AG, Switzerland). Hybrid devices incorporate both relative and absolute tracking such as controller haptic devices. Output devices denote devices that transform signal intensities to human perception for an immersive experience in the virtual world. Mazuryk et al. noted that human sensory perceptive experience is likely to be an assembly composed of a 70%, 20%, 5%,

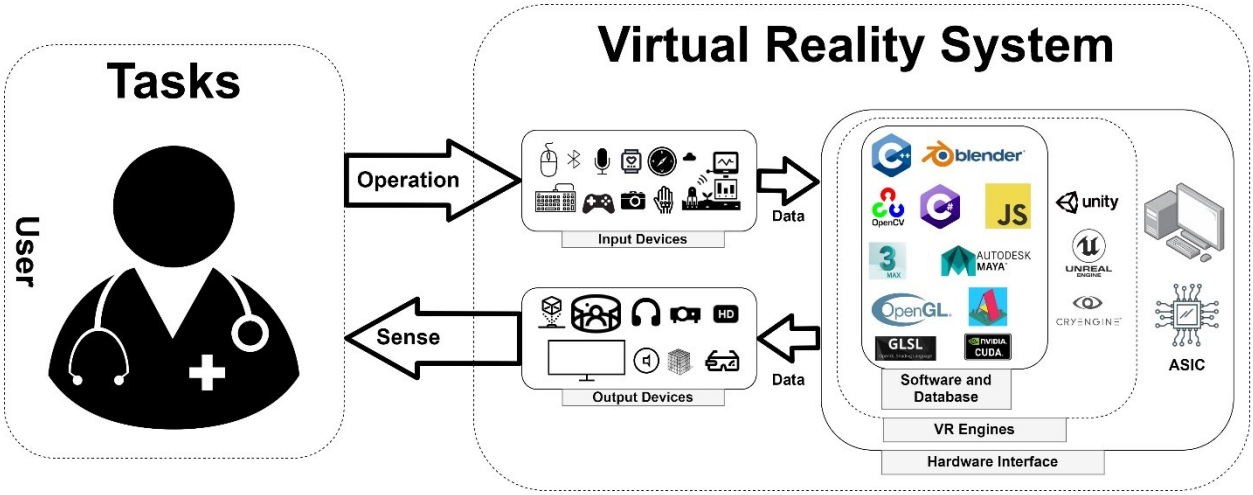

Figure 1-7: Virtual Reality Component Breakdown

4% and a 1% contribution of the sight, hearing, smell, touch and taste, respectively [337]. Visual VR display devices may be categorized into screens (e.g. Flat screens and 3D screens), projectors (e.g. Flat screen fabric and curved multi-screen fabric), HMD (e.g. high screen resolution or small optical projectors) and holograms (e.g. Holographic emitters). In addition to IO devices, VR systems are usually equipped with Graphical Processing Units (GPU) that offer immense number of threads for parallel processing of specific tasks in graphical rendering or for backend force computation using FEM framework, for example, to increase real-time performance. The virtual scene and adopted interactive hardware are usually employed within a specific system architecture. Figure 1–8 displays a typical VR system architecture that employs a haptic device and position sensor as the hardware available to interact with the VR scene. The system initiates with typical user-friendly (i.e. plug and play) hardware that connect to a

hardware interface (e.g. game console or desktop computer). This hardware interface communicates via a unified standard platform formed of low-level standard libraries and APIs that follow a specific protocol defined by basic implementations (as shown in the top level of the hierarchy).

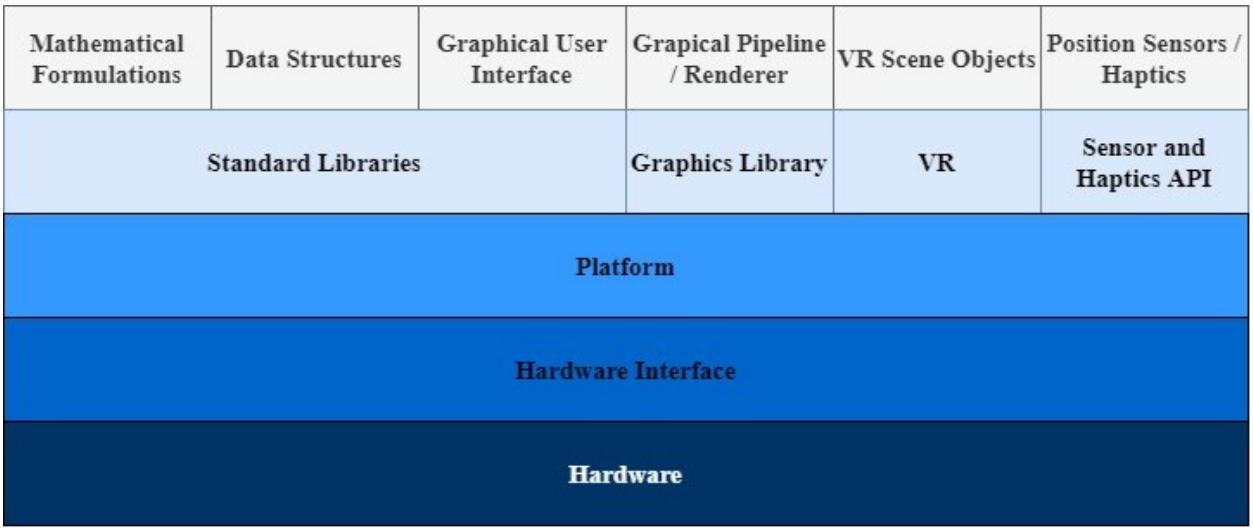

Figure 1-8: Engine Hierarchy

Haptic devices have received great interest in medical VR simulators, yet, are considered to be, generally, the most neglected component [338]. Haptic feedback serves a crucial role in the surgical experience given that touch is the most proficient sense in the body and, recently, one of the main tools that surgeons depend on especially when conducting visually impaired operations such as minimally invasive surgeries. This is the result of the inherent nature of the "touch" sense such that it is not localized to a specific region of the body, in comparison to the other four main senses, and is distributed in the skin, joints, muscles and tendons [339]. In fact, Alaker et al. noted in their comparison between VR simulators and box-trainer simulators that VR simulators that lacked haptic feedback were observed to be even less effective than box-trainers which become closer to real-life situations of force tissue feedback [340]. Two modalities form the touch sense; *Kinesthetic* which include force and torques sensed in the muscles, tendons and joints and *Tactile* which include pressure, shear and vibration acquired by specialized sensory end organs such as the mechanoreceptors embedded in the skin. Fast-adapting mechanoreceptors capture dynamic signals while slow-adapting

mechanoreceptors respond to static stimuli. In specific, Meissner corpuscles are fast-adapting and capture low frequency vibrations, Pacinian corpuscles respond to wider high range high frequency vibrations responding to dynamic contact, Merkel disks are slow-adapting receptors that capture edges and spatial features, and Ruffini endings sense skin stretch and allow for the perception of direction of object motion and force.

Generally, the types of haptic devices divide into:

1. Graspable systems can be kinesthetic force-feedback devices that are grounded and allow the user to hold a tool and push on them or can be tactile ungrounded devices (e.g. tool with flywheel embedded to provide inertial forces).
2. Wearable systems are mostly tactile (cutaneous) devices mounted on a hand or other body parts to provide direct stimulus to the skin (e.g. local shear and normal skin stretch and vibrations). These systems may be ungrounded (e.g. gloves) or grounded (e.g. exoskeleton).
3. Touchable systems that allow the user to actively explore a full system. A haptic surface may provide specific stimuli (e.g. friction) on surfaces that are reliant the location or may change shape, mechanical properties and surface properties accordingly.

Kinesthetic graspable devices refer to the sensation of movement and force associated with force-displacement relationships [339]. Such devices typically target the involvement of muscle spindle that transduce a stretch to the muscle in general and Golgi tendon organs that sense these stretches. Applying a stimulus on these organs result with an illusion of motion and/or force whereby a force is applied about a joint in movement conceiving a resistance to that movement. While the literature is extensive in relation to such devices, the impressive dynamic range, high DOF and sensational thresholds by the human force sensing system poses a challenge on a designing proper force-displacements to meet the precision and scale of human force sensing and motor control. Traditional kinesthetic devices (e.g. Phantom Premuim haptic device (SensAble Technologies, USA) enable 3 DOFs with high force and bandwidth force feedback with low frequency impedance. Such devices may be divided based on the control formulation that composes the system, i.e. Impedance and Admittance control [341]. Impedance control-based haptic devices (or position-based) operate on the basis of

measuring position based on the operator's motion input and sends force back to the operator. While admittance control-based haptics measure forces fed by the operator and render the corresponding position. Admittance controlled devices are usually troubled when dynamic interaction with stiff real surfaces and low inertia and is easier to be used when rendering of stiff virtual surfaces is required. Impendence control, on the other hand, is better employed in rendering low inertia but becomes challenged when rendering stiff virtual surfaces [342].

Today, haptic devices have become widely available commercially having specific capabilities based its use. For instance, Touch® (3DSystems, South Carolina, USA) operates with 6 DOF and a can provide a force feedback up to 3.3 N. Similarly, Touch X® allows 6DOF with a force feedback up to 7.9 N, OMEGA® and SIGMA® (Force Dimensions, Nyon, Switzerland) have 7 DOF with up to 12 N and 20 N of force feedback, respectively. A haptic device is usually rated based on bandwidth, back-drivability, friction, maximum exertable force, continuous force and stiffness to define its capabilities. Table 1.12 lists a non-exhaustive set of commercially available haptic devices.

Table 1.12: List of commercially available haptic devices

Haptic Device	Manufacturing Company	DOF	DOFF	Maximum Force	Maximum Torque
Touch	3D Systems	6	3	3.3 N	-
Touch X	3D Systems	6	3	7.5 N	-
3D Systems Phantom Premium 1.5, 1.5-6DOF, 3.0-6DOF	3D Systems	6	3 or 6	8.5N, 37.5N or 22N	170 mNm for Yaw, 515 mNm for pitch roll
Delta.3	Force Dimension	3	3	20 N	-
Omega.7	Force Dimension	7	4	12N translation 8N grasping	-
Omega.6	Force Dimension	6	3	12 N	-
Omega.3	Force Dimension	3	3	12 N	-
Sigma.7	Force Dimension	7	7	20N translation 8N grasping	400mNm
Falcon	Novint	3	3	9N	-
W3D	Entact	6	3	15N	-
W5D	Entact	6	5	15N	-
W6D	Entact	6	6	-	-
Virtuose3D Virtuose3D High Force	Haption	6	3	35N 70N	-
Virtuose6D	Haption	6	6	35N	3.1 Nm
Virtuose6D Desktop	Haption	6	6	10N	0.8 Nm
Virtuose3D Desktop	Haption	6	3	10N	-
HD^2 High Definition Haptic Device	Quanser	6	6	19.71N	1.72 Nm

1.3.4. MEDICAL SIMULATORS

The first application of a virtual reality simulator was documented in the training of air force pilots in flight in the 1970s. Technological advancements in hardware and software in the 21st century has allowed for the expansion of the virtual reality market. For example, visualization plays a great role in interpreting data in various technical and scientific applications including the field of art, medicine, architecture and archeology. Behavioral experiments have exhibited a need for the use of virtual systems to capture action-perception behavioral cycles whereby the experimenter would control the environment which may not be possible using traditional systems that single out perceptive features in investigations such as reaction-time measures, grasping behavior, eye movements, etc. [343, 344]. Furthermore, the entertainment

industry has observed increased interest in VR with the rapid development of the input/output (I/O) devices technology such as Head-Mounted Displays (HMD) (e.g. unibody devices Oculus Rift or HTC Vive) [345]. For instance, driving simulators for airplanes, helicopters, trucks and even wheelchairs have leveraged virtual reality simulators that aim to train and/or familiarize students to instrumentation, handling, navigational tasks, or integration of updates [346].

Medical simulators have been progressively incorporated into educational services for medical students, fellows, practicing physicians, paramedical personnel and certified medical staff. VR simulator integration gained higher momentum with the increasing adoption of minimally invasive surgeries which accompanied concerns such as training time and patient safety [347]. Previous reports on the usage of generic VR simulators that obtain, enhance and maintain complex skills and achieve basic competence in fields of laparoscopy, endovascular surgery, endoscopy, gynecology and urology [348-350]. In laparoscopy, for instance, surgical training has been described as going through a paradigm shift whereby it has become unethical for surgical trainees to practice their skills in the operating room such that the 100–year–old Halstedian mantra “see one, do one, teach one” has become obsolete [351]. As such, apprentice-tutor models of surgical training has improved to include zero-risk to patients by learning technical and non-technical skills outside the operating room [352]. In fact, previous research has shown that such acquired skills transfer to real operations in a variety which has been suggested to improve patient safety [353, 354]. In addition to training, the relatively simple customization provided by VR simulators have allowed it to be utilized by certification boards for assessing physician skills and knowledge. This has already been conceived in some specialties whereby the certification board utilizes VR simulators for assessment such as vascular surgery [355].

In essence VR systems provide an easy access to clinical experiences. VR systems usually comprise of a laptop and a limited number of hardware accessories that are commercially available and made to run with simple and ease of use in comparison such that trainers can operate it at any time without confinement to large centers or high budget setups [356]. This flexibility of access has been suggested to be one of the main reasons that motivate its incorporation into everyday learning activities practices. Issenberg et al. conducted a systematic review to identify the main features and uses of high-fidelity medical simulations leading to an effective training by screening a final pool of 109 relevant articles that have investigated simulators as educational intervention, assessment or were involved in comparative experimental

or quasi-experimental research about simulators [357]. In general, they observed a positive outcome with the effect of employing simulators in facilitation of learning. The journal articles mostly identified the capability of providing feedback to the user based on performance as the most essential feature of VR simulators (47%). This is followed by the opportunity for learners to engage in repetitive practice to improve performance (39%), necessity of incorporation of simulators into curriculum integration for effective use (25%), variation in range of difficult level to enhance skills progressively (14%), inclusion of multiple learning strategies such as instructor-centered involving small or large groups, independent small groups or independent individual learning (10%), properly capturing clinical variations and the capability to represent a wide variety of patient problems from a broad universe of patient demographics (10%), a controlled environment such that learners can make, detect and correct errors without risking a patient and instructors can focus on the learner instead of the patient (9%), individualized learning for active learning (9%), defined outcomes with benchmarks for tangible well-founded goals (6%) and validity of simulators defined by the degree or fidelity compared in approximation to real clinical situations (3%). Pottle et al. also mentioned that, in addition the to the psychological safety induced when employing a VR-simulator, the enjoyable nature and game-like setup encourages involvement and autonomous learning [356]. Nevertheless, it has been noted that medical VR systems allow simulation at reduced cost and fewer resources. However, the exact assessment of financial costs are often difficult to conduct and, when attempts are made, they are under-reported [358]. In perspective, fully immersive medical simulators have been approximated to have a setup cost of US$876,485 for a full renovation of the facility such that fixed cost per year totaled US$361,425 while variable costs were US$311 per course hour [359]. Similarly, Iglesias–Vasquez stated that the incurred costs for a 4–day course on advanced life support is US$1,423.18 per passed participant [360]. In comparison, VR simulators have been approximated to have an averaged hardware cost of US$3,745 and a software cost defined by the provider which is frequently under one–tenth the cost of physical simulations independent of the provider [356]. In addition to direct financial savings, VR setups can deliver an immersive clinical experience all within a 2 x 2 m space within a relatively short setup–time. Additionally, the adoption of VR simulators, generate a significant amount of data that may be used towards the identification of struggling students who would benefit from further training. This hardware-software flexibility and reduction in cost allows for the global

distribution of the platform over different entities dealing with different populations which devise interesting prospects in healthcare training.

In terms of effectiveness, Haque et al. conducted a meta-analysis on VR simulators and concluded that VR training does indeed reduce the time taken by participants to complete surgical tasks as well as clearly distinguishes between a professional and novice participant (~10 min reduction) [361]. Other clinical trials focused on VR simulators have similarly validated that the employment of these simulators does indeed result with a reduction of surgical errors and an improved development of trainee surgical skills [362-364]. Enhancement by VR training has been shown to be associated with elevated motor and visuospatial skills [365]; the two main aspects related to surgical performance [366]. This, complemented with feedback from an instructor and operation–room training, have proved to have a high impact on the surgical learning curve [367]. In fact, the feedback for trainees is based on specific metrics measured according to special, force intensity and specific surgical performance criteria (e.g. blood loss, tissue volume removal, tool tip path, operation time, etc.) [368]. Metrics are incorporated assessment tools that measure the performance of the user. They evaluate parameters such as path distances, velocity, acceleration, errors, operation time to deliver quantified objective values that may be used to assess the trainee's performance (e.g. hand-eye coordination status) if the simulator meets the construct validity criteria. Otherwise, human experts would play the role of the evaluator and intervene in providing performance criteria [369]. These metrics have been previously deemed to be extremely beneficial in terms of system feedback to the extent that Miyata et al., in validating a laparoscopic VR simulator with a pool of participants consisting of ten experts, 9 intermediates and 14 novices noticed considerable differences in resulting metrics such as blood loss and total number of errors to be deemed as a system suitable for skill assessment [370]. Upon completion of the developmental phase of simulators, it is customary to conduct validation steps to conceive a stable well–founded simulator. Table 1.13 provides an exemplary list of previously developed VR surgical simulators.

Table 1.13: List of VR-based medical simulators

VR Surgical Simulator	Manufacturing Company	Surgery Simulated	Description
NeuroVR™	CAE	• Cranial Surgery • Endoscopic Surgery	• Two Touch® Haptic Devices • Pedal Trigger System • Stereoscopic and 2D view • Real Instrument mountable Set
Minimally Invasive Surgical Trainer-Virtual Reality MIST-VR™	Wolfson Centre and VR Solutions	Laparoscopic surgery	• Adjusted to six difficulty levels • No haptic feedback • Transferability of skills controversial • Ergonomic task analysis-based development
LaparoscopyVR LapVR™	Immersion	Laparoscopic surgery	• Supports haptic hardware for force feedback • Validated transferability of skills to real procedure • Adjustable levels of difficulty • Camera Navigation • Allows individual and team training • Includes basic skills training modules for hook electrode, cutting, clipping, suturing and knot tying
LapMentor™	3D Systems	Laparoscopic surgery	• High fidelity • Haptic Feedback • Includes basic laparoscopic skills such as suturing, laparoscopic cholecystectomy, ventral hernia, gastric bypass and gynecology • Metric-based simulations • Demonstrated construct validity • Transferrable skills
LapSim™	Surgical Science	Laparoscopic surgery	• Incorporates basic skills modules including anastomosis, suture scenario, laparoscopic cholecystectomy, gynecology • Demonstrated construct validity
SINERGIA [371]	Universidad Politécnica de Madrid	Laparoscopic surgery	• Transferrable skills • Demonstrated construct validity • Modules for basic laparoscopic surgical skill development • Didactic design based
Xitact LS500®	Xitact SA	Laparoscopic surgery	• Transferrable skills • Demonstrated construct validity • Modules for basic laparoscopic surgical skill development such as laparoscopic cholecystectomy and peritoneal dissection for opening Calot's Triangle • Hybrid system that combines a physical object with computer-based virtual simulation

ProMIS3™	Haptica	Laparoscopic surgery	• Transferrable skills • Demonstrated construct validity • Real Instruments used • Comprehensive metrics • Hybrid System with benchtop system connected • Modules for basic laparoscopic surgical skill development such as laparoscopy Orientation, Instrument handling, dissection suturing, knot tying, SAGES/ACS FLS Module
GIMentor™	3D Systems	• Oesophagogastroduodenoscopy (OGD) • Colonoscopy • Endoscopic Retrograde Cholangiopancreatography (ERCP)	• Currently the only validated system for OGD and ERCP • Effective with novices more than experienced users • Chosen by SAGES as the platform for the Fundamental of Endoscopic Surgery™ Examination
EndoVR™	CAE Healthcare	• Bronchoscopy • Endoscopy: Upper Gastrointestinal Tract • Endoscopy: Lower Gastrointestinal Tract • ERCP	• Demonstrated construct and predictive validity • Replicates endoscopic procedures with accurate haptic technology • Didactic Content • Compares output metrics with
Olympus Endo TS-1	Olympus	Endoscopy	• 3D Real-time movement of colonoscope rendered to screen • Demonstrated construct and predictive validity
Immersive Touch™	ImmersiveTouch	• Spine Surgery • Neurosurgery • ENT surgery • Opthalmology	• Validated for thoracic pedicle screw placement (face and predictive validity), clipping aneurysm (face validity) and percutaneous trigeminal rhizotomy (construct validity) • Positive learning effect • Deemed to being capable of accelerating the learning curve such as neurosurgical procedures such as ventriculostomy, vertebroplasty and finding anatomical landmarks for various intervention techniques
ROBO-SIM [372]	Institute of Applied Sciences in Medicine	Minimally Invasive Neurosurgery	• Adopts actual patient datasets with ventricular tumors • Includes all planning modules • Employs same surgical tools
VIVENDI	University of Tubingen	Minimally Invasive Neurosurgery Neuro-endoscopy (endoscopic Transsphenoi)	• Includes all planning modules • Employs haptic feedback via tactile tool manipulators
Vascular Intervention Simulation Trainer, VIST®	Mentice AB	• Endoscopy: Carotid Angiography • Endovascular Surgery	• Focus on coronary, carotid, renal intervention, stenting and pacemaker lead placement • Employs haptic feedback, dual monitors and synthetic x-ray imagery

EasyGuide Neuro [373]	Philips Medical Systems	Stereotactic Neurological Surgery	• 3-D optical system (2 IR cameras) embedded • Employs haptic feedback, dual monitors and synthetic
ANGIO Mentor™	3D Systems	• Interventional Cardiology • Interventional Radiology • Vascular Surgery • Electrophysiology Interventional Neuroradiology • Neuro-surgery and Trauma • Endovascular Surgery	• Over 30 endovascular procedures and 230 patient-scenarios • C-Arm and Patient Table maneuvering • Real-time ultrasound features • Use of actual tools • Complex scenarios with real-time complications
Dextroscope	Volume Interactions Pte Ltd.	Neurosurgery: Tumor Resection and Skull Base	• Complex scenarios with real-time complications • Surgery conducted through mirror-based display • Allows for virtual segmentation and polygonal meshes • One hand holds on to an ergonomically shaped handle that allows manipulation of geometry and second hand holds on to a stylus
Anatomical Simulator for Pediatric Neurosurgery [374]	Pediatric Neurosurgery Center/CENEPE and Pro Delphus Company	Endo-neurosurgery	• Built with synthetic thermo-retractile and thermo-sensible rubber (i.e. Neoderma®) • Physical head manikin connected to body by a structure with acrylic composition • Artificial real bleeding with saline solution • Dimensions of ventricular cavities estimated from volumetric MRI and used to construct the VR object rendered to screen
Vimedix™	CAE Healthcare	Ultrasound Training for cardiology and cardiothoracic surgery	• Facilitates learning process for cardiac, lung, abdominal and Ob/Gyn ultrasound • Recent introduction of training to exploit COVID-19 related lung-damage • Equips the Hololens to provide images unrestricted from the dimension of the screen • Consists of a mannequin and a transducer transthoracic or transesophageal echocardiogram
Nakao Cardiac Model [375]	Kyoto University	Cardiovascular Surgical Simulator	Haptic enabled virtual reality system that provides interactive visualization of a 3-D beating heart for practicing surgical palpations
Minimally Invasive Cardiac Surgery	Berlage and Co.	Cardiovascular Surgical Simulator	Non-haptic virtual reality system displaying beating heart, ribs and chest based on patient's unique CT images

da Vinci Surgical System™ (dVss™)	Mimic Simulation	Cardiovascular Surgical Simulator	Employs VR robotic training Performance tests previously to show that trainees on the dVSS modules performed better than control group
URO Mentor™	3D Systems	Urology	• Incorporates numerous training modules for the various urologic fields • Shown to have educational benefit in cystoscopy and ureteroscopy including essential skills, stone extraction, stone lithotripsy • Considered to be realistic and useful for endourological procedures
Phantom® Haptic Interface	3D Systems	Orthopedics	• Employed in numerous simulators as the main haptic accessory • Provides stand-alone simulations in spinal needle placements
HAL S2001® HAL S3000®	Gaumard	Orthopedics	• Even though employed as mannequin for simulators, it includes a patient monitor that provides real-time feedback about the physical components embedded • Employed for standalone vertebroplasty simulation training
Novint	Falcon	Orthopedics	• Employed in numerous simulators as the main haptic accessory • Employed for standalone vertebroplasty simulation training
Arthro Mentor™	3D Systems	• Orthopedics • Endovascular Surgery	• Displayed face, content and construct validity • Detailed realistic anatomical models • Haptic feedback embedded • Fundamentals of Arthroscopic Surgery Training (FAST) • Shoulder and Knee procedures
ArthroSim™	TolTech	Orthopedics	• Displayed face, content and construct validity • High fidelity tactile feedback with the usage of two haptic devices • Incorporation of an FEM technique for real-time deformations

Validation normally includes face, content and construct validity to prove reliability. Face validity is usually used by experts to assess whether the outcome of a test measures what is intended to do. This step usually equates the surgical simulator to reality. For example, previous studies have employed questionnaires containing multiple questions on a 5-item Likert scale to assess ease-of-use, realism of exercises, visual realism of simulator, hardware realism and realistic movement [376, 377]. Content validity measures whether the skills targeted for

development by the simulation do indeed prove to be useful and are appropriate and correct. For example, questions addressed by several studies concerned the usefulness of simulators for training and the feasibility of integration into the curriculum [378]. Construct validity signifies the ability of a simulator to differentiate between novice and expert performances on any given task within the simulator [379] which, in turn, provides clinically meaningful assessments [380].

While surgical simulators provide numerous advantages over traditional surgical simulators when adopted for training purposes, current simulator accuracy and efficacy suffer from limitations. Krishnan et al. provided a general break down the cons of simulators in healthcare and explained that medical simulators continue to lack a complete mimic of the human system, defective learning may result if not properly followed, learners participating in the system have a different attitude when approaching a simulator, high cost factor, technical and programming difficulties inherent within the complex development of these systems and learning specific features including physical indicators due to inaccurate rendering limitations such as skin color changes [381]. Zhoa investigated the most important current problems in VR technology including simulation computational models, complexity, model credibility, model measurement similarities, image quality, real-time fidelity, material properties and their integration and performance evaluation criteria [382]. Furthermore, density, palpable properties, convex surfaces and high accelerations remain very challenging to simulate in a virtual environment [383]. Nevertheless, response rates and intensity feedbacks of commercially used haptic devices remain low when required to reproduce vibrations when drilling [384]. Kolivand et al. mentioned that disadvantages of employing VR surgical training simulators involve the high initial cost of such machines as well as the requirement of a simulator staff to explain the modules. Moreover, they noted that, in terms of human-computer interfaces, time delays in the simulator's response to user movements including lagging issues exist as well as shortcomings in perfect visual realism of the models used [385].

1.3.5. Realtime Computational Techniques and Puncturing Models in Surgical Simulators

Modelling has been a basic but crucial engineering task whereby different options are investigated to achieve a well–founded solution between the computational expense and accuracy of the simulations performed [386]. In general, engineers combine available knowledge

of physical processes with innovation and creativity to achieve compelling methods that shape the world in a spectacular way. These techniques are usually bound by the available engineering tools, hardware and software. As such computational surgery has been conceived and is defined as “the application of mathematics and algorithm design, enabling imaging, robotics, informatics, and simulation technologies, incorporating biological and physical principles to improve surgery” [387]. With the ascending adoption of endoscopic and minimally invasive procedures, on one hand, and robot-surgery surgery, on the other hand, surgical training has become an important task to be completed by surgeons in recent years [388]. This presented a challenge initially with the incorporation of state–of–the–art constitutive equations in the simulators. In essence, a virtual surgery simulator requires a haptic peripheral that communicates with a simulation engine which detects contact between a virtual tool and virtual organ. The computed stresses due to the tool–tissue interaction, which deformed the tissue, provides the user’s hand with a realistic sense of force feedback. This conceives one of the bottlenecks of the system since a realistic sensation of touch requires a rendering frame rate of 1 KHz (which coincides with the free hand gesture frequency) [389]. This specifically becomes challenging given the non-linear large deformation of soft tissues which require complex modelling. Relative to real-time computation requirements, current “offline” simulations take up considerable time with current computer machines.

“Offline” simulations typically refer to the engineering practice of modelling and simulating structures to analyze their resulting behavior whereby preparation and pre-processing of the models initiate the workflow within a specific framework. In recent times, structural analysis basically incorporates the adoption of the finite element method (FEM) which has imposed itself as the most powerful tool that allows efficient modelling and simulation of structures that have complex geometries and arbitrary initial and boundary conditions. However, this heavily relies on the hardware adopted and, hence, computations of this numerical technique remains highly demanding [386]. In essence, the FE method operates on the basis that the total potential energy should be a minimum when an external force is applied to the body (i.e. the strain distribution that is actually generated among all other profiles makes the potential energy minimum). In practice, it splits the computational domain into small individual patches (e.g. triangles (2D) or tetrahedrons (3D)) then finds a local solution that satisfies the differential equations bound within these patches (i.e. the partially differentiated with respect to the

displacement to obtain an equilibrium). Recombining these individual solutions back together allows for the obtaining of a general solution [390]. Delingette et al. [388] simplified the taxonomy of these real-time computational methods into three classes which are most commonly used including:

1. Direct Methods: which solve static or dynamic equations at each iteration (quasi-static motion) by incorporating pre-computations. These methods conceive a high frequency update and are not suitable for rendering stiff material given their low relaxation time. This also hinders the inability to simulate cutting or suturing due to the pre-computation step which affects the change of topology in cutting, for instance.
2. Explicit Iterative Methods: whereby the deformation is computed as the limit of a converging series such that the closer the initial value is to the solution, the faster the solution converges. Such methods can be based on explicit or implicit schemes whereby explicit schemes obtain the next position of the tissue model from the application of internal forces estimated at the previous timestep.
3. Semi-Implicit Iterative Methods: whereby semi-implicit schemes obtain the next position of the tissue from the application of internal forces. Hence, a linear system of equations needs to be solved entirely or partially. This results with an increase of the time step by an order of magnitude. While this conceives more realistic dynamic behavior of tissues, it suffers from a high computation time.

Satava et al. proposed a taxonomy of virtual anatomy that he divided into five different generations [391]. The first generation was composed of systems that accurately represent the geometry of the anatomical organs macroscopically (usually conceived by reconstructing MRI and CT scan images through methods such as segmentation) whereby simulators within this category allow the user to navigate within the human body with minimal interaction with its modelled organ. The second generation incorporate an accurate description of the physical dynamics of the body whereby users employing simulators that adopt such techniques are able to better interact with soft tissues defined by biomechanical properties to perform basic surgical tasks such as cutting or suturing. While going beyond the second generation remains a challenge imposed on real-time surgical simulators, he further included a description of three generations that incorporate accurate, state–of–the–art models for soft tissue on the continuum level. In

specific, the advancements include an accurate model of the physiology, microscopic anatomy, and finally biochemical systems, respectively listed in order of complexity.

To obtain a reasonable compromise between realism and computational speed, simulators in the past, and still in the present, have adopted a variety of so-called “physically-based models”. The early works of Terzopoulos et al. [392], Waters [393] and Platt et al. [394] have shown the advantages of using physically based models over prior computer animation techniques for surgical simulators. Hence, early research showed significant interest in mass-spring models which essentially transform a mesh by defining elastic forces between vertices based on the edge length. In specific, a soft tissue becomes composed of a number of discrete masses connected with each other by springs such that a deformation response of the object would be conceived through a compression and tension of these springs. Despite the significant simplifications, its ease in implementation and resulting high speed have posed it as a viable solution in medical simulators [395, 396] such as its incorporation as a model for muscles [397]. However, such a technique is effective mostly at a low number of vertices and its stability strongly depends on the value of its parameters as the traditional technique was previously reported not to properly represent the inner structure appropriately (i.e. non-linear tissue deformation) and is more suitable for low deformations [398]. Hence, several variations were developed such as the technique conceived by Hrennikoff in 1941 with the use of nonlinear mass-spring models [399], the enforcement of homogeneity within the lattice [400] or the controlled anisotropy in mass-spring models which involves the usage of additional forces to control a constant volume deformation [401]. Furthermore, the “chain-mail” technique was proposed by Gibson et al. [402] for medical simulators that account for the volume of the organs with deformation laws derived from the spring-mass model. Nevertheless, researchers have proposed solutions to refine linear FE models to solve the governing mechanical equations which have been shown to require similar computational effort such as the mass–spring technique to provide more accurate results [403]. Kuehnapfel et al. presented a simulation of endoscopic surgery based on a surface spring–mass model whereby interactions were driven by instruments with motion sensors and no force feedback.

FE models provide relatively accurate results through fine discretization (i.e. meshing). However, this results with higher dimensional systems of equations which, in turn, is the most demanding part of FE. Hence, authors have developed different methods to perform model order

reductions such that the resulting lower dimensional system of equations remains reasonably close to the initial system of equations. For example, Multi-body systems (MBS) represent the superposition of rigid-body motion and local deformations. Hence, an MBS–FEA co–simulation provides a high-fidelity approach with high accuracy but at the cost of higher computational requirements. As such, modal vectors and coordinates were proposed such that most of the computations are conducted prior to the simulation [404, 405]. Authors have proposed more complex methods than mass-spring models which are more related, to some degree, to continuum mechanics. For example, tensor models have been proposed to extend the limitation proposed by quasi-static techniques for tasks such as cutting and tearing. In particular, these dynamic techniques permit a topological change and are derived with the simplification of applying a mass–lumping (i.e. decoupling of the motion of all nodes such that the equations are written as a set of independent differential equations for each node). However, this technique suffers from the inability to simulate large displacements accurately. Thus, Cotin et al. devised a hybrid technique that combines the spring-mass model and the tensor–mass model to achieve both large deformations of muscles and cutting on complex anatomical structures which is based on a set of pre–computed equilibrium solutions [406]. Yet, the drawback of this method includes the instability in handling varying stiffness models (i.e. physical contact, geometrical and nonlinearity or topological changes resulting from cutting). Interestingly, Huang et al. aimed at enhancing the use of structural analysis by employing AR technology. In specific, they developed a system that embeds sensors, in addition to an FE framework, such that the network of wireless sensors acquires spatially distributed loads and the FEA generates fast solutions for the sensed loads. It is worthy to note that the high computation speed achieved via FEM was a result of assuming linear and quasi–static behavior, whereby the inverse of the stiffness matrix is pre-computed [407]. Fiorentino et al. created a visualization of the output by overlaying the FE results into the real model. The user would be able to interact with the models, hence, changing their boundary conditions which would deform based on the FE results assessing the stress/strain distribution [408].

Adopting Linearly elastic models have been a trade–off between the real-time computational expense and the realistic biomechanical behavior of soft tissue. While the FEM sustains an excellent alternative, in terms of accuracy, its application in early simulators presented a challenge with the high computation overhead. Hence, condensation techniques were

implemented to reduce the computation time to a complexity order equivalent to the surface model. This assumed that the internal DOFs have no significance from a visual standpoint, thus, the stiffness matrix is condensed which, in turn, reduces the computation required [409]. Cotin et al. proposed physical models based on FEM that leverage linear elasticity whereby precomputed deformations were combined to enable real-time simulations [406]. Pincinbono et al. developed various biomechanical models based on linear elasticity and FEM with anisotropic mechanical behavior included whereby they implemented transversely isotropic properties along with adding an external elastic membrane to represent the stiffer skin [410].

Current innovation in the field includes the incorporation of nonlinear FE formulations for real-time simulations. Given the high computational effort, reduction in the rigorous numerical formulations is achieved by relaxing certain nonlinear effects such that the solution remains stable but accounts for the geometrical nonlinearities extensively. The most interesting of which is the co-rotational FEM formulation [411] which basically accounts for large local rigid-body rotations by means of a local coordinate frame attached to the structure. This simplifies the formulation complexity by the resulting linearized local deformations with respect to the local coordinate frames. Hence, the influence of the local deformations and resulting stress onto the tangent stiffness matrix are neglected as the latter is precomputed and only rotated based on the difference between the current and local coordinate frames. Later, researchers extended this approach to 3D elements (tetrahedrons) also referred to as the “warped stiffness” [412]. Commercially available FEA programs in simulators most commonly employ the Updated or Total Lagrangian Explicit Dynamics (TLED) with the difference of choice depending on the required reference configuration [413]. These techniques are highly accurate and efficient but requires significant numerical effort and may have convergence issues. Szekely et al. applied the TLED method combined with nonlinear material properties to model soft tissue deformations for Laparoscopic surgical simulation [414]. In specific, they addressed the high computational demand of the approach by using the “brute force” method (i.e. parallelizing the computation on a large 3D network of GPUs), however, they reported a low quality, in terms of realism, of the uterus tissue deformation.

In addition to Mass Spring Models (MSM) and Finite Element Models (FEM), Meshless Models (MM) denote the third most commonly used technique in VR surgical simulators [415]. In MM, the soft tissue is defined as a problem domain with a large number of discrete nodes

distributed within the region without a fixed neighborhood relationship between these set of particles. Shape functions are designated to connected nodes to develop a stiffness matrix, hence, any nodal displacement achieved can be used to represent the soft tissue's deformation. In comparison with FEM, the MM are able to simulate the deformation in real-time which is not bound by the constructed mesh. This, however, may lead to divergence problems in situations of high deformations which would be a numerical challenge or may even have no solution (i.e. would require remeshing). Furthermore, this technique does not require any cell meshing data defined for the domain and would evade problems such as mesh distortion or entanglement during real-time simulations. In general, MMs are classified according to the type of shape function they possess, i.e. Moving least square method (MLS) shape functions, integral form shape functions and point interpolation method (PIM) shape functions. Xu Shaojian introduced a viscoelastic model of the liver and performed collision detection experiments on the model to report simplicity in mathematical formulation, proper deformation and a powerful representation of advanced tissue responses for real-time surgical simulators. Such techniques are relatively new (in comparison with the FEM), hence, several advancements have been incorporated to address limitations of the technique (e.g. Element-free Galerkin method) [416]. However, the MM does not come without disadvantages as previous developments of the techniques have shown that it is, in fact, computationally more expensive than FEM. Thus, it becomes more suitable for the animation of physical phenomena without the existence of a mesh (e.g. melting, fluid and solid combination) [417].

Simulation of basic surgical tasks deserve a special comment. In specific, tissue-destructive tasks such as cutting and puncturing were not met without a challenge when adopted in simulators. Cutting has been previously developed within spring-mass systems [406]. This technique removes the tetrahedra that are in contact with the cutting tool which ensures no stability issues arise (no new elements are formed). However, this technique violates the mass–conservation law and the resulting cut may have visual artifacts. Bielser et al. developed cutting tasks by the subdivision of underlying tetrahedra according to a predefined template replacing the contacted tetrahedron by up to 17 new elements following the trajectory of the cut [418]. Similarly, Mor and Kanade subdivided the elements along the trajectory of the cut by generating a minimal set of new elements to replace the cut tetrahedron [419]. However, these techniques conceived ill-shaped elements which often lead to numerical instabilities. Nienhuys et al.

snapped the nodes of the existing elements to the cut trajectory, however, this led to degenerated elements which were identified and removed [420]. Molino et al. introduced the virtual node algorithm whereby one or more replicas of the cracked element and the graphical representation within the original element is fragmented such that the portions are assigned to specific replicas [421]. The usage of MMs described above have thought to have an advantage given the mitigation of mesh constraints, however, this technique proved to be difficult if adopted for cutting since additional structures to identify the topologically separated particles are required and dynamic resampling in the vicinity of the cut is nontrivial [417]. However, continuum mechanics preferred the adoption of eXtended FEM techniques (X-FEM), a technique used in fracture mechanics to predict how objects deform as cracks form and propagate such that the material discontinuities arising in the FEM meshes may be handled without the need of adaptation and remeshing (which have been seen to require a great amount of computation in normal FEM) [422]. Further studies have been developed for cutting that leverage the GPU's parallelized operations for real-time implementations [423].

Puncturing is another basic surgical task most often integrated into surgical simulators for training purposes. Such a task is currently mostly implemented in needle-based training simulators which has currently been extended to train nurses and paramedics in addition to physicians. In such cases, force feedback retrieved from haptics devise main stimulus that novices train on. Furthermore, needle insertion has been considered as a vital element in most minimally invasive procedures [424]. This is specifically given the highly recorded failure rates (up to 32%) found among practitioners [425]. Needle insertion modelling is usually divided into three main phases, needle deflection model, tissue deformation model and needle–tissue interaction forces [426]. Goksel et al. modeled a needle as a discrete structure composed of a finite number of rigid rods that were further decomposed into two springs that aim to unbend and untwist used to study the effect of such deformations on the overall insertion forces [427]. Kataoka et al. modeled a needle using the Euler-Bernoulli (EB) beam theory which employed a distributed load along the shaft of the tool to evaluate the deflection of the needle tip [428]. Similarly, Lehmann et al. employed the EB theory but considered the location of the force resultant at the centroid of the distributed load such that the force applied on the needle base is equivalent to the summation of the load per unit length of the needle shaft [429]. Okamura et al. measured needle forces experimentally using a robotic-assisted setup by decomposing the

interaction force into a cutting and frictional force. The cutting force being conceived as a result of tissue fracture during needle insertion and the friction force attributed to the sliding occurrence of the shaft within the tissue [430]. Misra et al. modelled needle steering using an energy–based formulation interacting within a nonlinear hyperelastic material capable of achieving 2–DOF (lateral and axial deflections of the needle) [431]. Mahvash and Dupont investigated the effect of insertion velocities on tissue deformation and needle insertion forces whereby they classified the insertion procedure into loading deformation, rupture, cutting and unloading deformation events considering nonlinear viscoelastic Kelvin models for the rupture force and tissue deformation relationship [432]. Farber et al. modelled the needle as a rod which decomposes the forces into a pre–puncture, cutting and friction force [433].

Needle modelling has been previously employed within various real-time techniques including Beam-based models, Mass Damper models and FEM-based models. In beam-based models, needle insertion forces are computed and the bending/twisting of the needle are accounted for by calculating the resultant reaction forces [434]. Spring–Damper systems are usually employed in situations when tissue deformation is of interest such that deformation forces may be considered as pre–puncture and post–puncture forces [435]. To account for needle deflection, angular spring models have been previously employed such that the needle is represented as a beam connected at one end and is represented as a series of rigid rods connected to each other by rods having rotational DOFs. The resulting nonlinear equations between the force and joint angles are solved by direct vector algebraic equations [427]. FEM–based models have been previously employed using triangular elements whereby the non–linear inelastic forces as a function of displacement are used to conceive a set of nonlinear algebraic equations solved numerically [436]. Moreover, previous FEM–based models have further incorporated the use of non-linear Euler-Bernoulli Beam elements such that transverse and axial strain/displacements employ cubic and linear interpolation functions, respectively and equilibrium equations are used for the axial force, lateral force and torque using iterative methods.

In quantification of insertion forces, Hing et al. employed a 6 DOF force transducer to acquire the total interactive force of a needle, which they identified as being the sum of the frictional forces and the cutting force whereby the frictional force was measured during the withdrawal of the needle [437]. Similarly, Brett et al. investigated the force output variation with

respect to depth for 1 DOF force transducer at different velocities and observed that maximum forces in the muscle reached up to 5 N within the muscle but increased to 15 N when penetrating through the ligamentum flavum; the highest recorded force within a tissue in needle insertion [438]. Moreover, they observed a reduction in the maximum force recorded as the velocity on insertion increases. In general, modelling of needle forces involve cutting forces, dynamic friction, static friction, compression forces and torque.

The major challenge in the development of needle simulators is the modelling of needle-tissue interaction forces [426]. Due to such complexities, it is recommended to conceive a proper modelling for both needle and tissue separately. Numerous researchers conducted various studies to conceive real-time tissue models which are basically classified into three main categories, namely, phenomenological, structural and structurally based phenomenological models [439]. Phenomenological models consider the tissue homogenous neglecting structural properties of the tissues generated using constitutive equations relating stress and strain. Structural models consider the tissue to be a composite described by nonlinear constitutive equations. The third type joins the two aforementioned models for the definition of the structural arrangement suitable for a specific deformation resultant. DiMaio et al. [440] and Goksel et al. [427] modelled the tissue using an FE framework discretized using triangular elements and considered the tissue as homogenous, linear and elastostatic deforming in the axial and transverse directions. Tissue deformation was formulated using the total strain energy phenomena as a function of stress and strain. Glozman et al. modelled the tissue as a set of springs such that the number of springs increased with increasing depth of the needle [441]. Hing et al. experimentally quantified the deformation of the tissue during needle insertion to model a 3–D liver within the FEM framework [437]. Xu et al. employed the MM framework modelling the tissue and tool as a set of nodes establishing the relation between them based on the formulation that the potential energy is the difference between strain energy accumulated within the tissue and the work done by the needle [442].

Glozman et al. developed a robotic needle simulator and modelled the interaction forces using simplified virtual spring models whereby the flexible needle was considered as a linear cantilevered beam supported by a series of those virtual springs [441]. Forward kinematics were used to compute the position of the end effector to enable needle insertion path planning and inverse kinematics to compute the joint parameter for real-time correction of the path. Similarly,

Simone et al. assumed the force response to be linear for small displacements and modeled the total interaction force as the sum of the lateral forces along the needle shaft in the virtual springs and frictional forces parallel to the needle axial direction [443]. Yan et al. modelled the needle as a BE beam and modelled the tissue as nonlinear elastic material, formulating the system dynamics using Hamiltons principle [434]. Barbe et al. compared between modelling the viscoelastic phase of insertion using a Kelvin-Voigt (KV) model and Hunt-Crossley (HC) model to realize that the HC model is more appropriate for computing viscoelastic force components [444]. Asadian et al. modelled needle insertion forces decomposed into two main phases, the insertion and retraction force [436]. Dynamics forces were mainly modelled based on the LuGre model while assuming a constant velocity during insertion and dependent on depth of penetration. Similarly, Kikuuwe et al. modelled insertion and withdrawal phases of needle forces but used the Coulomb friction model by extending it from 1–D to 3–D considering motion and forces in the axial direction [445].

2

RESEARCH RATIONALE, OBJECTIVES AND HYPOTHESIS

Surgical simulators have introduced a new technique for medical training. The utilization of state–of–the–art hardware technologies has permitted the development of high–fidelity simulators capable of recreating realistic scenarios for practitioners to enhance their cognitive skills. The challenges in adopting traditional techniques include medical regulations that require practitioners to train at a faster pace, legislative acts forbidding residents from training on live animals and zero-risk patient laws inhibiting trainees from learning skills inside the operating room. Hence, surgical simulators have been presented as a solution given the flexibility in development, customization and operation. Over the past two decades, numerous simulators have emerged to target the different surgical operations developed. Consequently, scientific publications that validate the usability, functionality and impact of such simulators on medical performance have surfaced reinforcing the effectiveness of simulators. Moreover, the progressive evolution of surgical methods favoring Minimally Invasive Surgeries (MIS), which adopt new technologies and tools, have created a need for simulators to accelerate hands-on training.

The ***general objective*** of the project was the development of a VR module for the access gaining stage of the OLLIF minimally invasive surgery that may be employed for training and assessing medical students, residents and surgeons.

To address the general objective, virtual models, based on MRI imaging, were acquired then pre-processed to be made fit–for–use within the surgical simulator. In addition to preparing the visual model employed in the VR module developed, the anatomical model would allow for further biomechanical investigation and insight of the human torso for an elaboration of the existing forces using “offline” FEA. In essence, the extracted forces would quantify the boundary conditions and initial state of the VR model prior to real-time

operation. However, the high computational effort required to employ the FE method resulted with the revision of adopted pipeline to render the haptic force feedback on an independent thread. Subsequently, to attend to the realism of the simulator, an experimental setup, pertinent to a set of experiments conducted on cadaveric torso specimens, was constructed and employed to acquire the mechanical response of the tool-tissue interaction. This conceived the necessary requirements to develop a high-speed empirical-based haptic algorithm. Thereafter, a VR scene was developed by programming the gameplay, complementary visual components, training tools, surgical aiding features, auditory feedback, force-feedback and metrics along with the integration of the prior elements to conceive a performant simulator module applicable for training on the access gaining stage of the OLLIF procedure. The latter was made possible by the completion of the following objectives:

Objective 1: Develop a 3D virtual model for the simulator;
Objective 2: Exploit the VR model to possibly extract the boundary conditions of the involved soft tissue prior to surgical intervention via offline simulation and gain insight into tissues involved;
Objective 3: Design and construct cadaveric test bench and conduct cadaveric experimentation to acquire mechanical response of tool-tissue interaction for tasks employed in the "Access Gaining" module of the OLLIF procedure;
Objective 4: Design and develop a force-feedback algorithm that utilizes the cadaveric data;
Objective 5: Develop and integrate anatomic VR-based model, tool VR models, auditory feedback, scene events and components, force-feedback algorithm and metrics with the hardware/software interface to conceive the "Access Gaining" module of the OLLIF procedure.

The ***central theme*** addressed in this thesis is:
High–fidelity medical simulators for MIS may be developed by the utilization of an anatomically accurate model, the employment of accurate force feedback and the implementation of a VR scene that integrates the various surgical components for an immersive experience. This central theme was divided into the following hypotheses:

Hypothesis 1: Offline simulations may play a preparatory role in establishing the initial state of a VR model constructed for real-time simulations;
Hypothesis 2: Quantification of forces may be conceived via cadaveric experimentation regardless of the human interactive forces;
Hypothesis 3: An immersive experience is achievable by medical simulators that employ objective force feedback via direct implementation of force responses achieved from cadaveric experimentations.

The objectives and corresponding hypotheses of this doctoral dissertation were explored and assessed sequentially as presented in Figure 2–1. Acquiring and pre–processing the MRI–based objects in *Objective 1* permitted the *in-silico* study in *Objective 2* and the investigation of *Hypothesis 1*. Further preparation of these objects conceived the graphical model to be integrated in *Objective 4*. Cadaveric experimentation conducted in *Objective 3* allowed for the exploration of *Hypothesis 2.* This data further permitted the development of the haptic model in *Objective 4*, which, in turn, permitted the inspection of *Hypothesis 3*. This ultimately worked towards the completion of the VR development for *Objective 5*. As a result, 3 manuscripts were submitted for publication in peer reviewed journals detailed in *Chapter 3*, *Chapter 4* and *Chapter 5*. *Chapter 6* details the VR model developments and the integration of the components developed in the previous chapters. Finally, an overview combining the studies conducted are discussed in *Chapter 7*, followed by the conclusions conceived in *Chapter 8*.

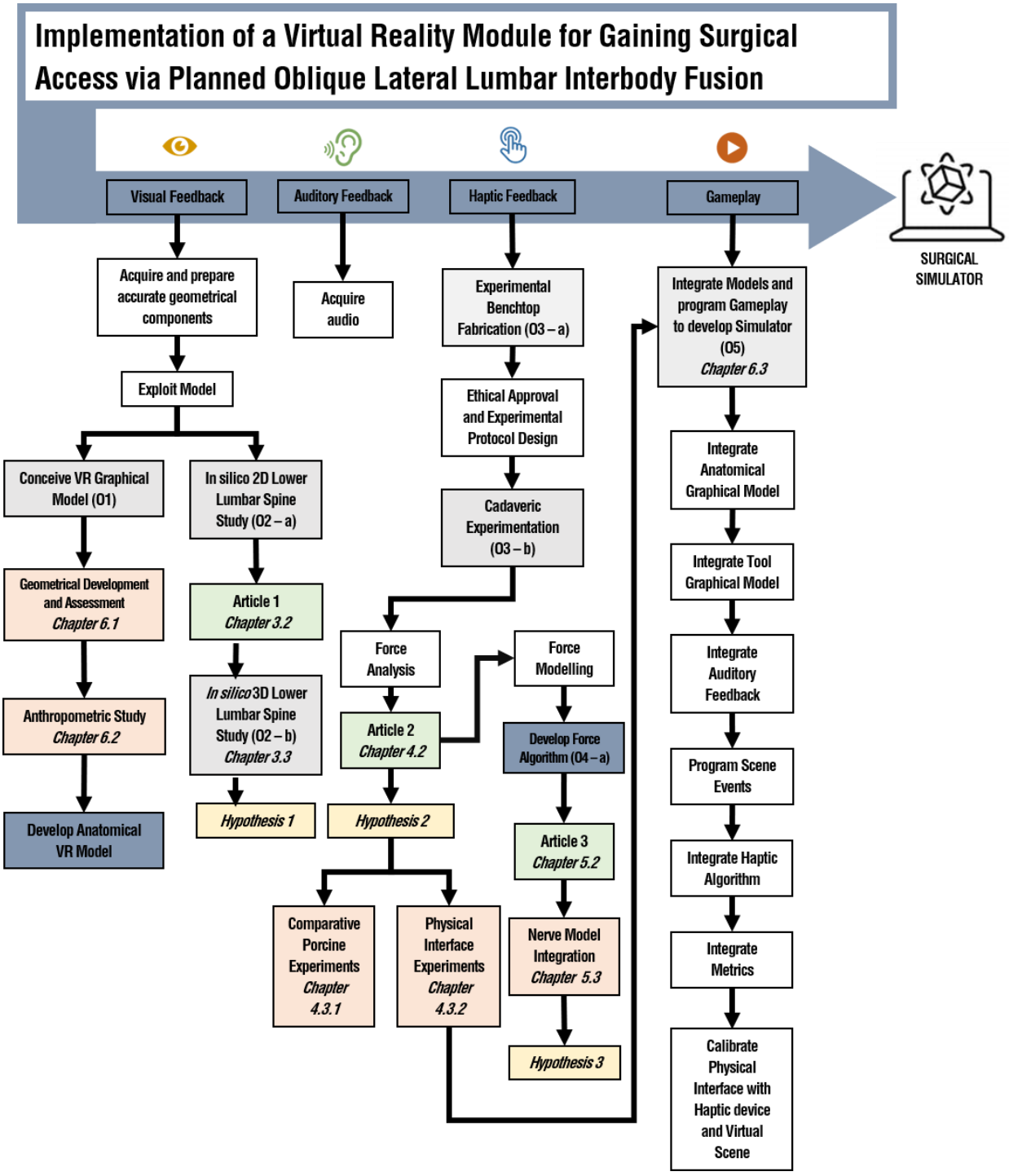

Figure 2-1: Thesis workflow designating Objectives (O), Hypotheses, Articles and thesis chapters

3

STUDY OF THE LOAD TRANSMISSION WITHIN THE LOWER SPINAL STRUCTURE

3.1. FRAMEWORK OF THE FIRST ARTICLE

This study aimed to analyze the forces inherently present within the spinal structures prior to any external surgical intervention. This was conceived by adopting an FE model extracted from the MRI-based segmented tessellation model employed for the surgical simulator. In specific, it sheds light on the incorporation of the Thoracolumbar Fascia (TLF) and Intra-Abdominal Pressure into FE studies, which have often been neglected in previous spinal structural analysis. This study seeks to achieve a better understanding of the force transmission that occurs within the various lower spinal tissues. The outcome of this study provided a baseline for the 3D lower lumbar study which permitted the definition of the initial state of the muscular tissue prior to any real-time tool contact. In specific, the TLF–abdomen complex was given particular attention as a result of its anatomy which engulfs the spinal tissues. Given that the VR model would require a certain level of simplification, this presented an opportunity to single out the fascial structure including its embedded muscular tissue. Hence, the forces achieved including the follower load, abdominal pressure, intramuscular paraspinal pressure and vertebral reaction forces would prescribe the boundary conditions of the TLF-muscle model used within the VR scene. However, the high computational overhead of incorporating the full muscular structure did not permit the use of the finite element method. Instead, as described in Chapter 5, the algorithm directly utilized the cadaveric data extracted in Chapter 4. Nevertheless, this study provided insightful implications of the possible mechanical roles of the compartments which work towards a better general comprehension of spine biomechanics. The attainment of objective 2 and hypothesis 1 are presented in the manuscript entitled “A Finite Element of the Intra-

Abdominal Pressure and Paraspinal Muscle Compartment Pressure through the Thoracolumbar Fascia" for which the contribution of the first author is considered to be 85%. This manuscript was published in the journal of *Computer Methods in Biomechanics and Biomedical Engineering* on April 23, 2020.

3.2. ARTICLE 1: A FINITE ELEMENT ANALYSIS OF THE INTRA-ABDOMINAL PRESSURE AND PARASPINAL MUSCLE COMPARTMENT PRESSURE INTERACTION THROUGH THE THORACOLUMBAR FASCIA

Khaled El-Monajjed, M.Eng., Jr.Eng.[1]; Mark Driscoll, Ph.D., P. Eng.[1]

[1]*Musculoskeletal Biomechanics Research Lab, Department of Mechanical Engineering, McGill University, Montreal, Quebec, Canada*

Address for notification, correspondence and reprints:

Mark Driscoll, Ph.D., P.Eng., Assistant Professor

Associate Member, Biomedical Engineering

Canada NSERC Chair Design Engineering for Interdisciplinary Innovation of Medical Technologies

Department of Mechanical Engineering

817 Sherbrooke St. West

Montreal, QC, H3A 0C3 Canada

T: +1 (514) 398 - 6299

F: +1 (514) 398 – 7365

E-Mail: Mark.Driscoll@mcgill.ca

3.2.1. ABSTRACT

Thoracolumbar fascia involvement is often neglected when studying the biomechanics of the spine. The purpose of this study was to develop, validate, and explore the use of a novel finite element model of the spine, inclusive of the Thoracolumbar Fascia, paraspinal muscular compartment (PMC) and the Intra-Abdominal Pressure (IAP) based on published clinical studies. Reaction forces were acquired at five critical anatomical locations. Results showed that elevated IAP decreased the posterior force and balanced the anterior forces when PMC pressure was asymmetric. This novel finite element study demonstrated a link between the TLF compartments supporting its involvement in spinal stability.

Keywords: Finite Element Method, Thoracolumbar Fascia, Intra-abdominal Pressure, Paraspinal Compartmental Pressure, Spine Stability

3.2.2. INTRODUCTION

It has become evident through research that the inherently unstable standalone spine gains its stability by the harmony of neurologic, active and passive stabilizing mechanisms [1]. This harmonization efficiently sustains the body's kinematic ranges of motion and kinetic capabilities allowing the body to perform normal daily tasks. Active muscular stimulations present the primary movement effects by creating internal tensile forces which, in turn, increases their pressures in the compartment in which they are embedded. In accordance with muscle contraction, stabilizing muscular strength requires the assistance of a set of load-reducing mechanisms when substantial external loads are to be lifted [2].

While the thoracolumbosacral spine arguably provides the foundational structural support of our bodies, its stabilization has been believed to be complemented via of a spring-like structure of fascial substance surrounding the torso; the Thoracolumbar Fascia (TLF) [3, 4]. Composed of interweaved aponeurotic and fascial layers, the TLF divides the torso transversally into compartmental regions occupied by different skeletal muscles (Fig.1) and spans longitudinally between the thoracolumbosacral spine to connect with different active muscles. The unique structure of the TLF has for long enticed researchers to investigate its capability in withstanding and transferring forces between different regions of the body under static and dynamic loads who hypothesize its potential functions. Mathematical modelling of the TLF connectivity suggests its necessity in stabilizing the vertebral column when tensioned as a result of Paraspinal and Abdominal muscles [2, 5]. Barker et al. [6] conducted cadaveric studies and observed an effective transmission of low values of tensional force (up to 5N) when applying 10N between the Transverse Abdominis and the anterior (ALF) or posterior (PLF) layer of the TLF. *In-vitro* experimentation of the TLF by Vleeming et al. [7] studied the Paraspinal muscle activation and observed a clear transfer of force from the ALF to PLF realizing a point of equal tension within the Common Transversus Tendon (cTrA).

While a great deal of research has been conducted on quantifying isometric strengths and Intra-abdominal pressures (IAP) solely, the observed values can give us little information on the force distribution and actual responses. Mueller et al. [8] was the first, and to the authors' knowledge the only, to investigate the relationship between IAP and the Paraspinal Muscle Compartmental (PMC) Pressure. This study concluded no correlation between the IAP and PMC

pressure under different postures. It would therefore appear that the TLF's function remains to be fully elaborated in this regard.

This novel study, thus, seeks to objectively investigate the function of thoracolumbar fascia by way of a controlled experimental platform using the Finite Element Method. Specifically, the transverse force distribution in the TLF sustained in daily human tasks was evaluated in order to explore the hypothesis that IAP and PMC pressure interact through the TLF to potentially enhance stability.

3.2.3. METHOD

Model Preparation

A two-layered Thoracolumbar Fascia (TLF) model was chosen for this study and explored via a multi-purpose finite element analysis software ANSYS (V18.1, Canonsburg, USA). For the preparation of the two-dimensional finite element model (Fig. 1), a full-scale three-dimensional model that was previously assembled from a patient-specific graphical body was acquired from an open-source Database [9]. The anatomical parts obtained were based on a whole-body set of segmented MRI images (2 mm intervals) of a healthy adult human male who was 22 years old, weighed 65.0 kg and was 172.8 cm tall. The volunteer was chosen based on his physical dimension proximity to the recorded average stature and weight data of the Japanese male population of ages 18-30 years. An approach similar to the experiment conducted by Vleeming et al. [7], was adopted whereby a transverse section between L2 and L3 was chosen with a fictitious 2 mm thickness, but at an angle of 19° from the transverse plane in the extension direction to capture the entire L3 vertebra geometry. The body was cut at the intersecting plane and the curves were extracted. The first part of the TLF was traced around the erector spinae outline to form the Posterior Layer of the TLF (PLF) and Anterior layer of the TLF (ALF) that join at the Lateral Raphe (also known as Lateral Interfacial Triangle). It is noteworthy to mention that the ALF in the two-layered model is equivalent to the Middle Layer of the TLF (MLF) in a three-layered model [3]. A mean width of 0.5 mm for the entire model was chosen based on the study conducted by Barker and Briggs [10]. The interior abdominal wall was then traced and joined with the TLF to complete a closed cavity. At the interconnection between the Abdominal Muscles and the Erector Spinae, the lateral raphe was drawn manually based on the natural curvatures that the muscles would trace to at this location. The width of the abdominal wall was

chosen to be 0.5 mm, as well, to standardize the thicknesses and since actual deformational effects of the abdomen were not within the scope of this study. After creating the two-dimensional model, a quad mesh generation was performed using the ANSYS Multizone Method with an element size of 0.5 mm. The 2D surface mesh consisted of 6058 four-node quadrilateral elements that shared 22 nodes. The minimum Jacobian ratio (i.e. measure of deviation from ideal square element shape) recorded of the generated mesh was 0.46. Element types were generated and consisted of PLANE182 and SURF153.

Material properties for the TLF were extracted from the force-strain graph in an experiment conducted by Yahia et al. who studied the unidirectional viscoelastic mechanical response of the Lumbosacral fascia using cadaveric specimens of TLF generating various responses among which is the load-strain curve [144]. The graph was digitized, and the specimen cross-sectional area was used to generate the stress-strain curve. The resulting linear properties were used (E = 450 MPa, $\upsilon = 0.4999$). The material properties for the abdominal structure (composed of the Linea Alba, Rectus Sheath, Rectus Muscle, Internal Abdominal Oblique, External Abdominal Oblique and the Transverse muscle) were based on a study conducted by Pachera et al. [12] on the assessment of the Intra-Abdominal Pressure (IAP) in different daily tasks via numerical modelling. The study achieves constitutive parameters based on best fit of tensile tests of which the resulting value of the initial bulk modulus is adopted (K = 2000 MPa). This was used as an input along with the Poisson Ratio based on Arjmand et al.'s [13] study of the abdominal muscle's role in producing IAP using FEA ($\upsilon = 0.45$). The material properties of the vertebra were defined based on linear properties of the cortical vertebra bone previously reported [14, 15]. Table 1 lists the material properties adopted in the simulations.

Three main boundary conditions were required to define the status of the model. The first, secured the vertebrae and remained constrained throughout all simulations assuming that the vertebra is motionless and marked as the reference. The remaining boundary conditions were varied in accordance with the objective being evaluated and were defined as:

P_L and P_R: Paraspinal Muscle Compartmental (PMC) Pressure (mmHg); and

P_A: Intra-abdominal Pressure (mmHg).

For each simulation three main forces were calculated by taking local measurements on the contacting surfaces to describe:

T_{PLF}: PLF Reaction Force at the interface between the spinous process and the PLF (N);

T_{ALFL} & T_{ALFR} or T_{ALF}: ALF Reaction Force at the interface between the transverse process and the ALF (N); and

T_{CL} & T_{CR} or T_C: Reaction Force at the connection interface at the interface between the TLF and Abdominal Muscle (N).

Testing Sequence

To test the hypothesis that the IAP and PMC pressure interact through the TLF to potentially enhance stability, the reaction forces (T_{PLF}, T_{ALF} and T_C) were calculated and the correlation between IAP, PMC pressure and reaction forces were investigated and based on:

Test 1

The *in-vivo* experiment of the study conducted by Mueller et al. [8] for posture-oriented tasks (Set A) and weight-oriented tasks (Set B) (Table 2). The correlation between the input and outputs were, then, evaluated. Finally, the difference (D) between T_{ALFR}, T_{ALFL} and T_{PLF} was computed by using Eq. (1).

$$D = \frac{T_{PLF} - (T_{ALFR} + T_{ALFL})}{(T_{ALFR} + T_{ALFL})}$$

Equation 1: Relative Difference between T_{PLF} and T_{ALF}

Test 2

The experimental study conducted by Vleeming et al. [7] using three incremental PMC inflation pressures (79.1 mmHg, 99.8 mmHg, and 106.5 mmHg) and a cTrA tension of 8.5 N (equivalent to T_{CR} and T_{CL} in this study). To achieve the joint force, the IAP was established through trial-and-error until both, T_{CR} and T_{CL}, recorded 8.5 N for each of the three inflations. The relative T_{PLF} was then measured with respect to the neutral condition (i.e. zero abdominal pressure) as shown in Eq. (2).

$$T_{PLF}^{Relative\ Tension} = T_{PLF}^{Absolute\ Tension} - T_{PLF}^{Neutral\ Tension}$$

Equation 2: Deviation Difference of T_{PLF} from Neutral Position

The standing position defined as Task 1 (Table 2) was used as the baseline. This was later used to validate the model results with the experimental results achieved in Vleeming et al.'s [7] study.

Test 3

The stiffness defining the material properties of the TLF and Abdominal Muscles was varied for each to analyze the effect on the output force that may result from active muscle contraction as well as biomechanical and anatomic variations. As such, the range boundaries were chosen to encompass previously published values. Arjmand et al.'s [13] defined a bulk modulus for the incompressible fluid filling the abdominal cavity as 250 MPa. Hence, the sensitivity analysis studying the effect of material property variations initiated at 200 MPa and spanned to the bulk modulus adopted in this study (i.e. 2000 MPa). The TLF Young's Modulus was initially E = 100 MPa and incremented by 50 MPa to a maximum of 450 MPa as previously reported by Otsuka et al. [16] for the Fascia Lata.

Test 4

The effect of asymmetric PMC pressure by defining $P_L/P_R = 0.5$ then $P_L/P_R = 0.8$ with the variation being in P_L and compared with the symmetric PMC pressure ($P_L = P_R = 24.2$ mmHg) at a constant IAP.

Test 5

The effect of a higher abdominal pressure between the two studies. Cobb et al. [17], measured the IAP values for healthy individuals at various postures. They recorded a higher IAP value (20.4 mmHg) in the neutral standing position. The IAP in this study was, thus, increased from $P_A = 3.4$ mmHg to 20.4 mmHg by increments of 1 mmHg while maintaining a constant symmetric PMC pressure. The simulation was then repeated but for asymmetric PMC pressure values.

3.2.4. RESULTS

The resulting mesh and an exemplary result for the simulation outputs are depicted in Fig. 2a and Fig. 2b demonstrating the resultant mesh and deformation output result for Task 1. In this case, the Paraspinal Muscle Compartmental (PMC) Pressure was larger than the IAP which

results in a posterior lateral movement of the Lateral Raphe, a posterior movement of the PLF layer and an anterior stretch of the abdominal cavity. The reaction forces at the connection between the Thoracolumbar Fascia (TLF) and abdominal muscles were all in pure tension.

Test 1

In simulating the reaction forces, the pressure input values of P_A, P_L and P_R were specified according to Tasks 1-3 (Table 2) for three different postures without any weights in a Neutral Orientation. The values of the $T_{ALFL,}$ T_{ALFR} and T_{PLF} increase from an upright position to a squatting position then to a Kyphotic back position. The T_{PLF} increases to 19.46 N in Task 3. T_{CR} and T_{CL} remain relatively unchanged throughout these tasks and were equal for every task (0.6 N for Task 2 and -0.11 N for Task 3). While T_{ALFL} increases from 0.42 N to 5.89 N then 8.85 N as compared to T_{ALFR} which changes from 1.36 N to 6.84 N then 9.52 N. In every case, the T_{ALFR} was higher than the T_{ALFL} (Fig. 3).

The weight increment for each identical set of tasks (Set B) from 10 kg to 20 kg (Table 2), always increases the reaction forces for all cases (Fig. 4). In general, the T_{PLF} was always greater than all other force results in every case. The highest value of T_{PLF} value was recorded in the Kyphotic Back Posture holding the 20 kg weight away from the body (43.07 N). Similarly, the T_{ALF} peaked at the same posture as the T_{PLF} (18.71 N). T_{ALFR} and T_{ALFL} was lowest in Task 4 (0.96 N and 0.57 N respectively), but constantly increased from Task 4-9 and Task 10-15 recording lower values in Task 14 for both 10 kg (3.04 N) and 20 kg (3.96 N). However, T_{CL} and T_{CR} were always equal in value recording a peak in Task 15 (8.15 N).

The comparison of T_{ALFR} and T_{ALFL} depended on the corresponding values of the Right and Left PMC pressure (P_R and P_L), respectively, as depicted in Fig. 5. The simulated input suggested an existing relationship between T_{PLF} and both, P_R and P_L ($R^2 = 0.701$). Moreover, T_{ALFL} and T_{ALFR} were directly proportional with P_L and P_R, respectively ($R^2 = 0.996$). While, both T_{CR} and T_{CL}, were only strongly correlated with P_A ($R^2 = 0.983$). There was no apparent linear correlation between the weight increase and the overall simulated reaction force results.

The percentage difference (Fig. 6) observed the highest difference between total ALF and PLF forces in Task 10 (84%), Task 5 (80.7%), Task 4 (64%) and decreased to almost no difference in Task 7 (< 2%).

Test 2

To achieve a reaction force of 8.5 N at the connection between the TLF and Abdominal Wall, the IAP was set at ~33 mmHg for all cases. The relative T_{PLF} measured 2.17 N, 1.62 N and 1.49 N for PMC pressures of 79.1mmHg, 99.8 mmHg and 106.5 mmHg, respectively. The output results agreed with the unidirectional tension measured in their experiment serving as a direct validation of the model. While maintaining a constant joint force of 8.5 N, they recorded a maximum force within the PLF of 2 N at a PMC pressure of 79.1 mmHg which decreased to ~1 N at a PMC pressure of 99.8mmHg. Using the same input values, the model adopted in this study achieved a value of 2.17N at 79.1 mmHg which decreased to 1.49N at 99.8 mmHg.

Test 3

The variation of the Young's Modulus of elasticity for the TLF (Fig. 7a), and the bulk modulus of elasticity for the abdominal muscles (Fig. 7b) in a uniform manner, had no significant effect on all force reactions (0.05% change).

Test 4

The standing posture in Task 1 (Table 2) was defined as the baseline with a symmetric PMC pressure value (24.2 mmHg). The decrease of P_L at a constant IAP and P_R resulted with no change in the T_{ALFR}, T_{CR} and T_{CL}. A 20% decrease in the P_L resulted in a 26.8% decrease in the T_{ALFL} and a 10.8% decrease in the T_{PLF}. However, a 50% decrease in the P_L resulted in a 67.1% decrease in the T_{ALFL} and a 26.8% decrease in the T_{PLF} (Fig. 8).

Test 5

The effect of using mean IAP values from a different study for the standing posture baseline was mainly an assessment of the study variations. The study conducted by Cobb et al. [17], illustrates a higher IAP (20 mmHg) than the published values by Mueller et al. [8]. For the Symmetric PMC pressure case, the T_{ALFL} and T_{ALFR} were identical and recorded a decrease from 1.34N at an IAP of 3.4 mmHg to 0.38 N at 15.4 mmHg to increase to 0.68 at 20.4 mmHg. T_{CR} and T_{CL} maintained an increasing trend from 0.86 N (IAP = 3.4 mmHg) to 5.24 N (IAP = 20.4 mmHg). However, the T_{PLF} constantly decreased from 3.8 N (IAP = 3.4 mmHg) to 1.43 N (IAP = 20.4 mmHg). The T_{PLF} was equal to both T_{CR} and T_{CL} at an IAP of 11.4 mmHg. While the T_{CR} and T_{CL} were equal to T_{ALFR} and T_{ALFL} at an IAP of 4.9 mmHg (Fig. 9a).

The asymmetric case showed similar trends for all reaction forces except for the T_{ALFL} whereby its inflection point was calculated at an IAP of 6.4 mmHg. The T_{CR} and T_{CL} remained constantly decreasing with the same values as the symmetric case. The T_{PLF}, however, was 2.76 N at 3.4 mmHg and decreased to 0.12 N at an IAP of 20.4 mmHg. The equivalent point of T_{PLF} and both, T_{CR} and T_{CL}, decreased (compared to symmetric case) to an IAP of 8.4 mmHg. The T_{ALFR} and T_{ALFL} intersected at an IAP of 11.4 mmHg (Fig. 9b).

The mesh with an element size of 0.6 mm was deemed suitable after no further change in the output results occurred with decreasing the element size further. The forces and displacements converged after the 17th iteration. In terms of verification, the variation in the mesh size showed little to no change in the output results when element size was increased to 1mm or decreased to 0.1 mm.

3.2.5. DISCUSSION

The two-layered model of the Thoracolumbar Fascia (TLF) was used in this study in the aim of investigating the relation between Intra-abdominal Pressure (IAP), Paraspinal Muscle Compartmental (PMC) pressure and tensile transmission within the TLF while gaining further insight into the TLF's involvement in spinal stability. This was conceived by employing an MRI reconstructed 3D model that was based on the average Japanese male population stature and weight data to achieve average representative results [18]. Furthermore, the term stability in this paper is used in the sense of the ability of the spine to perform its biomechanical functions in load transmission addressed within a planar scope.

The abdominal cavity is a compact assembly of muscular layers capable of sustaining internal pressure elevations upon contraction which limits subsequent expansion [13]. The abdominal wall forms a heterogeneous composite tissue of muscular and fibrous layers that completes the cavity envelopment. Biaxial tests on the Linea Alba alone have been reported to record a transverse Elastic Modulus of 335 MPa [19]. This value suggests that the Bulk Modulus adopted in this study was within a reasonable range of the muscular wall capabilities in the transverse direction.

The TLF separates the Abdominal Cavity from the PMC and creates a structure that has been suggested to play a significant role in transferring loads within the spine [20, 21]. Mainly, lateral tension to the TLF was explained to produce a vertical force (caudocranial force) that

results with an extensor moment [22]. This lateral tension is achieved by the active contraction of various muscles attached at different levels on the TLF designated by the pressure induced within the compartments in this study. Barker et al. [6] applied a 10 N traction on the various muscles connected to the TLF and observed the highest tensile force in the PLF due to the Latissimus Dorsi (18.8 N) and Transversus Abdominis (8.1 N) and the highest tensile transmitted on the ALF (or MLF in three-layered model) by the Transversus Abdominis (10.5 N). Tesh et al. [23] conducted experimental studies on the TLF and deduced that it is capable of transmitting up to 335 N in caudocranial force by applying a 98 N tension to the cTrA, in contrast to the theoretical value of 1015 N as calculated by Gracovetsky et al. [5, 24]. The maximum calculated force in this study was achieved in PLF (43.07 N) at a Kyphotic Back Posture holding a 20 kg weight away from the body and according to the previously mentioned values is tolerable by the TLF. The 2D study conducted in this paper simulates one planar level of the TLF transverse forces that produce the out-of-plane caudocranial force when summed. Moreover, both, the TLF thickness adopted for this study (0.5 mm) as well as the thickness of the samples tested in Yahia et al.'s [11] study (1 mm) fall within the experimentally measured thickness values of previous anatomical studies [10, 21].

The results of Test 1 in Fig. 3 and Fig. 4 showed no apparent correlation between the IAP and PMC pressure. Fig. 5 depicts the influence of the IAP on all the forces which suggests that it may play a role in stability given that it negatively correlates with the T_{PLF}, T_{ALFL} and T_{ALFR}. Moreover, the results show a considerable increase in the T_{PLF} and T_{ALF} but a decrease in the T_C when comparing results of the simulations described herein having pressures associated with the different simulated positions (squatting to the Kyphotic back posture). This large difference can be observed specifically when carrying 20 kg weights. Furthermore, Fig.5 shows a clear correlation between P_A and both, T_{CR} and T_{CL} whereby the variation of T_C depends on the input P_A. This may suggest that the increase in IAP resulting an increase with the T_{CR} and T_{CL}, decreased the PLF and ALF reaction forces. Additionally, this alludes towards the hypothesis that lifting in the squatting position could reduce the risk of injury in comparison with stooping when performing a lift [25, 26].

In their experiment, Vleeming et al. applied an 8.5 N load on the equivalent of the T_{CR} and T_{CL} of this study to simulate the aggregate effect of the engagement of abdominal pressure and PMC pressure [7]. The close agreement of such output reaction forces, with those measured

in the present study, works towards indirectly validating the model described herein. Moreover, with the exclusion of Tasks 5 and 11, Fig. 6 shows a clear increase in the difference, when comparing incremental weight tasks, which is in concert with Vleeming et al.'s observations that the force is transferred exclusively to the PLF.

A variation of the Modulus of Elasticity of the TLF and the Bulk Modulus of the Abdominal Cavity, as demonstrated in Test 3, produced no significant changes in any of the reaction forces (Fig. 7a and Fig. 7b). This is likely explained by the fact that linear elastic properties are assumed for the model components.

In Test 4, the standing posture baseline with a symmetric PMC pressure was subjected to an increased pressure up to the value of IAP (20.4 mmHg) measured by Cobb et al. (Fig.9a) [17]. The inflection point as a result of increasing IAP may suggest that the T_{ALF} sustains loading when IAP is elevated while T_{PLF} decreases continuously. As a result, one may observe that the elevated IAP mechanism decreases the loading on the T_{PLF} incorporated with an increased loading sustained in the T_{ALF}. The asymmetric PMC pressure showed no linear correlation but shows that, in this case, the T_{PLF} is reduced (Fig.8 and Fig.9b). However, the IAP variation in Test 5 shifted the asymmetric pressure difference in the PMC from the right to the left with a point of equal tensioning. In both cases, the T_C and T_{PLF} have a point of equal tension. This suggests that the role of elevated IAP reduces the loading on the PLF in elevated pressures engaging the ALF and compensates the asymmetric PMC pressure. IAP has been previously suggested to be influenced by postural asymmetry [27].

Limitations of the study include omission of the true viscoelastic property of the TLF. Also, there is a distinction in the anatomy of the TLF and muscle connectivity which was not considered. This would be better reflected in a 3-D study that would account for the overall geometry of the abdominal wall, abdominal cavity and spine. Furthermore, this will address the approximations that have been introduced within this study including the abdominal wall thickness, change in TLF thickness and cavity volume along different vertebral levels and accounting for sagittal and coronal forces. Finally, it is necessary to realize that elevated IAPs are usually recorded as momentarily and thus, should be accounted for. Further studying which takes these into consideration is necessary. Despite such potential limitations, this objective study limits interpretation to baseline and relative comparisons. Further, several sensitivity

analyses were conducted and only robust differences, in light of such computational perturbations, were reported.

The preliminary results conceived in the present study suggests that the IAP plays a complementary role in the achievement of stability in accordance with muscle activation when the system deviates from the normal standing posture or when externally loaded. While this may seem secondary, such a role, in properly adjusting the structure, may contribute to the high efficiency and optimization capabilities of the spine. Furthermore, this study highlights the importance of considering both TLF and IAP in future FE models that aim to approximate spinal forces.

3.2.6. REFERENCES

[1] M. M. Panjabi, "The stabilizing system of the spine. Part II. Neutral zone and instability hypothesis," *Journal of spinal disorders,* vol. 5, pp. 390-390, 1992.
[2] J. E. Macintosh, N. Bogduk, and S. Gracovetsky, "The biomechanics of the thoracolumbar fascia," *Clinical biomechanics,* vol. 2, no. 2, pp. 78-83, 1987.
[3] F. Willard, A. Vleeming, M. Schuenke, L. Danneels, and R. Schleip, "The thoracolumbar fascia: anatomy, function and clinical considerations," *Journal of anatomy,* vol. 221, no. 6, pp. 507-536, 2012.
[4] M. Driscoll, "Fascia–The unsung hero of spine biomechanics," *Journal of bodywork and movement therapies,* vol. 22, no. 1, pp. 90-91, 2018.
[5] S. Gracovetsky, H. Farfan, and C. Lamy, "The mechanism of the lumbar spine," *Spine,* vol. 6, no. 3, pp. 249-262, 1981.
[6] P. J. Barker, C. A. Briggs, and G. Bogeski, "Tensile transmission across the lumbar fasciae in unembalmed cadavers: effects of tension to various muscular attachments," *Spine,* vol. 29, no. 2, pp. 129-138, 2004.
[7] A. Vleeming, M. Schuenke, L. Danneels, and F. Willard, "The functional coupling of the deep abdominal and paraspinal muscles: the effects of simulated paraspinal muscle contraction on force transfer to the middle and posterior layer of the thoracolumbar fascia," *Journal of anatomy,* vol. 225, no. 4, pp. 447-462, 2014.
[8] G. Mueller, M. M. Morlock, M. Vollmer, M. Honl, E. Hille, and E. Schneider, "Intramuscular pressure in the erector spinae and intra-abdominal pressure related to posture and load," *Spine,* vol. 23, no. 23, pp. 2580-2590, 1998.
[9] N. Mitsuhashi, K. Fujieda, T. Tamura, S. Kawamoto, T. Takagi, and K. Okubo, "BodyParts3D: 3D structure database for anatomical concepts," *Nucleic acids research,* vol. 37, no. suppl_1, pp. D782-D785, 2009.
[10] P. J. Barker and C. A. Briggs, "Attachments of the posterior layer of lumbar fascia," *Spine,* vol. 24, no. 17, p. 1757, 1999.
[11] L. Yahia, P. Pigeon, and E. DesRosiers, "Viscoelastic properties of the human lumbodorsal fascia," *Journal of biomedical engineering,* vol. 15, no. 5, pp. 425-429, 1993.
[12] P. Pachera, P. Pavan, S. Todros, C. Cavinato, C. Fontanella, and A. Natali, "A numerical investigation of the healthy abdominal wall structures," *Journal of biomechanics,* vol. 49, no. 9, pp. 1818-1823, 2016.
[13] N. Arjmand, A. Shirazi-Adl, and M. Parnianpour, "A finite element model study on the role of trunk muscles in generating intra-abdominal pressure," *Biomedical Engineering: Applications, Basis and Communications,* vol. 13, no. 04, pp. 181-189, 2001.
[14] L. M. Ruberté, R. N. Natarajan, and G. B. Andersson, "Influence of single-level lumbar degenerative disc disease on the behavior of the adjacent segments—a finite element model study," *Journal of biomechanics,* vol. 42, no. 3, pp. 341-348, 2009.
[15] J. R. Williams, R. N. Natarajan, and G. B. Andersson, "Inclusion of regional poroelastic material properties better predicts biomechanical behavior of lumbar discs subjected to dynamic loading," *Journal of biomechanics,* vol. 40, no. 9, pp. 1981-1987, 2007.

[16] S. Otsuka *et al.*, "Site specificity of mechanical and structural properties of human fascia lata and their gender differences: A cadaveric study," *Journal of biomechanics,* vol. 77, pp. 69-75, 2018.
[17] W. S. Cobb, J. M. Burns, K. W. Kercher, B. D. Matthews, H. J. Norton, and B. T. Heniford, "Normal intraabdominal pressure in healthy adults," *Journal of Surgical Research,* vol. 129, no. 2, pp. 231-235, 2005.
[18] T. Nagaoka *et al.*, "Development of realistic high-resolution whole-body voxel models of Japanese adult males and females of average height and weight, and application of models to radio-frequency electromagnetic-field dosimetry," *Physics in Medicine & Biology,* vol. 49, no. 1, p. 1, 2003.
[19] C. R. Deeken and S. P. Lake, "Mechanical properties of the abdominal wall and biomaterials utilized for hernia repair," *Journal of the mechanical behavior of biomedical materials,* vol. 74, pp. 411-427, 2017.
[20] S. R. Garfin, C. M. Tipton, S. J. Mubarak, S. Woo, A. R. Hargens, and W. H. Akeson, "Role of fascia in maintenance of muscle tension and pressure," *Journal of Applied Physiology,* vol. 51, no. 2, pp. 317-320, 1981.
[21] A. Vleeming, A. Pool-Goudzwaard, R. Stoeckart, J.-P. van Wingerden, and C. Snijders, "The posterior layer of the thoracolumbar fascia," *Spine,* vol. 20, no. 7, pp. 753-758, 1995.
[22] N. Bogduk and J. Maclntosh, "The morphology of the lumbar erector spinae," in *Meeting of the International Society for the study of the Lumbar Spine, Rome, Italy*, 1987.
[23] K. Tesh, J. S. Dunn, and J. Evans, "The abdominal muscles and vertebral stability," *Spine,* vol. 12, no. 5, pp. 501-508, 1987.
[24] S. Gracovetsky, H. Farfan, and C. Helleur, "The abdominal mechanism," *Spine,* vol. 10, no. 4, pp. 317-324, 1985.
[25] B. Bazrgari, A. Shirazi-Adl, and N. Arjmand, "Analysis of squat and stoop dynamic liftings: muscle forces and internal spinal loads," *European Spine Journal,* vol. 16, no. 5, pp. 687-699, 2007.
[26] S. M. McGill, "The biomechanics of low back injury: implications on current practice in industry and the clinic," *Journal of biomechanics,* vol. 30, no. 5, pp. 465-475, 1997.
[27] J. Troup, T. Leskinen, H. Stalhammar, and I. Kuorinka, "A comparison of intraabdominal pressure increases, hip torque, and lumbar vertebral compression in different lifting techniques," *Human Factors,* vol. 25, no. 5, pp. 517-525, 1983.

3.2.7 FIGURES AND TABLES

Table 3.1: Material Properties of different anatomical structures for FE simulations

Tissue	Material Properties			Sensitivity Analysis Range
	Modulus of Elasticity (MPa)	Bulk Modulus (MPa)	Poisson Ratio	
Thoracolumbar Fascia	450	-	0.49	100 - 450
L3 Vertebra	12000	-	0.3	-
Abdominal Wall	-	2000	0.45	200 - 2000

Table 3.2: Measurements of compartmental pressures in posture-oriented tasks (Set A) and weight-oriented tasks (Set B) by Mueller et. al, 1998 with a depiction of the different tasks

Set	Task Number	Posture	Orientation	Weight	IAP (mmHg)	ICP Left (mmHg)	ICP Right (mmHg)
A	1	Upright	-	-	3.4	11.8	24.2
	2	Squatting	-	-	6.2	88	100.3
	3	Kyphotic Back	-	-	3.1	122.3	131
B	4	Upright Standing	Weight Above Head	10	3.9	14.4	19.6
	5	Upright Standing	Weight on Thigh	10	9.1	25	32
	6	Squatting	Floor	10	11.8	81.3	110
	7	Kyphotic Back	Floor	10	1.4	167.5	194.9
	8	Upright Standing	Away from body	10	10.7	47.8	56.4
	9	Kyphotic Back	Floor, away from body	10	17.1	215.8	232.1
	10	Upright Standing	Weight Above Head	20	8.7	23.3	30
	11	Upright Standing	Weight on Thigh	20	10.1	30.9	47.4
	12	Squatting	Floor	20	21.7	101.9	133.4
	13	Kyphotic Back	Floor	20	10.3	206	212.2
	14	Upright Standing	Away from body	20	23.6	84.8	85.7
	15	Kyphotic Back	Floor, away from body	20	32.7	290.3	285.8

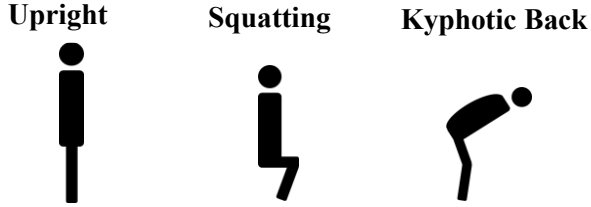

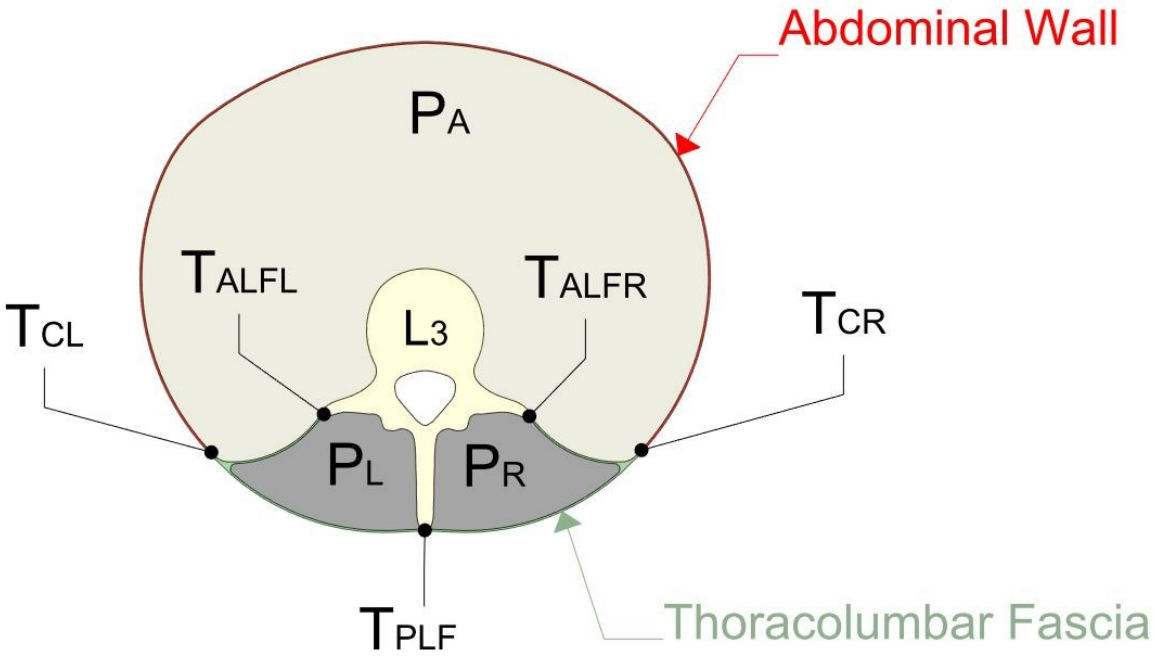

Figure 3-1: Finite element model of the two-layered Thoracolumbar Fascia. The Fascia encloses three regions specified in the model by their respective pressure effects; P_R: Right Paraspinal Muscle Compartmental Pressure, P_L: Left Paraspinal Compartmental Pressure and P_A: Intra-Abdominal Pressure. The corresponding reaction forces measured in this study are shown; T_{ALFL}: Left Anterior Layer of the Thoracolumbar Fascia Reaction Force, T_{ALFR}: Right Anterior Layer of the Thoracolumbar Fascia Reaction Force, T_{PLF}: Posterior Layer of the Thoracolumbar Fascia Reaction Force, T_{CR}: Right Joint Reaction Force and T_{CL}: Left Joint Reaction Force

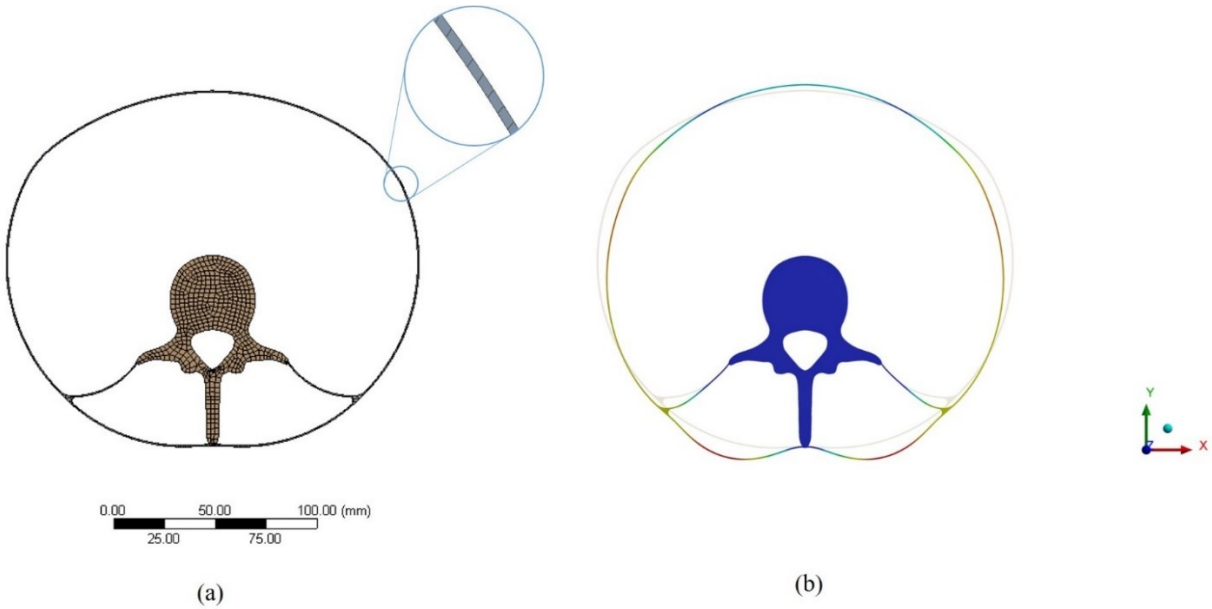

Figure 3-2: (a) Mesh of 2D Model and (b) Resulting Reaction Forces

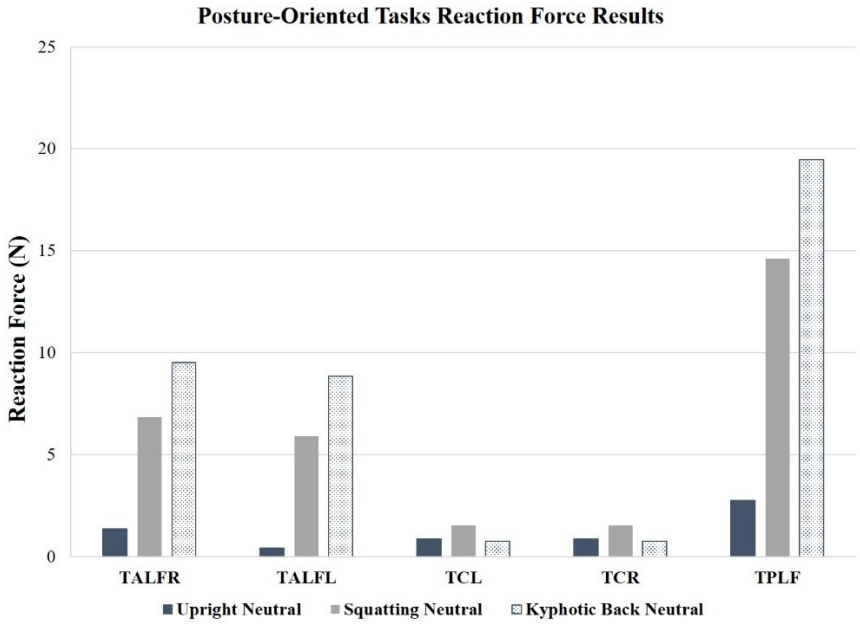

Figure 3-3: Reaction Force Results based on Posture-Oriented Tasks of Table 2, Set A.

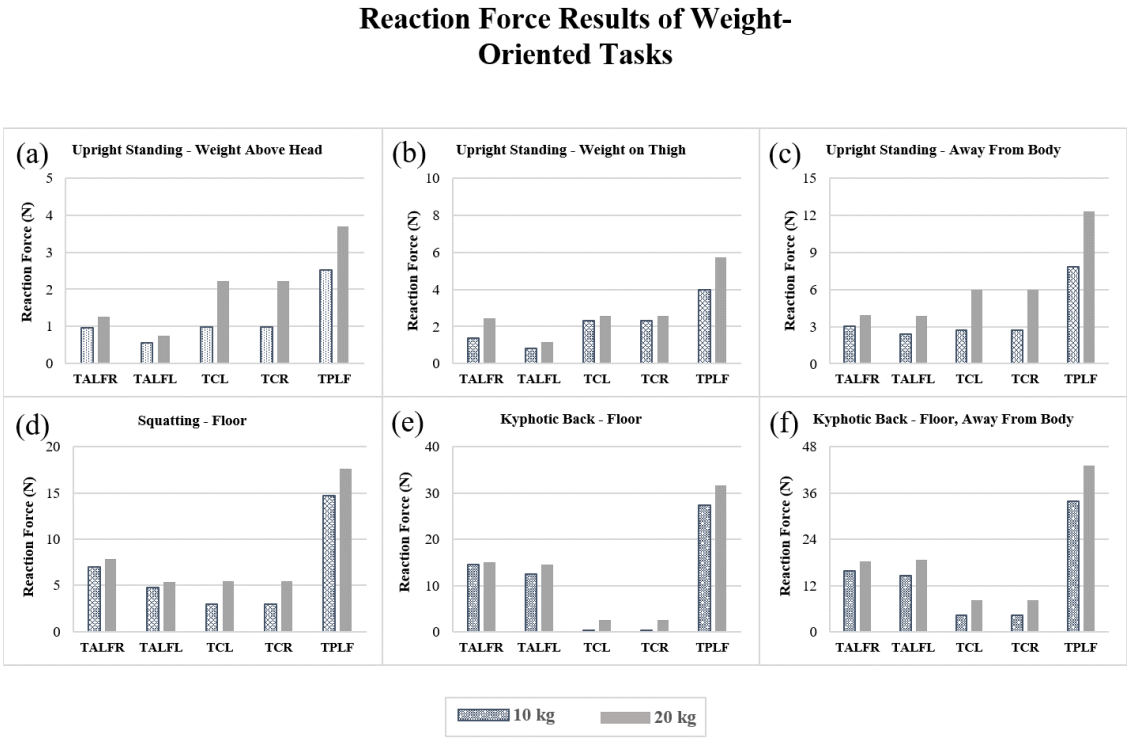

Figure 3-4: Reaction Force Results based on Weight-Oriented Tasks of Table 2, Set B. The figure depicts the force resultant in an (a) upright standing posture with weight above head, (b) upright standing posture with weight on thigh, (c) upright standing posture with weight away from body, (d) squatting position with weight near the body, (e) Kyphotic back position with weight near the body and (f) Kyphotic back position with weight 25 cm away the body for each of a 10kg and 20kg weight

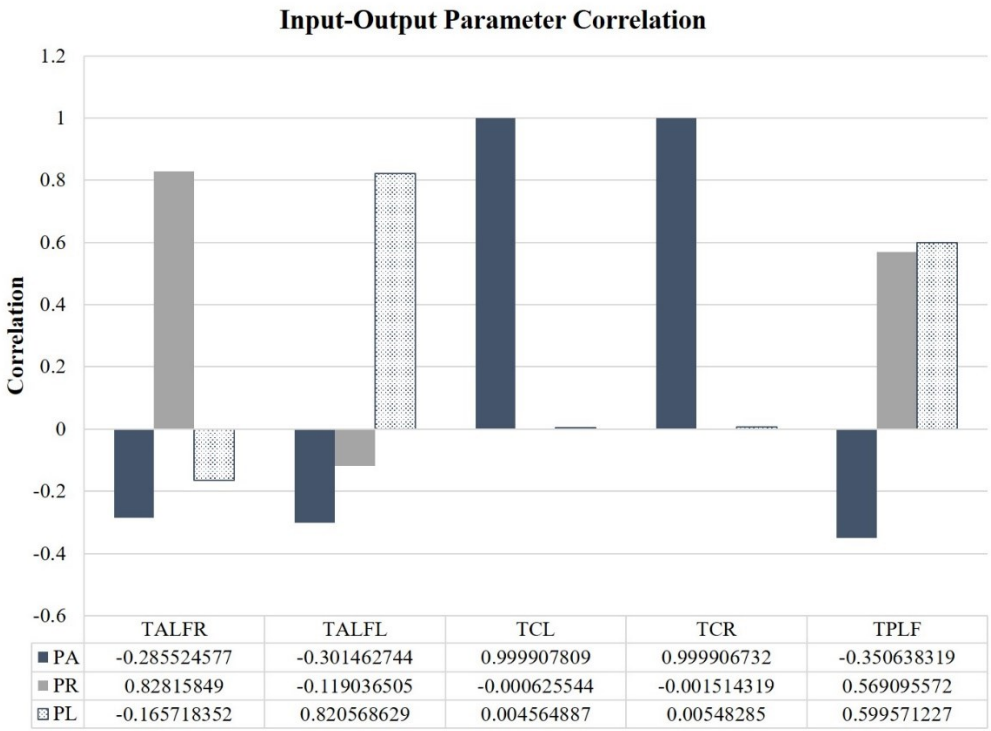

	TALFR	TALFL	TCL	TCR	TPLF
PA	-0.285524577	-0.301462744	0.999907809	0.999906732	-0.350638319
PR	0.82815849	-0.119036505	-0.000625544	-0.001514319	0.569095572
PL	-0.165718352	0.820568629	0.004564887	0.00548285	0.599571227

Figure 3-5: Correlation between pressure input parameters (P_A, P_R, P_L) and reaction forces (T_{ALFL}, T_{ALFR}, T_{CL}, T_{CR}, T_{PLF})

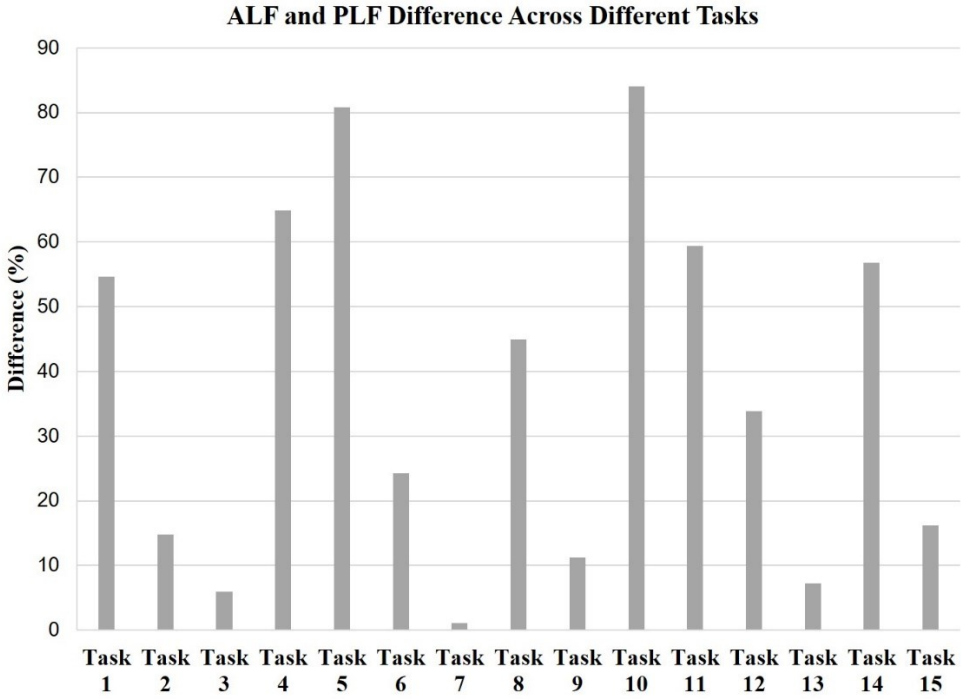

Figure 3-6: Percentage difference between T_{PLF} and Total T_{ALF} (i.e. T_{ALFL} + T_{ALFR})

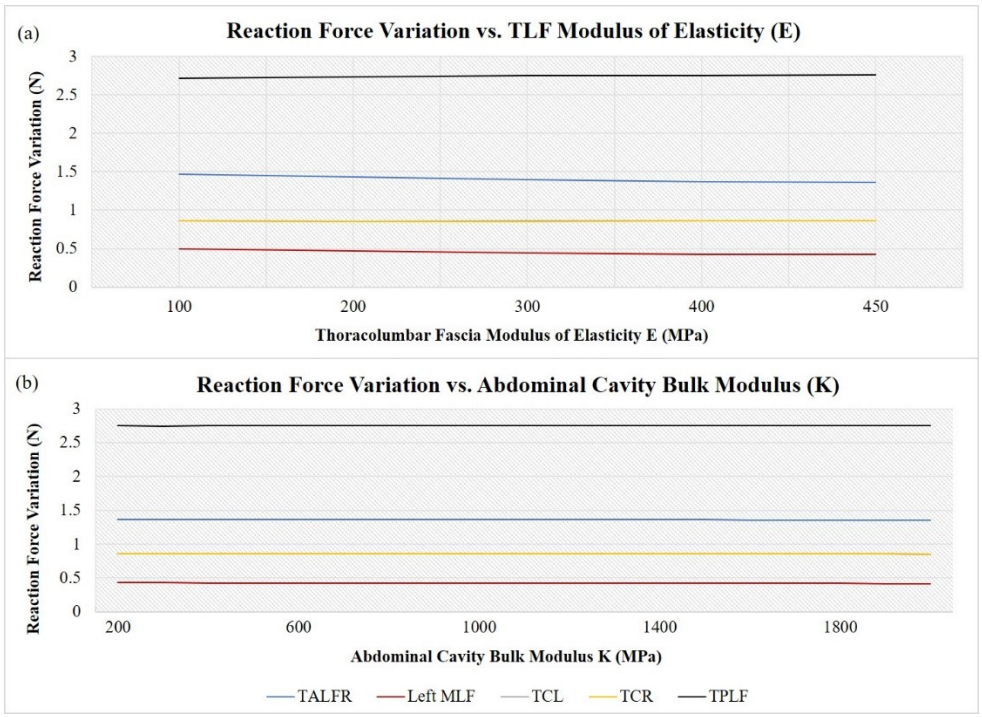

Figure 3-7: (a) Effect of varying abdominal cavity Bulk Modulus and (b) thoracolumbar fascia Modulus of Elasticity (E) on reaction forces (T_{ALFL}, T_{ALFR}, T_{CL}, T_{CR}, T_{PLF})

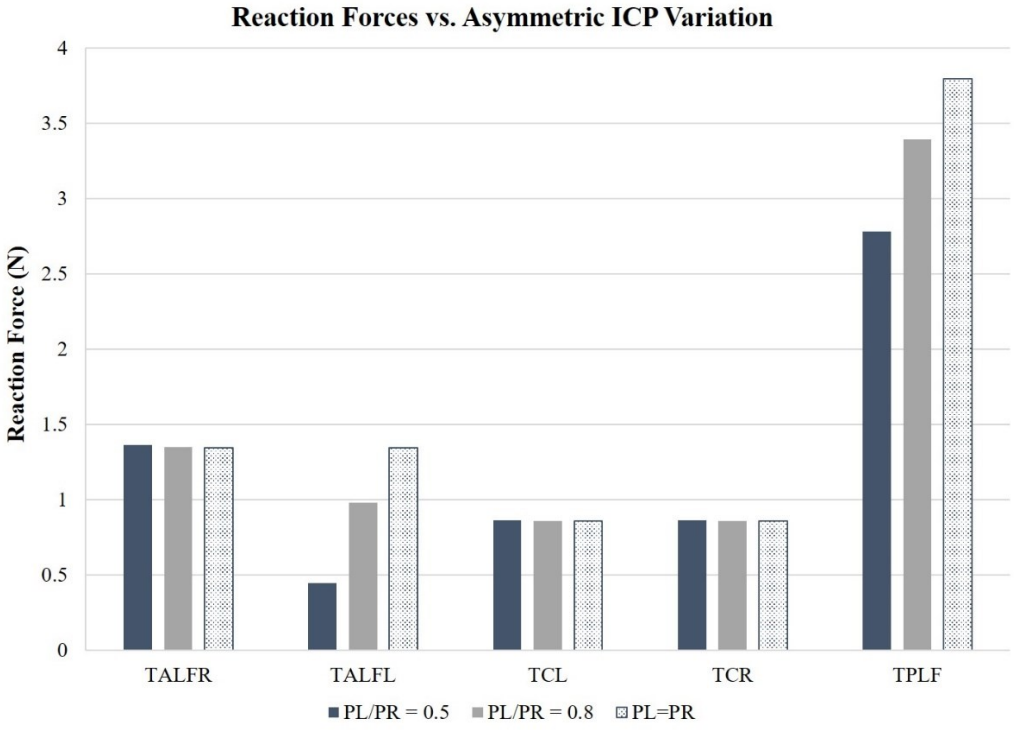

Figure 3-8: Effect of symmetric ($P_L = P_R$) and asymmetric PMC pressure ($P_L/P_R = 0.8$, $P_L/P_R = 0.5$) on reaction forces (T_{ALFL}, T_{ALFR}, T_{CL}, T_{CR}, T_{PLF})

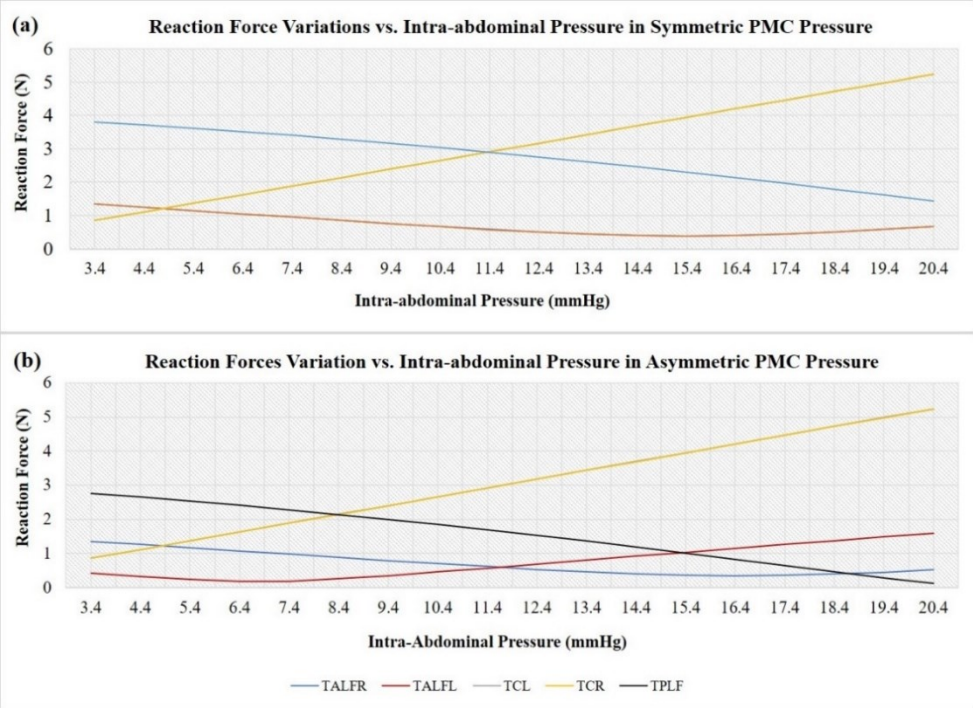

Figure 3-9: Effect of increasing Intra-Abdominal Pressure on reaction forces (T_{ALFL}, T_{ALFR}, T_{CL}, T_{CR}, T_{PLF}) in (a) symmetric paraspinal muscle compartmental pressure and (b) asymmetric paraspinal muscle compartmental pressure case

3.3. ADDITIONAL STUDIES RELATED TO ARTICLE 1

3D STUDY OF THORACOLUMBAR FASCIA

In accordance with the anatomical connectivity of the thoracolumbar fascia to the various spinal protrusions as well as past suggestions, such as Gracovetsky et al. [141] and Fairbank et al. [148] who suggested that forces may be transmitted between the transverse and axial directions to form of an extensor moment, the prior model was further expanded to a 3D model. This aimed to explore the out–of–plane effects of the Thoracolumbar Fascia in collaboration with the abdominal pressure. This study highlighted the utilization of offline simulations for the benefit of real-time VR simulations. In specific, prior to the development of the real-time simulation, an offline FE study may be employed to extract boundary conditions that may be defined for simplified soft tissue geometries. Ideally, the inclusion of a full-scale VR model would result with a high computational overhead which degrades the immersive quality of the real-time simulation. In other words, the larger the VR meshes, the more lags may be present. Hence, upon identifying the portions of the meshes to be included in the scene, one technique to identify the preloading and initial boundary conditions would be via offline simulations. This study confirmed Hypothesis 1 and established the boundary conditions that may be utilized within the workflow of the VR module development. In specific, the resulting forces along the boundary of the fascia, the follower load, the intra-abdominal pressure and the paraspinal muscular pressure would act as the initial state of the model. Hence, the study concludes with the input pertaining to the prone position. This position was selected to emulate the position of the patient during the surgery in a relaxed sedated state. Assumingly, at this stage, the patient most likely suffers from a degenerated disc, hence, degenerative mechanical variations were accounted for. Thus, the main objective of this study was to investigate the axial force and posterior forces across the TLF in the prone position for a DDD–adjusted case to set the boundary conditions required for a well-defined VR model.

The 2D FE model developed in Chapter 3.2 was extracted from the 3D MRI-based segmented model achieved in Objective 1 for the VR simulator. The same source for the set of components that were used for latter studies have been adopted in the current study as well. However, the variation is notable with the components of the model employed. The planar section of the 2D model employed in Chapter 3.2 included only the L_3 vertebra, TLF and

abdominal wall. However, the 3D model in this study was scoped to the entire lower lumbar section (L_3–S_1) which included the intervertebral discs embedded between the vertebrae. Since the VR module developed was scoped to the L_4/L_5 level, its corresponding IVD was further divided into Annulus Fibrosis and Nucleus Pulposus. Nevertheless, this 3D model included both the posterior and anterior layers of the assumed two–layered TLF model connected to the abdominal wall layer via the common tendon of the Transversus Abdominis (cTrA). Figure 3–10 depicts the 3D model employed in this study. To achieve the above objectives, this study progressed in the following manner:

1. Conduct FE simulation utilizing the 3D model using upright input defined in Article 1 without any follower load and compare the forces specifically at the L_3 level with the 2D analysis of Article 1.
2. Conduct FE simulation utilizing the 3D model using upright, squatting with 20 kg weight and kyphotic back with 20 kg weight input defined in Article 1 with a follower load of 800 N, 2350 N and 3185 N and validate IDP values from literature
3. Conduct FE simulation utilizing the 3D model using prone position input specific to *normal* cases with a follower load of 144 N and validate IDP value from literature
4. Conduct FE simulation utilizing the 3D model using prone position input specific to *LBP* cases with a Grade 3 degenerated disc with a follower load of 144 N and degenerated disc disease adjusted material properties

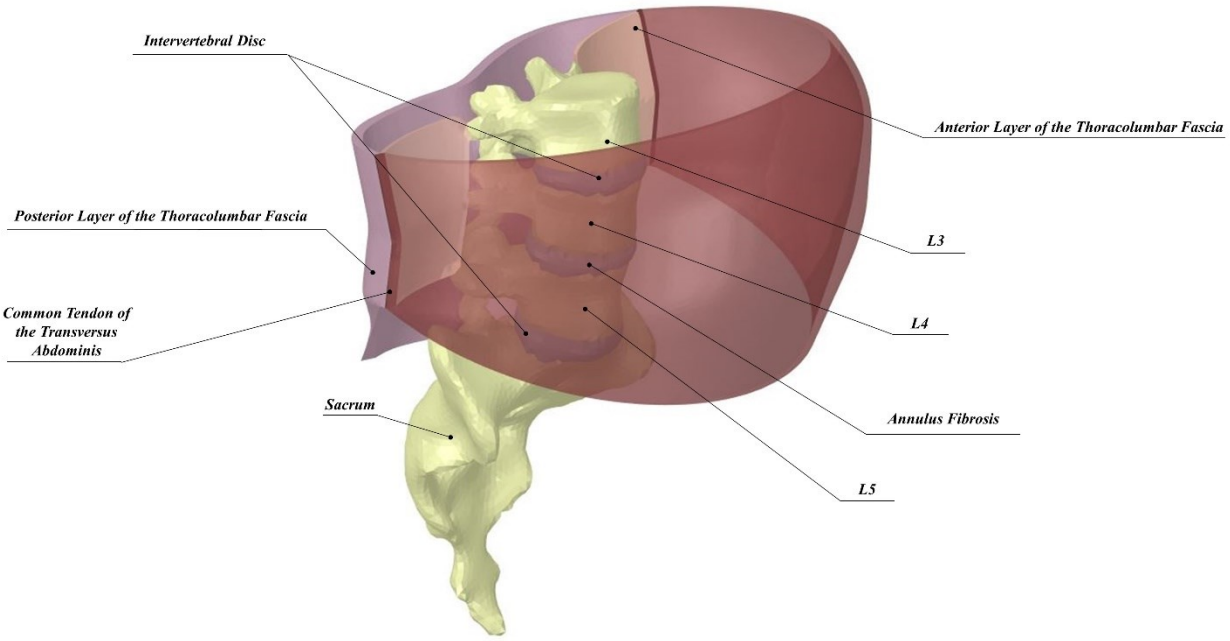

Figure 3-10: Depiction of the 3-D FE model employed for analysis of the lower lumbar region

After acquiring the full-scale three-dimensional model that was previously assembled from a patient-specific graphical body acquired from the selected open-source database [446]. An approach identical to that of Article 1 was utilized to conceive the geometry of the abdominal wall and the TLF shown in Figure 3–10. In specific, 2 mm transverse planes were placed along the spine's axial curvature for segmentation and a 0.5 mm thickness was used to trace the planar linings of the abdomen and the TLF along their respective compartments. The planar linings were then blended together to achieve a 3D body. Furthermore, the same methodology developed to accomplish Objective 1 (in Chapter 6) was employed to prepare the FE model for the mesh. In brief, the scoped components (shown in Figure 3–10) were all assembled in ANSYS Spaceclaim Design Modeler© (V18.1, Canonsburg, USA) and the "Shrinkwrap" feature was utilized to generate a uniform mesh with edge size of 0.5 mm. The open-source 3D graphics creation suite, Blender, was employed to merge the vertices together as described in Chapter 6. The created surface mesh conceiving tessellation models were then re-imported into Spaceclaim with conforming vertices and edges. Subsequently, each of the surface meshes were converted to solid bodies without merging edges to complete the meshing workflow. The bodies were then imported into ANSYS Mechanical (V18.1, Canonsburg, USA) for a static structural analysis.

Figure 3–11 depicts the resulting L_4/L_5 IVD structure, the generated mesh and the resulting conformity between the different components.

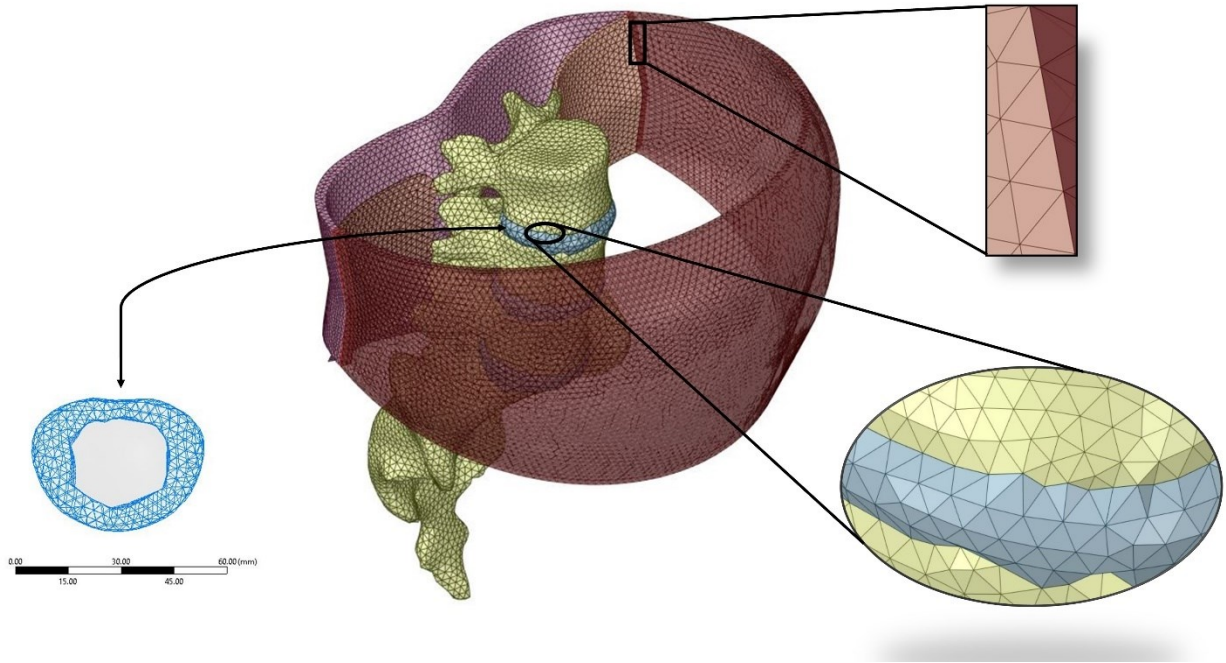

Figure 3-11: Depiction of intervertebral disc showing Annulus Fibrosis and Nucleus Pulposus distinction (left), the 3D generated mesh in Spaceclaim as a tessellation model (middle) and a zoomed view showing the conformity of the mesh between the corresponding bodies (right)

Material properties of the TLF (E = 450 MPa, υ = 0.4999), vertebra (E = 12000 MPa, υ = 0.3) and the abdominal wall (K = 2000 MPa, υ = 0.45) were used similar to that adopted in Chapter 3.2, Article 1. In addition, the cTrA was defined as linearly isotropic such that E = 1200 MPa and υ = 0.49 [125]. The intervertebral disc was defined as a linearly isotropic structure with an effective modulus of E = 5.7 MPa and υ = 0.37 for L_3/L_4 and L_5/S_1 [218]. However, the Annulus Fibrosis was defined as E = 4.2 MPa and υ = 0.45 and the Nucleus Pulposus was defined as E = 1 MPa and υ = 0.49 for the L_4/L_5 [447]. To account for degenerative disc progression in Task 4, the Nucleus Pulposus was then changed to adopt mechanical properties as E = 1.35 MPa and υ = 0.32 while the Annulus was maintained without change [218]. To account for the hydrostatic nature of the nucleus pulposus, HSFLD242 denoting 3D hydrostatic fluid elements were adopted such that a pressure extended from the centroid of the object would be defined. This was conceived via an APDL command snippet added to the diagram tree which

further allowed the extraction of the intradiscal pressures (IDP). The boundary conditions designated in this study are shown in Figure 3–12. Basically, four fixed supports were defined at the inferior and superior side of the PLF layer, inferior side of the abdominal wall and the sacrum. The follower loads were applied as 0 N for Task 1, 800 N (Upright posture) [448], 2350 N (Squatting posture carrying a 20 kg weight) [449] and 3185 N (Kyphotic Back Posture carrying a 20 kg weight) [449] for Task 2 and 144 N (prone posture) [448] for Tasks 3 and 4. The follower load was defined via 3 preloaded springs set at the centroids of the successive vertebra for all cases, as shown in Figure 3–12 [450]. While the superior layer of the PLF deforms due to the axial tensile force, the faces were fixed for probing the reaction force of the simulation. The intra-abdominal pressure and corresponding paraspinal muscle compartmental pressure inputs were designated as defined in:

a. Table 3.2, Set A, Upright Posture and Set B, Squatting Posture while carrying a 20 kg weight and Kyphotic Back while carrying a 20 kg weight of Chapter 3.2 for the first objective;
b. Table 3.3 to study the force output for normal and LBP cases in a prone position.

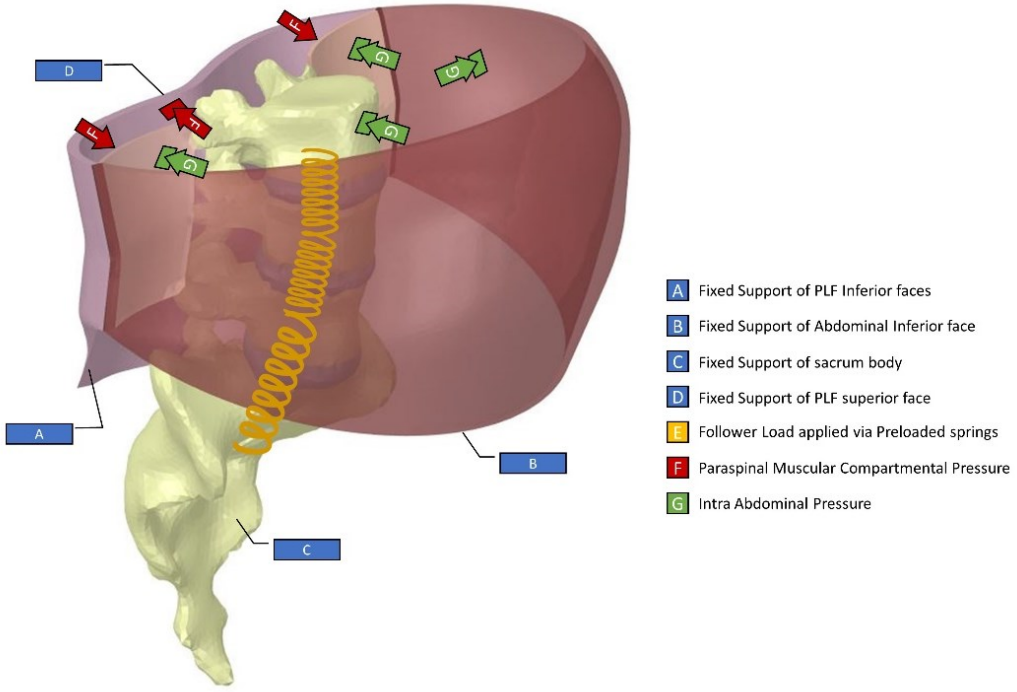

Figure 3-12*: Designated Boundary Conditions for 3D Model*

Table 3.3: Intra-Abdominal Pressure (IAP) and Inter-compartmental Pressure (ICP) input values for Normal and Low Back Pain (LBP) subjects

Case Number	Posture	Status	IAP (mmHg)	ICP (mmHg)	Reference
1	Prone	Normal	6.62	10	[451, 452]
2	Prone	LBP	9.27	17.1	[212, 451]

It is worth noting that the same compartmental pressure inputs within the 2D analysis were used for the 3D analysis. In specific, P_A denoted the Intra-abdominal pressure which represented the pressure build-up within the abdominal cavity resulting from the abdominal muscular contraction. Moreover, PL and PR denoted the muscular compartmental pressure of the Left and Right paraspinal sets that represent the pressure felt on a micro-transducer inserted within the muscular set which is induced as a result of the muscular activation.

A total of 32 named selections were defined within the model to identify the selected triangular surfaces at which the loading was applied. Furthermore, large deflections were set to 'ON' and all output Controls were set to 'Yes'. Force probes were set to capture the:

- Force Reaction at contact between PLF and spinous process of L_3 ($T_{PLF/L3}$);
- Force Reaction at contact between PLF and spinous process of L_4 ($T_{PLF/L4}$);
- Force Reaction at contact between PLF and spinous process of L_5 ($T_{PLF/L5}$);
- Force Reaction at fixed support of the superior side of the TLF (T_S);
- Intradiscal Pressure of the L_4/L_5 Intervertebral Disc (IDP).

The automatic meshing algorithm was employed in ANSYS (V18.1, Canonsburg, USA) without redefining the original surface mesh input. The resulting mesh was with a total of 188,961 tetrahedral elements and 272,442 nodes generated from the original unchanged tessellation surface mesh. Moreover, the average time per simulation was 31 seconds. Table 3.4 reports the output values achieved for each of the four previously defined tasks.

Table 3.4: Resulting simulation output for each of the tasks

			Task 1	**Task 2**			**Task 3**	**Task 4**
			FL = 0	**FL = 800 N**	**FL = 2350 N**	**FL = 3185 N**	**FL = 144 N**	
			Upright	(a) Upright	(b) Squatting with 20 kg	(c) Kyphotic Back with 20 kg	Prone (Normal)	Prone (LBP)
Input	**IAP**	mmHg	3.4	3.4	21.7	10.3	6.62	9.27
	ICP	mmHg	18	18	117	206	10	17.1
Output	**T_{PLF}/L_3**	N	2.72	12.613	31.526	43.291	2.293	1.77
	T_{PLF}/L_4	N	2.377	35.73	99.331	134.23	6.276	5.723
	T_{PLF}/L_5	N	1.786	17.031	50.67	71.081	3.61	3.725
	Ts	N	9.481	83.825	253.01	350.37	17.913	25.279
	L_4/L_5 IDP	MPa	0.00125	0.545	1.606	2.255	0.0986	0.113

It is worth mentioning that a sensitivity analysis was conducted for the meshes of the both the 2D and 3D models. In the 2D analysis, the mesh size was initially set at 1 mm. Upon reducing the mesh, the output showed a difference less than 5% at an edge size of 0.5 mm. Similarly, for the 3D mesh generated for this model, reducing the edge size below 1 mm resulted with an 8.7% difference, hence, a 1 mm edge–size was deemed sufficient for the analysis.

In simulating an upright position without a follower load (i.e. Task 1), the results conceived show that a similar resulting posterior force was achieved (1.44% difference) at the L_3 vertebral spinous process. However, this value increased by 363.71% when adding a follower load (800 N) in Task 2 (a) with an IDP of 0.545 which increased by 43500% in comparison with the IDP in Task 1. Moreover, the addition of a follower load increased the TLF axial reaction force by 784%. Squatting with a 20 kg weight achieved an output resultant of 31.526 N, 99.331 N and 50.67 N for L_3, L_4 and L_5 PLF force at the spinous process, respectively, with an IDP value of 1.606 MPa. These values increase significantly by 37.31%, 35.13%, 40.28% for L_3, L_4 and L_5 PLF force spinal levels, respectively, when carrying a 20 kg load in kyphotic back posture. Moreover, the IDP at the L_4/L_5 IVD increased by 40.41% and the TLF axial reaction force increased by 38.4%. In a prone position (i.e. Task 3), the posterior TLF forces decreased by approximately 80 % for each spinal level and the TLF axial reaction force. In the LBP case (i.e. Task 4), the TLF forces decreased by 23% and 8.81% at the L_3, L_4 spinal level PLF reaction force, respectively, but increased by 3.18% for the L_5 spinal level PLF reaction force. However, the axial reaction force increased significantly by 41.12% and the IDP increased by 14.6%.

The follower load had a large effect on the output forces and IDP computed. In specific, the results showed the significant difference achieved with the inclusion of the follower load. This has been studied in depth within the literature. Patwardhan et al. realized the importance of including a follower load when they designed an experiment suitable to load the spine. In specific, the load followed the curvature of the spine and reached up to 1200 N [173]. Rohlmann et al. reported on the influence of the follower load. They noticed a significant increase of the intradiscal pressure to physiologic values [453]. More recent studies studied the effect of the follower load on the kinematics and stiffness of the thoracic spine with an intact rib cage [454]. They observed that the follower load decreased the combined segmental range of motion by an average of 34% for all modes. This aligns with the conclusion achieved from this study.

The outputs observed showed that the three dimensional PLF reaction forces were within a close range of the two-dimensional study which works towards validating the force output model (Task 1). To ensure, that the output results were applicable for the 3D model, the IDP was also compared with the literature. In specific, Task 2 showed that the upright posture resulted with an IDP value of 0.545 at the L_4/L_5 IVD and Task 3 showed that the IDP in a prone position was 0.0986 MPa. In their study, Katsuhiko et al. investigated IDP in normal discs at the L_4/L_5 level in different postures in healthy individuals and reported an IDP of 0.539 ± 0.179 MPa in upright postures and 0.091 ± 0.027 MPa and calculated the follower load to be 144 N and 800 N for the prone and upright postures, respectively [448]. Thus, the values achieved by Task 2 (a) and Task 3 fell within the reported ranges when subjected to the same follower loads. Similarly, Wilke et al. reported on absolute values of IDP for different postures and exercises. In lifting a 20 kg weight with bent over round back (i.e. kyphotic back), the IDP was reported as 2.3 MPa, while, lifting 20 kg as taught in back school (i.e. squatting), the IDP was reported 1.7 MPa with follower loads calculated as 3185 N and 2350 N, respectively [449]. In the case of this study, the resulting IDP for each of Task 2 (b) (i.e. squatting) and Task 2 (c) (i.e. Kyphotic Back), was 2.25 MPa and 1.606 MPa corresponding to a 2.17% and 5.52%, respectively. Hence, the IDP values recorded at L_4/L_5 fell within the reported values in literature. Furthermore, the results show the advantage in force transmission across all TLF peripherals within the L_3–S_1 when a squatting posture is adopted in lifting weight. This is especially evident with the high increase in the caudocranial TLF force (up to 350 N) when carrying a 20 kg weight in kyphotic back. This value

increased by 40% when compared to that of a squatting posture accompanied with a reduction in the IDP of approximately the same percentage.

To simulate the prone posture for a degenerated disc case, the material properties were adjusted accordingly in addition to the reported IAP and ICP inputs. In investigating the resultant outputs, the PLF reaction forces decreased more towards the higher spinal levels while the overall TLF axial pressure increased significantly (41.12%). In specific, the increase in IAP and ICP from an upright posture to higher demanding postures, always resulted with an increase of all reaction forces. However, in the prone position case, the increase of IAP and ICP observed in the LBP case, did not result with the same pattern of variation (i.e. forces decreased for the L_3 and L_4 spinal levels as well as the fascia axial force but increased for the L_5 spinal level). It is worthy to note that the IDP increased by 14%, however, previous *in-vivo* studies have observed a decrease in the IDP with the progression of the discal degeneration (0.073 ± 0.042 MPa in Grade 2 (mild) discal degeneration and 0.032 ± 0.045 in Grade 3 (moderate) discal degeneration [448]). This may be the result of not incorporating porosity to the nucleus pulposus characterization whereby the decrease of IDP has been suggested to be a result of the decrease in the water content. Moreover, the IDP discrepancy may be the result of the limitation of not accounting for the geometrical change of the nucleus pulposus which has been observed to have a decrease in height. Hence, further studies that incorporate the two prior variations are necessary which may be conceived via modeling the intervertebral disc with poro-elastic material properties. Furthermore, while the three-dimensional TLF axial force increased significantly in the upright, kyphotic back and squatting postures when compared to the two-dimensional study, the magnitudes computed exceeded the marked strain-limits after which collagen fibers were shown to fail [144]. This may be due to the absence of including the biomechanical variations along the TLF and using a simplified constant thickness model. Furthermore, while the 3D study provided the magnitudes of the forces which may be used to define the initial state for the real-time simulation, it is necessary to investigate the changes that would occur during the real-time simulation. In other words, viscoelastic behavior of the tissue should be incorporated in future studies to provide a complete definition of the change in magnitude of the boundary conditions during the simulation.

In addition to investigating the IDP and PLF force (in comparison to the 2D model), the caudocranial force axial force (Ts) of the TLF was investigated. The axial TLF force (Ts)

achieved in an upright posture was within the ranges previously reported in the literature. In specific, Gracovetsky et al. computed the forces within the thoracolumbar fascia mathematically by depicting a net mechanism that relates the lateral forces to the caudocranial force. In their study, they accounted for the collagen fiber orientation composing the TLF. Hence, they established that the TLF may experience a maximum caudocranial force of 1015 N during a simulated 110 N weight lift [141]. Tesh et al. later conducted a set of experiments on the TLF by tensioning the TLF, both on isolated vertebral column segments and whole cadavers. The results of their experiments showed that the maximum, limiting caudocranial force, is 335 N [102]. However, this was later refuted by Adams et al. whereby they suggested that the TLF caudocranial force can exceed 1 kN [143].

To the author's knowledge this is the first 3D study that incorporates the TLF in a finite element study. Moreover, further novelty of this study includes the incorporation of intra-abdominal pressure effects as well as accounting for mechanical variations resulting from disc degeneration in the prone position which may be utilized to establish the initial stage for the real-time simulation module developed. Nevertheless, the results conceived in this study have concluded the following:

1. The follower load must be accounted for any finite element analysis which includes real-time FE studies;
2. Carrying weight using a squatting position may reduce the caudocranial force applied on the TLF in comparison to a Kyphotic Back posture;
3. Offline FE studies may provide readily available preloading and boundary conditions required to define the initial state of a VR model within an FE scheme should the VR model be simplified.

The original workflow of constructing the physics-based simulator was inclusive of a finite element model projected from the visual model (which the user sees on the display). The development of such a VR module, in addition to preparing the geometries and VR scene, requires the definition of the initial state of the computational models. This is conceived via pre-loading the necessary models (i.e. follower loads) and applying the necessary boundary conditions (i.e. Intra-Abdominal Pressure, Paraspinal Muscular Pressure and Peripheral fascia forces). As such, the muscular layers embedded within the Thoracolumbar Fascia (given its muscle-engulfing anatomical quality) would be used as the computational model. While the

boundary conditions were successfully achieved from the above study, initial investigations of the scene preparation showed that the adoption of a Finite Element (FE) method for computing the force feedback was not possible given the high computational overhead sustained using the in-house VR scene creator. In specific, the motion of the tool controlled by the user's hand and the tool within the fluoroscopic scene became asynchronous. Furthermore, any contact between the tool and the finite element model resulted with significant lags whereby the frame rate reduced significantly below 10 Hz. It is worthy to mention that any computation of forces from the tool-tissue interaction running at a frame rate below 1000 Hz, would form a bottleneck for the haptic feedback. Hence, the boundary conditions extracted were not utilized in the following pipeline as the method described in Chapter 5 directly implemented the extracted cadaveric data in Chapter 4. However, future progression of the hardware allowing for FE-based real-time computation necessitates the definition of the initial state, hence, the offline simulations described above provide a basis for such developments shedding light on the transition and its possible use within the pipeline of real-time simulations.

4

CADAVERIC EXPERIMENTAL STUDY TO EXTRACT TOOL-TISSUE INTERACTION

4.1. FRAMEWORK OF SECOND ARTICLE

This study aimed to acquire the quantifiable behavior of the tissue response subject to a probe's interaction. The probe was the main and only haptic-integrated and scene-integrated tool in the developed medical simulator of the present thesis. In the access gaining stage, the tool punctures and penetrates through the muscle tissue to reach the intervertebral disc. This defines a safe trajectory to conduct the subsequent surgical tasks. To extract the tool-tissue interactions, a set of experiments were particularly designed to mimic the possible maneuvers and degrees-of-freedom when utilizing the tool. This was followed by the design, manufacturing and assembly of an experimental benchtop necessary to carry and control the orientation of the cadaveric specimens. Furthermore, the outcome of this study provided a set of force–displacement and torque–angular displacement curves suitable for rendering the haptic feedback. The attainment of objective 3 and hypothesis 2 are presented in the manuscript entitled "Analysis of Surgical Forces Required to Gain Access using a Probe for Minimally Invasive Spine Surgery via Cadaveric-Based Experiments toward use in Training Simulators" for which the contribution of the first author is considered to be 85%. This manuscript was published in the journal of *IEEE Transactions on Biomedical Engineering* on May 25, 2020.

4.2. ARTICLE 2: ANALYSIS OF SURGICAL FORCES REQUIRED TO GAIN ACCESS USING A PROBE FOR MINIMALLY INVASIVE SPINE SURGERY VIA CADAVERIC-BASED EXPERIMENTS TOWARD USE IN TRAINING SIMULATORS

Khaled El-Monajjed, M.Eng., Jr.Eng.[1]; Mark Driscoll, Ph.D., P. Eng.[1]

[1]*Musculoskeletal Biomechanics Research Lab, Department of Mechanical Engineering, McGill University, Montreal, Quebec, Canada*

Address for notification, correspondence and reprints:

Mark Driscoll, Ph.D., P.Eng., Assistant Professor

Associate Member, Biomedical Engineering

Canada NSERC Chair Design Engineering for Interdisciplinary Innovation of Medical Technologies

Department of Mechanical Engineering

817 Sherbrooke St. West

Montreal, QC, H3A 0C3 Canada

T: +1 (514) 398 - 6299

F: +1 (514) 398 – 7365

E-Mail: Mark.Driscoll@mcgill.ca

4.2.1. ABSTRACT

Introduction: Virtual Reality haptic-based surgical simulators for training purposes have recently been receiving increased traction within the medical field. However, its future adoption is contingent on the accuracy and reliability of the haptic feedback. *Goal*: This study describes and analyzes the implementation of a set of haptic-tailored experiments to extract the force feedback of a medical probe used in minimally invasive spinal lumbar interbody fusion surgeries. *Methods:* Experiments to extract linear, lateral and rotational insertion, relaxation and extraction of the tool within the spinal muscles, intervertebral discs and lumbar nerve on two cadaveric torsos were conducted. *Results:* Notably, mean force-displacement and torque-angular displacement curves describing the different tool-tissue responses were reported with a maximum force of 6.87 (± 1.79) N at 40 mm in the muscle and an initial rupture force through

the Annulus Fibrosis of 20.550 (± 7.841) N at 6.441 mm in the L_4/L_5 disc. *Conclusion:* The analysis showed that increasing the velocity of the probe slightly reduced and delayed depth of the muscle punctures but significantly lowered the force reduction due to relaxation. Decreasing probe depth resulted with a reduction to the force relaxation drop. However, varying the puncturing angle of attack resulted with a significant effect on increasing force intensities. Finally, not resecting the thoracolumbar fascia prior to puncturing the muscle resulted with a significant increase in the force intensities. *Significance:* These results present a complete characterization of the input required for probe access for spinal surgeries to provide an accurate haptic response in training simulators.

4.2.2. INTRODUCTION

The employment of virtual reality (VR) haptic-based simulators for practical training in healthcare has previously demonstrated to have substantial impact on surgical practice learning curves [1]. Generally, its advantages transpire with the mitigation of the high cost and time constraints associated with obtaining cadavers for training and the risk-mitigation in real-life situations when dealing with patients. Specifically, simulators have recently been improved with modular options having scenario-based learning. Williams et al. [2] demonstrated positive learning outcomes, including the development of clinical reasoning and confidence, by conducting a cross-cultural comparative study to assess the impact of simulators on a total of 511 student participants.

Advancements in robotics have rendered the feasibility of adopting haptic devices [3, 4] that provide the user with the, conscious (e.g. direct pressure forces) and unconscious (e.g. frictional forces), kinesthetic feedback resulting from the virtual contact between the actual user-handled tool mounted to the haptic arm and the components in the virtual scene. The importance of this kinesthetic pressure resistance, achieved by haptics, was highlighted in Minimally Invasive (MI) surgeries whereby surgeons depend on force differentials between the various soft and hard tissue to make decisions whereby training on fine motor skills and hand-eye coordination [5–7].

The Lumbar Decompression Fusion Surgery is one type of surgery that has transitioned from an open surgery to an MI surgery [8]. MI surgeries have become increasingly popular in recent years given its benefits including smaller incisions, faster recovery times including shorter

hospital stay, reduced pain, improved cosmesis, lower blood loss and improvements in back pain [9–12]. However, the need for training for such MI surgeries becomes a necessity when observed outcomes show elevated radiation exposure as a result of a higher employment of radiographic imagery due to visual restrictions [13–15]. Diminished internal visualization has shown to be more likely to result with an increase in hardware-associated complications such as misplaced screws which require later revisions [16, 17]. The use of a training simulator incorporates metrics including radiation exposure, trajectory assessment and operation time to enhance surgical performance.

The future of haptic integration into VR medical simulators depends, in fact, on the degree of realism achieved through the force feedback [18]. The complexity arises in haptic rendering when the accumulation of strain energy due to soft-tissue deformation defines the force feedback. This is especially evident in finite element (FE) based platforms that have been observed to be computationally costly [19]. Thus, researchers have been developing different point-based models of force feedback tailored for integration into the haptic interfaces based on vectorial and spatial cartesian-based coordinates.

The following paper presents a set of cadaveric-based experiments for a fluoroscopy-aided multi-purpose probe for haptic applications in MI spinal fusion surgical simulators. A series of experimental tasks conducted on fresh frozen cadaveric torsos were performed and analyzed to provide a complete definition of tool-tissue interaction.

4.2.3 METHODS

The experiments conducted were all designed to mimic the mechanical interactions of a multi-purpose probe at the initial stage to achieve visual and physical access to the intervertebral disc (IVD) for a general postero-lateral minimally invasive spinal lumbar interbody fusion surgery. The probe handled by surgeons would be used to puncture through the different muscle layers inserted through a single 10–15 mm incision applied on the skin and posterior layer of the Thoracolumbar Fascia (TLF) as they progressed towards the IVD of interest. Thus, the soft tissue tested were spinal muscles in the lumbar region, lumbar IVDs and peripheral lumbar root nerves.

Cadaveric Preparation

Two un-embalmed fresh frozen human cadaveric torsos from Science Care, Inc. were acquired for the experiments. The cadaveric torsos were selected based on pre-screening x-ray

images, cause of death and DEXA scans for bone density, which observed no major spinal deterioration. Table I lists the specimen characteristics and measured dimensions

Appropriate ethical approvals were obtained from the local research ethics committee. The torsos, stored at -20°C initially, were placed in a refrigerator for 5 days at 2°C then thawed at room temperature for approximately 30–36 hours in preparation for the experiments. The preparation time for each of the tests in the protocols was consistent.

The lumbar spinal levels within T_{12}–L_5 were defined by the apparent spinous process of each of the lumbar vertebra and a 30 cm x 30 cm area of the skin layer was excised using a scalpel (Fig. 1(a)). The TLF was separated from the muscles and retracted to expose the muscle layer directly using a scalpel (Fig. 1(b)). Upon the completion of the muscle experiments, the entire muscle layers were excavated to provide sufficient access to the nerve and, later, the IVD. The apparent exiting nerve roots along the different spinal levels were strapped by high strength cable ties (Fig. 1(d)) in preparation for their testing.

Upon completion of the nerve experiments, the deep muscle layers were detached using scalpels and the spinous processes, superior articular processes and the posterior spinal ligaments were removed using a Rongeur to reveal the IVDs so that the tool can easily penetrate through the IVD linearly without any interference from muscles or ligaments (Fig. 1(c)). The torso specimens were then placed on a benchtop frame oriented at an angle of 65° for the muscle and IVD penetrations. It is worthy to note that no saline water or lubrication was added to the specimen at any time to maintain integrity of tissue behavior and properly replicate the conditions of the surgery.

Instrumentation and Testing Sequence

All linear tests were performed on a custom-made servo-hydraulic traction/compression testing machine (MTS 858 BIONIX II, MTS Systems Corporation, U.S.A. It was equipped with a 100 N axial load cell (661.09B-21, MTS Systems Corporation, U.S.A.) whose resolution is 0.02 N. Torsion tests were performed on a standard servo-hydraulic traction/compression/torque testing machine (MTS 858 MINI-BIONIX II, MTS Systems Corporation, U.S.A.) equipped with a 25 N·m torque transducer with a resolution of 0.005 N·m

A custom benchtop frame structure was designed to support the cadaver (Fig. 2(a)). The frame was designed to allow for angular fixations of the cadaver to achieve the desired

trajectories as well as meet the required height to achieve sufficient linear displacements by the machine's hydraulic cylinder. Furthermore, a high-resolution GoPro camera was mounted on the benchtop frame and used to record all experimental footage for post-processing. Three tools were employed to conduct the experimental sets. Tool 1 (Fig. 2(b)) replicated a standard surgical probe tool used in spinal fusion surgeries and was employed for insertion, relaxation, extraction and torque tests. Specifically, Tool 1, resembling a ball pen dilator, conceived a 0.5 mm rounded tip with a major and minor diameter of 4 mm and 1 mm, respectively, occurring over a length of 7 mm. The tool material was medical grade stainless steel 304. The other end of the tool was modified by cutting an external thread on the shaft using a die to form an M4-0.7 thread size. An M4/M6 thread-adapter was then used to fit the tool to the load cell. To ensure a tight fit and to avoid any tool deflection at the tool-load cell assembly, high strength metal-based Teflon was winded along the threads. Tool 2 (Fig. 2(c)) was a perpendicular fixation of Tool 1 used for the lateral resistance tests. Tool 3 (Fig. 2(d)), originally a 4-mm-diameter eyebolt, was adapted to have a wider opening for the high-strength cable-ties wrapped around the nerves.

Due to vision impairment in muscle experiments, industrial needles were used to penetrate and measure the safety depth after which the marked length was measured and fixed for the entire experimental sets. Blue ink was used to cover the surface of Tool 1, prior to insertion, to measure the actual displacement of the tool within the muscle. The incorporation of the ink was later tested to examine its possible effect on the results by conducting two trial runs, without ink markings (control) and with ink markings.

Table II provides the detailed experimental protocols for each of experiments, listed in sequential order. Each procedural run was conducted in a series of three tasks: (1) 40 mm insertion of the tool; (2) 10-second pause; and (3) Full extraction of the tool. All the experimental test runs, with the exception of Experiment VII, for the muscles and IVDs followed the above described procedure.

Experiments I, II, III, IV, V, and VII were conducted using Tool 1 (Fig. 5(a)), Experiment VI employed Tool 2 (Fig. 5(b)) whereas Experiment VIII employed Tool 3 (Fig. 5(c)). With the exception of Experiment VII which was conducted on the servo-hydraulic torque testing machine (MTS 858 MINI-BIONIX II, MTS Systems Corporation, U.S.A.), all the other experiments were conducted on the servo-hydraulic traction/compression testing machine (MTS 858 BIONIX II, MTS Systems Corporation, U.S.A.). T_{12}/L_1 vertebral levels were reserved for

trial testing, if necessary, to ensure the procedure properly worked prior to performing the experiments on the desired levels.

Data Preparation

Time (t), Force (F) and Displacement (d) were recorded throughout the linear experimental tests whereas torque (τ_x) and angular displacement (θ) were recorded throughout the angular experimental tests. The measured force values and their corresponding displacement values were subtracted to begin from zero increasing with positive values. The relaxation force data was adjusted to begin initially from the final force value recorded in the overall mean force values. The extraction force data was subtracted to end at zero denoting that the tool has been completely removed from the soft tissue. Extracted data statistics employed the unpaired sample Wilcoxon test for reporting on comparative values. Inadequate results, which were related to faulty experimental runs due to improper torso orientation, were filtered out prior to post-processing data.

4.2.4 RESULTS

A total of 173 test runs were conducted, however, 140 pertinent experiments were reported in this study due to the filtration of inadequate results. The linear insertion of the probe (Experiment I-a) in the spinal muscle tissues within the lumbar region resulted with a total of three main punctures defined by a global maxima followed by a global minima, which can be particularly clear in the maximum standard deviation (Fig. 3(a)). Three global maxima punctures were extracted from the mean curve, by subtracting the minimum from the maximum force values for each recorded drop. The first puncture was recorded with a mean force of 1.62 (± 0.65) N at a displacement of 15.45 mm followed by an abrupt descent to 1.54 (± 0.50) N, the second puncture was recorded with a mean force of 2.95 (± 1.27) N at a displacement of 22.06 mm followed by a drop to 2.63 (± 0.98) N and a final third puncture with a mean force of 6.13 (± 2.23) N at a displacement of 29.70 mm followed by a drop to 5.51 (± 1.26) N to plateau, thereafter, with a final force of 6.87 (± 1.79) N at 40 mm. The average actual depth of the tool within the muscle, inclusive of the muscle deformation, was recorded to be 27.60 (± 12.10) mm. Furthermore, the test conducted to examine the effect of the ink markings showed no apparent difference with the resulting force as both curves fell within the standard deviation reported

above. Finally, the post-processing of the video recordings captured by the camera fixed to the benchtop showed no tool deformation during the experimental runs and no significant deflections at the tool-load cell fixture assembly (deflection < 0.2°).

The linear relaxation of the probe (Experiment I-b) recorded a response force reduction of 2.05 (± 0.476) N during the 10-second displacement pause (Fig. 3(b)). The linear extraction experiment (Experiment I-c) on the muscle tissue recorded what appeared to be a parabolic form with a peak linear extraction force of -1.12 (± 0.51) N (Fig. 3(c)).

For the lateral resistance experiment (Experiment VI), the spinal muscle response (Fig. 3(d)) recorded a semi-linear increase of the force to reach a maximum of 18.59 (± 0.74) N at a displacement of 30 mm with a relaxation force reduction of 3.76 (± 0.21) N (Fig. 3(e)). Upon the retraction of the tool, the force decreased to zero after 30 mm (Fig. 3(f)) in what appeared to be an exponential form.

Torqueing Tool 1 (Experiment VII) was conducted at 40 mm penetration depth of the tool inside the muscle (Fig. 3(g)). Initially the tool was rotated forward in a clockwise direction while measuring the torque up to 50° then retracted counterclockwise back to its initial position (i.e. 0°). The tool, then, rotated backwards in counterclockwise direction up to -50° followed by a clockwise return to 0°. This was conducted without any stops or intervention between the forward and backward rotations. The torque response in the opposite direction followed a similar trend to that of Fig. 3(g) with minute differences. The maximum recorded Torque was 9.36 (± 0.48) N·mm at an angular rotation of 50° in the forward direction. Retraction of the tool recorded a maximum value of 5.72 (± 0.32) N·mm at the initial position and a maximum of -10.53 (± 0.21) N·mm at - 50°.

In studying the effect of depth on the linear force response and relaxation (Experiment IV), the observed data reported a statistically significant effect ($p < 0.05$) with a 0.2 N difference from the mean value at a depth of 10 mm but remained within the linear muscle insertion reported standard deviation of Experiment I-a. However, varying the depth of the displacement showed a considerable effect ($p < 0.05$) on the force reduction due to muscle relaxation reducing by 0.42 (± 0.05) N at a displacement of 10 mm.

Varying the speed of the tool insertion similarly recorded 3 global minima and maxima with no apparent pattern. The incremental test speeds of 0.5, 2.5 and 4.5 mm/s were all within

the reported standard deviation of Experiment I-a. The increase of tool velocity of 1.5 mm/s, 2.5 mm/s and 3.5 mm/s resulted with a force reduction of 3.17 N, 3.02 N and 2.47 N, respectively.

The change in angle of attack from 65° to 85° (Experiment III) similarly resulted with three punctures. However, the punctures occurred at shorter spans with higher force values whereby the first puncture recorded a force of 3.63 N at a displacement of 22.13 mm, a second puncture of 5.56 N force peak at 26.24 mm and a third puncture at 14.04 N at 32.28 mm. Both angle tests resulted with a relaxation response within the previously reported standard deviation with no variation in the extraction force resultant.

In regard to the effect of maintaining the TLF intact, Experiment V recorded three main punctures during the linear insertion with a peak force of 19.56 (± 0.91) N at 15.03 mm, 20.81 (± 0.90) N at 16.48 mm following a continuous increase to 29.75 (± 1.16) N at 20 mm. The linear relaxation response without resecting the TLF resulted with 7.36 (± 0.19) N.

The linear insertion of the probe (Experiment I-a) in the lumbar IVDs resulted with various punctures through the different annulus fibrosis layers. The first punctures at the L_1/L_2, L_2/L_3 L_3/L_4 and L_4/L_5 IVDs recorded a mean force of 8.44 (± 2.87) N at a displacement of 4.43 mm, 9.73 (± 2.05) N at 4.63 mm, 11.30 (± 2.96) N at 5.14 mm and 20.55 (± 7.84) N at 6.44 mm, respectively (Fig. 4(a)) thereafter the force, then, continued to rise. The linear relaxation of the probe (Experiment I-b) recorded a response force reduction of 8.36 (± 2.11) N, 9.74 (± 3.32) N, 6.11 (± 2.79) N and 6.17 (± 5.06) N for L_1/L_2, L_2/L_3, L_3/L_4 and L_4/L_5 IVDs, respectively (Fig. 4(b)). The linear extraction of the tool (Experiment I-c) from the IVD tissue recorded an increase to reach a maximum linear extraction force of -0.54 (± 1.19) N, -1.02 (± 1.54) N, -1.24 (± 1.46) N and -1.26 (± 2.39) N at a displacement of 9.89 mm, 10.50 mm, 9.63 mm and 9.34 mm for L_1/L_2, L_2/L_3, L_3/L_4 and L_4/L_5, respectively (Fig. 4(c)). The increase in linear velocity of 1.5, 2.5, then 3.5 mm/s recorded responses within the standard deviation of the reported mean without any specific pattern.

In Experiment VIII, the nerve was tensioned using Tool 3. With the exception of Nerve L_1/L_2 of cadaver CT-02 which failed at a displacement of 38.25 mm measuring at a force of 60 N , the final force response of all nerves reached the 80 N cut-off force but only 40 mm displacement was reported (Fig. 5). Tensioning the nerve recorded a mean force response of 25.38 (± 8.78) N, 55.03 (± 19.17) N and 53.96 (± 6.31) N for L_1/L_2, L_2/L_3, L_3/L_4 lumbar nerve

roots at a 40 mm displacement. The relaxation test showed a mean force reduction response of 7.04 (± 0.41) N for all nerves.

4.2.5. DISCUSSION

Surgical forces of a 4-mm-diameter and 150-mm-long slender probe tool, employed for surgical soft tissue puncturing, was explored in this study. In MI spinal surgeries, aiming for IVD intervention, the surgeon punctures the spinal muscle tissue while being careful not to contact the nerve root and then penetrates through the first few annular layers of the IVD. This, probe alignment then provides the surgeon with the necessary trajectory required for, comfortable minimally invasive, spinal access. It is thus important to have a firm understanding of the forces involved in this important first surgical step for those seeking to leverage such data towards physics-based surgical simulation. In order to achieve such measures certain experimental assumptions were made.

Human tissue inter- and intra-variability has been well documented in the literature, in terms of morphology, anatomy and mechanical characterization due to natural age progression and genetic predisposition [20–24]. Hence, the specimens in this study were chosen on the basis that they possess relevant features and are relatively representative of mean values. As such the extracted experimental results in this study are pertinent to spinal fusion surgeries related to progressive pathologies such as degenerated disc disease. Initially, the specimens were pre-screened for history of trauma and trauma-related deaths. X-ray imagery and DEXA scans for bone density provided information regarding spinal deterioration and vertebral slippage. In a recent study that investigated the trend in lumbar fusion procedure rates for degenerative spinal diseases in the United States (U.S.) between 2004 to 2015, the reported characteristics of the patients showed a mean age of 54.6 which later increased to 59.9 in 2015 [25]. In a similar statistical investigation conducted in the U.S. between 1998 to 2008, the mean patient age showed an increasing trend from 52.47 years in 1998 to 56.85 years in 2008 [26]. Hence, to achieve results that are representative of the mean ages and to respect the increasing trend over the years, the cadaveric samples were selected to have an age between 60 – 69 years. Furthermore, spinal lumbar interbody fusion is an effective treatment of several spinal pathologies including degenerated discs [27] which, in turn, has been strongly associated with naturally age-induced biological and morphological changes [28]. As such, discal degeneration

has been previously measured according to a variety of grading systems that define its progressive state [29] such that an initial grade mostly defines a normal disc with no degenerative conditions and the final grade defines a complete collapse of the disc. To incorporate these effects and to attain representative means of all grades, the cadaveric specimens were chosen such that they cover the lower (specimen C-01) and higher (specimen C-02) end of the degenerative disc disease grading spectrum beyond a normal disc. The variation in disc health of the specimens may be further noticed in Table I, whereby the intersegmental measured discal heights of C-01 are larger than C-02 at all levels. Furthermore, inferior progression along the lumbar spine showed an increasing discal height trend interrupted by the degenerative effects present at the L_4/L_5 discal level. These degenerative effects purposefully served the attainment of specimen that are representative of potential spinal fusion surgery candidates.

The cadaveric preparation procedure in the present study was carefully conducted to ensure minimal tissue degradation. Hence, the cadaver was thawed in a single freeze-thaw cycle at 2°C to avoid detrimental biomechanical effects on the soft tissue [30]. Previous studies have reported that the Just-Noticeable-difference (JND), a measure of the minimum difference between two stimuli necessary to reliably perceive the difference, for the human sensing has approximate value of 7% along different base forces ranging between 2.5 N and 10 N when pinching fingers [31] and a JND of 5% – 9% in elbow extensors [32]. Hence, the load cell was chosen to provide a resolution appropriate with that of the human kinesthetic detection difference threshold while sufficiently encompassing maximum forces expected during the experimental trials.

The experiments were carried out sequentially (as enumerated in Table II) to avoid tissue destruction that may affect the succeeding experiments. Based on the trial-and-error piercing administered in the lumbar region using test needles, a depth of 40mm was measured to be sufficient to reach the IVD and was, thus, maintained across all puncturing experiments of the muscle. This piercing was performed on the T_{12}/L_1 spinal level as to not influence subsequent measures. Similarly, a depth of 20 mm from the surface of the IVD was fixed throughout the experiments to avoid moments on the load cell should the probe contact bone. The relaxation time was chosen as 10 seconds to provide the soft tissue sufficient time to reach a steady-state plateau result based on trials conducted on the T_{12}/L_1 level. The displacement for the lateral

resistance experiment (Experiment VI) was chosen to exceed the expected lateral displacement of 20 mm when the tool is fully inserted. Similarly, the axial angular rotation (Experiment VII) was chosen to accommodate a full wrist kinematic axial flexion-to-extension [33] while holding the tool at 50°. It is worthy to note that the displacements reported in the plots of Fig. 3, 4 and 5 correspond to tool displacement directly, as recorded by the MTS servo-hydraulic testing machine, without accounting for tissue deformation or deformation errors that may result during penetration events. Force–displacement and torque–angular displacements have been previously adopted in medical simulators with puncturing events [34–38]. To capture the difference between the tool displacement and actual tool penetration, which is different due to tissue deformation, marking ink was employed, and the wiped length was measured as described and reported above. The ink used showed no effect on the output of the forces. Furthermore, the cadaver was placed in prone positioning during experiments without any incorporation of gravitational or muscular induced spinal loading (i.e. follower loads) since the cadaveric torso used was intact and, hence, closely resembling the conditions of an actual spinal surgery. During spinal surgeries, unnecessary nerve contact is generally always preferred. However, given the tight vicinity of IVD region, the nerve may be contacted and, hence, the tensile resistance of the nerve may be contacted (Experiment VIII). Consequently, a 40 mm displacement, similar to that of the lateral resistance experimentation (Experiment VI), was used. Such careful experimental considerations yielded relevant force characterization of the initial probe task in spinal surgery.

Experiment I-a provided a characteristic response of the number and intensity of punctures including an aggregate of the nondestructive direct and shear forces experienced when using a probe to gain access for both muscle and IVD along the axial direction (F_x). Force outputs resulting from the same cadaveric specimen conducted on the left and right side of their spine showed varying results whereby the left side had less punctures but condensed into smaller displacement and marked higher force values (i.e. puncture 1 was 10 N at a 20 mm displacement on the left side compared with 6 N at 15 mm at the L_4/L_5 spinal level for C-02). However, this difference was not significant in specimen C-01 as the force patterns were similar with no significant difference in puncturing events (i.e. < 5%). This is inline with previous investigations showing a notable difference between human muscular cross-sectional area and composition in both humans with and without low back pain [39, 40]. The stiffness resulting from the tissue response before the initial puncture in Fig. 3(a) signified an indentation applied equal to 0.102

N/mm. This value is significantly lower than previously measured posteroanterior stiffness in the lumbosacral spine (~ 15 N/mm depending on spinal level) [41]. However, this is expected given that posteroanterior stiffness values are measured non-invasively and using a different probe size. In other words, reported values of a gross response which included skin, fat and fascia in comparison with the muscle stiffness measurements in this study which were conducted after an incision to the latter tissues was conducted. However, this value is close to previously measured puncturing stiffness values measured for needle forces (0.17–0.59 N) [34]. Furthermore, little difference was observed on average between stiffness values at different segments of the lumbar spine. The difference between the largest and lowest reported mean stiffness along the lumbar spinal segments was 0.2 N/mm. This result is in line with Owens et al. who reported minute segmental differences [42]. The tool insertion into muscle showed a muscle relaxation of 2.05 (± 0.476) N over a 10 s period which is close to previously shown relaxation ranges of skeletal muscles in a study conducted by McHugh et al. who reported ranges between 4.2 (1.55) N up to 11.35 (1.75) N [43]. However, their study was conducted over a 45s period and a stretch (instead of compression) was applied instead which could explain the higher values. These observations were similarly conclusive in the intervertebral disc experiments. However, no studies were found to report on comparable observations for intervertebral discs and nerves.

The punctures observed as a result of using Tool 1 along the different lumbar spinal segments showed no significant conclusive patterns. In general, the results observed in Fig. 3(a) measured singular mean force drops of 0.63 N with a maximum reported force drop of 1.02 N. Similarly, intervertebral discs reported mean puncture force drops of 1.52 N with a maximum reported force drop of 11.2 N. However, as a result of the slight variation in the displacement occurrence and force magnitude of the puncture events, the mean values normalized the actual effects of the drops. As such, the force drops in individual puncturing events were observed to be higher. The maximum force drops were calculated as 7.22 N at the left side of the L_1/L_2 level for C-01 and 8.11 N measured on the left side of the L_3/L_4 level of C-02. A maximum puncture drop of 25.3 N was observed at the L_4/L_5 IVD of C-01 and 22.03 N was observed at the L_3/L_4 IVD of C-02. Puncture force drops have been previously reported in needle puncturing studies tailored for medical simulator integration and reported major force drops up to 2 N [34–36, 38, 44–46]. This is likely due to the difference in diameter between needles and the dilator probe adopted in this study which interacts with more tissue area at the tip-tissue interface. It is worth to noting

that the sudden high force drops inevitably result with a sudden loss of control within the tissue which at sensitive areas, e.g. in vicinity of nerve roots at deeper muscular layers, is further motivation for controlled training via surgical simulators. The potential of adopting medical simulators in training has been previously associated with large effects on the outcomes of knowledge, skills and behavior of surgeons [47, 48]. While the exact effect of medical simulators on motor skills enhancement has not been quantified, researchers have agreed that it plays a positive role in elevating motor skills [49–51]. In our case, the effect of medical training on psychomotor skills, such enhancements may be studied by the incorporation of metrics related to the user's ability to control the tool within tissue punctures.

The mean curves for the muscle and IVD could be fit to piecewise equations [52] such that the functions are fit to either exponential or polynomials depending on the quality of fit (such as coefficient of determination). This method is applicable given the puncturing events of the present study which renders a discontinuous function as previously described by Gordon et al. [53]. This method does not require direct tissue material properties and mechanical approximations which, in turn, require complex computations but, instead, can be readily used to model accurate puncturing events for application in medical simulators which require simplicity for high-speed calculations. In the case of the output presented in this paper, each of the piecewise functions would denote a puncturing event. For instance, in Fig. 3(a), each of the four specified muscular layers would be represented by an exponential or polynomial function bounded by their corresponding displacements. Similarly, the data presented may readily employ a Fourier series expansion as described by Li et al. [54]. This technique would provide a more accurate rendering of the forces, capturing even the minor puncturing events using triangular periodic functions defined by Fourier coefficients expanded to N terms depending on the required accuracy. These techniques combine theoretical models with experimental models as opposed to mechanical characterization. The reduction of force, due to relaxation, was recorded in Experiment I-b to provide a realistic response of the tissue viscoelastic effect. The apparent continuous nature of the response can be curve fit using a single exponential or polynomial function. Finally, Experiment I-c was conducted to extract the response in the event of removing the tool from within the muscle or IVD ($-F_x$). The literature contains very few studies on analyzing tool extraction responses from soft tissue even though they have been reported as part of tool insertion [44]. In specific, the extraction curve may be divided into two portions and

modelled using a piecewise function. The first part follows a non-linear decrease which can be fitted to a logarithmic function given that it decreases abruptly followed by a plateau. The second curve can be modelled using boundary-specific parabolic functions. In the case of Fig. 3(c), the first curve runs between a displacement of 0–10 mm while the second curve runs between 10–40 mm. Experiment VI-a and VI-b incorporated the extraction of the lateral forces and relaxation response experienced while handling the tool within the muscle tissue (F_y and F_z), whereby, the corresponding moments, M_y and M_z, can be calculated using the Euler-Bernoulli Beam Theory. The results achieved in this document can readily construct moment responses and embedded to a model similar to Kang et al. [55] whereby they extracted and analyzed needle transverse loading and bending inside soft tissue to be modelled for haptic integration of a surgical simulator. This response would depend on the depth of the tool in the tissue. Experiment VII consisted of the tasks that extract the torque about the tool's axis if it is rotated axially within the muscle tissue (τ_x). The described forward and backwards rotation were intentionally conducted consecutively without any intervention to examine and report on the effect of the forward rotation on a backward rotation within the full kinematic boundaries of the human hand. Such 1-DOF torque tests have been previously conducted for needle haptic integration purposes [45] which to the authors' knowledge has not been previously reported. Finally, Experiment VIII-a and VIII-b extracted the nerve contact resistance and relaxation, respectively. The nerve tensioning and relaxation output exhibit a continuous non-linear response which can be fit using exponential functions.

Complementary to the main experiments, Experiment II, III, IV and V studied the effect of speed, angle, depth and puncturing through the muscle without incising the TLF on the force resultant and force relaxation, respectively. Given that the tool mainly interacts with the muscle tissue and scarcely punctures the first few layers of the IVD in normal surgical procedures, the effect of the previously mentioned variables was only conducted for the muscles, with the exception of speed. The results showed that an increase in the velocity of the tool resulted with a slight decrease in the puncture force magnitude occurring at a higher displacement with a decreased force reduction response due to relaxation which agrees with previous studies exploring needle puncture [56]. Varying the final probe insertion displacement depth through the muscle (i.e. 10 mm instead of 40 mm) resulted with an insignificant mechanical effect (0.2 N difference) on the force intensity response, even though it was observed to be statistically

significant ($p < 0.05$). However, it significantly affected the force reduction, both statistically ($p < 0.05$) and mechanically. This is comparable to a study conducted by Ahn et al. [57] who investigated the effect of indentation depth on the relaxation. The posterior layer of the TLF is a high-strength interweaved ligamentous layer. Repeating Experiment I without applying an incision to the TLF has shown to have a high effect on the initial puncture force. Hence, it is customary for surgeons to incise and retract the TLF before commencing with puncturing through the muscular layers [58], to avoid unnecessary elevated consequential internal stresses. The consideration of the angle of attack within the soft tissue was previously considered by Kang et al. [55] but did not report findings on its effect. However, this study provided a baseline of angular change that could be interpolated to provide sufficient response variability when puncturing through spinal muscles.

4.2.6. CONCLUSION

The experimental results conceived in the present study provided a comprehensive characterization of a standard puncturing probe tool, used in general spinal surgeries, which interacts with soft tissue that exists in various minimally invasive surgeries. Such experimental results provided a baseline for the conscious and unconscious force and torque experiences which may be leveraged in haptic-specific models for surgical training simulators in the medical field.

4.2.7. REFERENCES

[1] K. Rangarajan, H. Davis, and P. H. Pucher, "Systematic Review of Virtual Haptics in Surgical Simulation: A Valid Educational Tool?," *Journal of surgical education,* 2019, doi: 10.1016/j.jsurg.2019.09.006.
[2] B. Williams, C. Abel, E. Khasawneh, L. Ross, and T. Levett-Jones, "Simulation experiences of paramedic students: a cross-cultural examination," *Advances in Medical Education and Practice*, vol. 2016, no. Issue 1, pp. 181-186.
[3] G. Tholey, J. P. Desai, and A. E. Castellanos, "Force feedback plays a significant role in minimally invasive surgery: results and analysis," *Annals of surgery,* vol. 241, no. 1, pp. 102-9, 2005.
[4] P. Lamata, E. J. Gómez, F. M. Sánchez-Margallo, F. Lamata, F. del Pozo, and J. Usón, "Tissue consistency perception in laparoscopy to define the level of fidelity in virtual reality simulation," *Surgical Endoscopy And Other Interventional Techniques,* vol. 20, no. 9, pp. 1368-1375, 2006, doi: 10.1007/s00464-004-9269-z.

[5] D. Wang, Y. Guo, S. Liu, Y. Zhang, W. Xu, and J. Xiao, "Haptic display for virtual reality: progress and challenges," vol. 1, no. 2, pp. 136-162, 2019, doi: 10.3724/SP.J.2096-5796.2019.0008.
[6] T. P. Grantcharov, V. B. Kristiansen, J. Bendix, L. Bardram, J. Rosenberg, and P. Funch-Jensen, "Randomized clinical trial of virtual reality simulation for laparoscopic skills training," *Br J Surg,* vol. 91, no. 2, pp. 146-50, Feb 2004, doi: 10.1002/bjs.4407.
[7] P. Ström, L. Hedman, L. Särnå, A. Kjellin, T. Wredmark, and L. Felländer-Tsai, "Early exposure to haptic feedback enhances performance in surgical simulator training: a prospective randomized crossover study in surgical residents," *Surgical Endoscopy,* vol. 20, no. 9, pp. 1383-1388, 2006.
[8] D. Zhang, K. Mao, and X. Qiang, "Comparing minimally invasive transforaminal lumbar interbody fusion and posterior lumbar interbody fusion for spondylolisthesis: a STROBE-compliant observational study," *Medicine,* vol. 96, no. 37, 2017.
[9] Y. Park and J. W. Ha, "Comparison of one-level posterior lumbar interbody fusion performed with a minimally invasive approach or a traditional open approach," *Spine,* vol. 32, no. 5, pp. 537-543, 2007.
[10] C. Seng *et al.*, "Five-year outcomes of minimally invasive versus open transforaminal lumbar interbody fusion: a matched-pair comparison study," *Spine,* vol. 38, no. 23, pp. 2049-2055, 2013.
[11] A. T. Villavicencio, S. Burneikiene, C. M. Roeca, E. L. Nelson, and A. Mason, "Minimally invasive versus open transforaminal lumbar interbody fusion," *Surgical neurology international,* vol. 1, 2010.
[12] S. W. Terman, T. J. Yee, D. Lau, A. A. Khan, F. La Marca, and P. Park, "Minimally invasive versus open transforaminal lumbar interbody fusion: comparison of clinical outcomes among obese patients," *Journal of Neurosurgery: Spine,* vol. 20, no. 6, pp. 644-652, 2014.
[13] J. Wang, Y. Zhou, Z. F. Zhang, C. Q. Li, W. J. Zheng, and J. Liu, "Comparison of one-level minimally invasive and open transforaminal lumbar interbody fusion in degenerative and isthmic spondylolisthesis grades 1 and 2," *European Spine Journal,* vol. 19, no. 10, pp. 1780-1784, 2010.
[14] J. Wang, Y. Zhou, Z. F. Zhang, C. Q. Li, W. J. Zheng, and J. Liu, "Comparison of the clinical outcome in overweight or obese patients after minimally invasive versus open transforaminal lumbar interbody fusion," *Clinical Spine Surgery,* vol. 27, no. 4, pp. 202-206, 2014.
[15] K. Phan, P. J. Rao, A. C. Kam, and R. J. Mobbs, "Minimally invasive versus open transforaminal lumbar interbody fusion for treatment of degenerative lumbar disease: systematic review and meta-analysis," *European Spine Journal,* vol. 24, no. 5, pp. 1017-1030, 2015.
[16] S. S. Dhall, M. Y. Wang, and P. V. Mummaneni, "Clinical and radiographic comparison of mini–open transforaminal lumbar interbody fusion with open transforaminal lumbar interbody fusion in 42 patients with long-term follow-up," *Journal of Neurosurgery: Spine,* vol. 9, no. 6, pp. 560-565, 2008.
[17] G. Gu *et al.*, "Comparison of minimally invasive versus open transforaminal lumbar interbody fusion in two-level degenerative lumbar disease," *International orthopaedics,* vol. 38, no. 4, pp. 817-824, 2014.

[18] O. A. J. Meijden and M. P. Schijven, "The value of haptic feedback in conventional and robot-assisted minimal invasive surgery and virtual reality training: a current review," *Surgical Endoscopy,* vol. 23, no. 6, pp. 1180-1190, 2009.
[19] M. Dragan and Z. Manfred, "Survey of Finite Element Method-Based Real-Time Simulations," *Applied Sciences*, vol. 9, no. 14, doi: 10.3390/app9142775.
[20] M. Kostek, M. J. Hubal, and L. S. Pescatello, "The role of genetic variation in muscle strength," *American Journal of Lifestyle Medicine,* vol. 5, no. 2, pp. 156-170, 2011.
[21] Y. Feng, B. Egan, and J. Wang, "Genetic factors in intervertebral disc degeneration," *Genes & diseases,* vol. 3, no. 3, pp. 178-185, 2016.
[22] S. Lois Zlolniski *et al.*, "3D geometric morphometric analysis of variation in the human lumbar spine," *American journal of physical anthropology,* vol. 170, no. 3, pp. 361-372, 2019.
[23] G. K. Stebbings, C. I. Morse, A. G. Williams, and S. H. Day, "Variability and distribution of muscle strength and its determinants in humans," *Muscle & nerve,* vol. 49, no. 6, pp. 879-886, 2014.
[24] J. M. Peloquin *et al.*, "Human L3L4 intervertebral disc mean 3D shape, modes of variation, and their relationship to degeneration," *Journal of biomechanics,* vol. 47, no. 10, pp. 2452-2459, 2014.
[25] B. I. Martin, S. K. Mirza, N. Spina, W. R. Spiker, B. Lawrence, and D. S. Brodke, "Trends in lumbar fusion procedure rates and associated hospital costs for degenerative spinal diseases in the United States, 2004 to 2015," *Spine,* vol. 44, no. 5, pp. 369-376, 2019.
[26] M. Pumberger, Y. Chiu, Y. Ma, F. Girardi, M. Mazumdar, and S. Memtsoudis, "National in-hospital morbidity and mortality trends after lumbar fusion surgery between 1998 and 2008," *The Journal of bone and joint surgery. British volume,* vol. 94, no. 3, pp. 359-364, 2012.
[27] R. J. Mobbs, K. Phan, G. Malham, K. Seex, and P. J. Rao, "Lumbar interbody fusion: techniques, indications and comparison of interbody fusion options including PLIF, TLIF, MI-TLIF, OLIF/ATP, LLIF and ALIF," *Journal of Spine Surgery,* vol. 1, no. 1, p. 2, 2015.
[28] M. Benoist, "Natural history of the aging spine," in *The aging spine*: Springer, 2005, pp. 4-7.
[29] A. Kettler and H.-J. Wilke, "Review of existing grading systems for cervical or lumbar disc and facet joint degeneration," *European Spine Journal,* vol. 15, no. 6, pp. 705-718, 2006.
[30] A. C. Klop, M. E. M. Vester, K. L. Colman, J. M. Ruijter, R. R. Van Rijn, and R. J. Oostra, "The effect of repeated freeze-thaw cycles on human muscle tissue visualized by postmortem computed tomography (PMCT)," *Clinical anatomy (New York, N.Y.),* vol. 30, no. 6, pp. 799-804, 2017, doi: 10.1002/ca.22917.
[31] X.-D. Pang, H. Z. Tan, and N. I. Durlach, "Manual discrimination of force using active finger motion," *Perception & psychophysics,* vol. 49, no. 6, pp. 531-540, 1991.
[32] L. A. Jones, "Matching forces: constant errors and differential thresholds," *Perception,* vol. 18, no. 5, pp. 681-687, 1989.
[33] M. W. Holmes, J. Tat, and P. J. Keir, "Neuromechanical control of the forearm muscles during gripping with sudden flexion and extension wrist perturbations," *Computer methods in biomechanics and biomedical engineering,* vol. 18, no. 16, pp. 1826-34, 2015, doi: 10.1080/10255842.2014.976811.

[34] L. H. Poniatowski, S. S. Somani, D. Veneziano, S. McAdams, and R. M. Sweet, "Characterizing and simulating needle insertion forces for percutaneous renal access," *Journal of endourology,* vol. 30, no. 10, pp. 1049-1055, 2016.
[35] X. Bao, W. Li, M. Lu, and Z. Zhou, "Experiment study on puncture force between MIS suture needle and soft tissue," *Biosurface and Biotribology,* vol. 2, no. 2, pp. 49-58, 2016.
[36] A. M. Okamura, C. Simone, and M. D. O'leary, "Force modeling for needle insertion into soft tissue," *IEEE transactions on biomedical engineering,* vol. 51, no. 10, pp. 1707-1716, 2004.
[37] S. Chae, S.-W. Jung, and H.-S. Park, "In vivo biomechanical measurement and haptic simulation of portal placement procedure in shoulder arthroscopic surgery," *PloS one,* vol. 13, no. 3, 2018.
[38] K. W. Ng, J. Q. Goh, S. L. Foo, P. H. Ting, and T. K. Lee, "Needle insertion forces studies for optimal surgical modeling," *International Journal of Bioscience, Biochemistry and Bioinformatics,* vol. 3, no. 3, p. 187, 2013.
[39] R. Niemeläinen, M.-M. Briand, and M. C. Battié, "Substantial asymmetry in paraspinal muscle cross-sectional area in healthy adults questions its value as a marker of low back pain and pathology," *Spine,* vol. 36, no. 25, pp. 2152-2157, 2011.
[40] M. Fortin, Y. Yuan, and M. C. Battié, "Factors associated with paraspinal muscle asymmetry in size and composition in a general population sample of men," *Physical therapy,* vol. 93, no. 11, pp. 1540-1550, 2013.
[41] A. Viner, M. Lee, and R. Adams, "Posteroanterior stiffness in the lumbosacral spine: the correlation between adjacent vertebral levels," *Spine,* vol. 22, no. 23, pp. 2724-2729, 1997.
[42] E. F. Owens Jr, J. W. DeVocht, M. R. Gudavalli, D. G. Wilder, and W. C. Meeker, "Comparison of posteroanterior spinal stiffness measures to clinical and demographic findings at baseline in patients enrolled in a clinical study of spinal manipulation for low back pain," *Journal of manipulative and physiological therapeutics,* vol. 30, no. 7, pp. 493-500, 2007.
[43] M. P. McHugh, S. P. Magnusson, G. W. Gleim, and J. A. Nicholas, "Viscoelastic stress relaxation in human skeletal muscle," *Medicine and science in sports and exercise,* vol. 24, no. 12, pp. 1375-1382, 1992.
[44] M. Mahvash and P. E. Dupont, "Mechanics of dynamic needle insertion into a biological material," *IEEE transactions on bio-medical engineering,* vol. 57, no. 4, pp. 934-43, 2010, doi: 10.1109/TBME.2009.2036856.
[45] G. Ravali and M. Manivannan, "Haptic Feedback in Needle Insertion Modeling and Simulation," *IEEE reviews in biomedical engineering,* vol. 10, pp. 63-77, 2017, doi: 10.1109/RBME.2017.2706966.
[46] K. Naemura, Y. Uchino, and H. Saito, "Effect of the needle tip height on the puncture force in a simplified epidural anesthesia simulator," in *2007 29th Annual International Conference of the IEEE Engineering in Medicine and Biology Society*, 2007: IEEE, pp. 3504-3507.
[47] D. A. Cook *et al.*, "Technology-enhanced simulation for health professions education: a systematic review and meta-analysis," *Jama,* vol. 306, no. 9, pp. 978-988, 2011.
[48] C. I. Nesbitt, N. Birdi, S. Mafeld, and G. Stansby, "The role of simulation in the development of endovascular surgical skills," *Perspectives on medical education,* vol. 5, no. 1, pp. 8-14, 2016.
[49] D. Gaba, "Improving anesthesiologists' performance by simulating reality," ed, 1992.

[50] Y. Zausig *et al.*, "Simulation as an additional tool for investigating the performance of standard operating procedures in anaesthesia," *British journal of anaesthesia,* vol. 99, no. 5, pp. 673-678, 2007.
[51] R. Kneebone, D. Nestel, C. Vincent, and A. Darzi, "Complexity, risk and simulation in learning procedural skills," *Medical education,* vol. 41, no. 8, pp. 808-814, 2007.
[52] D. F. Pepley, M. A. Yovanoff, K. A. Mirkin, S. R. Miller, D. C. Han, and J. Z. Moore, "Integrating Cadaver Needle Forces Into a Haptic Robotic Simulator," *Journal of medical devices,* vol. 12, no. 1, pp. 0145011-145015, 2018, doi: 10.1115/1.4038562.
[53] A. Gordon, I. Kim, A. C. Barnett, and J. Z. Moore, "Needle insertion force model for haptic simulation," in *ASME 2015 International Manufacturing Science and Engineering Conference*, 2015: American Society of Mechanical Engineers Digital Collection.
[54] L. Feiyan *et al.*, "Real-Time Needle Force Modeling for VR-Based Renal Biopsy Training with Respiratory Motion Using Direct Clinical Data," *Applied Bionics and Biomechanics*, vol. 2019*,* doi: 10.1155/2019/9756842.
[55] S. G. Kang and D. Y. Lee, "Implementation of skin manipulation in a haptic interface of needle intervention simulation," in *2014 14th International Conference on Control, Automation and Systems (ICCAS 2014)*, 22-25 Oct. 2014 2014, pp. 768-772, doi: 10.1109/ICCAS.2014.6987882.
[56] S. Jiang, P. Li, Y. Yu, J. Liu, and Z. Yang, "Experimental study of needle-tissue interaction forces: Effect of needle geometries, insertion methods and tissue characteristics," *Journal of Biomechanics,* vol. 47, no. 13, pp. 3344-3353, 2014, doi: 10.1016/j.jbiomech.2014.08.007.
[57] B. Ahn and J. Kim, "Measurement and characterization of soft tissue behavior with surface deformation and force response under large deformations," *Medical image analysis,* vol. 14, no. 2, pp. 138-48, 2010, doi: 10.1016/j.media.2009.10.006.
[58] A. Guiroy, A. Sícoli, N. Masanés, A. Ciancio, M. Gagliardi, and A. Falavigna, "How to perform the wiltse posterolateral spinal approach: Technical note," *Surgical Neurology International,* vol. 9, no. 1, p. 38, 2018, doi: 10.4103/sni.sni_344_17.

4.2.8. FIGURES AND TABLES

Table 4.1: Cadaveric Torso Specimen Characteristics

Cadaveric Torso ID				C-01	C-02
Gender				Male	Male
Age				63	69
Stature			mm	1752.6	1778
Body Mass Index				23.63	27.26
Weight			kg	72.57	86.18
Intervertebral Disc Dimensions	L_1/L_2	Height	mm	9.95	5.20
		Width[a]	mm	44.70	49.36
	L_2/L_3	Height	mm	10.26	7.60
		Width[a]	mm	46.11	45.73
	L_3/L_4	Height	mm	11.62	5.70
		Width[a]	mm	47.60	60.62
	L_4/L_5	Height	mm	10.34	3.10
		Width[a]	mm	54.12	-
Nerve Dimension	L_1/L_2 - L	Diameter	mm	3.141	4.521
	L_1/L_2 - R		mm	3.693	4.346
	L_2/L_3 - L		mm	4.544	6.557
	L_2/L_3 - R		mm	6.812	5.524
	L_3/L_4 - L		mm	7.031	-
	L_3/L_4 - R		mm	9.648	-
Scoliosis				No	Yes
Degenerated Disc				No	L_4/L_5
Trauma				No	No

[a]Width reported represents the lateral width of the disc; L = Left, R = Right

Table 4.2: Description of Experimental Test Protocols and Specifications

	EXPERIMENTS	SPECIFICATION	NUMBER OF TRIALS	FREQUENCY	Stopping Criteria
I	(a) Tool Insertion (b) Relaxation (c) Extraction Resistance	0.5 mm/s for muscle tissue 1 mm/s for disc	1 per spinal level per side per cadaver	150 Hz	40 mm displacement with cut-off force of 70 N
II	Speed Effect	0.5 mm/s, 2.5 mm/s, 4.5 mm/s for muscle 2 mm/s, 3 mm/s, 4 mm/s for disc	1 test per speed on C-02	200 Hz	40 mm displacement with cut-off force of 70 N
III	Angle Effect[a]	65° and 85° orientation	1 test per angle on C-02	150 Hz	40 mm displacement with cut-off force 70 N
IV	Depth Effect	10 mm displacement	2 tests on cadaver 2	200 Hz	10 mm displacement
V	Fascia Effect	0.5 mm/s	2 tests on cadaver 2	200 Hz	25 mm displacement
VI	(a) Lateral Resistance (b) Lateral Relaxation	0.1 mm/s	3 trials on cadaver 2	200 Hz	40 mm displacement with cut-off force of 70N
VII	Torque Resistance	2° /s	5 trials on cadaver 2	100 Hz	50° to -50° angular displacement
VIII	(a) Nerve Tensioning (b) Nerve Relaxation	0.5 mm/s	6 trials per cadaver	150 Hz	100 mm with a cut-off force of 80 N

[a]Angle effects were measured based on an orientation in the sagittal plane about the spinal axis

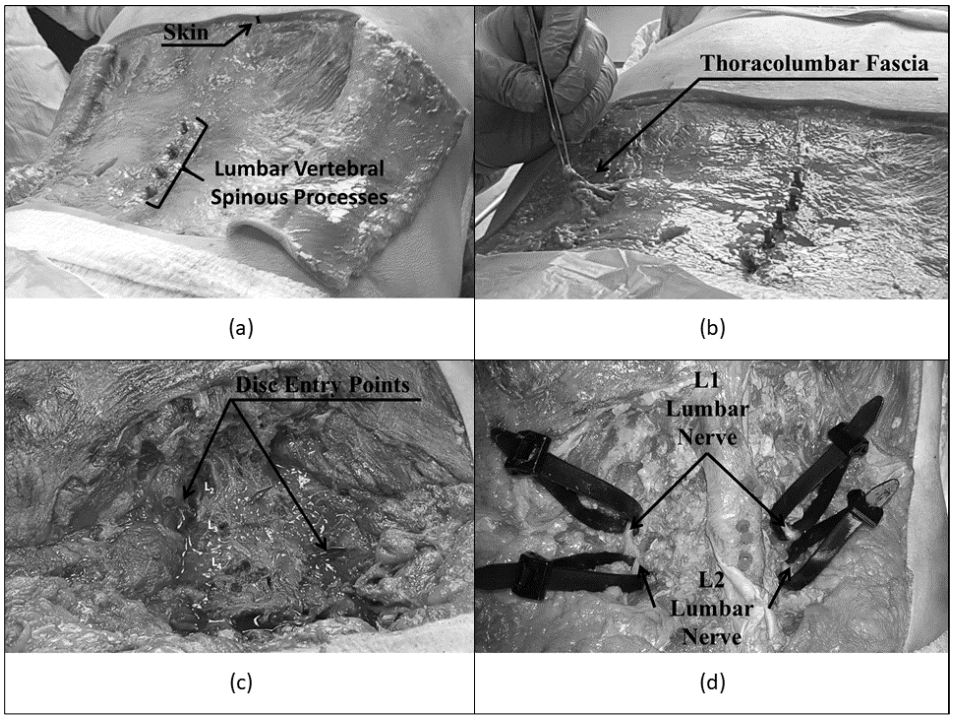

Figure 4-1: (a) 30 cm x 30 cm skin layer dissection showing markings of lumbar vertebrae and skin layer thickness (b) Depiction of incision and retraction of Thoracolumbar Fascia to expose muscle (c) Depiction of workspace within the cadaver after muscle excavation (d) Depiction of the torso preparation for the Nerve Experiments

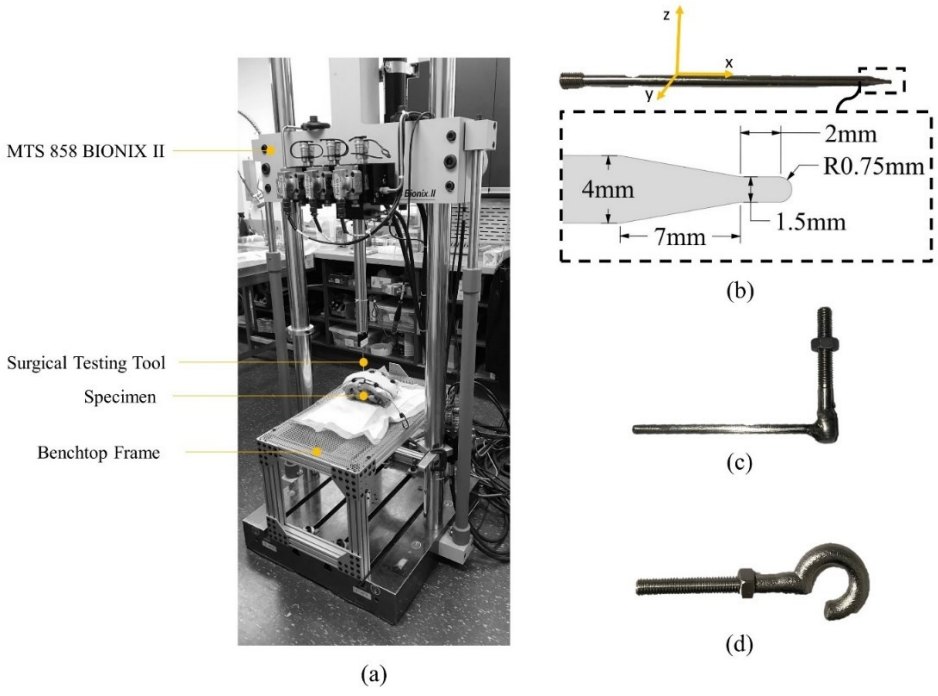

Figure 4-2: (a) CAD of the employed experimental test bench fixed to the custom-made servo-hydraulic MTS BIONIX II machine (actual specimen not shown) (b) Tool employed for linear Insertion, Relaxation and Extraction resistance experiments superimposed with reference cartesian system adopted in this article (c) Tool employed for lateral resistance experiments (d) Tool employed for nerve tension and relaxation experiments

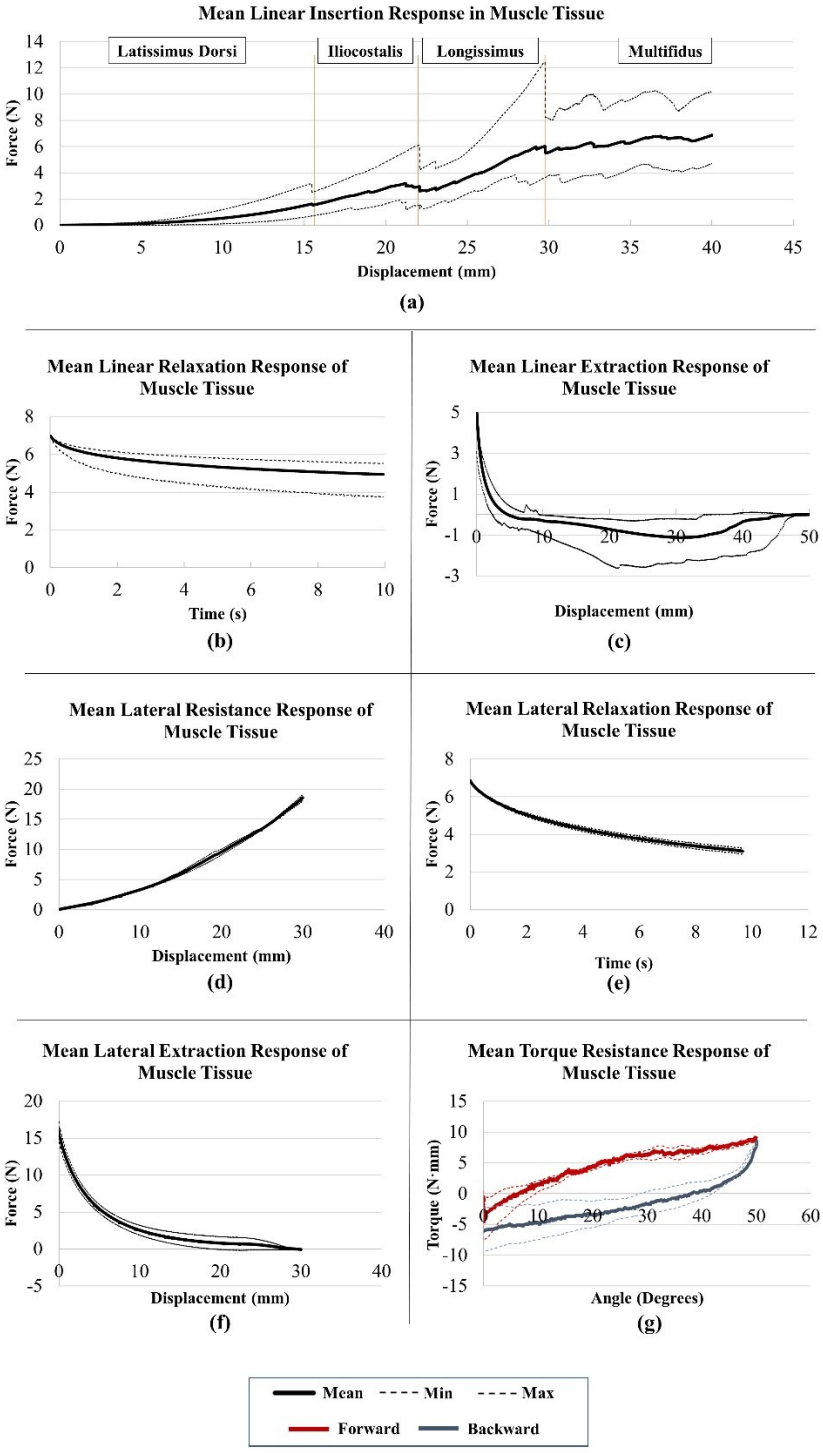

Figure 4-3: Chart depicting (a) mean linear insertion response of muscle with division showing the skeletal muscle punctured (b) mean linear relaxation response of muscle (c) mean linear extraction response of muscle (d) mean lateral resistance response of muscle at 40mm tool insertion within the muscle (e) mean lateral relaxation response of muscle (f) mean lateral extraction response of the muscle (g) mean torque response of tool within the muscle set

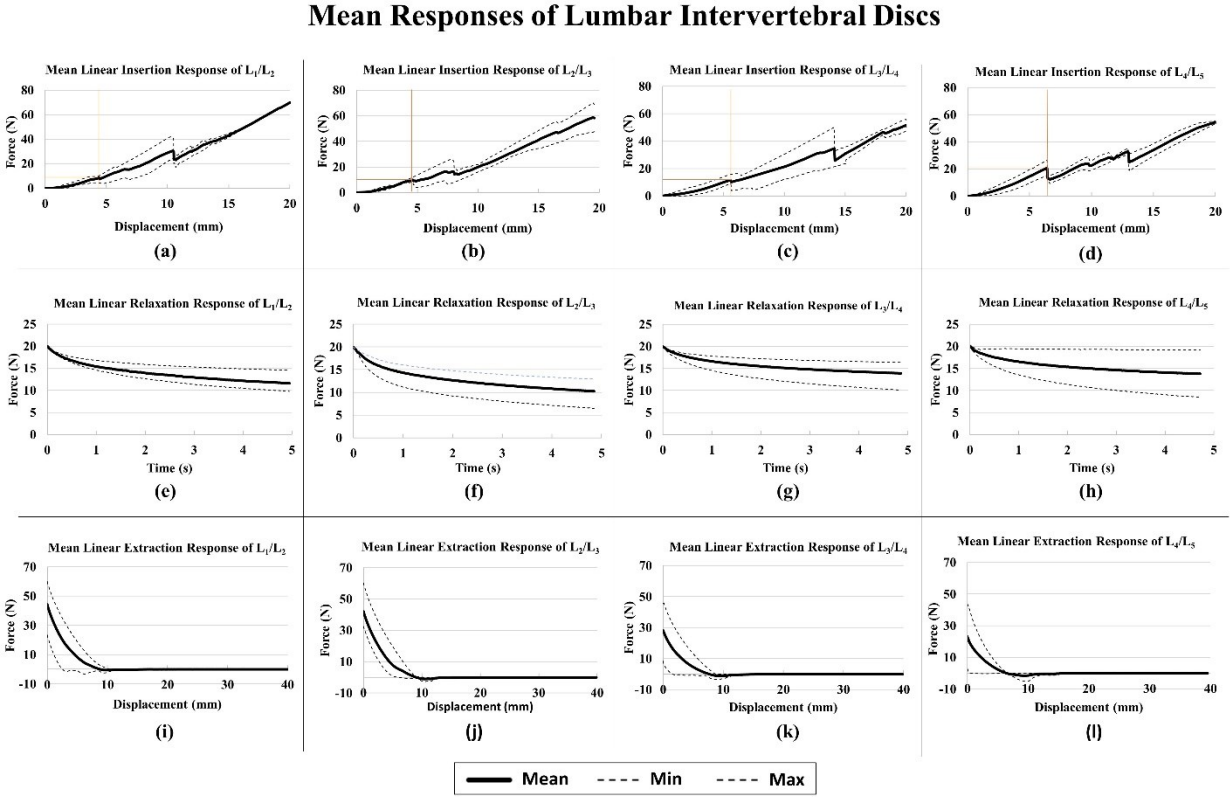

Figure 4-4: Chart depicting (a) mean linear insertion response of L_1/L_2 intervertebral disc (b) mean linear insertion response of L_2/L_3 intervertebral disc (c) mean linear insertion response of L_3/L_4 intervertebral disc (d) mean linear insertion response of L_4/L_5 intervertebral disc (e) mean linear relaxation response of L_1/L_2 (f) mean linear relaxation response of L_2/L_3 (g) mean linear relaxation response of L_3/L_4 (h) mean linear relaxation response of L_4/L_5 (i) mean linear extraction response of L_1/L_2 (j) mean linear extraction response of L_2/L_3 (k) mean linear extraction response of L_3/L_4 (l) mean linear extraction response of L_4/L_5

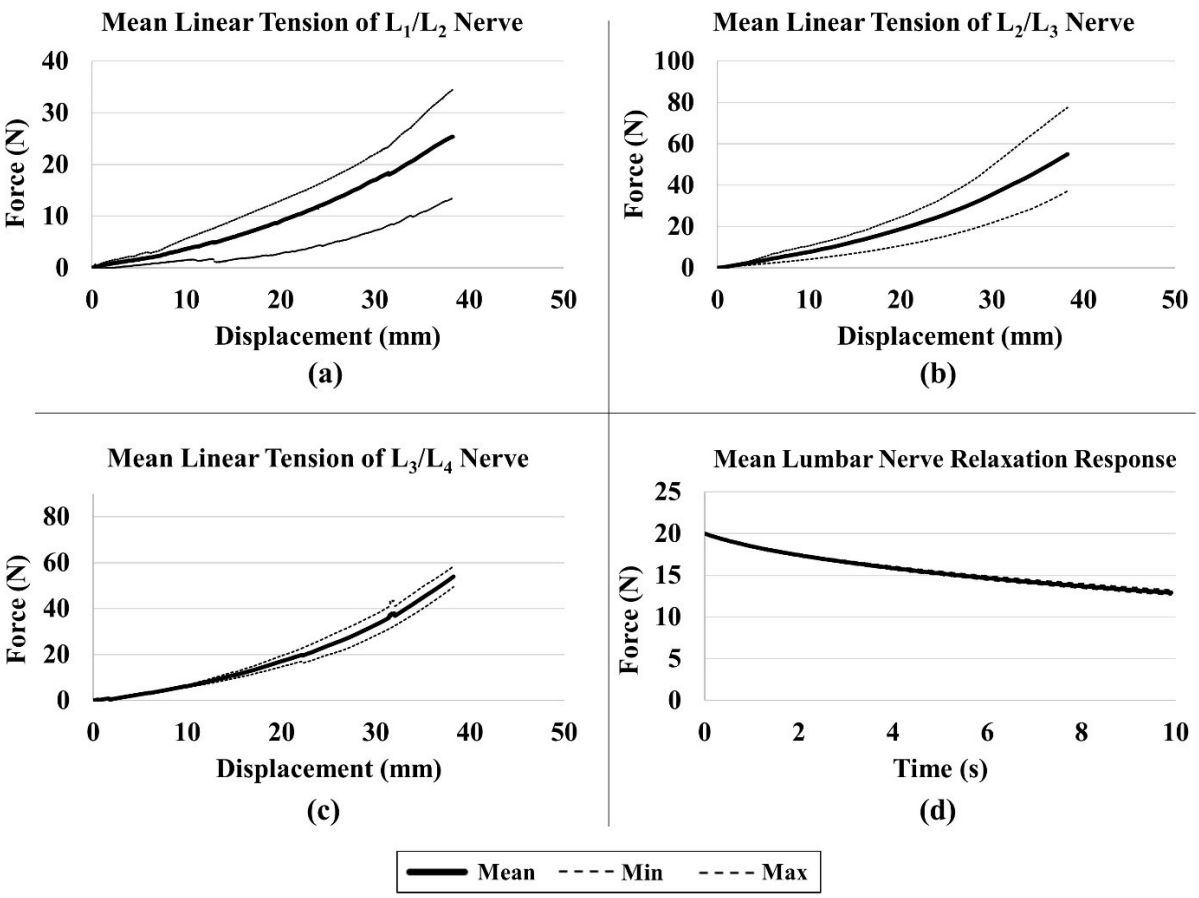

Figure 4-5: Chart depicting (a) mean tensioning response of L_1/L_2 Nerve (b) mean Tensioning response of L_2/L_3 Nerve (c) mean tensioning response of L_3/L_4 Nerve (d) mean tensioning response of L_1/L_2 Nerve

4.3. ADDITIONAL STUDIES RELATED TO ARTICLE 2

4.3.1. NOTES ON ARTICLE 2

The following section serves to further clarify the experimental studies conducted in Article 2. In specific, this includes a further discussion on the experimental setup and procedure, the influence of utilizing cadaveric specimens in comparison to live specimens and the statistical analysis conducted.

Within the pipeline of the development of the access gaining VR module, the experimental tasks served as the baseline required to establish the force-feedback. This played a crucial role in the immersive quality of the simulator. Specifically, the bio-fidelity of the results conceived may impact the surgeon's decisions while running the simulation. More importantly,

this may lead to negative learning, whereby the surgeon's perception of the tissue contacted may be altered [455]. During the access gaining stage of the OLLIF surgery, the surgeon utilizes several tools including guidewires, scalpels, a probe, 3 dilators and an access port (listed in order of surgical tasks) as described further in Chapter 7. Given that the probe was the only tool designated as suitable for the simulation (explained further in detail in Chapter 7), it was the only tool accounted for within the experiments. However, given the complex nature of the setup, variations of the tool were made (as shown in Figure 4–2 (b), (c) and (d)). These variations were made to enable access to the tissue without greatly modifying the cadavers. In specific, the original surgical probe (Figure 4–2 (b)) was cut to 70 mm and fit to the force transducer as described under methods in section 4.2. To confirm the straight alignment of the tool with the tensile/compression testing machine's vertical motion, the entire movable crosshead was descended as shown in Figure. 4–2(a). The vertical alignment of the tool was, then, confirmed using a leveler. The technique was utilized for all three tools. However, the main challenge was to align the tool with the insertion point specified on the skin of the cadaver. The alignment was required to properly adjust the orientation of the cadaver to be pointed towards the disc as the tool punctured the muscle. Hence, the onsite neurosurgeon who aided with the cadaveric preparation utilized industrial sewing needles of a diameter ~1.8 mm (8847K61, McMaster Carr Supply Company, USA). In specific, after the entire skin and fascial layer were excised, the location of the intervertebral disc based on Anterior-Posterior fluoroscopic imagery was estimated. The needles were then pushed posterolaterally about 20 mm from the spinous process through the muscle until the neurosurgeon confirmed that the disc was reached. Additional markings were drawn transversely along the muscle from the position of the needles. These trajectories were then used for alignment when the cadaver was tested. In other words, the cadaver was oriented until the probe connected to the transducer was parallel to the needles. Even though the diameter of the needle is 2.2 times the diameter of the probe, additional precautions were taken to avoid the effect that the needle, and its corresponding puncture, may have on the punctures of the probe. Hence, the cadaver was oriented further, at an angle of 65° (to approximate the insertion point close to the OLLIF surgery) and moved laterally by 12 cm [277]. This would in turn ensure that the position of the probe when inserted would have no detrimental effects from the needle puncture. Upon the completion of the experiments related to the muscle layers, the back muscles were excavated as described in section 4.2 and the discs

were directly exposed. This permitted conducting the experiments on the disc and nerve tissue directly.

Tool 1 (as described in Figure 4–2(b)) was utilized for the linear insertion, relaxation, extraction and torsion experiments of the muscle and disc tissue. However, given the one-dimensional motion of the tensile testing machine, lateral movements were not possible using Tool 1. Thus, a lateral tool was constructed by welding a replica of Tool 1 (consisting of the same material) to an M6 threaded eye screw. Hence, the cadaver was oriented at 90° and the depth of Tool 2 within the cadaver was noted (72 mm). This value would later be used to compute the lateral forces within the algorithm described in section 5.2. It is worthy to note that the excavation of the muscles was conducted such that a 90° angle would be formed at the sides of the hole. Hence, no alignment was necessary at this point. Finally, Tool 3 which was basically an M6 threaded eye hook screw (shown in Figure 4–2(d)), was utilized to tension the nerve. In specific, Tool 3 was mounted to the force transducer and descended to the point where the nerve could be lightly slipped inside the hook. For all the above experiments, the cadaver was tightly fixed to the constructed benchtop (described in section 4.2 and depicted in Figure 4–2(a)). Orientations were measured using a digital protractor and the angle formed between surface of the benchtop and the needle.

The entire set of experiments were displacement controlled. Linear Insertion, Linear Relaxation, Linear Extraction and Torsion resistance employed Tool 1 for all the tests. Lateral Insertion and Lateral Relaxation tests employed Tool 2. Finally, Nerve Tensioning and Nerve Relaxation tests employed Tool 3. The speed of displacement and data acquisition rate prescribed for each test were described in Table 4.2. The speeds designated for the experiments were estimated based on data recorded from two neurosurgeons who conducted the surgery through the simulation while using the haptic device. In specific, the surgeons were asked to move the probe in the same speed they would during a surgery within the physical interface. To provide further confidence, a constant force of 2 N was sustained during the simulation. Each surgeon conducted 3 trial runs and the spatial and temporal data of the tool while connected to the haptic arm was recorded. Hence, the mean insertion velocity value was 2.5 mm/s (± 2.0 mm/s) for linear insertion through the muscle and 2 mm/s (± 1.0 mm/s) disc. As such, the variation of the speed was accounted for in the linear tests. However, lateral tests proved to be more challenging given the risk Tool 2 may have if moments were exerted on the transducer.

While the mean value of the speed for the lateral tasks was recorded to be 2 mm/s (± 1.5 mm/s), the minimum value used was within the reported range. Linear insertion tests were prescribed with a downward motion of Tool 1 (in the compression direction) into the muscle layers and disc. During relaxation tests, the tool was fixed in place while it was embedded within the muscular layer and disc and the force decrease was recorded. Moreover, during extraction tests, the tool was moved upwards from within the tissue. Torsion tests rotated the tool clockwise from its initial position to 50° then reverted back to -50° anti-clockwise at a speed of 2°/s. Only Tool 1 was employed for the torsion test. In the Lateral resistance test, the tool descended pushing into the muscle and was fixed in space to measure the lateral relaxation. Finally, the nerve tests employed Tool 3 to tension the nerve as it ascended then paused to record the nerve relaxation. Furthermore, Tool 1 was utilized for Speed, Angle, Depth and Fascia effects. The results of these tests were reported in section 4.2.

The linear and torsional transducers were a 100 N axial load cell whose resolution is 0.02 N and a 25 N·m torque transducer with a resolution of 0.005 N·m as mentioned previously in section 4.2. These transducers were chosen to record values at an acceptable resolution and meet the expected range of forces. However, it is worth mentioning that the transducers remain limited according to several factors. For instance, the cabling length, calibration, electric noise and environmental conditions play a significant role in the precision of the data. Hence, the load cells were calibrated one week prior to the experiments. The maximum reported error during the calibration process was reported to be 0.29% and the accuracy of each of the two load cells was 0.1% of the full-scale output. Hence, while the data in Article 2 was reported to a higher precision, it is necessary to note that is optimistic. As such, it is necessary to note that the data is reliable to only one significant figure after the decimal with an uncertainty of ±0.29%.

A total number of 173 tests were conducted out of which 140 were deemed adequate results. In specific, 24 tests were considered trials conducted at the T_{12}/L_1 level. Particularly, the tests served to ensure that the cadaver and tool were properly fixed. Hence, the remaining 9 tests were deemed unsuccessful because either the tool was not properly fixed, alignment between the tool and cadaver was not correct or the cadaver moved during the test. Within the scope of this study, the spinal level L_1/L_2 designates the muscle layers between the L_1 and L_2 vertebrae and the corresponding L_1/L_2 disc. While the T_{12}/L_1 spinal level was reserved for trials, the 4 spinal levels between L_1/L_5 were utilized for the tests with particular attention given to the L_4/L_5

vertebra. This was the result of adopting the L_4/L_5 spinal level for the VR simulator. In other words, the reported tests in Table 4.2, namely Tests II – VII, were conducted at the L_4/L_5 level. Test VIII was conducted on the nerve roots of the L_1/L_4 spinal levels. This was due to the restriction of access to the L_4/L_5 nerve roots as a result of the iliac crest. Test I was conducted at each level along the L_1/L_5 spinal levels. As a result, a total of 8 intervertebral discs (L_1/L_2, L_2/L_3, L_3/L_4, L_4/L_5 for each of the 2 cadavers) and 4 paraspinal muscle sets (Left and Right for each of the 2 cadavers) were employed. Each intervertebral disc was tested twice (i.e. Left and Right) for the insertion, relaxation and extraction tasks in Test I for each cadaver. This achieved a total of 48 tests. Similarly, the muscular sets were tested twice (i.e. Left and Right) for each spinal level (i.e. L_1/L_5) for each of the three tasks in Test I per cadavers to total 48 tests. To study the influence of speed (Test II), angle of attack (Test III) and depth (Test IV) on the output, the paired two-samples Wilcoxon test was utilized. In specific, the test was utilized to compare two groups of samples and the statistical software R was employed. This test was chosen given that the number of tests were relatively small. Specifically, one test for each displacement speed, one test for each insertion angle and one test for each depth was conducted within the same cadaver on the same spinal level. The independent variables for Test II were defined as the speed each compared to the baseline value. In specific, the independent variables were 0.5 mm/s and 2.5 mm/s for the first test and 0.5 mm/s and 4.5 mm/s for the second test. Similarly, the independent variables were the variation of the angle of attack 65° and 85° for Test III. Finally, the independent variables were the variation of the displacement 40 mm and 10 mm for Test IV. The linear force output was considered the dependent variable. The resulting output for statistical significance was reported in section 4.2. It is worthy to note that Figure 4–3(a) specifies the tissue related to the different peaks on the graph. However, it is necessary to note that the following labelling was informally established based on the description of the on-site surgeon assisting with the cadaveric operation. Hence, it is important to note that the following depiction serves as clinical guidance to explain the tissue punctured and should not be taken as a commitment between the force peaks and the tissue displaced. This is specifically the case given that the muscle deforms in addition to being punctured. This was evident given the recorded difference between the actual displacement of the tool and the depth of puncturing within the muscle.

It is necessary to note the limitations of employing cadavers to extract data that would later be used for surgical simulators. The cadavers were freshly frozen and stored at a temperature of –20°C then utilized after a single freeze/thaw cycle at a thawing temperature of 2°C. This was conducted to avoid the adverse effects of repeated freeze–thaw cycles on human tissue and based on previously reported recommendations [456]. Moreover, a single freeze–thaw cycle has been previously shown to have minimal detrimental effects on the IVD's creep and stiffness [457]. The tests were conducted on the cadavers five months post-mortem. However, the cadavers were frozen following the rigor mortis stage (i.e. post–rigor) which was ~24 hours following the reported death time and handled with minimal motion. Van Ee et al. investigated the effect of post-mortem time and freezing storage on the muscle properties. They observed that a post–rigor freeze–thaw cycle was found to sustain more stable results which may affect the stress–strain response, no–load strain and modulus if compared to non-frozen muscle. This was not the case with specimens frozen 1–hour post-mortem as freezing the specimen delayed the rigor process increasing the muscle stiffness before decaying. This was conducted as such to ensure that the dynamic changes that occur post–mortem would stabilize. The process of freezing, thawing and exposure time prior to testing were all kept constant between the specimens. As such, this would result with a higher repeatability and provide a more reliable estimation when comparing cadaveric and live properties. Nevertheless, Leitschuh et al. found that the failure load decreased by 37% and the failure strain decreased by 44% following freezing. However, Gottsauner-Wolf et al. reported a reduction of the failure force by 58.8% with no significant change in the displacement to failure. Van Ee et al. observed a 53% decrease in failure stress in post–rigor frozen tests. However, the stress–strain response, no–load strain and modulus were not found to significantly affect the stress–strain response. Hence, it is necessary to account for the latter variations for a more realistic simulation model. Moreover, for more accurate computation of the force feedback, more experiments can be conducted to estimate the hysteresis and creep of the various tissue. Furthermore, a fracture toughness test may be conducted to better estimate the puncturing event and its corresponding drop in force in the force-displacement curve. However, for the purpose of this thesis mainly aiming to create a simulator that may mitigate the utilization of cadavers, it was deemed sufficient to directly utilize the cadaveric experimental responses.

4.3.2. PORCINE EXPERIMENTS

Prior to conducting the experiments described in Chapter 4.2, a porcine sample was utilized to conduct mock experiments to ensure that the benchtop model, tools and tensile testing machine all worked properly. Hence, this section reports on the output of the porcine experiments and compares it with that of the human cadaveric samples achieved. In specific, there were no variations to the hardware utilized except the sample itself. Figure 4–6 depicts the experimental setup. The specimen chosen was extracted from the loin section with the vertebral set incorporated to relate it to the cadaveric specimens used. Moreover, the skin and underlying fascia were incised before the experimental runs and rotated to provide a trajectory that punctures towards the intervertebral disc.

Figure 4-6: Porcine Sample Experimental Setup

The experimental protocols followed a direct puncturing within the muscle tissues at velocities of 3 mm/s, 5 mm/s, 7 mm/s and 8 mm/s. The stopping criteria defined was based on

reaching a displacement of 70 mm. Figure 4–7 plots the force-displacement output resulting from the experiments for each of the two velocities. The graph shows that the experimental runs conducted at different speeds did not show any specific pattern in the output. This observation is in line with the output achieved from the experiments conducted on the cadaveric specimens, in Chapter 4.2.

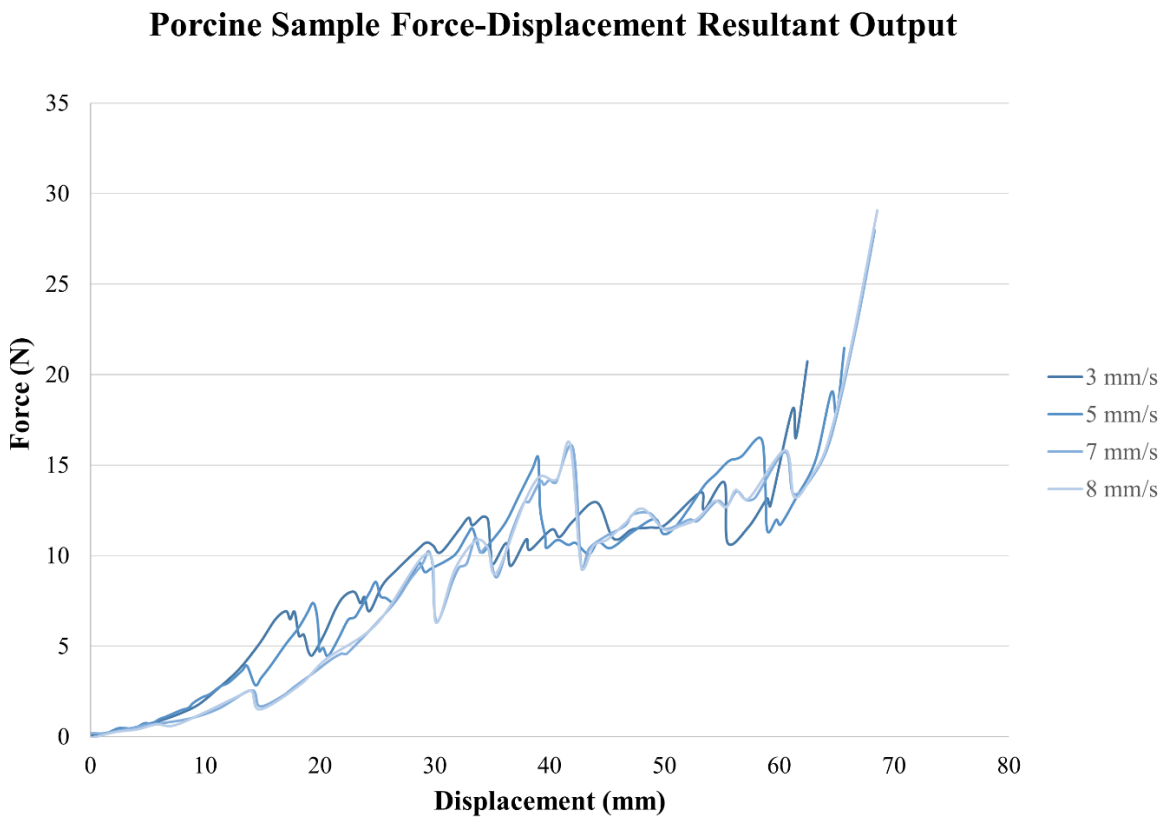

Figure 4-7: Resultant Force-Displacement output of porcine sample at different velocities

In comparison to the cadaveric experimentation conducted in Chapter 4.2, the resulting output at the same speed (3 mm/s) is depicted in Figure 4–8. Evidently, the output forces of the porcine sample exceed that of the mean cadaveric output over the entire range. Interestingly, the initial continuous portion of the porcine sample output continues well beyond the first puncture of the cadaveric sample. This may likely be the result of the high adipose layer observed within the paraspinal region in comparison to the cadavers.

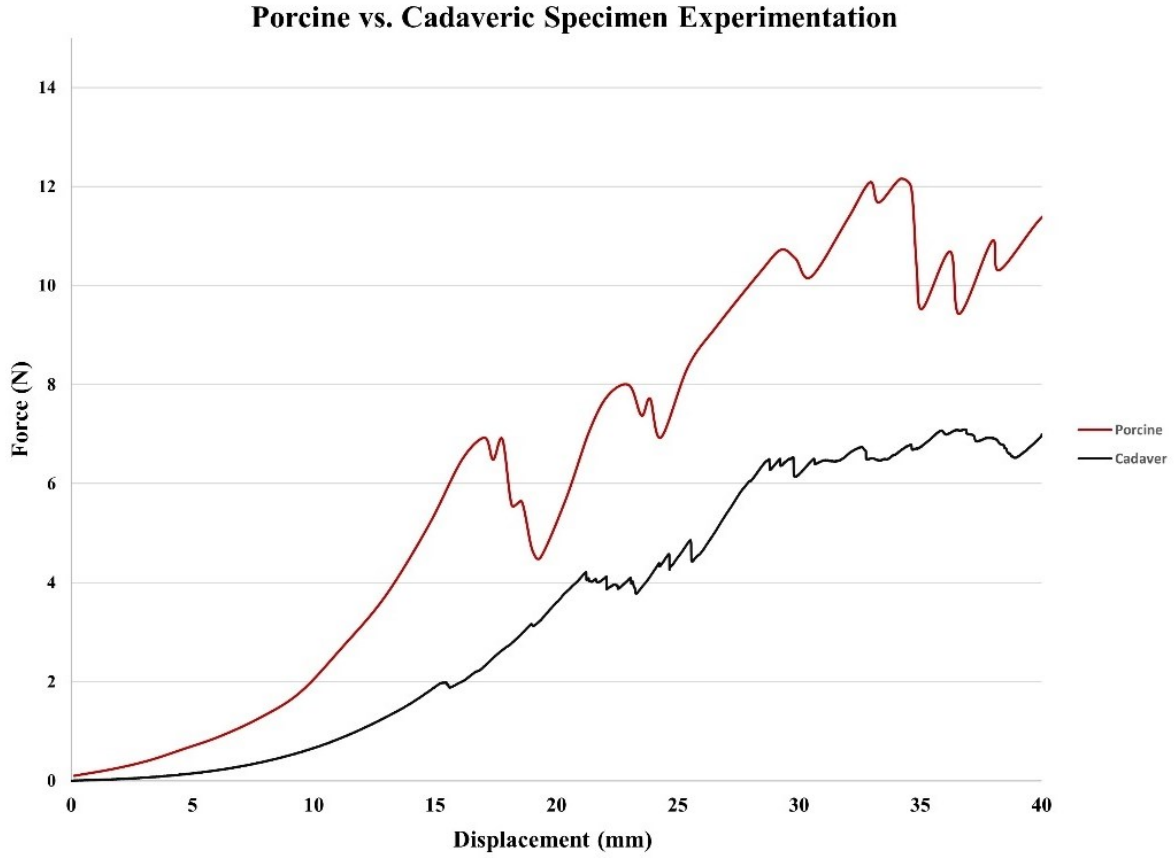

Figure 4-8: Chart depicting the comparison between the mean output of the force-displacement curves from the cadaver and the output of the porcine specimen

4.3.3. PHYSICAL INTERFACE EXPERIMENTS

To quantify the force output from the tool interaction with the VR simulator physical interface used, the top layer of the physical model was placed on the benchtop table but kept in its normal state as it would be present in the simulator. These experiments were necessary to identify the additional forces that would inevitably result from the friction that arises as the tool inserts into the layer. As shown in Figure 4–9, the incisions applied onto the benchtop were numbered from 1 to 7. As such, the protocol entailed the linear insertion of the tool through the incisions. The incisions were conducted as follows:

1. Incision 1: a 50 mm single slit applied by the manufacturer;
2. Incision 2: a 15 mm single slit applied by the manufacturer;
3. Incision 3: a 15 mm single slit applied by the manufacturer slightly degraded;

4. Incision 4: a 15 mm single slit applied by the manufacturer but has been extensively utilized prior to the experiment such that a pedicle cylinder was passed through it;
5. Incision 5: a 10 mm cross slit applied;
6. Incision 6: a 10 mm cross slit applied and extensively utilized;
7. Incision 7: a 30 mm cross slit applied;
8. Incision 8: no incision (Not shown in Figure 4–9)

Figure 4-9: Experimental setup of physical interface showing the order of the incisions (1–7)

Incisions 1–3 described the force feedback when inserting the tool through slits that have been cut by the manufacturer. In specific, the slits were created by a cryogenic process to ensure a clean cut without artifacts. Incision 4 was further incised by the manufacturer, however, its high prior usage for demonstrations has resulted with wearing of the slit edges. Hence, this slit represented the forces experienced after considerable usage of the simulator. Incision 5–7 denoted the output resulting from using a cross slit instead of a single slit. In specific, incision 5 described the forces experienced without much degradation of the material. Incision 6 represented the forces experienced after a great number of uses of the simulator. Incision 7 represented the output conceived from a larger slit and incision 8 denoted the forces experienced from a pure puncture into the layer without any incision.

The main objective of this study was to account for the forces that would inevitably be experienced when using the probe tool to penetrate through the muscle. The output of this experiment ultimately worked as the deciding factor to account for these additional forces by reducing the haptic forces conceived from the cadaveric experiments in Chapter 4.2. This would be resolved by subtracting the cadaveric forces by a fixed value should the output of this experiment be a constant force. Otherwise, the force effects from the physical interface would be omitted by increasing the slit sizes.

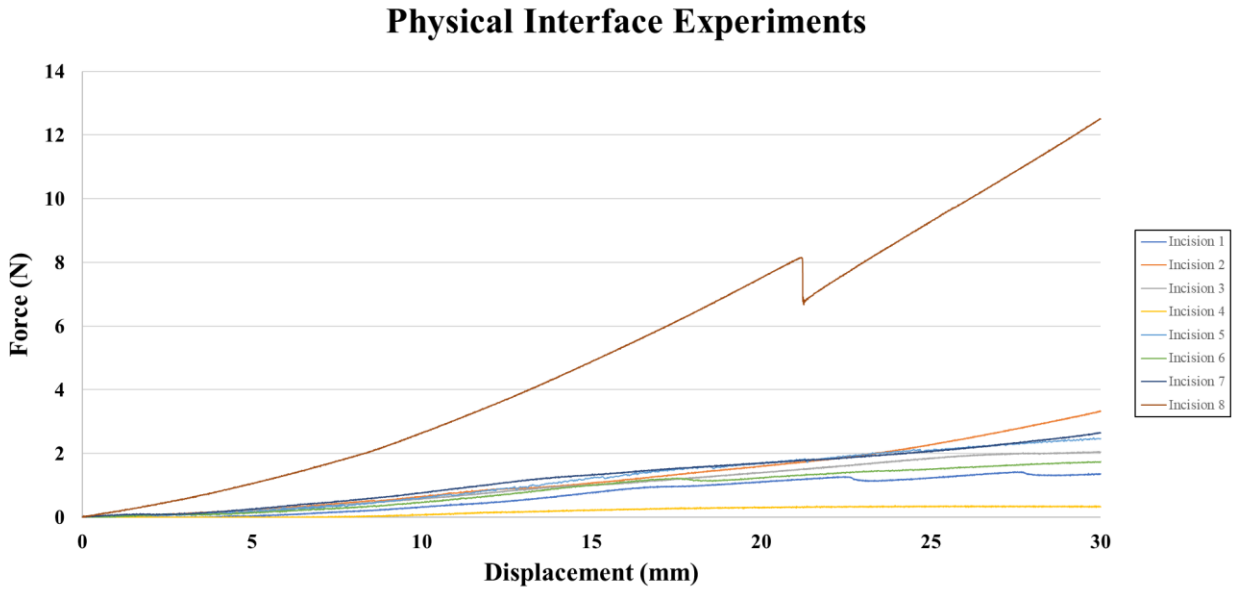

Figure 4-10: Physical Interface Experimental Results

The output results were scoped to a displacement of 30 mm for consistency between the experiments. The results show that incision 8 resulted with the largest force response with a positively increasing trend reaching 12 N at a displacement of 30 mm with a single puncture that marked the puncturing of the topmost layer before continuing (linearized stiffness K = 0.4171 N/mm). Incision 7 marked the lowest value in the clean non-degenerated slits (K = 0.0896 N/mm) followed by Incision 5 (K = 0.0927 N/mm) and Incision 2 (K = 0.1046 N/mm). However, Incision 4 achieved the lowest force output within the degenerated slits (K = 0.0155 N/mm) followed by Incision 6 (K = 0.0657 N/mm), then Incision 3 (K = 0.077 N/mm). Finally, Incision 1 recorded a lower value than Incision 7 (K = 0.0577 N/mm) (Figure 4–10).

The output results showed that none of the curves showed a constant force response. This was mostly highlighted with the high variation in force response output due to the wear of the material. Instead, the force magnitude should be reduced to ensure the minimal addition of such forces while maintaining a visually accepted slit for MIS procedures. It is evident that the 50 mm incision slit conceived by the manufacturer recorded the least force intervention. However, a large sized incision reduces the reality of an MI procedure. Thus, incisions of cross forms, at a length of 30 mm, sufficed to serve the purpose.

5

STUDY OF THE DEVELOPMENT OF THE FORCE FEEDBACK ALGORITHM

5.1. FRAMEWORK OF THIRD ARTICLE

The objective of this study was to integrate the force responses, acquired from the cadaveric experiments in Chapter 4, to develop the haptic interface of the VR simulator. The extracted data was initially adjusted to fit mathematical formulations suitable for haptic integration. Subsequently, an algorithm that directly implements the empirical data to conceive a proper time-dependent behavior was developed. The haptic algorithm was programmed such that it runs independently of the visual rendering during runtime. This technique leveraged the fact that no visuals of tool-tissue interaction may be present in accordance with the steps of the Access Gaining module of the MI spinal fusion procedure adopted within this thesis. In particular, the probe punctures through the muscle tissue, prior to a 4–5 cm incision of the skin and the underlying fascia. This is conceived to reach the intervertebral disc which denotes the end of the Access Gaining stage. The haptic device and connected probe tool were calibrated with the physical and virtual interfaces included in the VR system. While the algorithm was developed specifically for this procedure, it would be possible to be employed for any surgical procedure that incorporates a tool-tissue interaction without the need of visual rendering. As such, the force response was validated using a case-study. Finally, a study to integrate the nerve tissue stiffness for future integration was presented. The outcome of this chapter marked the completion of objective 5 and hypothesis 3 as presented in the manuscript entitled “Haptic integration of data-driven forces required to gain access using a probe for minimally invasive spine surgery via cadaveric-based experiments towards use in surgical simulators” for which the contribution of the first author is considered to be 85%. This manuscript was submitted to the *Journal of Computational Science* on May 25, 2020.

5.2. ARTICLE 3: HAPTIC INTEGRATION OF DATA-DRIVEN FORCES REQUIRED TO GAIN ACCESS USING A PROBE FOR MINIMALLY INVASIVE SPINE SURGERY VIA CADAVERIC-BASED EXPERIMENTS TOWARDS USE IN SURGICAL SIMULATORS

Khaled El-Monajjed, M.Eng., Jr.Eng.[1]; Mark Driscoll, Ph.D., P. Eng.[1]

[1]*Musculoskeletal Biomechanics Research Lab, Department of Mechanical Engineering, McGill University, Montreal, Quebec, Canada*

Address for notification, correspondence and reprints:

Mark Driscoll, Ph.D., P.Eng., Assistant Professor

Associate Member, Biomedical Engineering

Canada NSERC Chair Design Engineering for Interdisciplinary Innovation of Medical Technologies

Department of Mechanical Engineering

817 Sherbrooke St. West

Montreal, QC, H3A 0C3 Canada

T: +1 (514) 398 - 6299

F: +1 (514) 398 – 7365

E-Mail: Mark.Driscoll@mcgill.ca

5.2.1. ABSTRACT

The employment of force-feedback haptic devices has proved to have a considerable effect on the user experience of surgical simulators but has faced several challenges given the high computational cost and accuracy required. In minimally invasive surgeries, the internal tissue deformation cannot be visually perceived which presents an opportunity to render haptic forces on an independent thread. Hence, this paper proposes an efficient algorithm designed specifically to exploit this opportunity while employing cadaveric experimental data. This was previously achieved via conducting a set of tests designed specifically to obtain an exhaustive set of *in-vivo* data to simulate the tool-tissue interaction.

Keywords: Medical Simulator; Soft Tissue Realtime Simulation; Spinal Fusion Surgery; Haptic Algorithm

5.2.2. INTRODUCTION

The objectives and techniques underlying surgical training are continuously redefined as a result of branching specializations in surgery, adopting advanced technologies such as minimally invasive techniques and meeting the demanding needs of various economic factors [1]. While traditional training strategies concentrate on reducing surgical errors, educators have emphasized that consequential slow learning curves towards competency through trial-and-error should no longer be accepted [2]. With the realization that training methods may be improved to increase patient safety [3], educational systems have begun adopting strategies tailored towards more structured approaches aimed at achieving precise learning outcomes [4]. The motive to achieve inflated learning curve rates is, further, reinforced with the observed positive correlation between the surgeon's experience and the surgical outcome. Vickers et al. conducted a retrospective study to examine the association between surgeon's experience and surgical outcomes by examining post-operative cancer recurrence, in real laparoscopic radical prostatectomy procedures [5]. They noticed a reduction in recurrent cases for surgeons that have performed between 750 and 10,250 procedures. This observation has been previously confirmed by numerous studies that have investigated the interrelationship between a surgeon's experience and the success rates of post-surgical results [6–9].

There is growing evidence suggesting that simulators play a valuable role in acquiring and enhancing surgical skills [10–13]. This devises an incentive for potentially integrating validated medical simulators into formal surgical education. Evidentially, simulators have previously demonstrated reliability in effectively distinguishing between novice and advanced surgeons [1]. In perspective, education has driven the development of expertise-based simulators whereby expert performance is designated as the benchmark [14]. In general, the employment of surgical training modules have been shown to be most effective with the incorporation of goal-directed tasks associated with the opportunity to provide feedback based on performance [15], contextual interference during the simulation and inducing unpredictable environments [16].

Analogous to graphical rendering, haptic feedback systems have been developed to virtually simulate the tactile and kinesthetic "feel" of an object in real-time to convey information to the user [17]. Its applications have met considerable relevancy in the virtual reality medical training simulator field given the advantages simulators offer [18] as researchers have asserted that effective training requires the inclusion of haptic functioning [19–21]. The

current state of the art of haptic devices in medical training simulators is often the most neglected part of the system [22]. This becomes problematic when haptic feedback plays a vital role in enhancing surgical training. For example, in cancer biopsy surgeries, surgical simulators should effectively render accurate force feedback differentials for surgeons to train on identifying cancerous tumors which are normally characterized by a "stiffer" feeling in different circumstances [23]. Advanced frameworks that adopt real-time finite element (FE) techniques, such as the Total Lagrangian explicit dynamic (TLED) formulation [24], can compute forces based on non-linear tissue deformation that results from tool-tissue contacts [25–27]. While these methods greatly serve the accuracy of deformation and, hence, the visual perception, they can be too computationally expensive or too slow to serve haptic-specific frame rates. Specifically, graphical rendering in the range of 30–60 Hz is considered acceptable for the human visual perception system while haptic rendering must run at a minimum of 1 kHz for an acceptable experience [28]. This requirement has been suggested to even be underestimated as Choi et al. observed that a 5–10 kHz haptic rendering rate is required for a sensible experience [29]. Hence, FE methods in conjunction with linear elasticity were suggested to compensate for the computational speed permitting the integration of haptic feedback into the simulator, such as the co-rotational method for example [30]. This is achieved by updating a pre-inverted stiffness matrix [31]. However, this algorithm suffers from a small-strain limitation which may not be suitable with the large-deforming time-dependent soft tissues and has been observed to lead to incorrect results when rotations are applied. Other methods have been proposed which utilize pre-computational techniques but for geometrically non-linear deformations [32, 33]. However, these methods remain burdensome with the requirement of the presence of a collision-model and numerical force computations albeit the elastic assumption does not permit non-linear deformation.

In the case of surgical operation modules whereby physicians depend solely on touch feedback due to visual inaccessibility, no graphical rendering is required when developing its corresponding simulator for training. In needle insertion applications, such as epidural anesthetic administration whereby the needle is applied posteriorly through the skin to reach the epidural space, no internal visual feedback is available to the physician [34]. In such a case, adding an internal visual view may in fact reverse the training effect leading to a false sense of security, also known as negative training [35], which may ultimately lead to harmful effects. Similarly, in

Minimally Invasive (MI) spinal fusion surgeries, surgeons rely on the somatosensory feedback, especially in early stages of the surgery whereby no visual feedback is possible, to identify anatomical landmarks that enables them to reach the desired destination within the soft and hard tissue complex. This presents an opportunity to develop haptic forces on an independent thread from the visual system specifically when assisted by a benchtop model placed within the haptic system's workspace to provide further realism to the user's experience.

In this work, an algorithm was developed such that it utilizes data conceived from cadaveric experimentation to render realistic forces of puncturing events. This is tailored for a multi-purpose probe used in the access gaining module of Minimally Invasive (MI) spinal lumbar interbody fusion surgery but may be adopted for any surgery that utilizes the same tool. The implemented algorithm stands alone of a serial communication with a virtual model for a 3 degree-of-freedom force point-based haptic device capable of rendering force feedback without a computationally heavy collision-detection method using primitive geometrical objects. Initially, the designed experiments that achieved force-displacement and force-time output curves are described. This is followed by an explanation of the curve fitting techniques adopted for cadaveric force extraction. Finally, the proposed algorithm suitable for rendering at high frame rates and a case study specific to its implementation are illustrated.

5.2.3. METHODS

The haptic framework was developed such that it can exactly recreate any set of curve-fitted forces extracted in the form of force-displacement and force-time responses from cadaveric experiments using data processed within the haptic thread solely. As such, cadaveric experiments were designed to replicate the various actions possibly exercised by a surgeon using a multi-purpose dilator during an actual minimally invasive surgery with the aim that these results could ultimately be integrated into a haptic model for simulator training.

Cadaveric Experimentation and Force Extraction

A series of experiments were conducted on two male fresh frozen cadavers. Cadaver 1 (i.e. C-01) was aged 63 and had no underlying spinal-related diseases while cadaver 2 (C-02) had a degenerated L4-L5 disc. The appropriate ethical approvals were obtained from the local research ethics committee. The experiments were tailored to provide an exhaustive characterization of the forces corresponding to the possible mechanical tasks achieved by the

probe handled by surgeons. In the spinal fusion surgery, the probe would be used to puncture through the different muscle layers as it is inserted through a single 10-15 mm incision applied on the skin and posterior layer of the Thoracolumbar Fascia (TLF) to achieve a trajectory spanning from the outer skin to the desired Intervertebral Disc (IVD). Along this route, the probe interacts and punctures the muscle layers to finally reach the IVD. Hence, the two soft tissues highlighted in this study include the spinal posterior musculature and the intervertebral discs.

A custom-made benchtop, designed to withstand and fix the cadaveric torso's orientation, was developed and employed during the experiments conducted. In specific, a three-step protocol was devised such that the tool displaced at a certain depth, followed by a 10-second pause then completed by a full extraction of the tool from the torso. This protocol was adopted for both the muscle and IVD tissues tested. The desired responses aimed for were the (1) linear resistance response of the tool as it penetrates through the muscle layer and (2) the lateral resistance achieved while the tool was placed inside the tissue for both designated tissues. The designated stop conditions were set for the linear insertion of the tool at a depth of 40 mm and for the lateral displacement at a depth of 30 mm within the muscular layers. An intact probe with the original tip geometry was used for linear insertion (Tool 1) and a shortened version of Tool 1 was welded in a perpendicular formation to a screw fit to the size of the load-cell adopted to conceive the lateral force resistance to be recorded along the repositioned cadaver with a full tool insertion within the hole. In the case of the IVD, the linear insertion experiment was only conducted and set at a depth of 20 mm. In addition to the basic experiments conducted, a series of complementary tests were conducted to test the effect of depth and speed on the force outputs. The experiments were all conducted on a custom-made servo-hydraulic tension/compression testing machine (MTS 858 BIONIX II, MTS Systems Corporation, U.S.A) equipped with a 100 N axial load cell whose resolution is 0.02 N. Fig. 1 depicts the assembly described previously including the geometrical description of Tool 1 tip.

Following the extraction of the force-displacement and force-time, the data was post-processed to attain an output that can be directly embedded into the haptic system. For instance, mean values and their corresponding standard deviations were plotted across the two cadavers to extract a baseline that is representative of the data. For linear insertion data, puncturing events took place such that force values drop suddenly to lower values. In that case, the force curves that consisted of sharp drops, as a result of puncturing, were subdivided. For each puncture force

drop, the local minima and local maxima were identified within the curve. A search algorithm was, then, scripted and implemented to identify the global maxima and minima. These global values established the displacement boundaries whereby each defines a specific layer. The force curves were then formulated as a piece-wise function described as:

$$F(d) = \begin{cases} F_0(d) & a_0 < d < a_n \\ \vdots & \\ F_n(d) & a_n \leq d < a_{n+1} \end{cases}$$

Equation 3: Piecewise formulation of Force-Displacement curves for Insertion puncture haptic rendering

Such that ***F*** denotes the force magnitude, ***d*** denotes the displacement and ***a*** denotes the displacement boundaries and ***n*** denotes the number of subdivisions.

Consequently, the force-displacement and force-time output were fitted using a 2nd order polynomial described as:

$$F(s) = as^2 + bs + c$$

Equation 4: 2nd Order Formulation used for curve fitting

Such that F denotes the force magnitude, s is replaced by d to denote the displacement in the case of force-displacement and replaced by t to denote time in the case of force-time, and the a, b and c coefficients are specific to the derived fitted constants.

Benchtop Setup

The benchtop model was constructed using silicon-based material that followed a pre-defined anatomical design. A base was constructed to hold the benchtop model in place as well as the haptic device for better precision. The design of the benchtop model was defined such that it had five preset incisions that allow the user to penetrate through to make their way towards the disc without any material hindering the trajectory. Hence, the puncturing events were based on the vertical location of the multitool while the accompanying axial forces were transformed along the angular displacement of the tool axes. Situated at the center of the benchtop model was a 3D printed set representing the L4 and L5 vertebral spinal functional unit which represented and was calibrated with its corresponding virtual model. The tool adopted was mounted onto the manipulator arm and situated at the center of the arm to minimize inertial loads and balance the tool naturally, as shown in Fig. 2.

Haptic Setup

The haptic system consisted of one five degree-of-freedom (5-DOF) impedance-control based haptic device, namely Entact W3D (Guelph, Canada), with three degree-of-freedom force (3-DOFF) controlled by three active DC motors capable of producing maximum output force of 15N. The surgical tool was mounted onto the point-based haptic device at its arm, such that the tool connects approximately at its center of gravity. The haptic device was connected using ethernet cable to an MSI GT73VR 7RF (MSI) Core i7 3.5 GHz 64GB RAM portable desktop equipped with an NVIDIA GTX 1080 GPU.

The haptic device was mounted at a specific distance from the benchtop unit and calibrated with the origin. In general, the force feedback during the simulation was rendered such that the soft-tissue resistance was conveyed by the haptic force feedback and hard-tissue was conveyed via a Tangible Interface (TI) which was 3D printed and included in the VR module. The graphical scene rendered a fluoroscopic view of the rigid object and the tool at each iteration. Fig. 2 provides a schematic of the haptic setup described above. Furthermore, the physical upper layer of the benchtop model was pre-punctured at a specific position to allow the tool to move through without any constriction while reaching the rigid objects.

Force Feedback Algorithm

At each iteration, the trajectory between the initial and final position of the tool tip was incorporated to achieve a smooth continuous motion. The general formulation of the trajectory can follow a 2D cubic spline formulation as:

$$u(t) = a_0 + a_1 t + a_2 t^2 + a_3 t^3$$

Equation 5: 2-D Cubic Spline formulation for displacement

Given the initial conditions:

$$u(0) = u_0, \;\; u(t_f) = u_f$$

whereby a_0, a_1, a_2, a_3 are constants to be calculated, t is time and u is position.

For continuous motion (i.e. no stops), the velocities at the intermediate points must be calculated.

Initial Conditions:

$$\dot{u}(0) = \dot{u}_0, \;\; \dot{u}(t_f) = \dot{u}_f$$

Solution:

$$a_0 = u_0$$

$$a_1 = \dot{u}_0$$

$$a_2 = \frac{3}{t_f^2}(u_f - u_0) - \frac{2}{t_f}\dot{u}_0 - \frac{1}{t_f}\dot{u}_f$$

$$a_3 = -\frac{2}{t_f^3}(u_f - u_0) + \frac{1}{t_f^2}\dot{u}_0 - \frac{1}{t_f}(\dot{u}_f + \dot{u}_0)$$

$$u(t) = a_0 + a_1 t + a_2 t^2 + a_3 t^3$$

$$\dot{u}(t) = a_1 + 2a_2 t + 3a_3 t^2$$

Equation 6: Velocity Formulation adopted for haptic rendering

$$\ddot{u}(t) = 2a_2 + 6a_3 t$$

Equation 7: Acceleration Formulation adopted for haptic rendering

The force feedback algorithm was designed to meet a set of specification requirements to ensure a realistic feel was attained. To achieve the latter, the forces were divided, as conceived by the cadaveric experiments, which entailed the force and torque components. However, given the adoption of a 3-DOFF haptic device, only forces were implemented, while moments were adjusted to give a lateral force effect depending on the angular displacement, and the axial torque was not incorporated. Hence, the force components were defined as follows:

- $\boldsymbol{F_z}$: *linear insertion* and *extraction* resistance consisting of $F_{INSERTION}$, $F_{RELAXATION}$ and $F_{EXTRACTION}$
- ***w(x)*:** *distributed* lateral resistance
- $\boldsymbol{F_y}$ and $\boldsymbol{F_x}$: *lateral* resistance ($F_{LATERAL}$, $F_{LATERAL\ RELAXATION}$) computed using ***w*** such that:

$$F_{LATERAL} = \frac{w}{L} * d \tag{6}$$

Whereby L is a constant dependent on the experimental tool used (70 mm) and d is the linear penetrated depth of the tool measured from the upper-most skin layer position

- $\boldsymbol{F_{Mx}}$ and $\boldsymbol{F_{My}}$: *moment* resistance computed using $F_{LATERAL}$ such that:

$$F_M = F_{LATERAL} \cdot \sin\theta \tag{7}$$

Whereby $\boldsymbol{\theta}$ is the angle measured between the tooltip and lateral force's corresponding base plane

Concomitantly, the system was designed to accommodate the cadaveric experimental force output while implementing a puncture feel of the system. Moreover, if the tool were fully removed, a second puncture should be allowed. Finally, in every case, force components should be applied according to the tool's local coordinate system. In complement to the feedback's basic output, a set of adjustments were incorporated to account for the viscoelastic nature of the tissue. In doing so, an interpolation between the boundaries of the maximum and minimum experimentally extracted curves in Table 1 was incorporated by:

$$y = \omega(x - x_1) + y_1 \tag{8}$$

Such that,

$$\omega = \frac{y_2 - y_1}{x_2 - x_1}$$

Equation 8: Linear Interpolation formulation employed for haptic rendering

whereby, ω is the slope of the line constructed by two points P_1 (x_1, y_1) and P_2 (x_2, y_2).

The entire algorithm was implemented to run a single time at each iteration within a continuous loop. The soft tissues included in the system were considered to be primitive objects and, hence, their spatial coordinates were used directly to implement the algorithm. That is, the muscle layers were rectangular with a thickness equivalent to the boundaries defined according to the piecewise function constructed in Equation (1) while the IVD was represented by a sphere of diameter defined by the anatomical diameter of the 3D printed vertebral unit. This *a posteriori* collision model algorithm begins with an initialization of all the system variables then constantly returns the identity number of the layer corresponding to the tooltip's z-coordinate value. The layer array is composed of the locations defined according to Table 1. Once the tool tip's z-coordinate becomes equal to the boundary layer defined for the first entry of the layer array, the insertion force coefficients, corresponding to the first muscle tissue layer as well as the relaxation and depth coefficients, activate only. Once the tool tip penetrates the second muscle layer, the initial transverse coordinates (x_0, y_0) are set throughout the rest of the simulation unless

the user removes the tool fully in order to conceive the feeling of a prior induced void from penetration. Furthermore, the equation set is redefined to contain the coefficients of layer 2. At this point, if the user removes the tool, the extraction force would be utilized. The transformed lateral displacement from the previously set initial coordinates define the lateral forces applied (x_d, y_d). At each run, the velocity calculated by Equation (4) and the corresponding depth defined the ΔF component added to the original insertion force. Furthermore, if the magnitude of the velocity is less than the defined threshold at any point, the soft tissue relaxation activates. Fig. 3 further details the logic sequence of the described algorithm.

5.2.4. RESULTS

A total of 143 experimental runs were conducted to record the different results across the two cadavers. While the number of experiments were conducted was high, the number of experimental protocols implemented was one. The variation for the different soft tissue were in terms of the stopping criteria. The first protocol was specific to the linear insertion of the muscle, the second protocol was specific to the linear insertion of the disc and the third protocol characterized the force feedback for the lateral resistance within the muscle. Further variations included the speed, depth and angle of attack to achieve higher realism and capture the viscoelastic nature of the soft tissue. Fig. 4 depicts an example of the output retrieved by puncturing through soft tissue muscles with designations of the specified global maxima and minima as the tool follows the above protocol.

It is evident that during the insertion phase, the insertion force increases continuously to reach a maximum force of 6.22 N, at the third puncture (72.93 mm), then decreases to reach a steady state before the relaxation phase. Furthermore, the soft tissues were observed to consistently possess a decreasing trend during relaxation (1.9 N decrease in Fig. 4). In addition, all extraction forces tested were observed to decrease to zero after which the force direction inverts due to the extension of the soft-tissue that follows direction of motion of the tool due to internal friction (minimum force recorded was -0.9 N in Fig. 4). The force insertion at a 1.5 mm/s velocity and 65° angle was adopted as the baseline and the two corresponding variations (v = 4.5 mm/s and angle = 85°) which were observed to have an effect on the baseline output ($p < 0.01$). Similarly, the linear relaxation baseline at a depth of 10 mm was considered as the baseline and an adjustment of the penetration depth was observed to have an effect ($p < 0.01$).

Moreover, the linear extraction and lateral resistance within the muscle were recorded. While some variations had more effect than others, for the purpose of this case study, all the characteristic variations were incorporated, even if the difference among the variations was insignificant.

The recorded data was, then, curve-fitted using Equation (2). Table 1 provides the complete curve fitted coefficients of the tests conducted. Each set of coefficients computed were combined with their corresponding depth at which they would be activated. All the extracted coefficients resulted with an acceptablSe fit ($R^2 > 0.9$) with the exception of one curve fit that adheres to the force behavior beyond the third puncture ($R^2 = 0.88$).

To test the integrated haptic models, the algorithm presented in Fig. 3 was implemented using the LUA language which feeds the data to the original framework provided with the haptic device by Entact W3D (Guelph, Canada) constructed using the C++ programming language. The coefficients in Table 1 along with their corresponding ranges were used to model the force output defined within the array variables. Upon integrating the curves directly into the system, the forces generated mimicked the exact force-displacement and force-time output extracted from the cadaveric experiments. Fig. 5 depicts an extract of the case study conducted of the resulting force profiles comparing the cadaveric experimental output, curve fitting output and the resulting rendered output. It is evident from the graph that the haptic forces closely match the cadaveric output.

Furthermore, Fig. 6 depicts an extract of the output of the force rendered by the haptic device as a user handled the tool and penetrated through the muscle layers. The force profile recorded during the puncturing of the muscle layers towards reaching the disc shows the high variability in the forces relevant to the user's position in time and their respective motion task. There were no specific tasks followed while conducting the simulation besides reaching the disc through the punctured hole in the benchtop model. This may be the result of a puncturing event taking place whereby the force exerted suddenly drops to a lower value resulting with a loss of control. This outcome fits well into previously suggested simulator position-based metrics that assess resulting velocity profiles (e.g. consistency in velocity profile, low peak velocities) [36].

5.2.5. DISCUSSION

The application of an effective haptic interface is composed of three subsystems: the control system, collision-detection algorithm and force-response models. The control system ensures that a stable evolution of the feedback response is enabled as to not be perceived as instabilities due to abrupt changes in the force directions and magnitudes upon collision detection. This could, further, relay a weak time-performance from the psychological context if an inappropriate control technique was correspondingly adopted [37]. For example, if the tool mounted onto the haptic device is expected to puncture soft-tissue, it is necessary for the collision model to be able to handle post-punctures at a sufficient rate and in a smooth manner for an immersive experience, otherwise, this would be perceived as unnatural by the user. The collision-detection algorithm ensures that the system efficiently and accurately detects the different virtual models within the system which would result with obvious and imprecise penetration of the models being interacted with, especially at high frequencies and motions [38]. The force-feedback methodology defines the magnitude and behavior of the force the user experiences when interacting with the simulator. In specific, impendence-based haptic devices read position-coordinates of a connected manipulator which, depending on the implemented computational method, ultimately generates force responses accordingly. While this technology currently faces considerable challenges, the future of haptic integration depends greatly on its capability to achieve realism [22]. For instance, the challenges include, but are not limited to, costly computation time, numerical instabilities from integration of body dynamics, time-delay artifacts and high cost of medical simulators that require extensive hardware to meet the communication requirements of high frequency haptic communications [39]. Furthermore, the perception of rigidity, usually defined with infinite stiffness, as compared to finite stiffness in soft-tissue successively provides a constriction when adopting concurrent contact algorithms due to the abrupt forces which render ineffective and low-quality force-feedback when handled with current refresh rates of 1 kHz [40]. Hence, this paper proposed the integration of a data-driven model that implements exact experimental forces for soft-tissue on an independent thread and was calibrated with a tangible benchtop model incorporated with the vertebrae to be validated with force feedback.

The first stage of a Minimally Invasive surgery entails gaining access to the disc whereby a surgeon employs a long slender probe to puncture through the muscle layers following an

incision applied to the skin and thoracolumbar fascia. Throughout this stage, the user may or may not make use of reconstructed CT-scans, fluoroscopic imagery and neuro-monitors. Hence, the user does not at any time during this module have access to internal soft tissue visualization. Therefore, no muscle tissue deformation is usually visualized and the only sensual experience in such a realistic surgery is somatosensory and auditory. In the case of the adopted algorithm, the model objects were calibrated according to the benchtop model. The inclusion of the benchtop model proved effective with the obvious interaction of the users whereby one hand would hold the tool and the other rests on the benchtop for extra support and additional tool control and guidance. The described benchtop setup supports previous recommendations in regards to the advantages for the incorporation of benchtop models into simulators to give the user a quasi-clinical encounter for a realistic feel [41].

While this study used the empirical output in its raw form, the novelty of the framework was highlighted in its ability to accurately capture longitudinal puncturing events and give a realistic information of a punctured hole in lateral movements. Furthermore, this framework mitigated the rigid-soft-tissue complexity and operates at a cheap computational cost, and thus is rapid to relay results, which can be embedded into any 3-DOFF haptic device. In addition, following a puncture event, the user loses control momentarily mainly due to the sudden drop in the force which is signified by a high acceleration. Given that no physical tissue is present to provide a natural resistant feel, the local increase in acceleration should be handled effectively. However, the high speed of the algorithm permitted a sustainable level of continuity in the capability to produce forces at these high accelerations.

5.2.6. CONCLUSIONS, LIMITATIONS AND FUTURE WORK

The present study supports the high level of reliability gained by directly implementing force profile models off of cadaveric experiments. In addition to reliability, the algorithm presented facilitates the addition of further force models extracted from cadaveric experimentation to generate different scenarios for the user of the simulator. With the considerable amount of research conducted on computational haptic models [42], this study demonstrated that further advancements in computational and material models that properly capture the realistic forms of soft-tissue responses from cadaveric-based experiments permit the rendering of the exact behavior when employing haptic feedback which may be sufficient for a realistic experience.

Limitations of the study included the compromise on accuracy of exact positions given the absence of a contact-algorithm rendered with a virtual model. Hence, full incorporation of the force feedback would be sufficient in a surgical simulator given that it does not require a great deal of virtual objects and contacts. However, the high-speed rendering may allow for the incorporation of accurate 3D virtual models with the incorporation of an interpolation function that elevates the visual rendering rate (~ 40 Hz) with the higher haptic rendering rate (~ 1 kHz). Moreover, given that the haptic device incorporated was 3-DOFF, it was only possible to validate the forces and moment-force effects whereas the torque was not included. A moment-effect, reconstructed by the use of forces, was possible given that the end-effector of the haptic arm was mounted at the center of the tool probe used. A moment was generated only if the position change of the tool tip was less than a specific threshold and the angle changed. Moreover, while the algorithm resulted with exact force feedback which is based on data extracted from cadaveric experimentation, validation by human surveying and perception was not conducted. It is worthy to note that the force response exhibited instabilities when the tool reached the intervertebral disc due to the relatively higher force increments. In specific, the haptic arm vibrated as the tool tip advanced within the disc and relaxation induced phases. This is the result of operating the device in an open-loop control system (i.e. non-feedback).

Hence, future works will include the transformation of the haptic framework to operate on a closed-loop system to provide force and position feedback. This does not affect the algorithm adopted as it would be maintained across the platform and a closed loop control system capable of providing feedback to position and force would be integrated into the system. Moreover, future work will incorporate the validation of the algorithm with professional medical surveys as well as the incorporation of data achieved from more cadaveric samples to provide a database for machine-learning incorporation.

5.2.7. REFERENCES

[1] M. V. Schaverien, "Development of expertise in surgical training," *Journal of surgical education,* vol. 67, no. 1, pp. 37-43, 2010.
[2] J. Hall, C. Ellis, and J. Hamdorf, "Surgeons and cognitive processes," *British Journal of Surgery,* vol. 90, no. 1, pp. 10-16, 2003.
[3] R. H. Bell Jr *et al.*, "Operative experience of residents in US general surgery programs: a gap between expectation and experience," *Annals of surgery,* vol. 249, no. 5, pp. 719-724, 2009.

[4] R. L. K. F. Bello, "Technology in surgical education," *Recent Advances in Surgery 28,* vol. 28, p. 9, 2005.
[5] A. J. Vickers *et al.*, "The surgical learning curve for laparoscopic radical prostatectomy: a retrospective cohort study," *The lancet oncology,* vol. 10, no. 5, pp. 475-480, 2009.
[6] P. Ström, A. Kjellin, L. Hedman, E. Johnson, T. Wredmark, and L. Felländer-Tsai, "Validation and learning in the Procedicus KSA virtual reality surgical simulator," *Surgical Endoscopy and Other Interventional Techniques,* vol. 17, no. 2, pp. 227-231, 2003.
[7] G. H. Eltabbakh, "Effect of surgeon's experience on the surgical outcome of laparoscopic surgery for women with endometrial cancer," *Gynecologic oncology,* vol. 78, no. 1, pp. 58-61, 2000.
[8] J. W. Hammond, W. S. Queale, T. K. Kim, and E. G. McFarland, "Surgeon experience and clinical and economic outcomes for shoulder arthroplasty," *JBJS,* vol. 85, no. 12, pp. 2318-2324, 2003.
[9] A. Larcher *et al.*, "The learning curve for robot-assisted partial nephrectomy: impact of surgical experience on perioperative outcomes," *European urology,* vol. 75, no. 2, pp. 253-256, 2019.
[10] K. Gurusamy, R. Aggarwal, L. Palanivelu, and B. Davidson, "Systematic review of randomized controlled trials on the effectiveness of virtual reality training for laparoscopic surgery," *British Journal of Surgery,* vol. 95, no. 9, pp. 1088-1097, 2008.
[11] J. R. Korndorffer Jr, J. B. Dunne, R. Sierra, D. Stefanidis, C. L. Touchard, and D. J. Scott, "Simulator training for laparoscopic suturing using performance goals translates to the operating room," *Journal of the American College of Surgeons,* vol. 201, no. 1, pp. 23-29, 2005.
[12] J. Park *et al.*, "Randomized controlled trial of virtual reality simulator training: transfer to live patients," *The American journal of surgery,* vol. 194, no. 2, pp. 205-211, 2007.
[13] T. P. Grantcharov, V. B. Kristiansen, J. Bendix, L. Bardram, J. Rosenberg, and P. Funch-Jensen, "Randomized clinical trial of virtual reality simulation for laparoscopic skills training," *Br J Surg,* vol. 91, no. 2, pp. 146-50, Feb 2004, doi: 10.1002/bjs.4407.
[14] R. K. Reznick and H. MacRae, "Teaching surgical skills—changes in the wind," *New England Journal of Medicine,* vol. 355, no. 25, pp. 2664-2669, 2006.
[15] S. Barry Issenberg, W. C. Mcgaghie, E. R. Petrusa, D. Lee Gordon, and R. J. Scalese, "Features and uses of high-fidelity medical simulations that lead to effective learning: a BEME systematic review," *Medical teacher,* vol. 27, no. 1, pp. 10-28, 2005.
[16] W. C. McGaghie, S. B. Issenberg, E. R. Petrusa, and R. J. Scalese, "Effect of practice on standardised learning outcomes in simulation-based medical education," *Medical education,* vol. 40, no. 8, pp. 792-797, 2006.
[17] A. Chatterjee, P. Chaubey, J. Martin, and N. Thakor, "Testing a prosthetic haptic feedback simulator with an interactive force matching task," *JPO: Journal of Prosthetics and Orthotics,* vol. 20, no. 2, pp. 27-34, 2008.
[18] C. Basdogan, S. De, J. Kim, M. Muniyandi, H. Kim, and M. A. Srinivasan, "Haptics in minimally invasive surgical simulation and training," *IEEE computer graphics and applications,* vol. 24, no. 2, pp. 56-64, 2004.
[19] D. B. Jones, S. D. Schwaitzberg, and C. G. L. Cao, "Effect of haptic feedback in laparoscopic surgery skill acquisition," *Surgical Endoscopy,* vol. 26, no. 4, pp. 1128-1134, 2012.

[20] S. Liang, P. P. Banerjee, and D. P. Edward, "A high performance graphic and haptic curvilinear capsulorrhexis simulation system," in *2009 Annual International Conference of the IEEE Engineering in Medicine and Biology Society*, 2009: IEEE, pp. 5092-5095.
[21] A. F. Abate, G. Acampora, V. Loia, S. Ricciardi, and A. V. Vasilakos, "A pervasive visual haptic framework for virtual delivery training," *IEEE Transactions on Information Technology in Biomedicine,* vol. 14, no. 2, pp. 326-334, 2010.
[22] D. Escobar-Castillejos, J. Noguez, L. Neri, A. Magana, and B. Benes, "A review of simulators with haptic devices for medical training," *Journal of medical systems,* vol. 40, no. 4, p. 104, 2016.
[23] M. Li *et al.*, "A novel tumor localization method using haptic palpation based on soft tissue probing data," in *2014 IEEE International Conference on Robotics and Automation (ICRA)*, 2014: IEEE, pp. 4188-4193.
[24] K. Miller, G. Joldes, D. Lance, and A. Wittek, "Total Lagrangian explicit dynamics finite element algorithm for computing soft tissue deformation," *Communications in numerical methods in engineering,* vol. 23, no. 2, pp. 121-134, 2007.
[25] A. O. Frank, I. A. Twombly, T. J. Barth, and J. D. Smith, "Finite element methods for real-time haptic feedback of soft-tissue models in virtual reality simulators," in *Proceedings IEEE Virtual Reality 2001*, 2001: IEEE, pp. 257-263.
[26] S. Cotin and H. Delingette, "Real-time surgery simulation with haptic feedback using finite elements," in *Proceedings. 1998 IEEE International Conference on Robotics and Automation (Cat. No. 98CH36146)*, 1998, vol. 4: IEEE, pp. 3739-3744.
[27] G. R. Joldes, A. Wittek, and K. Miller, "Suite of finite element algorithms for accurate computation of soft tissue deformation for surgical simulation," *Medical image analysis,* vol. 13, no. 6, pp. 912-919, 2009.
[28] S. H. Rizzi, C. J. Luciano, and P. Pat Banerjee, "Comparison of Algorithms for Haptic Interaction With Isosurfaces Extracted From Volumetric Datasets," *Journal of Computing and Information Science in Engineering,* vol. 12, no. 2, 2012, doi: 10.1115/1.4006465.
[29] S. Choi and H. Z. Tan, "Effect of update rate on perceived instability of virtual haptic texture," in *2004 IEEE/RSJ International Conference on Intelligent Robots and Systems (IROS)(IEEE Cat. No. 04CH37566)*, 2004, vol. 4: IEEE, pp. 3577-3582.
[30] C. A. Felippa, "A systematic approach to the element-independent corotational dynamics of finite elements," Technical Report CU-CAS-00-03, Center for Aerospace Structures, 2000.
[31] B. Lee, D. C. Popescu, B. Joshi, and S. Ourselin, "Efficient topology modification and deformation for finite element models using condensation," *Studies in health technology and informatics,* vol. 119, pp. 299-304, 2006.
[32] J. Barbič and D. L. James, "Real-time subspace integration for St. Venant-Kirchhoff deformable models," *ACM transactions on graphics (TOG),* vol. 24, no. 3, pp. 982-990, 2005.
[33] M. Mahvash and V. Hayward, "High-fidelity haptic synthesis of contact with deformable bodies," *IEEE Computer Graphics and Applications,* vol. 24, no. 2, pp. 48-55, 2004.
[34] C. b. G. Corrêa, F. t. L. S. Nunes, E. Ranzini, R. Nakamura, and R. Tori, "Haptic interaction for needle insertion training in medical applications: The state-of-the-art," *Medical Engineering and Physics,* vol. 63, pp. 6-25, 2019, doi: 10.1016/j.medengphy.2018.11.002.

[35] S. Haque and S. Srinivasan, "A meta-analysis of the training effectiveness of virtual reality surgical simulators," *IEEE Transactions on Information Technology in Biomedicine,* vol. 10, no. 1, pp. 51-58, 2006.
[36] A. L. Trejos, R. V. Patel, R. A. Malthaner, and C. M. Schlachta, "Development of force-based metrics for skills assessment in minimally invasive surgery," *Surgical endoscopy,* vol. 28, no. 7, pp. 2106-2119, 2014.
[37] M. J. Puerto, E. Sanchez, and J. J. Gil, "Control strategies applied to kinesthetic haptic devices," in *2009 IEEE Workshop on Robotic Intelligence in Informationally Structured Space*, 2009: IEEE, pp. 137-144.
[38] A. R. Choi and M. Y. Sung, "Performance improvement of haptic collision detection using subdivision surface and sphere clustering," *PloS one,* vol. 12, no. 9, 2017.
[39] F. Hamza-lup, D. Popovici, and C. Bogdan, "Haptic feedback systems in medical education," *Journal of Advanced Distributed Learning Technology,* vol. 1, no. 2, pp. 7-16, 2013.
[40] D. Constantinescu, S. E. Salcudean, and E. A. Croft, "Haptic rendering of rigid body collisions," in *12th International Symposium on Haptic Interfaces for Virtual Environment and Teleoperator Systems, 2004. HAPTICS'04. Proceedings.*, 2004: IEEE, pp. 2-8.
[41] T. Dornan, K. V. Mann, A. J. Scherpbier, and J. A. Spencer, *Medical education: theory and practice E-Book*. Elsevier Health Sciences, 2011.
[42] K. Salisbury, F. Conti, and F. Barbagli, "Haptic rendering: introductory concepts," *IEEE computer graphics and applications,* vol. 24, no. 2, pp. 24-32, 2004.

5.2.8. FIGURES AND TABLES

Table 5.1: 2nd Order Polynomial Curve Fitting Resultant coefficients

#	Component	Experiment	Soft Tissue	2nd Order Polynomial Coefficients			Range (mm) or (s) or (degree)	R^2
				a	b	c		
1	$F_{INSERTION\ 1}$	Linear Insertion v = 1.5 mm/s angle = 65°	Muscle	0.0084	-0.0337	0.0658	0-15	0.9967
	$F_{INSERTION\ 2}$			-	0.2864	-2.8951	15 -22	0.9954
	$F_{INSERTION\ 3}$			-	0.4975	-8.7087	22-30	0.99
	$F_{INSERTION\ 4}$			-0.0108	0.859	-10.44	30-40	0.8752
1.1	$F_{INSERTION\ 1}$	Linear Insertion v = 4.5 mm/s angle = 65°		0.0181	-0.0646	0.1424	0-15	0.9983
	$F_{INSERTION\ 2}$			-	0.6043	-8.7976	15 -22	0.9923
	$F_{INSERTION\ 3}$			-	0.4825	-9.8197	22-30	0.9965
	$F_{INSERTION\ 4}$			0.0663	-4.7419	89.925	30-40	0.9653
1.2	$F_{INSERTION\ 1}$	Linear Insertion v = 1.5 mm/s angle = 85°		0.0075	-0.0064	0.0519	0-15	0.9974
	$F_{INSERTION\ 2}$			-	0.4463	-6.3396	15 -22	0.9937
	$F_{INSERTION\ 3}$			-	1.2024	-26.578	22-30	0.9425
	$F_{INSERTION\ 4}$			-0.3769	28.212	-507.42	30-40	0.9446
2	$F_{MUSCLERELAXATION}$	Linear Relaxation d = 40 mm		0.0182	-0.3265	6.4874	0-10	0.9703
2.2	$F_{MUSCLERELAXATION}$	Linear Relaxation depth = 10 mm		0.004	-0.0684	6.2488	0-10	0.9542
3	$F_{EXTRACTION\ 1}$	Linear Extraction		0.0982	-1.2371	3.473	0-9	0.9097
	$F_{EXTRACTION\ 2}$			0.0026	-0.1464	1.052	10-50	0.9453
4	$F_{LATERAL}$	Lateral Resistance		0.0141	0.1877	0.0947	0-30	0.9998
5	$F_{LATERALRELAXATION}$	Lateral Relaxation		0.0333	-0.6365	6.3114	0-10	0.9881
7	$\tau_{FORWARD}$	Torque		-0.0049	0.4592	-2.8551	0-50	0.9761
	$\tau_{BACKWARD}$	Torque		0.0049	-0.039	-4.9642	50-0	0.9284
8	$F_{INSERTION\ 1}$	Linear Insertion	L_4/L_5 Disc	0.3196	1.3235	-0.3054	0-6.41	0.9993
	$F_{INSERTION\ 2}$			-	4.1743	-15.719	6.64-9.74	0.992
	$F_{INSERTION\ 3}$			-	3.0835	-7.5219	9.87 - 13	0.9583
	$F_{INSERTION\ 4}$			-	4.408	-31.956	13-20	0.9959
9	$F_{DISCRELAXATION}$	Linear Relaxation		0.255	-2.1851	18.739	0-4.5	0.9773

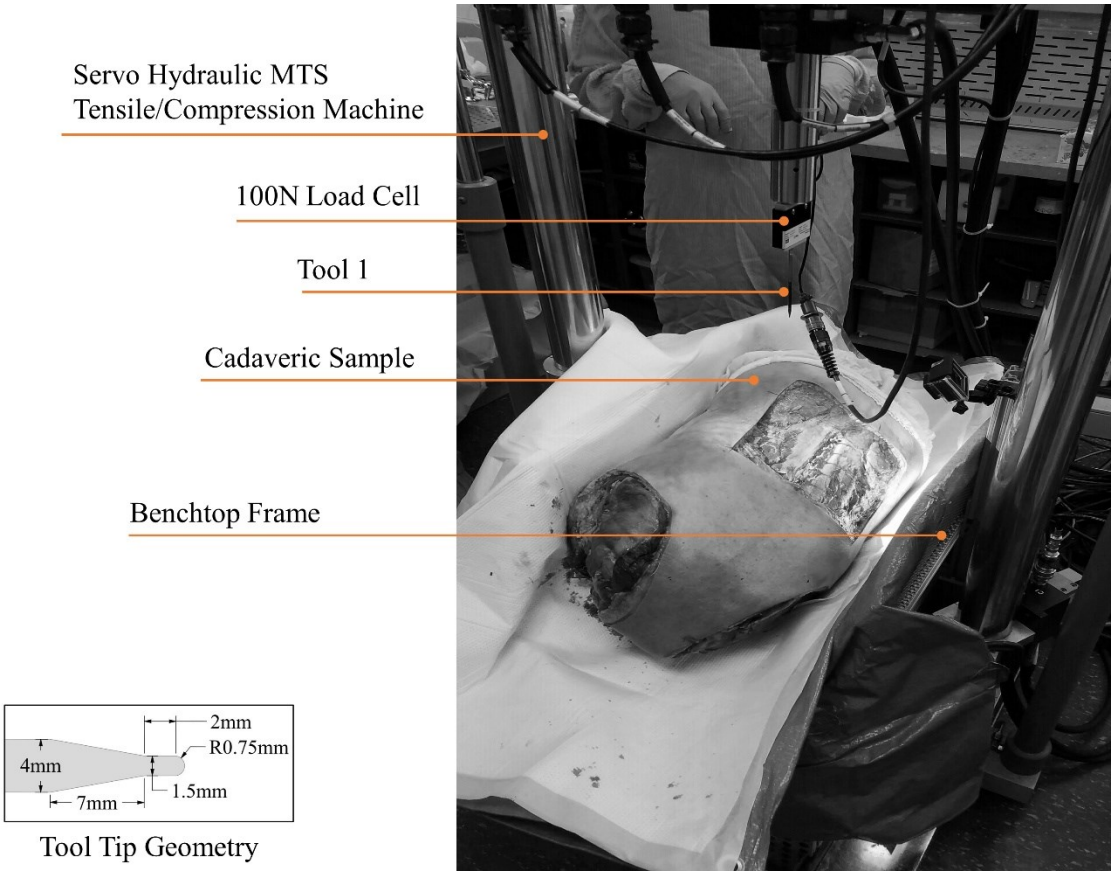

Figure 5-1: Depiction of the experimental setup designed to conduct the series of experiments including the geometrical description of tool 1 tip

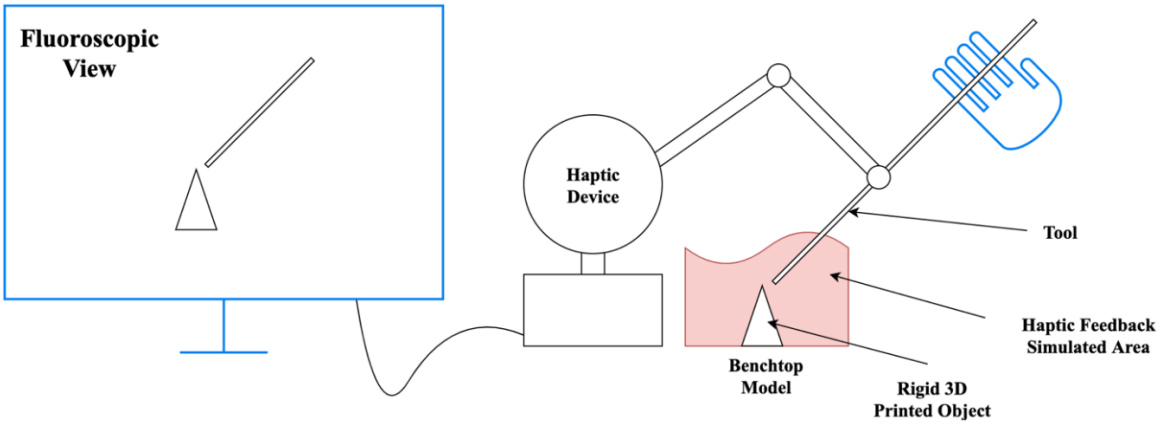

Figure 5-2: Schematic depicting proposed haptic setup applicable with the adopted algorithm

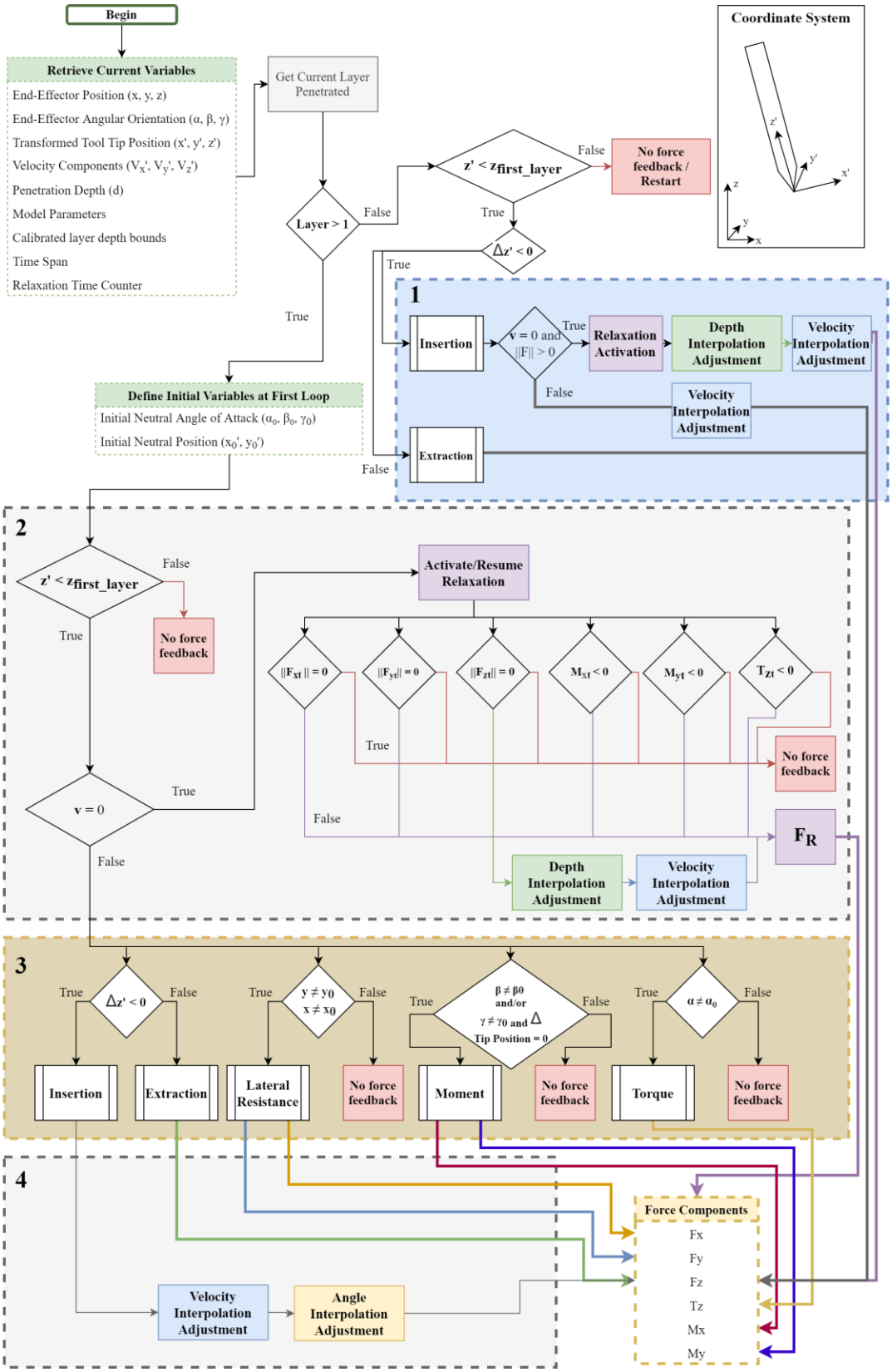

Figure 5-3: Force Computation Algorithm

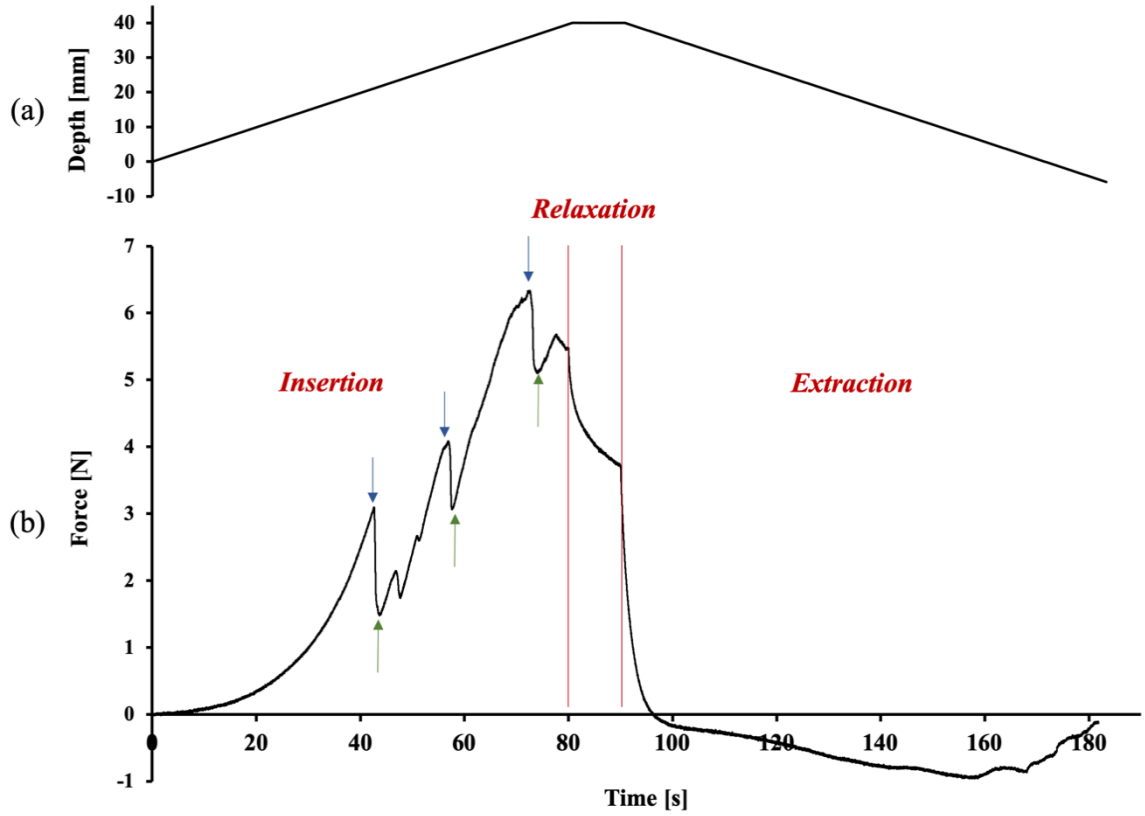

Figure 5-4: Depiction of (a) the depth of the tool at each respective time is plotted and (b) the corresponding output force is plotted with respect to time. The protocol followed a three-step phase whereby the tool was inserted initially to a depth of 40mm, followed by a 10-second pause to be, at the final phase, completely extracted. The blue and green arrows designate the global maxima and global minima, respectively.

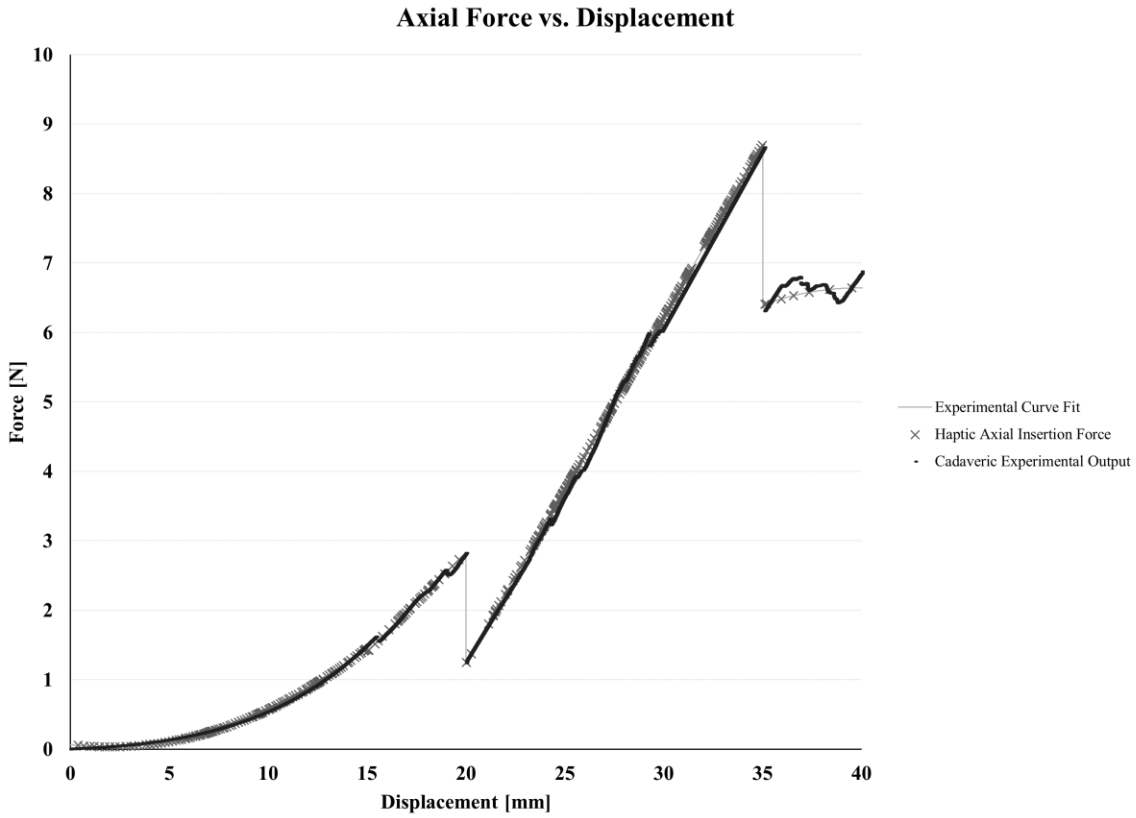

Figure 5-5: Case study output resultant depicting the extracted force-displacement curves within the muscle for the actual cadaveric experiments, curve fitted output that was fed to the haptic device and the resulting recorded haptic feedback force

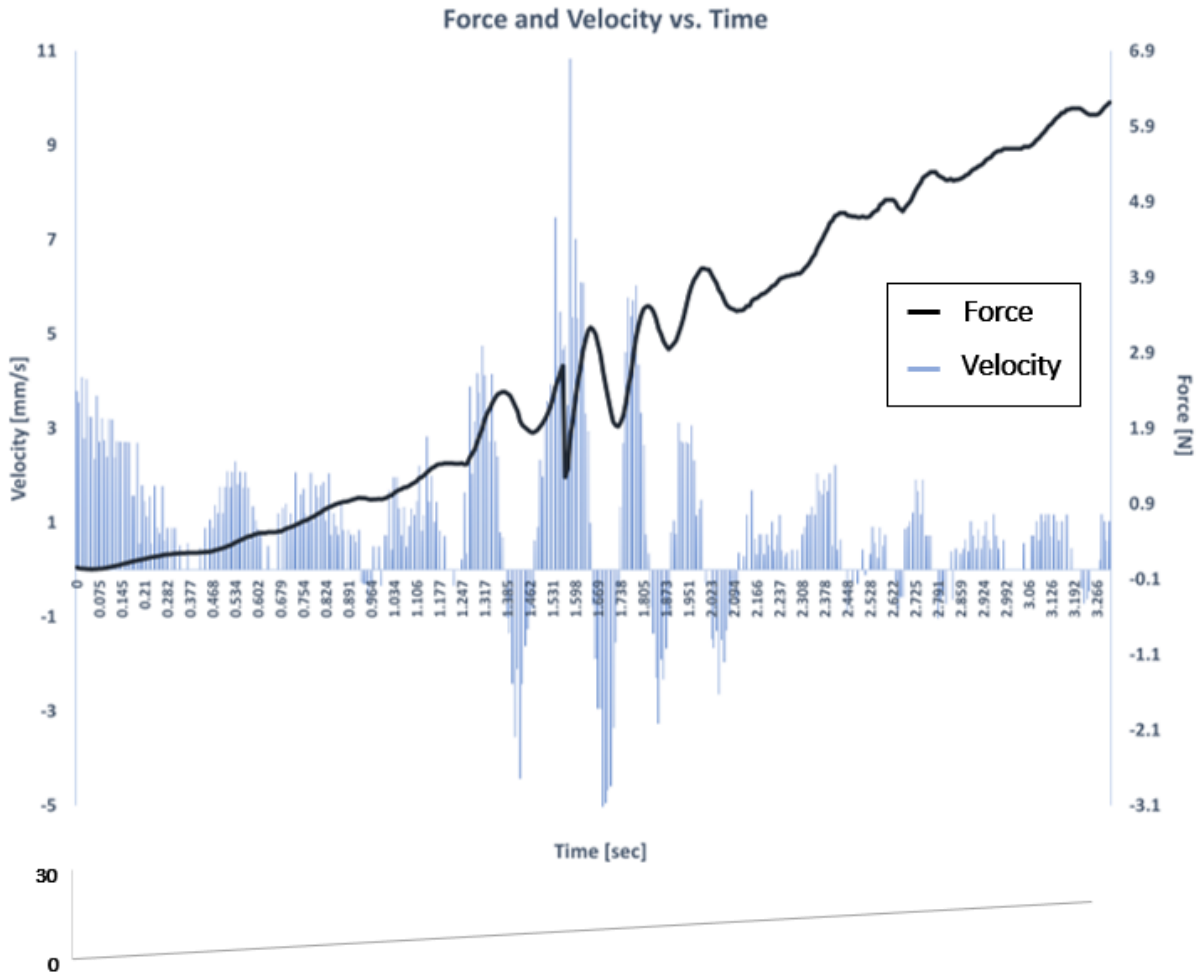

Figure 5-6: Case study force output resultant depicting the variation of the velocity and force with respect to time as the user punctured through the muscle layers targeting the intervertebral

5.3. ADDITIONAL STUDIES RELATED TO ARTICLE 3

5.3.1. NOTES ON ARTICLE 3

The following section serves to clarify the construction of the algorithm to compute the components of the forces generated by the haptic device. In particular, the haptic device is based on an impedance control whereby the user's position in space is measured and the force is fed back to the operator. Hence, the position of the tool in space controls the magnitudes of the force components experienced by the user. As such, the experiments devised in Article 2 extracted the forces felt by the tool when interacting with the tissue within the scope of the various maneuvers set within the surgical operation.

In designing an algorithm suitable to render forces based on the probe's tip position in space, it was necessary to provide the algorithm the capability to accommodate various scenarios. In other words, the trainee may be able to conduct the virtual surgical operation on different virtual patients. For instance, the forces experienced by a patient with a progressed form of Degenerative Disc Disease (DDD) may be different than that with an early form of DDD or a healthy person. To account for such variation and to provide the user with such versatility in choosing the scenario to train on, the two cadavers in Article 2 were chosen to account for such variations. While mean force values were reported in Article 2 and utilized to extract the coefficients reported in Table 5.1, it is necessary to note the algorithm described in Figure 5–3 allows for the use of single experimental results directly from one cadaver. The versatile nature of the algorithm may be highlighted with the developer's requirement to only modify the representative coefficients. To highlight this versatile quality, the force profiles utilized in Article 3's case study are different from the mean values depicted in Article 2. In specific, Figure 5–5 shows one subset of the cadaveric experimentations to illustrate the algorithm's direct utilization of the force profiles.

It is worthy to note that the variability depicted in Article 2 was not incorporated into the reporting of the force values in Article 3 to accommodate the nature of the algorithm developed. In other words, the algorithm utilizes the curve–fitted 2^{nd} order polynomial coefficients that construct the piece–wise continuous functions to compute the force based on the current position of the tool in space. Hence, a single set of input describing the force profile is required for this

algorithm. The inclusion of other specific scenarios would further require other sets of single input functions.

5.3.2. NERVE RESPONSE INTEGRATION

The coefficients and algorithm conceived in Chapter 5.2 incorporated the muscle and disc tissue only. This assumed that the surgeon would avoid striking the nerve as the probe approaches the intervertebral disc. In specific, the incorporation of a neuro–monitor within the access gaining module would alarm the user as it provides continuous detection of the distance between the nerve tissue and probe. However, given that the main objective of this thesis targets the development of a medical simulator, the user may strike the nerve. Moreover, advanced users may choose to operate without the presence of a neuro–monitor. In this case, the user would depend on the perception achieved from the tool and nerve tissue interaction to advance instead. Thus, to accommodate the independent haptic rendering feature developed, special attention was given to the nerve to serve its integration.

The tension responses acquired from the cadaveric experimentation, namely Experiment VIII in Table 4.2. Thus, the data were similarly fit into a 2nd order polynomial. Table 5.2 presents the corresponding nerve curve–fit coefficients for the tensioning and relaxion of the nerves.

Table 5.2: Nerve Tensioning and Relaxation experimental curve fit to 2nd order polynomial formulation

#	Component	Experiment	Soft Tissue	2nd Order Polynomial Coefficients			Range (mm) or (s) or (degree)	R^2
				a	b	c		
10	$F_{TENSION}$	v = 0.5 mm/s F_{CUTOFF} = 80 N	L1/L2 Root Nerve	0.0121	0.1912	0.4115	0–40	0.9998
	$F_{TENSION}$	v = 0.5 mm/s F_{CUTOFF} = 80 N	L2/L3 Root Nerve	-	1.3838	-5.5143	0–40	0.9624
	$F_{TENSION}$	v = 0.5 mm/s F_{CUTOFF} = 80 N	L3/L4 Root Nerve	0.0301	0.1901	0.9493	0–40	0.9985
11	$F_{RELAXATION}$	10-sec pause	Lumbar Nerve	-	-0.6528	18.849	0–10	0.9672

In specific, the nerve was modelled as a spline located in the 3D space. A corresponding line parallel to the tool's shaft was defined and a script that checks if the two lines intersect was patched onto the previous code. If the user's tool intersects the nerve spline an added lateral force, and corresponding moment, should be accounted for. Figure 5–7 depicts the conditional

block that was added to the original algorithm depicted in Figure 5–3. In specific, the block shown in Figure 5–7 was incorporated within the Lateral Resistance block shown in the 3rd main block in Figure 5–3.

.

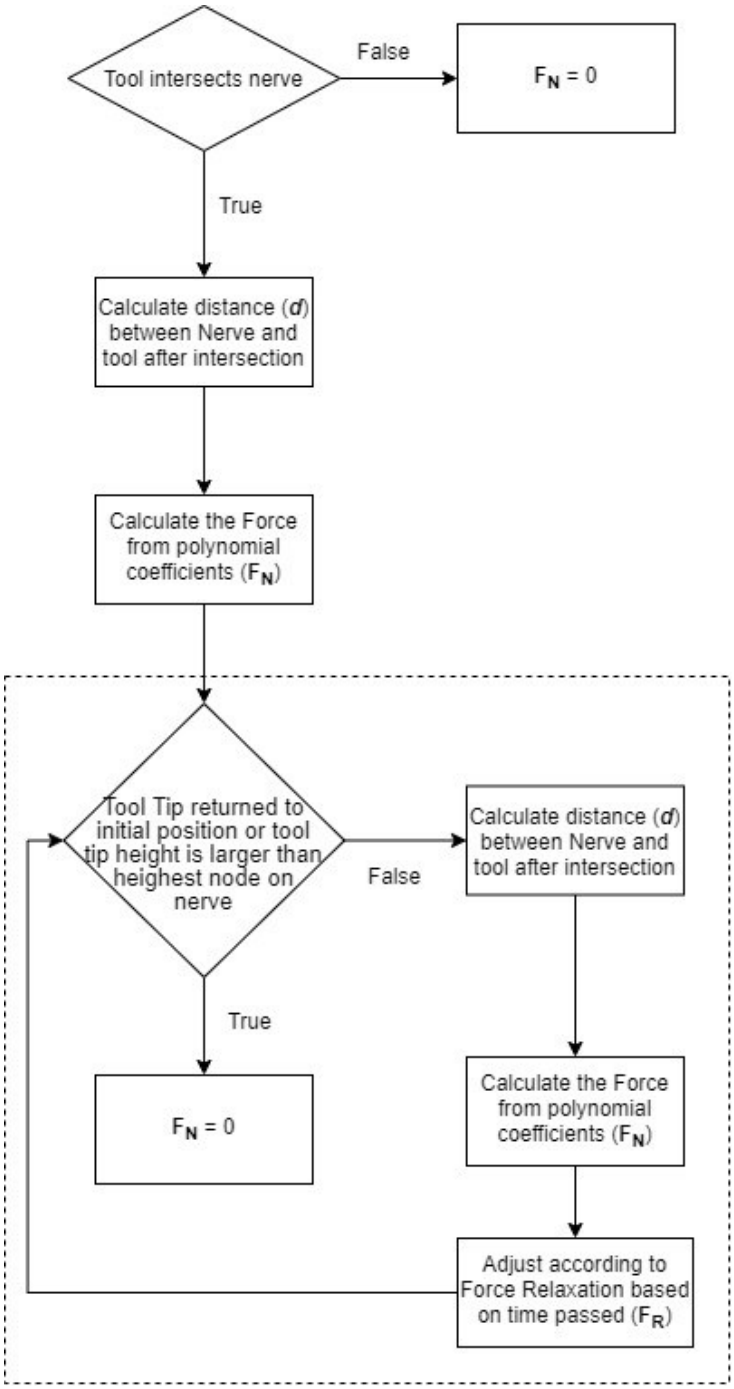

Figure 5-7: Force Computational Algorithm for Nerve

6

VIRTUAL REALITY MODULE DEVELOPMENT

The following chapter describes the development of the remaining components required to construct the medical simulator to render an effective training module. The simulator was developed to create a training environment specific to the MI OLLIF surgery that leverages an anatomical window, namely, the Kambin's Triangle. Initially, the surgeon places a guidewire on the patient's back perpendicular to the axis of the spine marking the axial line. The surgeon, then, positions the guidewire such that Anterior-to-Posterior fluoroscopic images show the tip of the guidewire transecting the center of the pedicles to mark another line using a surgical marker. Anesthesia is then injected locally to the L_4/L_5 site. The surgeon then applies a 1–1.5 cm incision on the skin and underlying fascia. The latter steps were not included in the simulator and a physical benchtop interface was used with a set of pre–incised cuts of length 30 mm for the reasons aforementioned in Chapter 4.3. Following the latter preparatory stage, three main modules defined the completion of the surgery which include access gaining, discectomy and cage insertion. The module adopted in this thesis included the access gaining stage only. The module begins with the surgeon handling a long slender probe tool that traverses the incision to puncture through the muscular layers. This is extended to reach the intervertebral disc while ensuring that the nerve root remains intact. Fluoroscopy, neuro–monitoring and navigation tools would be available for the surgeon to safely progress towards the disc. Upon reaching the intervertebral disc, the tool specifies a trajectory that is, then, used as a foundation to slide three dilators through the skin incision. Finally, a port tool inserted on top of the final dilator is fixed into place. The dilators are then removed to provide a safe access tunnel for next stages. This marks the end of the access gaining module.

6.1. GEOMETRICAL DEVELOPMENT AND ASSESSMENT

The following section describes the steps undertaken to generate geometrical models that are applicable to be used within the VR scene. In conformity with the in-house software used, the geometrical models used were developed to satisfy the following criteria to render a sufficiently stable accurate object without adding on a large computational overhead:

1. Meshes must consist of uniform edged size elements
2. Input surface meshes must only comprise of triangular elements
3. Low element and nodal count to maintain a high FPS
4. Contacting objects must have conforming nodes on shared surfaces
5. Surfaces must be smoothened to the fulfill realistic visuals of soft tissue
6. Fixed nodes must be identified and their respective RGB defined before adding it to the virtual scene

Moreover, the generated models must sustain a reasonable affinity to the original models conceived from MRI imaging. In addition, the virtual environment should provide enough resemblance to reality such that all necessary virtual biological components are included within the scene.

The developed online open-source dictionary–type library, namely BodyParts3D, was constructed on the framework of a voxel human model. In turn, this was conceived from a whole–body set of 2 mm interval MRI imagery of a male volunteer. In their description, Mitsuhashi et al. noted that anatomical segmentations were introduced in the original data then supplemented with the missing details. Furthermore, blurred contours were clarified using 3D editing programs by referring to atlases and mock-up models created by medical illustrators. An example of the breakdown of the biological systems available are shown in Figure 6–1.

The construction pipeline of the virtual model followed a specific set of tasks to ensure an efficient and accurate development. Figure 6–2 describes the workflow for the development of the virtual models.

Initially, the virtual models required were identified. This was conducted with the requirement of developing a realistic environment as a precursor.

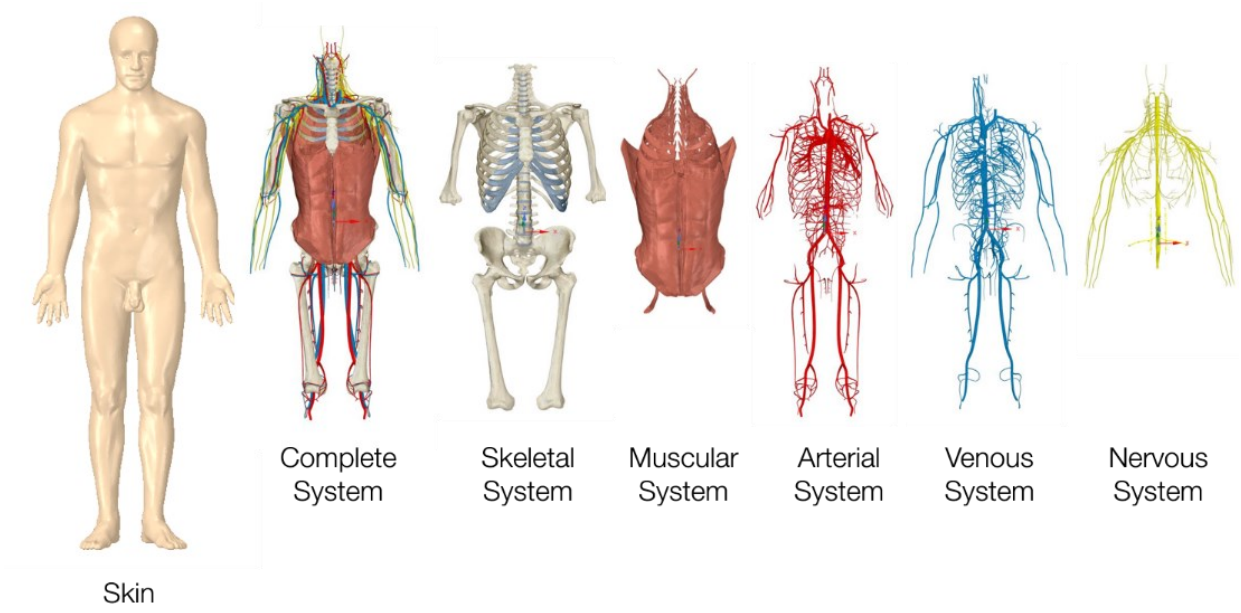

Figure 6-1: Depiction of the available systems by BodyParts3D

The simulator was developed for an MI surgery at the L_4/L_5 spinal level. Hence, the entirety of the Functional Spinal Unit (FSU) was considered which included the following:

1. Vertebrae: L_4 and L_5
2. Nerve Root: L_4/L_5 spinal nerve root and the Dura spanning from the L4 upper surface to the L5 lower surface
3. Intervertebral Disc: L_4/L_5 Annulus Fibrosus and Nucleus Pulposus
4. Epiphyseal Endplates: L_4 and L_5 Endplates
5. Muscular Tissue layer extending laterally to the skin

In the first section of the access gaining stage, the tool penetrates through an incision applied to the skin. At this point, only the tool and the corresponding vertebrae may be visible using live fluoroscopy. After the dilators have been inserted, the intervertebral disc and vertebra along with muscular tissue become visible. Hence, the above selected biological tissue objects were sufficient to meet the purpose.

Following the identification of the objects, the tessellation models were downloaded and imported into ANSYS Spaceclaim®. Initially, geometrical preparation entailed fixing the scaling errors that resulted from importing the objects. Then, the necessary rotational transformations re-oriented the objects to fix the inaccurate positioning.

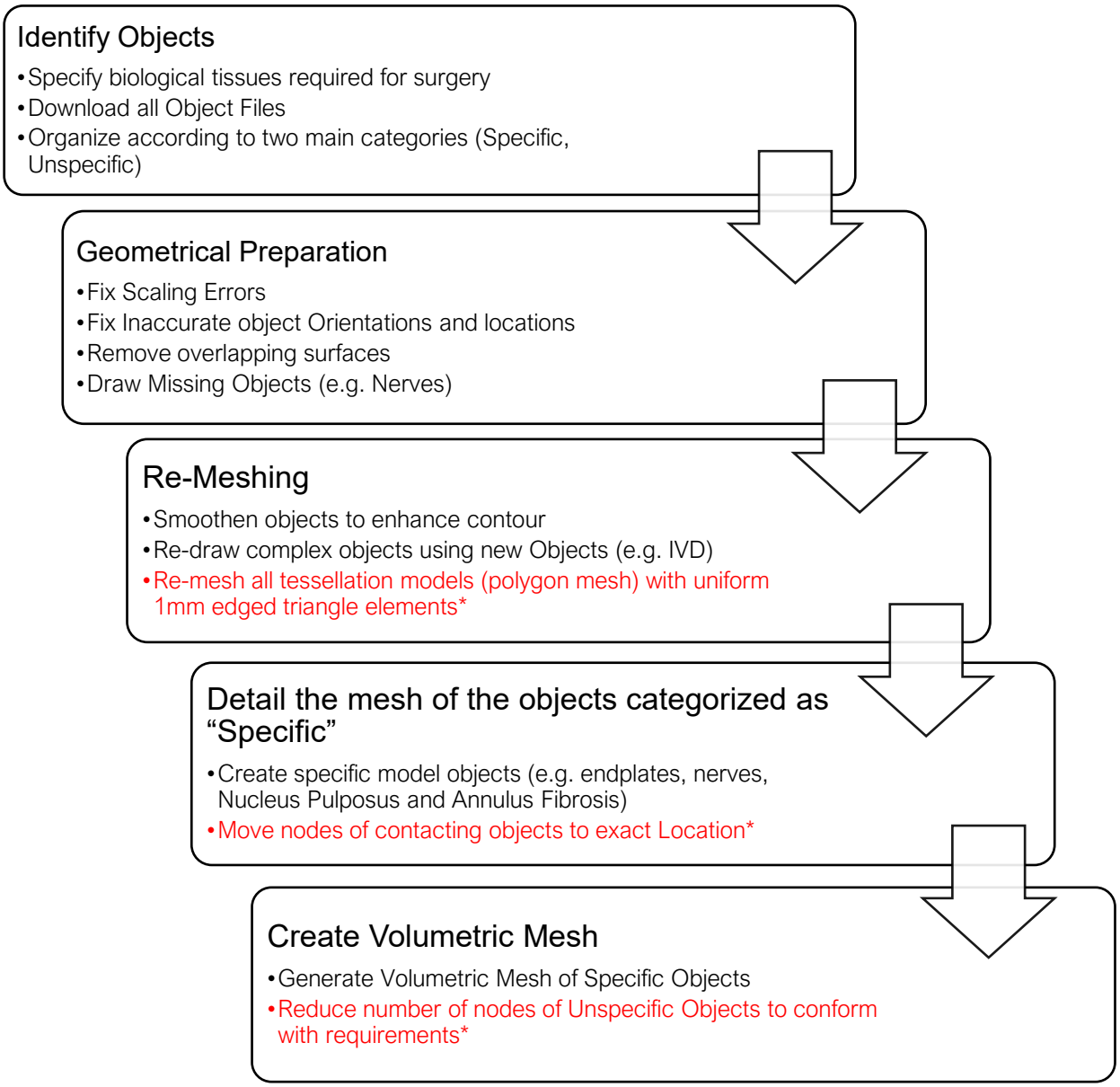

Figure 6-2: Mesh development pipeline (objects that appear in red conform to the virtual environment requirements)

The entire model was translated such that the center of the L_4/L_5 disc lied at the scene origin. Moreover, the overlapping surfaces from the segmentation procedure were removed. The nerve root object was missing from the available library; hence, it was constructed by referring to anatomical books.

The surface meshes of the tessellation models were first transformed into a homogenous mesh of constant edge size (i.e. 1 mm). However, the muscle layers were defined with an edge size of 4 mm instead. The *Shrinkwrap* tool available in Spaceclaim was utilized with *Preserve*

Feature set to *ON*. The objects were then exported as STL files to be imported into the open-source 3D creation software, namely Blender. In Blender, the objects were smoothened. Furthermore, the lower most surface of the L_5 endplate and the uppermost surface of L_4 were designated as the fixed nodes. Hence, these nodes were defined with an RGB of (255, 255, 255), but all other nodes were defined as (255, 0, 0).

In the case of contacting objects, a systematic procedure was defined to produce conforming meshes. Specifically, the annulus fibrosus, nucleus pulposus, adjacent endplates and their corresponding vertebrae were identified as being in contact. Hence, the nucleus pulposus was first selected and the lateral sides were copied/pasted then merged with the annulus fibrosis. The annulus fibrosis and the extracted sides were then imported into Blender. In Blender, the nodes of the nucleus pulposus surface were fixed in space and the nodes of the annulus fibrosis were moved to conform with the fixed NP nodes. This procedure was repeated iteratively until all the contacting nodes conformed with the NP mesh. Similarly, the endplates and vertebrae followed the same procedure ensuring that all contacting surfaces have nodes that are conforming. Figure 6–3 depicts the resulting meshes in exploded view. In particular, the Cauda Equina, Root Nerve, L_4 and L_5 vertebra were considered only as surface meshes and the rest of the components shown in Figure 6–3 were designated as a volumetric mesh which also included the muscle layer shown in Figure 6–4 (a).

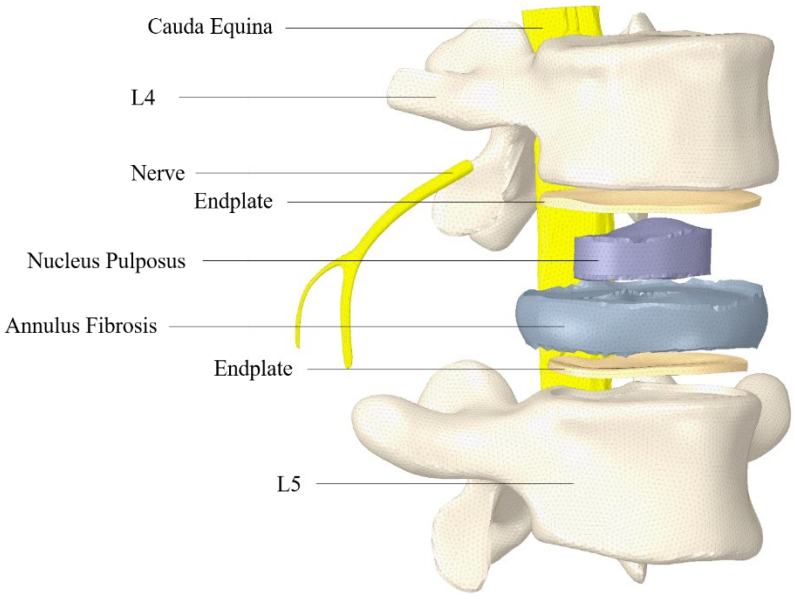

Figure 6-3: Exploded view of generated meshes

Figure 6–4 (a) depicts the visual elements added as surface meshes with a significant reduction in mesh size. This included the remaining set of lumbar vertebrae (L_1–L_3), thoracic vertebrae (T_1 – T_{12}), ribs, sacrum, hip bones, and femur. The presence of the latter elements supported realism in the visualization of the elements specifically in the fluoroscopic cameras within the system. Figure 6–4 (b) shows the two muscle components constructed for the scene. The Muscle layers were calibrated with the physical interface used and drawn accordingly. This component was designated as part of the volumetric mesh component.

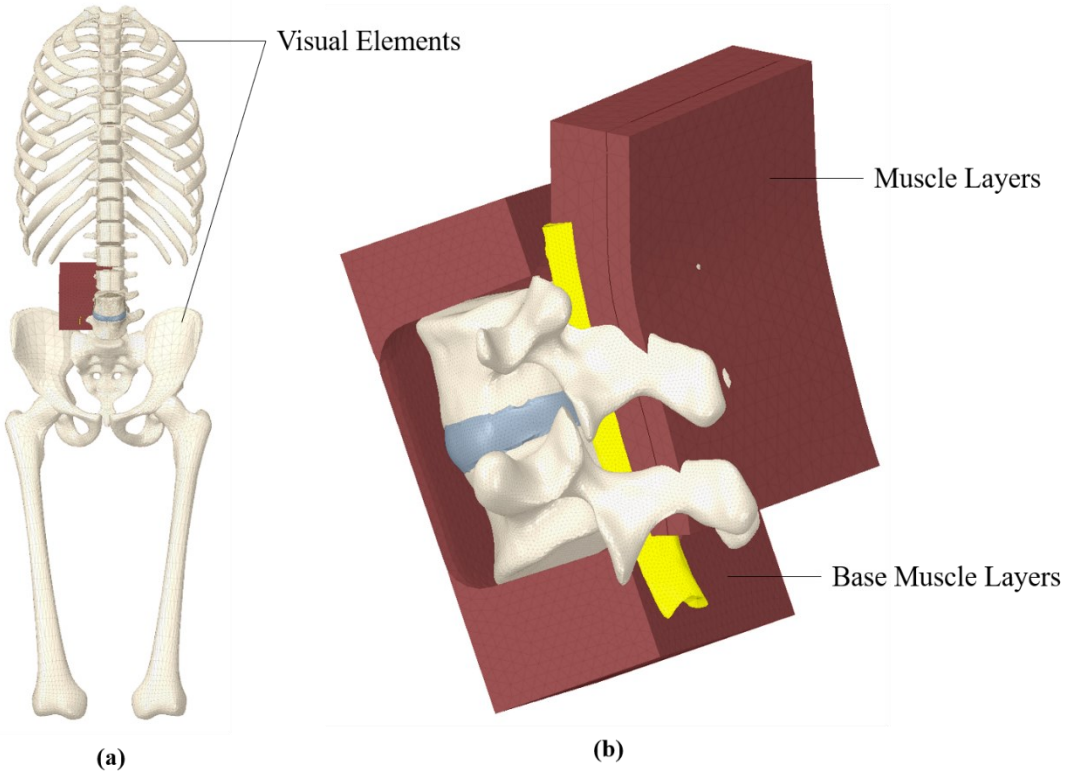

Figure 6-4: (a) Depiction of the entire geometric components and (b) a zoomed view of the L_4-L_5 vertebral unit with muscle layers

Figure 6–5 depicts the output of the verification conducted for the geometries developed. The reported deviation between the original raw models and the post-processed models shows an acceptable range with a maximum internal difference of 2 mm and an external difference of 1.32 mm. Moreover, the results show that the post-processed geometrical objects fell within the original 2–mm precision of the MRI segmentations. This satisfied the requirements set initially.

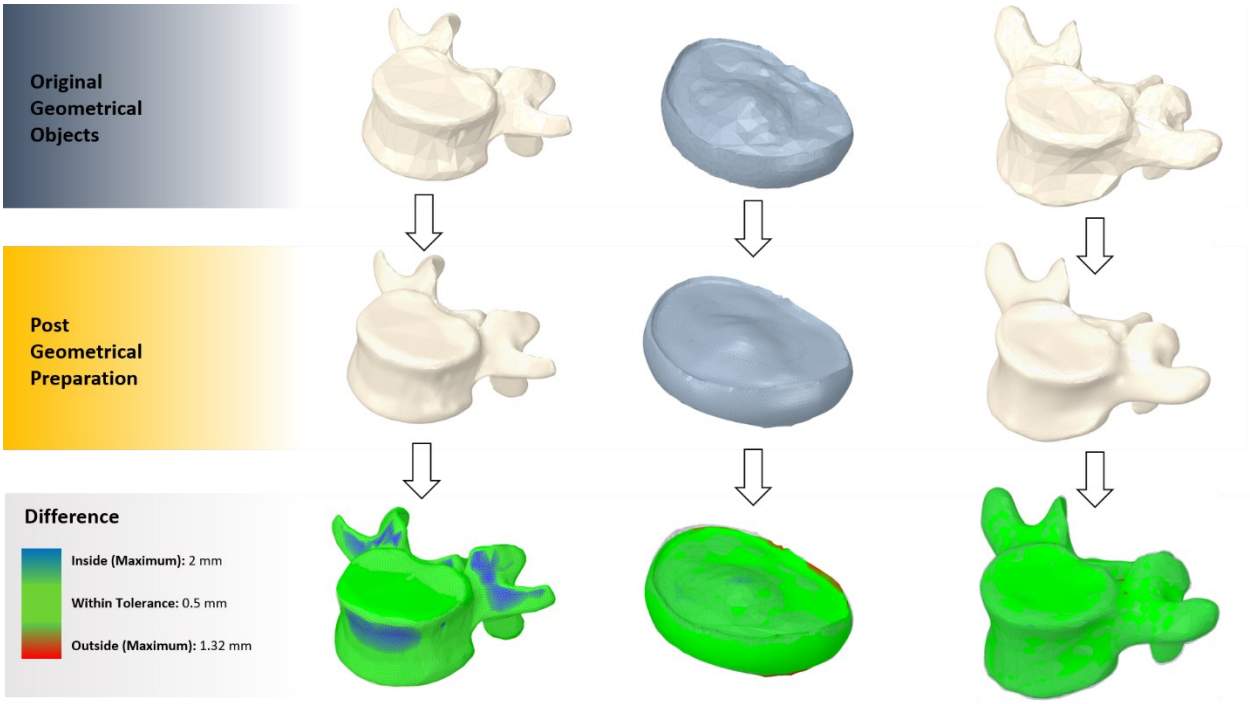

Figure 6-5: Depiction of the workflow of geometrical preparation showing original and post-prepared objects including their difference

The final step of the workflow required the generation of the volumetric mesh. The volumetric mesh generation was scoped to the top muscle layer, endplates, nucleus pulposus and annulus fibrosis. The latter objects were designated as the interactive mesh. In other words, the tool would only be able to interact with these models while the vertebrae and lower muscle layer were considered to be inactive surface meshes present only for visual purposes. The open-source volumetric mesh generator TetGen was utilized with an input of *-pqzVCYS0*. In specific, the command argument translates to tetrahedralize a piece-wise linear complex (i.e. tessellation model) with the default quality mesh generation (i.e. 2.0) suppressing any boundary facet splitting. The output mesh generated a total of 115,735 tetrahedrons as a result of a total of 35,710 facet inputs (i.e. surface mesh triangles) as denoted in Table 6.1.

Table 6.1: Generated Volumetric Mesh Statistics

Component	Facet Input Count	Tetrahedra Count
AF	9590	36329
NP	3440	13871
L4 Endplate	5396	22199
L5 Endplate	11863	25972
Muscle 1	2181	8645
Muscle 2	3240	8719
Total	**35710**	**115735**

Figure 6–6 depicts the resulting aspect ratio of the various components. The endplates, muscle layer 1 and muscle layer 2 resulted with the highest number of elements with an aspect ratio of 2–2.5, 4–6 and 2–2.5, respectively. However, the Annulus Fibrosis and Nucleus Pulposus resulted with largest element count with an aspect ratio ranging between 6–10. This is the result of having thicker layers for the AF and NP which resulted with an element formation extending from the top to the bottom layers of each of the components.

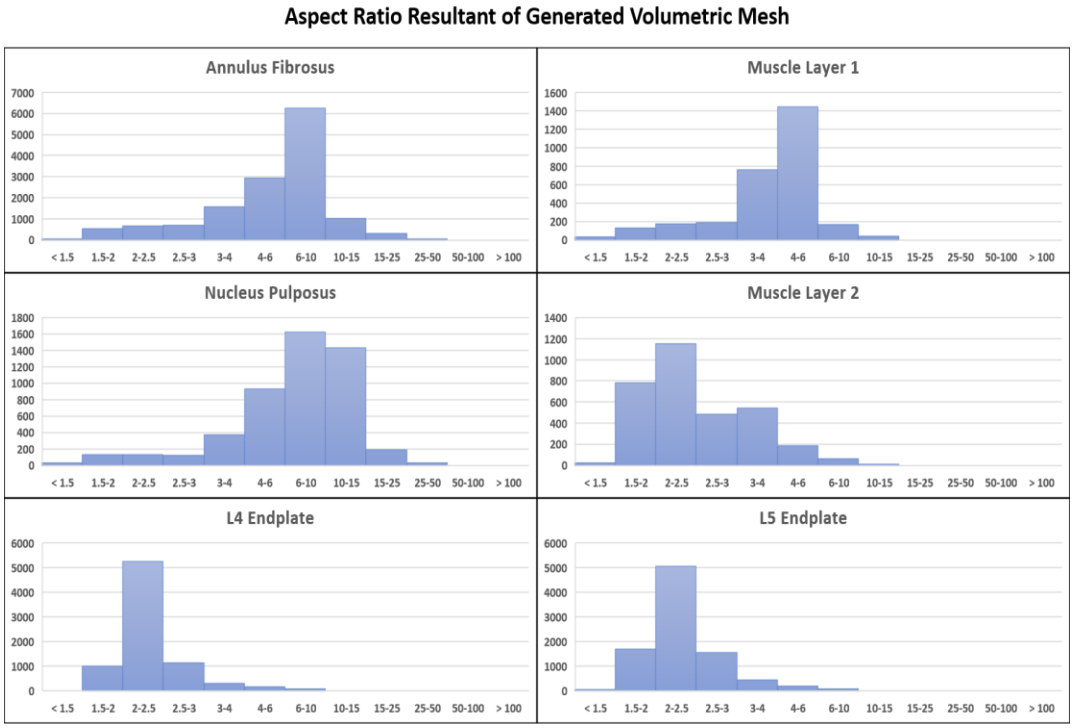

Figure 6-6: Histograms showing the distribution of elements based on Aspect Ratio as a metric for mesh quality

The overall mesh quality proved to be stable after conducting numerous trials of the simulator. The resulting mesh rendered at a mean refresh rate of 43 Frames Per Second (FPS) with no lags during the simulation. Figure 6–7 depicts the resulting volumetric mesh elements.

Figure 6-7: Resultant Volumetric Mesh

6.2. ANTHROPOMETRIC STUDY

The original data acquired from *3DBodyParts* in the previous section was extracted by segmenting 2 mm interval MRI imaging of a 22-year-old Japanese male with a height of 172.8 cm and weight of 65 kg. The volunteer was chosen based on his vicinity to the average reported Japanese height and weight for adults between 18 to 30 years old, 171.4 cm and 63.3 kg, respectively. However, the simulator targets training on the Caucasian population (European and North American). Hence, this study aimed to adjust the dimensions of the intervertebral disc and vertebra to advance the model closer to a Caucasian male. Figure 6–8 and Figure 6–9 depict the original dimensions of the intervertebral disc and vertebra, respectively.

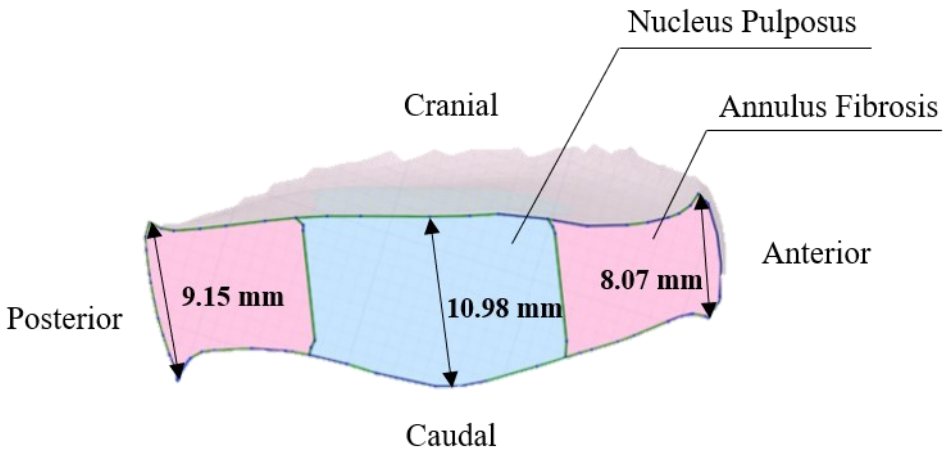

Figure 6-8: Original Japanese Intervertebral Disc Dimensions

Zhou et al. developed a database containing 378 lumbar vertebra from 126 patients who were admitted to the spinal clinic at the Hammersmith Hospital NHS Trust for low back pain [55]. In their study, they provided numerous dimensions for both male and female patients measuring vertebral features including Upper Vertebral Width (UVW), Upper Vertebral Depth (UVD), Lower Vertebral Width (LVW), Lower Vertebral Depth (LVD), Spinal Canal Width (SCW), Spinal Canal Depth (SCD), Transverse Process Length (TPL), Vertebral Body Height anterior (VBHa), Vertebral Body Height posterior (VBHp), Pedicle Width (PW), Pedicle Height (PH) and Disc Height (DH). The reported values from their study for the L_4 vertebrae, L_5 vertebrae and L_4–L_5 disc are included in Table 6.2.

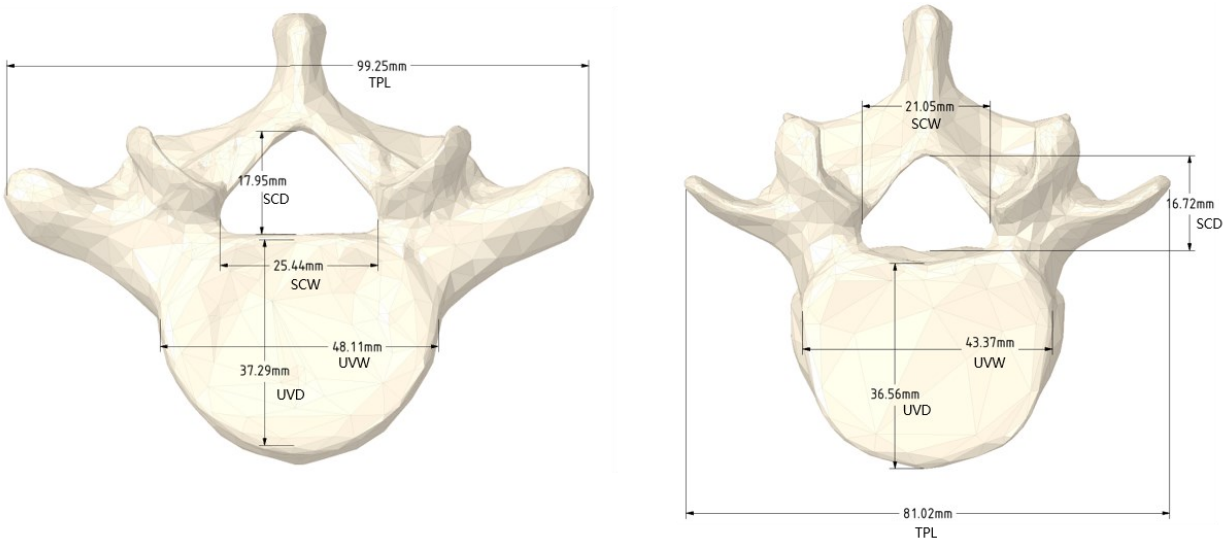

Figure 6-9: Original Japanese Vertebral Geometric Dimensions

Similarly, measurements of the disc and vertebra acquired from 3DBodyParts were extracted and included in Table 6.2. Furthermore, the percentage difference for each of the dimensions measured according to depth, width and height was calculated and reported in Table 6.2. The results conceived show a mean percentage difference of 15.52%, 1.18% and 11.55% for the width, depth, and height dimensions, respectively, of L_4 and 10.70%, 0.84% and 4.85% for the width, depth, and height dimensions, respectively of L_5 vertebra. Moreover, the L_4–L_5 disc height of the IVD in the original model, which measures at 10.98 mm, in comparison with 12.20 mm, the mean height measured by Zhou et al., had a difference of 10.53%. Hence, the L_4 vertebra may be scaled up with a factor of 1.168, 1.009 and 1.127 and L_5 scaled up with a factor of 1.100, 1.002 and 1.050 for the width, depth and height, respectively. As such, the major difference lies in the width and height of L_4 and L_5. Hence, the width and height of the vertebra may be scaled accordingly should such a model be desired.

Table 6.2: Vertebra and Disc geometric dimensions comparison

Components	Zhou et al.			3DBodyParts			Percentage Difference	
	L_4	L_5	L_4/L_5 Disc	L_4	L_5	L_4/L_5 Disc	L_4	L_5
Upper Vertebral Width (UVW)	50.8	54.5	-	43.37	48.11	-	15.78%	12.45%
Lower Vertebral Width (LVW)	55.1	56.7	-	46.8	49.51	-	16.29%	13.54%
Spinal Canal Width (SCW)	24.7	29	-	21.05	25.44	-	15.96%	13.08%
Pedicle Width (PW)	13.2	17.5	-	11.33	15.64	-	15.25%	11.23%
Transverse Process Length(TPL)	93.5	96.1	-	81.02	86.21	-	14.30%	10.85%
Upper Vertebral Depth (UVD)	36.4	37.6	-	36.56	37.29	-	0.44%	0.83%
Lower Vertebral Depth (LVD)	38.6	38.3	-	37.82	37.98	-	2.04%	0.84%
Spinal Canal Depth (SCD)	16.9	17.8	-	16.72	17.95	-	1.07%	0.84%
Vertebral Body Height Posterior (VBHp)	29.6	26.7	-	25.93	25.52	-	13.22%	4.52%
Vertebral Body Height Anterior (VBHa)	31	31.5	-	27.72	29.67	-	11.17%	5.98%
Disc Height (DH)	-	-	12.2	-	-	10.98	10.53%	-
Pedicle Height (PH)	14.8	14.9	-	13.22	14.31	-	11.28%	4.04%

Regarding the intervertebral disc, a 1.111 scaling factor should be applied. The disc data of lateral width and AP width after the scale also meet the reported data [458]. The sitting height of the model after scaling would also meet the reported Caucasian anthropometric data of 94.5 cm in comparison with the original mode measuring 98.5 cm, a 4.2% difference but within the ceiling of standard deviation of the reported data (1.3%). However, in a study conducted in the United States whereby comparison of the IVD height was conducted between different species [459] measured the IVD height as 11.3 mm and designated that figure as a representative medial value. This would result with a 2.87% difference. Furthermore, a study comparing IVD morphology in Germany for Degenerative Disc Disease reported a value of 11 mm for a Grade II degenerated disc of a male of age 37 years old at the L_4–L_5 level [460]. In other words, the height of the original disc may be representative of a degenerated disc for a Caucasian should it remain intact. The original Japanese model was maintained within the simulator and the development was conducted on that basis. However, the outcome of this study leading to the scaling factor adjustments were made available should the models be needed.

6.3. Access Gaining Module Development

The following section describes the development of the access gaining module. The components achieved in the previous sections were developed to lead to their integration into the base platform constructed within a VR-ready environment. It is worthy to note that certain sensitive details specific to the scene backend development including photographs depicting the specific hardware used were omitted to respect the confidential obligations requested by the research's industrial partners. Hence, no discussion of the software, its compatibility, architecture and usability were included within this dissertation.

Any VR scene may be thought of as a simple 3-Dimensional regular grid that allows the developer to place geometrical objects at certain coordinates and manipulate their behavior. It is customary within the VR field to label such an environment as a scene. In general, real-time rendering platforms require geometrical objects to be modelled via tessellation-based models; polygonal meshes. This is the result of the inherent advantage that polygonal meshes possess which allows for the manipulation of vertex sets and runs compatible with dataset management methods of graphic renderer Application Programming Interface (API) such as OpenGL and

Direct3D. In general, polygonal meshes are a collection of vertices, edges that connect them and the corresponding faces which bound together to form the object's 3D surface. These interconnected triangular (or rectangular) faces store information that would be used by the rendering engine to calculate certain visual aesthetics such as lighting and shadows. This is, in contrast to the smooth analytically constructed surfaces normally used in Computer Aided Design (CAD) software. Figure 6–10 depicts the triangular faces that form the bounding surface of the vertebral object and its corresponding reverse–engineered spline model.

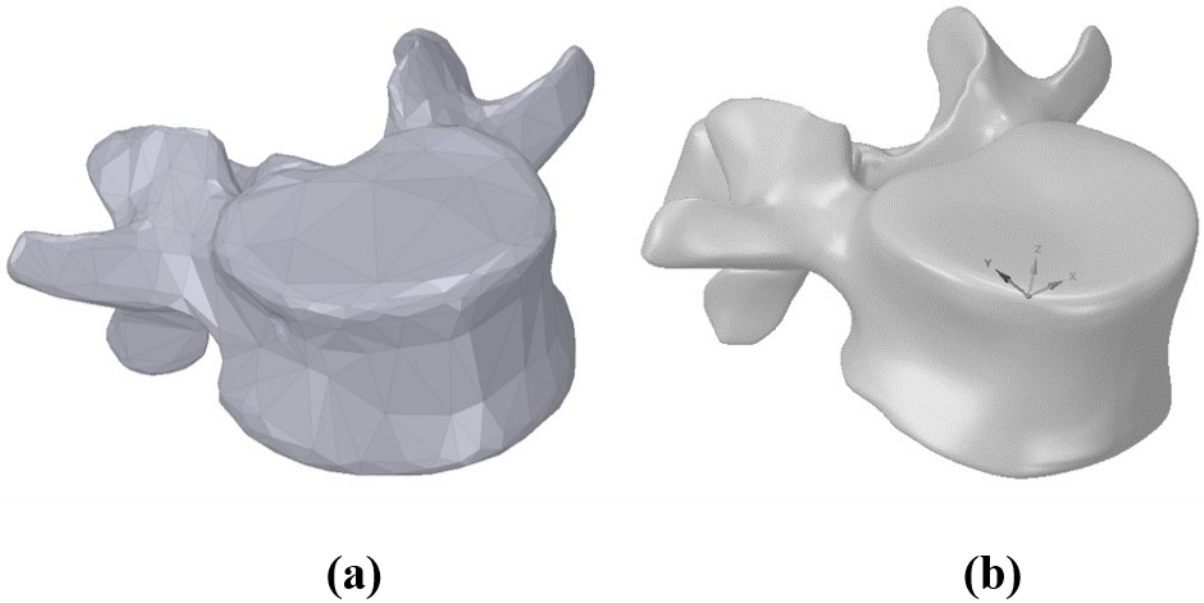

Figure 6-10: Depiction showing the difference between a (a) polygon model and (b) spline model

In addition to the geometric models, two main components are normally added to each VR–specific scene to bring the scene closer to reality, geometrical models are usually patched with surface material properties which define features such as color, refractive index, opacity and texture. In all cases, an object added to the scene may be designated as a child object to a parent and, if so, would inherit the component's transformation. Preparation of the scene necessitates the definition of other components including physics-based components that identify pre-sets in the scene including gravity. In addition to the main components, navigation and movement components define the controller methods of the object's behavior and dynamics within the scene. The components added to the scene would have the capability to be manipulated through

various features either previously embedded within the software utilized or would require additional programming. As previously mentioned, programming methods, for this work in particular, were implemented using LUA integrated scripts. Such implementations define the response of the objects' transformations, deformations and morphology subject to external controllers assigned to specific peripheral assets. Events predefined within the scene identify the flow of the simulation such that triggers based on specific monitored data during real-time simulation dispatch the events. This allows for the development of various predefined scenarios that engage according to the predefined triggers. In addition to the backend development of the VR scene, a graphical user interface patched to the software used is usually prepared to conceive a user-friendly platform capable of interacting with the user, performing systematic procedures, and providing insightful metrics at the completion of the simulator.

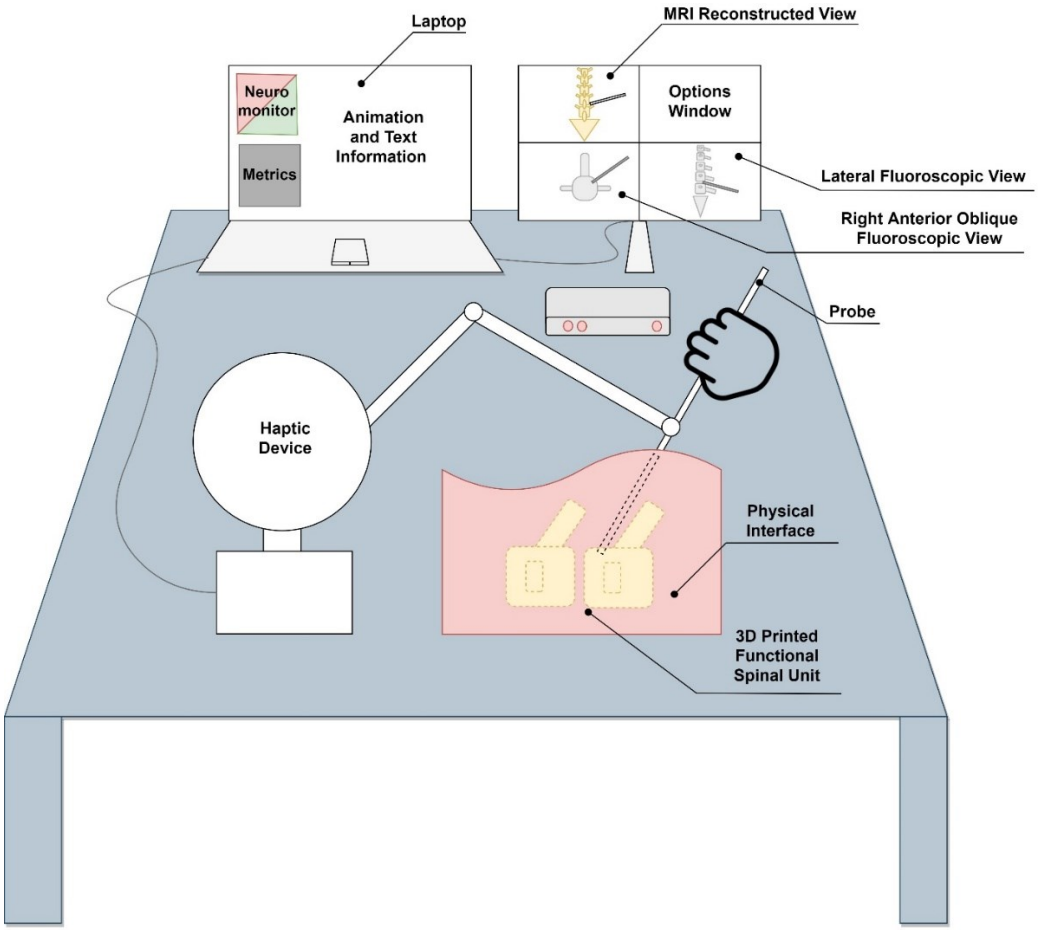

Figure 6-11: Module Simulator Setup for Access Gaining Stage 1

Figure 6–11 depicts a schematic of the access gaining module setup set at the first stage. The simulator comprised of an MSI GT73VR 7RF Core i7 3.5 GHz 64GB RAM portable desktop equipped with an NVIDIA GTX 1080 GPU defined as the central hub which operates the scene. Connected to the portable desktop was a second touch screen that was divided into four main quadrants. The first quadrant rendered an MRI Reconstructed view of the spine capable of overlaying the tool's transformation in space. The second quadrant presented a set of options that could be selected by the user to turn the aiding tools ON or OFF. The third and fourth quadrants were Anterior Oblique and Lateral fluoroscopic views overlaying the tool's transformation. The relevant textures were added to render a reconstructed and fluoroscopic view realistically. Both the portable desktop and the second screen extension rendered the scene through the constructed Graphical User Interface (GUI). The portable desktop also connected with the Entact 5–DOF haptic device using an ethernet cable. The haptic device peripheral arm was mounted with the probe tool. The physical probe interacts with a physical interface that comprises of soft layers that mimic muscular tissues of which contained a 3D printed L_4–L_5 functional spinal unit. The 3D-printed FSU was constructed using the original vertebral models detailed in Chapter 6.2.

The tools utilized for the access gaining module included the following:

- Probe
- 3-piece set dilators
- Port
- Port–Table fixture

These tools were the original set utilized in the Oblique Lateral Lumbar Interbody Fusion Surgery. Figure 6–12 depicts five surgical tools embedded within the physical interface. In reality, the number of tools utilized within this stage are more than five as described by Abbasi et al. [277]. Specifically, the toolset includes:

1. *Guidewires* that aid the surgeon in fluoroscopic imaging to estimate the position of the disc with respect to the skin;
2. *Markers* to specify the initial point of entry on the skin;
3. *Scalpel* to incise a cut through which the probe tool is inserted;

4. A *probe* (Dimensions shown in Figure 4–2) whereby the surgeon holds to puncture through the tissue;
5. *Dilator* set that slide on the probe to reach the intervertebral disc and expand the tunnel created;
6. *Port* that provides direct visual exposure of the disc from the skin.
7. *Port-Table Fixture* to fix the port relative to the table

The first three tools were not included within the simulator. This was not possible given the adoption of a physical interface that would reduce its lifetime as a result of cutting and marking. Moreover, the usage of these three tools is relatively straightforward and may not present a high risk in comparison to the main tool (4). Hence, training for these tools were not included within the simulator and not included within the toolset. Furthermore, the dilators (5), port (6) and port-table fixture (7) were present within the toolset available to the user when conducting the surgery using the simulator. However, 5, 6 and 7 do not show up in the virtual scene (with the exception of the inner wall of the port which is fixed). Hence, only tool 4 was employed in the simulator and connected with the haptic device. Furthermore, tool 4 from the toolset (i.e. probe) was the only tool accounted for in the experiments.

The access gaining module may be divided into three main stages that mark its beginning and completion. The first stage, shown in Figure 6–11 denotes the stage whereby the user handles the probe that mounts onto the haptic arm to puncture through the muscular layers moving along the L_5 transverse process towards the pedicle to reach the intervertebral disc. Within this stage, a neuro-monitor component programmed using a LUA script continuously calculates the distance between the probe's tip and a total of 36 spheres spread along the nerve's geometrical object. Should the calculated distance be less than the threshold set by the user, the neuro-monitor box shown within the portable desktop of Figure 6–11 turns red. Furthermore, an event was set to engage an alarm sound notifying the user that the distance has fell below the set threshold. The sound component was integrated into the system by importing a recorded sound similar to the actual neuro-monitor used in the surgery. The successful completion of this stage was marked by an event that captures whether the probe tool has contacted the disc nodes. The lower left corner of the portable desktop screen, shown in Figure 6–11, displays an area specific for metrics. For this module, four displayed metrics were specified:

1. Time to reach the intervertebral disc (seconds)
2. Was the disc reached successfully (Yes/No)
3. Is the user operating within the trajectory set as a requirement (Yes/No)
4. Minimum Distance to Nerve (mm)

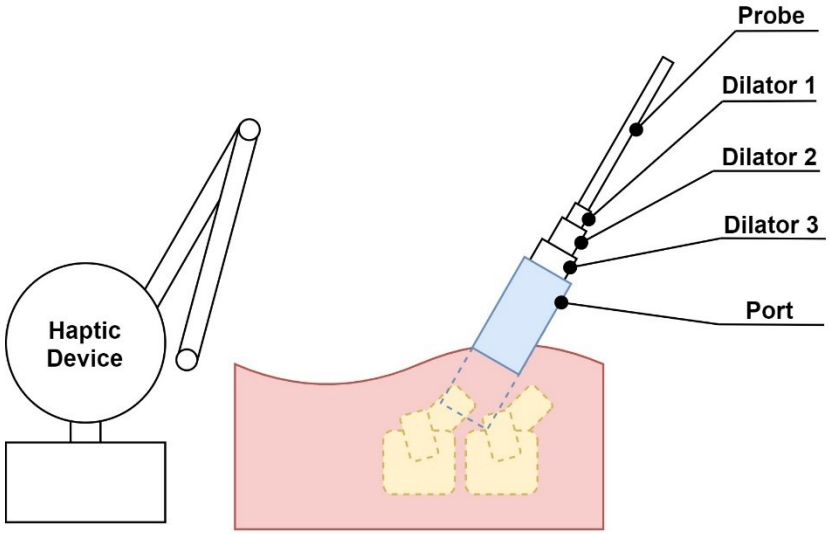

Figure 6-12: Module Simulator for Access Gaining Stage 2

It is worthy to note that a distinction was made between metric 2 and metric 3 as some surgeons may realize that trajectory they achieved when reaching the disc may not be ideal. Hence, even though the user reached the disc, they may find it necessary to conduct adjust the trajectory conceived by the probe. An aiding tool was added to help the user during the simulation should they require assistance. In specific, a feature that highlights a conical region of entry such that the tip of the cone lies within Kambin's Triangle. Should this feature be activated by the user, a highlighted cone oriented such that its base-to-tip spans from the outer skin to the intervertebral disc. Moreover, a video depicting the steps to be followed were made available to the user should they require assistance with the procedure tasks. In addition to the video demonstrating the surgical steps, text was made available to the user that follows their progress and explains the next steps based on the events dispatched. The aiding tools were added into features within the option menu such that the user may switch them based on their need.

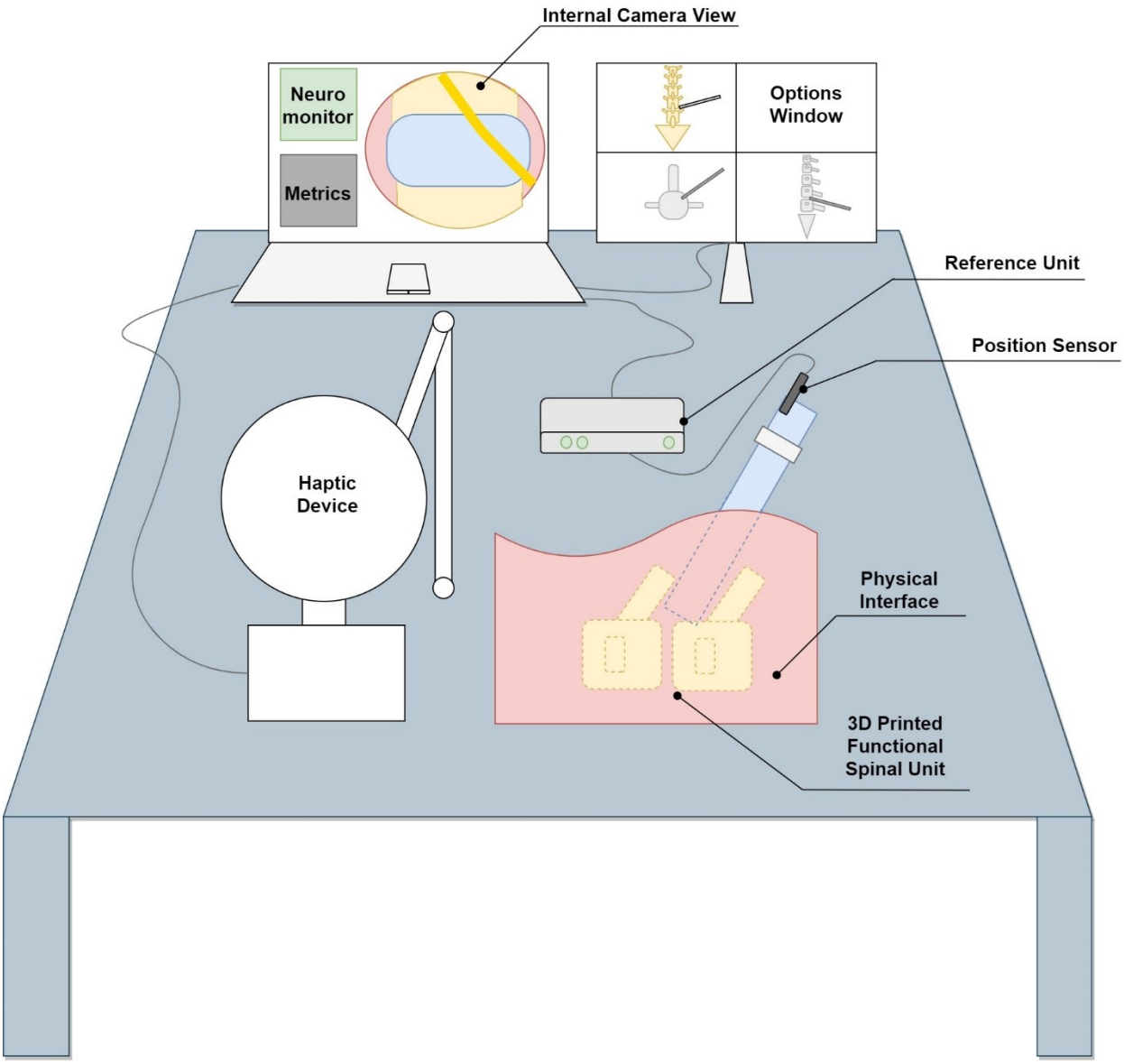

Figure 6-13: Module Simulator Setup for Access Gaining Stage 3

Upon achieving the intervertebral disc, the main window was made to switch to show to a video demonstrating the steps of the stage 2. During this stage, the haptic device was made to automatically switch off and no positional tracking or force response would be recorded. Hence, the user would dis-engage the probe from the haptic arm and the physical interface along with the surgical tools would be required. Figure 6–12 depicts the setup tasked by the user to complete this stage. Once the assembly is completed, the user would remove the probe and

dilators keeping the port only in place, as shown in Figure 6–13. The screens only provided assistance at this point working towards completing the assembly.

The last stage marks the completion of the access gaining module. Once the user was satisfied, they would be prompted to press on an additional metrics button which provides a view of the results achieved. Two metrics were made possible using the integration of the public domain script-driven engine for data visualization and curve-fitting, namely GNUPLOT. The first result was programmed to depict the recorded tool tip position throughout the entire simulation. The second resultant depicts the trajectory recorded of the tool when the intervertebral disc was punctured.

Calibration was a necessary task when developing the simulator. Specifically, the calibration was conducted to ensure that the haptic device which controlled the position of the tool in space and transformed the tool object in the scene was at the exact position with respect to the vertebral bodies in the scene in comparison to the 3D printed vertebral bodies. Hence, to simplify the situation a script was made to connect with a button found within the options menu such that if it were pressed, the tool resets to a position within the scene to a specific location. Thus, the user would place the tool at a pre-designated location within the physical interface then press the calibration button so that the tool moves to the location. The distances along each axial direction would be calculated then applied to the translational transformation to adjust the location of the tool in the scene. Rotational calibration was not necessary given the position of the physical interface; thus, only translational calibration was applied. In addition to the tool calibration with the 3D printed and virtual vertebral objects, the force-displacement curves were adjusted to initiate from the top-most layer of the physical interface to signify puncturing and penetration into the muscular layers.

The frame rate target maintained throughout the entire development steps was maintained at 40 FPS to ensure no lags would be evident to the user. This was successfully achieved using the addition of the graphical components described in Chapter 6.1 which balanced between visual realism and performance. To accommodate the port view, the tool tip was made to kill the muscle and intervertebral disc volumetric elements upon entry. Hence, as the user penetrates the muscle, the contact volumetric elements were killed. The described haptic responses and algorithm in Chapter 5.2 were programmed accordingly and integrated based on the calibration achieved between the physical interface and virtual model.

7

GENERAL DISCUSSION

VR simulators for medical training offer a great deal of advantages over conventional methods including faster setup times, cost effectiveness and quantifiable objective metrics [372]. This has been observed as beneficial especially with the development of MIS surgical procedures [361-364, 367]. A literature review of simulators indicated, however, the constraints and challenges facing current real-time VR simulators.

To account for these issues and construct a training platform for the first stage of the OLLIF spinal fusion surgery, a VR simulator was developed. The purpose of this thesis was to develop a surgical VR simulator of the access gaining module of the OLLIF procedure employing cadaveric experimental data to bring forth an objective training platform utilizing accurate MRI-based virtual objects.

The construction of the virtual model was an integral aspect of this thesis. The geometric objects proved to be useful for both real-time and offline simulations. The number of employed objects within the model was constrained to a reasonable number to suffice for real-time purposes for the VR model to permit a 43 frames-per-second (FPS) rendering rate. A minimum requirement of 30 FPS for the animation rate ensures no visual lags would be present [461]. It is important to note that although the real-time requirement is the major aspect in this thesis, the accuracy of the models used remains a crucial element given that simulator was developed for surgical training. Monserrat et al. noted that most previously developed simulators hardly satisfied both real-time computation speed and anatomic accuracy [462]. Thus, the results of comparing the processed virtual bodies and original MRI-based models showed that a maximum deviation of 1.32 mm externally was computed. This value remains less than the precision of the original bodies imported from the online database which set the MRI imaging spatial resolution at 2 mm [446]. While the visual objects did not affect the haptic response, the movement of the connected tool affected the visual objects created. In other words, the insertion

of the tool within the physical interface, deleted the contacted elements of the virtual object. This would create an accurate hole which becomes visible when the user moves on to the final stage of the surgery. The technique to delete mesh elements upon contact has been previously used in real-time operations [463]. This has, however, advanced to use current adaptive [464] and FE-based techniques [465]. However, the mesh of the muscle within of puncturing were reduced in size (i.e. 1 mm) to accommodate an accurate puncture such that the 4-mm-diameter tool exceeds the mesh significantly.

In general, the MRI models were extracted from the imagery of a Japanese male representative with morphological data representative to that of the Japanese population. Given that the target audience for utilization was North America and Europe, an anthropometric study was conducted to analyze the various features of the anatomical objects conceived. However, the author recommends that such MRI-based models be directly employed without scaling adjustments to maintain fidelity. It is worthy to note, that given the systematic methodology of geometrical construction, the use of the tessellation models of different patients permitted the 3D printing of the Functional Spinal Unit directly to be embedded into the physical interface. This workflow allowed for an effortless integration of patient-specific data suitable for current technologies. In specific, MRI data from patients spanning along the functional spinal unit of interest would initially require segmentation to achieve tessellation models which, using the workflow constructed, would, then be prepared and 3D printed to be integrated into the simulator. While the developed workflow achieved models within a reasonable timeframe, segmentation was not included. However, recent developments in computer vision have allowed for better image processing [466]. This, in turn, has allowed for the development of algorithms that can automatically identify the areas of interest and detect its boundaries [467].

Additionally, the virtual model permitted the construction of 2D and 3D models suitable for simulating force transmission within various structures in different postures. To some extent, assumptions were adopted to achieve convergent results within a reasonable time frame. However, despite the simplifications, additional validation and verification were conducted to ensure that results held true within the scope of study. Such analyses allowed for gaining engineering and clinical insights on in-body force transmissions without any external surgical intervention. This would serve as the initial state defining the pre-loading and boundary conditions of the real-time VR module as it would be defined within the pipeline of a general

offline Finite Element simulation. Nevertheless, several previous studies marked the use of offline FE methods for real-time simulation. Gibson et al. employed an offline FE solver for detailed deformation and stress/strain data which updates the real-time simulation [468]. Huynh et al. rendered haptic feedback using a simplified beam FE spine model based on an offline detailed FE model to analyze the biomechanical response of intervertebral discs [469]. In this study, the developed offline model was used to define the boundary conditions of the simplified online model. However, given the limitations of the in-house virtual reality framework adopted, the inclusion of a FE-based pipeline was not possible. Specifically, the refresh rate decreased to 5 Hz upon the insertion of a single set of the Erector Spinae when the minimum refresh rate requirement was 30 Hz. Thus, the muscle layers were cut to smaller dimensions covering the area of interest only. However, this resulted with an increase of graphical frame rate up to 18 Hz rendering it ineffective. Thus, the muscle layers were reduced greatly as described in Chapter 6.1. This resulted with refresh rates at 43 Hz. However, upon connecting the haptic device, the system experienced a great of lag given that the visual thread defined the bottleneck, running at 43 Hz, which remained well below the human haptic perception threshold. Hence, the pipeline was changed to directly utilize the experiments while maintaining the frame rate such that the haptic feedback operates independent of the visual computation. This separated the haptic rate from the visual refresh rate which would better meet the requirements of real-time. Thus, the extracted boundary conditions were not directly used for the development of the VR module. Nevertheless, the constructed study provided insight on the tissue within the surgery.

Initially, a 2D model for an FE study that incorporates the Thoracolumbar Fascia and Intra-abdominal Pressure at the L_3 spinal level was conducted utilizing the MRI-based models. In specific, TLF involvement is often neglected when studying the biomechanics of the spine. Hence, in addition to the general purpose serving the construction of the foundation for the 3D model and, ultimately, the initial state of the real-time model, the purpose of the study was to develop, validate, and explore the use of a novel finite element model of the spine, inclusive of the Thoracolumbar Fascia, paraspinal muscular compartment (PMC) and the Intra-Abdominal Pressure (IAP) based on published clinical studies. Reaction forces were probed to five critical anatomical locations that would generally serve as the boundary conditions for the VR model and provide insight in spine biomechanics in general. The results showed that elevated IAP decreased the posterior force and balanced the anterior forces when PMC pressures were

asymmetric. This novel finite element study demonstrated a link between the TLF compartments which may play role in spine biomechanics given the variations observed. Such observations have been observed given the force transmission between the caudocranial and transverse directions. In particular, Norris defined the term “hydraulic amplifier” whereby the contraction of the erector spinae resulted with a girdling structure around the spine [470]. Most importantly, the validated model provided a basis of validation for the construction of the 3D model required to extract boundary conditions that may be used within the pipeline of an FE-based real-time VR simulation. This further highlighted the force transmission occurring between the different directions. Furthermore, the 3D analysis expanded the study by incorporating the follower load which raised the force magnitudes to higher values at the different postures. This was a necessary step to undertake to ensure that the quantities achieved were modelled realistically. Particular attention was given to prone positions and degraded discs which investigated the forces pre-existing within the body prior to any external intervention. However, further studies are required to directly validate the spinal forces using clinical experimentation. Moreover, patients with LBP have shown variations beyond just the height and material properties of the intervertebral disc. For example, apophyseal joints may undergo morphological changes [221], the Annulus Fibrosis may develop increased lesions [215] and the endplate thickness may decrease [58].

As for any FEM analyses, one must remain aware of the constraints and limitations imposed. First, as previously described, assumptions were made that simplify the actual complexity within the human body. These must be further explored to understand the possible impact of expanding the number of objects included within the FEM. Second, material properties used were assumed to be linear. While the study at hand aimed for a static analysis, viscoelastic effects may further adjust the achieved boundary conditions. In general, while such analyses provide insightful information, one must remain conservative in ensuring that the insight gathered remains deductive in comparison to absolute values.

The next objective was the development of a haptic model suitable for real-time accurate force feedback. To achieve this, an experimental cadaveric study was conducted to extract the response behavior of the tool-tissue interaction. The employment of cadavers to extract forces for the benefit of haptic feedback has been conducted in previous studies. Lim et al. extracted force-displacement profiles for the indentation of human liver to achieve nonlinear viscoelastic models for real-time simulation [471]. However, they utilized the haptic device directly to extract the

forces instead of utilizing a tensile testing machine. Lin et al. utilized cadavers for surgical simulators. In contrast to the work presented in this thesis, their pipeline consisted of creating a bone drilling then validating a bone drilling force model [472].

In comparison to adopting a specific model from the previously developed models as described in the literature, an algorithm was developed that directly implements empirical data from cadaveric experimentation. This further mitigated the absence of a physics-based platform. Given the setup, it was observed that the algorithm may be developed without any need of direct communication with the developed scene. In specific, the haptic feedback operated at ~1 KHz, a value meeting the requirement for real-time purposes [466]. In that case, the tool orientation and tooltip position in space determined the force feedback. Curve-fitted coefficients of 2^{nd} order polynomials sustained a controlled output of the haptic position and force output. Pelliccia et al. developed a cadaver-based biomechanical model of acetabulum for medical simulators [473]. Force and torque profiles were similarly extracted from mechanical tests under similar conditions to the hip surgery. As such, they adopted cubic splines for the representation of their data. However, the representation would not account for punctures. Moreover, Pepley et al. utilized cadavers to extract needle forces into a haptic robotic simulator [474]. Similarly, they adopted a piece-wise function to describe the force profiles. Nevertheless, they utilized an exponential function to describe the forces. The use of such form functions would result with a significantly larger number of coefficients if adopted for this study which reduces the flexibility desired of the system. Force-Displacement curves were chosen given their inherent universal convenience which may be extracted via cadaveric experimentation or *in-silico* computation whereby variations may be accounted for by updating the polynomial coefficients directly. Alternatively, the implementation of the curve-fitting may be conducted using a Fourier Series, however, it may require higher orders to better capture the minor variations of the response. This has been previously conducted in simulators for needle insertions [475], however, this algorithm extends the haptic feedback to a multi-dimensional viscoelastic behavior.

While the response achieved via the algorithm provided realistic behavior based on experimental results, the data remains empirical. Hence, one must acknowledge the high variability that exists among the population. While mean values of the population were adopted for this study, patient-specific variations may affect the morphology, position and behavior response of the vertebra, intervertebral discs and nerve roots. As such, further research tailored

towards a better understanding of the variation that occurs may permit a better representation of the different pathomechanisms. For instance, a healthy intervertebral disc was adopted within the simulator, however, patients that reach to the point that surgery must be conducted would have a degenerated disc of Grade III or higher. Hence, such variations should be incorporated for a realistic training platform. Inoue et al. presented the structural changes that may occur in degenerated discs [216].

In addition to the variability, it is worthy to note that a stable control system should be embedded within the haptic thread for a closed control-loop feedback. The need for such control was highlighted at high force differential position specifically when the tool penetrated through the muscle and moved towards the intervertebral disc. Moreover, high force magnitudes reached when progressively puncturing through the intervertebral disc has at times invoked the occurrence of instabilities. Carignan et al. highlighted the importance of incorporated closed-loop feedback control for haptic simulation [476]. In particular, the quality of the force feedback would be enhanced. However, it is important to note that the implementation of a closed-loop system may result with the loss of the direct punctures that occur. Hence, at the time of writing this thesis, a control system was under development by the team in the Musculoskeletal Biomechanics Research Lab at McGill specifically tailored for this application.

To date, there have been no spinal fusion medical simulators developed for training specifically for the access gaining module. The simulator developed herein showed promising results in terms of user experience, user-friendliness, immersion and accuracy in various trials conducted. Hence, this achieved a successful simulator platform suitable for expanding to the next modules to complete the surgery.

8

CONCLUSION AND PERSPECTIVES

This doctoral dissertation achieved a VR module of the Access Gaining stage of the OLLIF procedure. A workflow was developed for the geometrical preparation of the acquired MRI-based segmented tessellations. This permitted the development of both an offline FEM analysis that would serve a real-time model suitable for VR simulations. While the outcomes of the offline simulations were not directly utilized in the VR simulator, the developed 2D and 3D FEM allowed for the exploration of possible biomechanical mechanisms underlying the interaction between the spinal components in different postures. Furthermore, the follower load applied in the 3D model showed to have the largest impact on the elevation of the forces probed at different critical positions within the spinal structure. The force transmission was particularly interesting to explore in the prone position given that that the OLLIF surgery requires a prone positioned patient. Evidently, the TLF experienced higher axial tensioning in a prone position with LBP when compared with normal inputs. Additional studies that examine the force transmissions via *in-vivo* experimentation and the effect of time-dependent material properties are recommended. Moreover, the effect of incising the fascia prior to insertion of the tool serves to prepare the initial state of the VR model more accurately.

In parallel to the offline simulations conducted, the geometric model was subject to an anthropometric study that investigated the morphological differences between average males of Japanese origin compared with a European Caucasian origin. The scaling factors were presented conservatively for each geometrical object used. However, it is recommended to follow original MRI patient-specific data to maintain the integrity of the model. While mean values present representative values, they may not represent patient-specific variability.

The experiments conducted were successful and provided cadaver-based data describing the soft tissue response of the basic components incorporated within spinal procedures. The force

outputs were analyzed and modelled to achieve actual patient-specific output. Inevitable variation among the data conceived was observed, however, mean values presented a reproducible output applicable for real-time rendering. In addition to achieving the mean output, the cadaveric muscle was compared with porcine muscle. This explored the interesting aspect typically observed should cadavers not be available for experimentation; the use of porcine samples may be representative of the values. Evidentially, the porcine samples resulted with a similar puncturing pattern with mean force values falling within the standard deviation of the human samples. Given the use of a physical interface and the inevitable interaction of the tool with its layers, the experiments were similarly conducted on the physical interface to quantify the resistance as a result. However, in analyzing the forces conceived along the varied slit sizes, it was noticed that the designation of a cross-slit may result with a significant resistance. This rested the concerns regarding possible unwanted force resistance with the capability of ensuring that all forces accurately render from the haptic device only.

The developed algorithm successfully rendered the output force responses. This offered a valuable insight for any future module development that can mitigate the communication between the haptic device and the scene elements. The resultant algorithm showed that such a technique may allow for the rendering of force responses at high refresh rates without concern of it affecting or being affected by the virtual scene events. One must remain aware of the calibration and adjustments required should a change in the patient be required. Furthermore, a closed loop feedback control system must be patched to ensure instabilities do not arise during the simulation.

The inclusion of the various components of the scene resulted with a successful immersive VR medical simulator capable of rendering accurate force responses and virtual models at high frame rates. Moreover, the simulator accurately modelled and presented metrics that may provide essential assessments of the user's performance. Further research, however, should be conducted in working towards benchmarking and quantifying metrics for a successful output. It is advisable that the next phase of development includes face, construct and content validity on the module to ensure that the system works as intended. Moreover, future incorporation of an FE-based pipeline for a higher accuracy of tissue response and behavior can further leverage the immersion aspect of the VR module developed.

References

[1] C. Glenday, *Guinness world records 2015*. Bantam, 2015.

[2] C. Glenday, *Guinness world records 2017*. Bantam, 2017.

[3] M. M. Panjabi, "The stabilizing system of the spine. Part I. Function, dysfunction, adaptation, and enhancement," *Journal of spinal disorders,* vol. 5, pp. 383-383, 1992.

[4] E. Hamed, I. Jasiuk, A. Yoo, Y. Lee, and T. Liszka, "Multi-scale modelling of elastic moduli of trabecular bone," *Journal of The Royal Society Interface,* vol. 9, no. 72, pp. 1654-1673, 2012.

[5] F. Mollica, L. Preziosi, and K. R. Rajagopal, *Modeling of biological materials*. Springer Science & Business Media, 2007.

[6] L. Gibson, "The mechanical behaviour of cancellous bone," *Journal of biomechanics,* vol. 18, no. 5, pp. 317-328, 1985.

[7] M. Kurutz, "Finite element modelling of human lumbar spine," 2010.

[8] M. Driscoll, "Design, optimization, and evaluation of a fusionless device to induce growth modulation and correct spinal curvatures in adolescent idiopathic scoliosis," École Polytechnique de Montréal, 2011.

[9] M. Dreischarf *et al.*, "Comparison of eight published static finite element models of the intact lumbar spine: predictive power of models improves when combined together," *Journal of biomechanics,* vol. 47, no. 8, pp. 1757-1766, 2014.

[10] V. K. Goel, S. A. Ramirez, W. Kong, and L. G. Gilbertson, "Cancellous bone Young's modulus variation within the vertebral body of a ligamentous lumbar spine—application of bone adaptive remodeling concepts," 1995.

[11] S. A. Shirazi-Adl, S. C. Shrivastava, and A. M. Ahmed, "Stress analysis of the lumbar disc-body unit in compression. A three-dimensional nonlinear finite element study," *Spine,* vol. 9, no. 2, pp. 120-134, 1984.

[12] T. Zander, A. Rohlmann, N. K. Burra, and G. Bergmann, "Effect of a posterior dynamic implant adjacent to a rigid spinal fixator," *Clinical biomechanics,* vol. 21, no. 8, pp. 767-774, 2006.

[13] H. De Visser, C. J. Adam, S. Crozier, and M. J. Pearcy, "The role of quadratus lumborum asymmetry in the occurrence of lesions in the lumbar vertebrae of cricket fast bowlers," *Medical engineering & physics,* vol. 29, no. 8, pp. 877-885, 2007.

[14] M. Argoubi and A. Shirazi-Adl, "Poroelastic creep response analysis of a lumbar motion segment in compression," *Journal of biomechanics,* vol. 29, no. 10, pp. 1331-1339, 1996.

[15] S. Kumaresan, N. Yoganandan, and F. A. Pintar, "Finite element analysis of the cervical spine: a material property sensitivity study," *Clinical Biomechanics,* vol. 14, no. 1, pp. 41-53, 1999.

[16] A. Rohlmann, T. Zander, H. Schmidt, H.-J. Wilke, and G. Bergmann, "Analysis of the influence of disc degeneration on the mechanical behaviour of a lumbar motion segment using the finite element method," *Journal of biomechanics,* vol. 39, no. 13, pp. 2484-2490, 2006.

[17] J. P. Little, M. T. Izatt, R. D. Labrom, G. N. Askin, and C. J. Adam, "An FE investigation simulating intra-operative corrective forces applied to correct scoliosis deformity," *Scoliosis,* vol. 8, no. 1, p. 9, 2013.

[18] S. Tadano, M. Kanayama, T. Ukai, and K. Kaneda, "Morphological modeling and growth simulation of idiopathic scoliosis," in *Computational biomechanics*: Springer, 1996, pp. 67-88.

[19] E. Chosa, K. Totoribe, and N. Tajima, "A biomechanical study of lumbar spondylolysis based on a three-dimensional finite element method," *Journal of Orthopaedic Research,* vol. 22, no. 1, pp. 158-163, 2004.

[20] H. N. Herkowitz, S. R. Garfin, F. J. Eismont, G. R. Bell, and R. A. Balderston, *Rothman-Simeone The Spine E-Book: Expert Consult*. Elsevier Health Sciences, 2011.

[21] A. Fantigrossi, F. Galbusera, M. T. Raimondi, M. Sassi, and M. Fornari, "Biomechanical analysis of cages for posterior lumbar interbody fusion," *Medical engineering & physics,* vol. 29, no. 1, pp. 101-109, 2007.

[22] F. Lavaste, W. Skalli, S. Robin, R. Roy-Camille, and C. Mazel, "Three-dimensional geometrical and mechanical modelling of the lumbar spine," *Journal of biomechanics,* vol. 25, no. 10, pp. 1153-1164, 1992.

[23] W. M. Park, K. Kim, and Y. H. Kim, "Effects of degenerated intervertebral discs on intersegmental rotations, intradiscal pressures, and facet joint forces of the whole lumbar spine," *Computers in biology and medicine,* vol. 43, no. 9, pp. 1234-1240, 2013.

[24] J.-L. Wang, M. Parnianpour, A. Shirazi-Adl, and A. E. Engin, "Viscoelastic finite-element analysis of a lumbar motion segment in combined compression and sagittal flexion: Effect of loading rate," *Spine,* vol. 25, no. 3, pp. 310-318, 2000.

[25] A. Kiapour and V. Goel, "Biomechanics of a novel lumbar total motion segment preservation system: a computational and in vitro study," *Bonezone,* vol. 8, pp. 86-90, 2009.
[26] G. Baroud, J. Nemes, P. Heini, and T. Steffen, "Load shift of the intervertebral disc after a vertebroplasty: a finite-element study," *European Spine Journal,* vol. 12, no. 4, pp. 421-426, 2003.
[27] Z.-C. Zhong, S.-H. Wei, J.-P. Wang, C.-K. Feng, C.-S. Chen, and C.-h. Yu, "Finite element analysis of the lumbar spine with a new cage using a topology optimization method," *Medical Engineering & Physics,* vol. 28, no. 1, pp. 90-98, 2006.
[28] L. M. Ruberté, R. N. Natarajan, and G. B. Andersson, "Influence of single-level lumbar degenerative disc disease on the behavior of the adjacent segments—a finite element model study," *Journal of biomechanics,* vol. 42, no. 3, pp. 341-348, 2009.
[29] M. Kurutz and L. Oroszváry, "Finite element analysis of weightbath hydrotraction treatment of degenerated lumbar spine segments in elastic phase," *Journal of Biomechanics,* vol. 43, no. 3, pp. 433-441, 2010.
[30] K. Goto *et al.*, "Effects of lumbar spinal fusion on the other lumbar intervertebral levels (three-dimensional finite element analysis)," *Journal of Orthopaedic Science,* vol. 8, no. 4, pp. 577-584, 2003.
[31] V. Lafage, N. Gangnet, J. Sénégas, F. Lavaste, and W. Skalli, "New interspinous implant evaluation using an in vitro biomechanical study combined with a finite-element analysis," *Spine,* vol. 32, no. 16, pp. 1706-1713, 2007.
[32] A. A. Ivanov, A. Kiapour, N. A. Ebraheim, and V. Goel, "Lumbar fusion leads to increases in angular motion and stress across sacroiliac joint: a finite element study," *Spine,* vol. 34, no. 5, pp. E162-E169, 2009.
[33] J. Cassidy, A. Hiltner, and E. Baer, "Hierarchical structure of the intervertebral disc," *Connective tissue research,* vol. 23, no. 1, pp. 75-88, 1989.
[34] C. M. Bellini, F. Galbusera, M. T. Raimondi, G. V. Mineo, and M. Brayda-Bruno, "Biomechanics of the lumbar spine after dynamic stabilization," *Clinical Spine Surgery,* vol. 20, no. 6, pp. 423-429, 2007.
[35] H.-G. Yoon, S.-J. Heo, J.-Y. Koak, S.-K. Kim, and S.-Y. Lee, "Effect of bone quality and implant surgical technique on implant stability quotient (ISQ) value," *The journal of advanced prosthodontics,* vol. 3, no. 1, pp. 10-15, 2011.
[36] M. Y. Lu, W. C. Hutton, and V. M. Gharpuray, "Can variations in intervertebral disc height affect the mechanical function of the disc?," *Spine,* vol. 21, no. 19, pp. 2208-2216, 1996.
[37] H. Schmidt, F. Heuer, and H.-J. Wilke, "Which axial and bending stiffnesses of posterior implants are required to design a flexible lumbar stabilization system?," *Journal of biomechanics,* vol. 42, no. 1, pp. 48-54, 2009.
[38] C.-S. Chen, C.-K. Cheng, C.-L. Liu, and W.-H. Lo, "Stress analysis of the disc adjacent to interbody fusion in lumbar spine," *Medical engineering & physics,* vol. 23, no. 7, pp. 485-493, 2001.
[39] J. Noailly, H.-J. Wilke, J. A. Planell, and D. Lacroix, "How does the geometry affect the internal biomechanics of a lumbar spine bi-segment finite element model? Consequences on the validation process," *Journal of biomechanics,* vol. 40, no. 11, pp. 2414-2425, 2007.
[40] A. Malandrino, J. A. Planell, and D. Lacroix, "Statistical factorial analysis on the poroelastic material properties sensitivity of the lumbar intervertebral disc under compression, flexion and axial rotation," *Journal of biomechanics,* vol. 42, no. 16, pp. 2780-2788, 2009.
[41] U. M. Ayturk and C. M. Puttlitz, "Parametric convergence sensitivity and validation of a finite element model of the human lumbar spine," *Computer methods in biomechanics and biomedical engineering,* vol. 14, no. 8, pp. 695-705, 2011.
[42] P.-L. Sylvestre, I. Villemure, and C.-E. Aubin, "Finite element modeling of the growth plate in a detailed spine model," *Medical & biological engineering & computing,* vol. 45, no. 10, pp. 977-988, 2007.
[43] S. J. Ferguson, K. Ito, and L.-P. Nolte, "Fluid flow and convective transport of solutes within the intervertebral disc," *Journal of biomechanics,* vol. 37, no. 2, pp. 213-221, 2004.
[44] Q. H. Zhang, Y. L. Zhou, D. Petit, and E. C. Teo, "Evaluation of load transfer characteristics of a dynamic stabilization device on disc loading under compression," *Medical engineering & physics,* vol. 31, no. 5, pp. 533-538, 2009.
[45] J. R. Williams, R. N. Natarajan, and G. B. Andersson, "Inclusion of regional poroelastic material properties better predicts biomechanical behavior of lumbar discs subjected to dynamic loading," *Journal of biomechanics,* vol. 40, no. 9, pp. 1981-1987, 2007.

[46] W. Suwito, T. Keller, P. Basu, A. Weisberger, A. Strauss, and D. Spengler, "Geometric and material property study of the human lumbar spine using the finite element method," *Journal of spinal disorders,* vol. 5, no. 1, pp. 50-59, 1992.
[47] H. Giambini, H.-J. Wang, C. Zhao, Q. Chen, A. Nassr, and K.-N. An, "Anterior and posterior variations in mechanical properties of human vertebrae measured by nanoindentation," *Journal of biomechanics,* vol. 46, no. 3, pp. 456-461, 2013.
[48] F. Xavier *et al.*, "Regional variations in shear strength and density of the human thoracic vertebral endplate and trabecular bone," *International journal of spine surgery,* vol. 11, no. 1, 2017.
[49] H. H. Bayraktar, E. F. Morgan, G. L. Niebur, G. E. Morris, E. K. Wong, and T. M. Keaveny, "Comparison of the elastic and yield properties of human femoral trabecular and cortical bone tissue," *Journal of biomechanics,* vol. 37, no. 1, pp. 27-35, 2004.
[50] H. Chen, X. Zhou, H. Fujita, M. Onozuka, and K.-Y. Kubo, "Age-related changes in trabecular and cortical bone microstructure," *International journal of endocrinology,* vol. 2013, 2013.
[51] M. A. Liebschner, D. L. Kopperdahl, W. S. Rosenberg, and T. M. Keaveny, "Finite element modeling of the human thoracolumbar spine," *Spine,* vol. 28, no. 6, pp. 559-565, 2003.
[52] L. Mosekilde, "Vertebral structure and strengthIn vivo andIn vitro," *Calcified tissue international,* vol. 53, no. 1, pp. S121-S126, 1993.
[53] O. Ardatov, A. Maknickas, V. Alekna, M. Tamulaitienė, and R. Kačianauskas, "The finite element analysis of osteoporotic lumbar vertebral body by influence of trabecular bone apparent density and thickness of cortical shell," *acta mechanica et automatica,* vol. 11, no. 4, pp. 285-292, 2017.
[54] B. Helgason, E. Perilli, E. Schileo, F. Taddei, S. Brynjólfsson, and M. Viceconti, "Mathematical relationships between bone density and mechanical properties: a literature review," *Clinical biomechanics,* vol. 23, no. 2, pp. 135-146, 2008.
[55] S. Zhou, I. McCarthy, A. McGregor, R. Coombs, and S. Hughes, "Geometrical dimensions of the lower lumbar vertebrae–analysis of data from digitised CT images," *European Spine Journal,* vol. 9, no. 3, pp. 242-248, 2000.
[56] I. A. Stokes and L. Windisch, "Vertebral height growth predominates over intervertebral disc height growth in adolescents with scoliosis," *Spine,* vol. 31, no. 14, p. 1600, 2006.
[57] C. T. Brighton, "Structure and function of the growth plate," *Clinical Orthopaedics and Related Research®,* no. 136, pp. 22-32, 1978.
[58] A. J. Fields, E. C. Liebenberg, and J. C. Lotz, "Innervation of pathologies in the lumbar vertebral end plate and intervertebral disc," *The Spine Journal,* vol. 14, no. 3, pp. 513-521, 2014.
[59] U. Zehra, K. Robson-Brown, M. A. Adams, and P. Dolan, "Porosity and thickness of the vertebral endplate depend on local mechanical loading," *Spine,* vol. 40, no. 15, pp. 1173-1180, 2015.
[60] V. Palepu, S. D. Rayaprolu, and S. Nagaraja, "Differences in Trabecular Bone, Cortical Shell, and Endplate Microstructure Across the Lumbar Spine," *International journal of spine surgery,* vol. 13, no. 4, pp. 361-370, 2019.
[61] M. P. Steinmetz and E. C. Benzel, *Benzel's Spine Surgery E-Book: Techniques, Complication Avoidance, and Management*. Elsevier Health Sciences, 2016.
[62] B. Ni, X. Guo, and Q. Guo, *Atlantoaxial Fixation Techniques: Commonly Used and New Techniques*. Springer, 2018.
[63] I. P. Herman, "Mechanical properties of the body," in *Physics of the Human Body*: Springer, 2016, pp. 247-329.
[64] M. Pearcy and S. Tibrewal, "Lumbar intervertebral disc and ligament deformations measured in vivo," *Clinical Orthopaedics and Related Research®,* vol. 191, pp. 281-286, 1984.
[65] P. P. Raj, "Intervertebral disc: anatomy-physiology-pathophysiology-treatment," *Pain Practice,* vol. 8, no. 1, pp. 18-44, 2008.
[66] J. Pooni, D. Hukins, P. Harris, R. Hilton, and K. Davies, "Comparison of the structure of human intervertebral discs in the cervical, thoracic and lumbar regions of the spine," *Surgical and radiologic anatomy,* vol. 8, no. 3, pp. 175-182, 1986.
[67] S. M. H. Mirab, M. Barbarestani, S. M. Tabatabaei, S. Shahsavari, M. Zangi, and M. Bagher, "Measuring Dimensions of Lumbar Intervertebral Discs in Normal Subjects," *Anatomical Sciences Journal,* vol. 14, no. 1, pp. 3-8, 2017.

[68] H. Schmidt, F. Galbusera, A. Rohlmann, and A. Shirazi-Adl, "What have we learned from finite element model studies of lumbar intervertebral discs in the past four decades?," *Journal of biomechanics,* vol. 46, no. 14, pp. 2342-2355, 2013.
[69] M. H. Berkson, A. Nachemson, and A. B. Schultz, "Mechanical properties of human lumbar spine motion segments—part II: responses in compression and shear; influence of gross morphology," 1979.
[70] A. Tencer, A. Ahmed, and D. Burke, "Some static mechanical properties of the lumbar intervertebral joint, intact and injured," 1982.
[71] T. Keller, D. Spengler, and T. Hansson, "Mechanical behavior of the human lumbar spine. I. Creep analysis during static compressive loading," *Journal of Orthopaedic Research,* vol. 5, no. 4, pp. 467-478, 1987.
[72] A. Rohlmann, N. K. Burra, T. Zander, and G. Bergmann, "Comparison of the effects of bilateral posterior dynamic and rigid fixation devices on the loads in the lumbar spine: a finite element analysis," *European Spine Journal,* vol. 16, no. 8, pp. 1223-1231, 2007.
[73] V. d. Moramarco, A. P. Del Palomar, C. Pappalettere, and M. Doblaré, "An accurate validation of a computational model of a human lumbosacral segment," *Journal of biomechanics,* vol. 43, no. 2, pp. 334-342, 2010.
[74] Y. Schroeder, W. Wilson, J. M. Huyghe, and F. P. Baaijens, "Osmoviscoelastic finite element model of the intervertebral disc," *European spine journal,* vol. 15, no. 3, p. 361, 2006.
[75] M. Fagan, S. Julian, D. Siddall, and A. Mohsen, "Patient-specific spine models. Part 1: Finite element analysis of the lumbar intervertebral disc—a material sensitivity study," *Proceedings of the Institution of Mechanical Engineers, Part H: Journal of Engineering in Medicine,* vol. 216, no. 5, pp. 299-314, 2002.
[76] G. Denoziere and D. N. Ku, "Biomechanical comparison between fusion of two vertebrae and implantation of an artificial intervertebral disc," *Journal of biomechanics,* vol. 39, no. 4, pp. 766-775, 2006.
[77] J. Crisco, M. Panjabi, I. Yamamoto, and T. Oxland, "Euler stability of the human ligamentous lumbar spine. Part II: Experiment," *Clinical biomechanics,* vol. 7, no. 1, pp. 27-32, 1992.
[78] S. M. McGill, S. Grenier, N. Kavcic, and J. Cholewicki, "Coordination of muscle activity to assure stability of the lumbar spine," *Journal of electromyography and kinesiology,* vol. 13, no. 4, pp. 353-359, 2003.
[79] S. M. McGill and J. Cholewicki, "Biomechanical basis for stability: an explanation to enhance clinical utility," *Journal of Orthopaedic & Sports Physical Therapy,* vol. 31, no. 2, pp. 96-100, 2001.
[80] N. Kavcic, S. Grenier, and S. M. McGill, "Determining the stabilizing role of individual torso muscles during rehabilitation exercises," *Spine,* vol. 29, no. 11, pp. 1254-1265, 2004.
[81] D. Yang, S. Morris, and L. Sigurdson, "The sartorius muscle: anatomic considerations for reconstructive surgeons," *Surgical and Radiologic Anatomy,* vol. 20, no. 5, pp. 307-310, 1998.
[82] G. Thews, E. Mutschler, and P. Vaupel, *Human Anatomy, Physiology, and Pathophysiology*. Elsevier, 1985.
[83] L. M. Schwartz, "Skeletal muscles do not undergo apoptosis during either atrophy or programmed cell death-revisiting the Myonuclear domain hypothesis," *Frontiers in physiology,* vol. 9, p. 1887, 2019.
[84] S. H. Brown, S. R. Ward, M. S. Cook, and R. L. Lieber, "Architectural analysis of human abdominal wall muscles: implications for mechanical function," *Spine,* vol. 36, no. 5, p. 355, 2011.
[85] B. Henson and M. A. Edens, "Anatomy, Back, Muscles," in *StatPearls [Internet]*: StatPearls Publishing, 2018.
[86] N. Bogduk and J. Maclntosh, "The morphology of the lumbar erector spinae," in *Meeting of the International Society for the study of the Lumbar Spine, Rome, Italy*, 1987.
[87] S. L. Delp, S. Suryanarayanan, W. M. Murray, J. Uhlir, and R. J. Triolo, "Architecture of the rectus abdominis, quadratus lumborum, and erector spinae," *Journal of biomechanics,* vol. 34, no. 3, pp. 371-375, 2001.
[88] S. R. Ward *et al.*, "Architectural analysis and intraoperative measurements demonstrate the unique design of the multifidus muscle for lumbar spine stability," *The Journal of bone and joint surgery. American volume.,* vol. 91, no. 1, p. 176, 2009.
[89] T. Mäki, P. Oura, M. Paananen, J. Niinimäki, J. Karppinen, and J.-A. Junno, "Longitudinal Analysis of paraspinal Muscle cross-Sectional Area During Early Adulthood–A 10-Year follow-Up MRi Study," *Scientific Reports,* vol. 9, no. 1, pp. 1-8, 2019.
[90] K. Sugawara, M. Katayose, and K. Watanabe, "The variation in the lumbar facet joint orientation in an adult Asian population and its relationship with the cross-sectional area of the multifidus and erector spinae," *Asian spine journal,* vol. 10, no. 5, p. 886, 2016.

[91] M. J. Jorgensen, W. S. Marras, and P. Gupta, "Cross-sectional area of the lumbar back muscles as a function of torso flexion," *Clinical Biomechanics,* vol. 18, no. 4, pp. 280-286, 2003.
[92] D.-E. Shin, Y.-S. Lee, H.-J. Lee, T.-K. Ahn, Y.-G. Jo, and S.-J. Lee, "Relationship of the Pre-operative Condition of Paravertebral Muscle with Post-operative Functional Disability in Patients with Degenerative Lumbar Spinal Disease," *Journal of Korean Society of Spine Surgery,* vol. 22, no. 4, pp. 153-159, 2015.
[93] R. Schweitzer, E. Zelzer, and T. Volk, "Connecting muscles to tendons: tendons and musculoskeletal development in flies and vertebrates," *Development,* vol. 137, no. 17, pp. 2807-2817, 2010.
[94] J. G. Reid and P. Costigan, "Geometry of adult rectus abdominis and erector spinae muscles," *Journal of Orthopaedic & Sports Physical Therapy,* vol. 6, no. 5, pp. 278-280, 1985.
[95] M. F. Tracy, M. J. Gibson, E. P. Szypryt, A. Rutherford, and E. N. Corlett, "The geometry of the muscles of the lumbar spine determined by magnetic resonance imaging," *Spine,* vol. 14, no. 2, pp. 186-193, 1989.
[96] D. B. Chaffin, M. S. Redfern, M. Erig, and S. A. Goldstein, "Lumbar muscle size and locations from CT scans of 96 women of age 40 to 63 years," *Clinical Biomechanics,* vol. 5, no. 1, pp. 9-16, 1990.
[97] Y. Tsuang, G. Novak, O. Schipplein, A. Hafezi, J. Trafimow, and G. Andersson, "Trunk muscle geometry and centroid location when twisting," *Journal of biomechanics,* vol. 26, no. 4-5, pp. 537-546, 1993.
[98] S. McGill, D. Juker, and P. Kropf, "Quantitative intramuscular myoelectric activity of quadratus lumborum during a wide variety of tasks," *Clinical Biomechanics,* vol. 11, no. 3, pp. 170-172, 1996.
[99] S. McGill, N. Patt, and R. Norman, "Measurement of the trunk musculature of active males using CT scan radiography: implications for force and moment generating capacity about the L4L5 joint," *Journal of biomechanics,* vol. 21, no. 4, pp. 329-341, 1988.
[100] P. Santaguida and S. McGill, "The psoas major muscle: a three-dimensional geometric study," *Journal of biomechanics,* vol. 28, no. 3, pp. 339-345, 1995.
[101] N. Tahan, K. Khademi-Kalantari, M. A. Mohseni-Bandpei, S. Mikaili, A. A. Baghban, and S. Jaberzadeh, "Measurement of superficial and deep abdominal muscle thickness: an ultrasonography study," *Journal of physiological anthropology,* vol. 35, no. 1, p. 17, 2016.
[102] K. Tesh, J. S. Dunn, and J. Evans, "The abdominal muscles and vertebral stability," *Spine,* vol. 12, no. 5, pp. 501-508, 1987.
[103] A. V. Hill, "The heat of shortening and the dynamic constants of muscle," *Proceedings of the Royal Society of London. Series B-Biological Sciences,* vol. 126, no. 843, pp. 136-195, 1938.
[104] S. Schleifenbaum *et al.*, "Load and failure behavior of human muscle samples in the context of proximal femur replacement," *BMC musculoskeletal disorders,* vol. 17, no. 1, p. 149, 2016.
[105] L. Hansen, M. De Zee, J. Rasmussen, T. B. Andersen, C. Wong, and E. B. Simonsen, "Anatomy and biomechanics of the back muscles in the lumbar spine with reference to biomechanical modeling," *Spine,* vol. 31, no. 17, pp. 1888-1899, 2006.
[106] S. S. Metan, G. Mohankumar, and P. Krishna, "Sensitivity analysis of shoulder joint muscles by using the FEM model," *Biomaterials and Biomechanics in Bioengineering,* vol. 3, no. 2, pp. 115-127, 2016.
[107] C. I. Buchanan and R. L. Marsh, "Effects of long-term exercise on the biomechanical properties of the Achilles tendon of guinea fowl," *Journal of applied physiology,* vol. 90, no. 1, pp. 164-171, 2001.
[108] C. R. Deeken and S. P. Lake, "Mechanical properties of the abdominal wall and biomaterials utilized for hernia repair," *Journal of the mechanical behavior of biomedical materials,* vol. 74, pp. 411-427, 2017.
[109] D. Taylor, N. O'Mara, E. Ryan, M. Takaza, and C. Simms, "The fracture toughness of soft tissues," *Journal of the mechanical behavior of biomedical materials,* vol. 6, pp. 139-147, 2012.
[110] C. Pailler-Mattei, S. Bec, and H. Zahouani, "In vivo measurements of the elastic mechanical properties of human skin by indentation tests," *Medical engineering & physics,* vol. 30, no. 5, pp. 599-606, 2008.
[111] J. Steege, D. Schnur, and D. Childress, "Prediction of pressure at the below-knee socket interface by finite element analysis," in *ASME Symposium on the biomechanics of normal and pathological gait*, 1987, pp. 39-44.
[112] T. Krouskop, A. Muilenberg, D. Doughtery, and D. Winningham, "Computer-aided design of a prosthetic socket for an above-knee amputee," *J Rehabil Res Dev,* vol. 24, no. 2, pp. 31-8, 1987.
[113] D. Reynolds and M. Lord, "Interface load analysis for computer-aided design of below-knee prosthetic sockets," *Medical and Biological Engineering and Computing,* vol. 30, no. 4, pp. 419-426, 1992.
[114] A. F. Mak, G. H. Liu, and S. Lee, "Biomechanical assessment of below-knee residual limb tissue," *Journal of rehabilitation research and development,* 1994.
[115] S. R. Ward *et al.*, "Passive mechanical properties of the lumbar multifidus muscle support its role as a stabilizer," *Journal of biomechanics,* vol. 42, no. 10, pp. 1384-1389, 2009.

[116] A. Noonan, "Investigating skeletal muscle passive mechanical properties: the effects of fibre type, muscle, age, and species," 2018.
[117] R. Close, "Dynamic properties of mammalian skeletal muscles," *Physiological reviews,* vol. 52, no. 1, pp. 129-197, 1972.
[118] D. Hawkins and M. Bey, "A comprehensive approach for studying muscle-tendon mechanics," 1994.
[119] W. Herzog, S. Kamal, and H. Clarke, "Myofilament lengths of cat skeletal muscle: theoretical considerations and functional implications," *Journal of biomechanics,* vol. 25, no. 8, pp. 945-948, 1992.
[120] P. Aimedieu Jr, D. Mitton, J. Faure, L. Denninger, and F. Lavaste, "Dynamic stiffness and damping of porcine muscle specimens," *Medical engineering & physics,* vol. 25, no. 9, pp. 795-799, 2003.
[121] M. B. Silver-Thorn, "In vivo indentation of lower extremity limb soft tissues," *IEEE Transactions on Rehabilitation Engineering,* vol. 7, no. 3, pp. 268-277, 1999.
[122] M. Kaya, N. Karahan, and B. Yılmaz, "Tendon Structure and Classification," in *Tendons*: IntechOpen, 2019.
[123] S. P. Magnusson, K. M. Heinemeier, and M. Kjaer, "Collagen homeostasis and metabolism," in *Metabolic Influences on Risk for Tendon Disorders*: Springer, 2016, pp. 11-25.
[124] F. E. Zajac, "Muscle and tendon: properties, models, scaling, and application to biomechanics and motor control," *Critical reviews in biomedical engineering,* vol. 17, no. 4, pp. 359-411, 1989.
[125] C. N. Maganaris and J. P. Paul, "In vivo human tendon mechanical properties," *The Journal of physiology,* vol. 521, no. 1, pp. 307-313, 1999.
[126] M. Creze, M. Soubeyrand, and O. Gagey, "The paraspinal muscle-tendon system: Its paradoxical anatomy," *PloS one,* vol. 14, no. 4, 2019.
[127] J. E. Macintosh, N. Bogduk, and S. Gracovetsky, "The biomechanics of the thoracolumbar fascia," *Clinical biomechanics,* vol. 2, no. 2, pp. 78-83, 1987.
[128] F. Willard, A. Vleeming, M. Schuenke, L. Danneels, and R. Schleip, "The thoracolumbar fascia: anatomy, function and clinical considerations," *Journal of anatomy,* vol. 221, no. 6, pp. 507-536, 2012.
[129] F. Willard, "Somatic fascia," *Teoksessa R. Schleip, TW Findley, L. Chaitow & PA Huijing (toim.) Fascia: The tensional network of the human body. China: Elsevier Ltd,* pp. 11-17, 2013.
[130] M. Benjamin, "The fascia of the limbs and back–a review," *Journal of anatomy,* vol. 214, no. 1, pp. 1-18, 2009.
[131] S. Standring, *Gray's anatomy e-book: the anatomical basis of clinical practice*. Elsevier Health Sciences, 2015.
[132] P. J. Barker and C. A. Briggs, "Attachments of the posterior layer of lumbar fascia," *Spine,* vol. 24, no. 17, p. 1757, 1999.
[133] N. Bogduk and J. E. Macintosh, "The applied anatomy of the thoracolumbar fascia," *Spine,* vol. 9, no. 2, pp. 164-170, 1984.
[134] M. Schuenke, A. Vleeming, T. Van Hoof, and F. Willard, "A description of the lumbar interfascial triangle and its relation with the lateral raphe: anatomical constituents of load transfer through the lateral margin of the thoracolumbar fascia," *Journal of anatomy,* vol. 221, no. 6, pp. 568-576, 2012.
[135] P. J. Barker, C. A. Briggs, and G. Bogeski, "Tensile transmission across the lumbar fasciae in unembalmed cadavers: effects of tension to various muscular attachments," *Spine,* vol. 29, no. 2, pp. 129-138, 2004.
[136] F. Vasques, C. Stecco, R. Mitri, R. C. De, P. Fusco, and A. U. Behr, "Blocking around the transversalis fascia: behind the scene," *Minerva anestesiologica,* vol. 85, no. 1, pp. 15-20, 2019.
[137] F. Willard, "The muscular, ligamentous, and neural structure of the lumbosacrum and its relationship to low back pain," in *Movement, stability & lumbopelvic pain*: Elsevier, 2007, pp. 5-45.
[138] A. Vleeming and R. Stoeckart, "The role of the pelvic girdle in coupling the spine and the legs: a clinical–anatomical perspective on pelvic stability," in *Movement, Stability & Lumbopelvic Pain*: Elsevier, 2007, pp. 113-137.
[139] P. J. Barker, D. M. Urquhart, I. H. Story, M. Fahrer, and C. A. Briggs, "The middle layer of lumbar fascia and attachments to lumbar transverse processes: implications for segmental control and fracture," *European spine journal,* vol. 16, no. 12, pp. 2232-2237, 2007.
[140] A. Vleeming, M. Schuenke, L. Danneels, and F. Willard, "The functional coupling of the deep abdominal and paraspinal muscles: the effects of simulated paraspinal muscle contraction on force transfer to the middle and posterior layer of the thoracolumbar fascia," *Journal of anatomy,* vol. 225, no. 4, pp. 447-462, 2014.

[141] S. Gracovetsky, H. Farfan, and C. Helleur, "The abdominal mechanism," *Spine,* vol. 10, no. 4, pp. 317-324, 1985.
[142] S. R. Garfin, C. M. Tipton, S. J. Mubarak, S. Woo, A. R. Hargens, and W. H. Akeson, "Role of fascia in maintenance of muscle tension and pressure," *Journal of Applied Physiology,* vol. 51, no. 2, pp. 317-320, 1981.
[143] M. A. Adams and P. Dolan, "How to use the spine, pelvis, and legs effectively in lifting," in *Movement, Stability & Lumbopelvic Pain*: Elsevier, 2007, pp. 167-183.
[144] L. Yahia, P. Pigeon, and E. DesRosiers, "Viscoelastic properties of the human lumbodorsal fascia," *Journal of biomedical engineering,* vol. 15, no. 5, pp. 425-429, 1993.
[145] A. Kureshi, P. Vaiude, S. N. Nazhat, A. Petrie, and R. A. Brown, "Matrix mechanical properties of transversalis fascia in inguinal herniation as a model for tissue expansion," *Journal of biomechanics,* vol. 41, no. 16, pp. 3462-3468, 2008.
[146] S. Otsuka *et al.*, "Site specificity of mechanical and structural properties of human fascia lata and their gender differences: A cadaveric study," *Journal of biomechanics,* vol. 77, pp. 69-75, 2018.
[147] D. L. Butler, E. S. Grood, F. R. Noyes, R. F. Zernicke, and K. Brackett, "Effects of structure and strain measurement technique on the material properties of young human tendons and fascia," *Journal of biomechanics,* vol. 17, no. 8, pp. 579-596, 1984.
[148] J. T. Fairbank, J. O'Brien, and P. Davis, "Intra-abdominal pressure and low back pain," *The Lancet,* vol. 313, no. 8130, p. 1353, 1979.
[149] N. Arjmand, A. Shirazi-Adl, and M. Parnianpour, "A finite element model study on the role of trunk muscles in generating intra-abdominal pressure," *Biomedical Engineering: Applications, Basis and Communications,* vol. 13, no. 04, pp. 181-189, 2001.
[150] J. Mens, G. H. van Dijke, A. Pool-Goudzwaard, V. van der Hulst, and H. Stam, "Possible harmful effects of high intra-abdominal pressure on the pelvic girdle," *Journal of biomechanics,* vol. 39, no. 4, pp. 627-635, 2006.
[151] I. A. Stokes, M. G. Gardner-Morse, and S. M. Henry, "Intra-abdominal pressure and abdominal wall muscular function: Spinal unloading mechanism," *Clinical Biomechanics,* vol. 25, no. 9, pp. 859-866, 2010.
[152] R. H. Overholt, "Intraperitoneal pressure," *Archives of surgery,* vol. 22, no. 5, pp. 691-703, 1931.
[153] C. R. Lam, "Intra-abdominal pressure: a critical review and an experimental study," *Archives of Surgery,* vol. 39, no. 6, pp. 1006-1015, 1939.
[154] W. F. Mengert and D. P. Murphy, "Intra-abdominal pressures created by voluntary muscular effort," *Surg Gynecol Obstet,* vol. 57, pp. 745-751, 1933.
[155] B. De Keulenaer, J. De Waele, B. Powell, and M. Malbrain, "What is normal intra-abdominal pressure and how is it affected by positioning, body mass and positive end-expiratory pressure?," *Intensive care medicine,* vol. 35, no. 6, pp. 969-976, 2009.
[156] S. J. Fletcher, "The effect of prone ventilation on intra-abdominal pressure," *Clinical Intensive Care,* vol. 17, no. 3-4, pp. 109-112, 2006.
[157] B. Goldstein, "Anatomy of the peripheral nervous system," *Physical Medicine and Rehabilitation Clinics,* vol. 12, no. 2, pp. 207-236, 2001.
[158] R. Payne, "Surgical Exposure for the Nerves of the Back," in *Nerves and Nerve Injuries*: Elsevier, 2015, pp. 155-167.
[159] J. A. Beel, L. S. Stodieck, and M. W. Luttges, "Structural properties of spinal nerve roots: biomechanics," *Experimental neurology,* vol. 91, no. 1, pp. 30-40, 1986.
[160] A. Singh, Y. Lu, C. Chen, and J. M. Cavanaugh, "Mechanical properties of spinal nerve roots subjected to tension at different strain rates," *Journal of biomechanics,* vol. 39, no. 9, pp. 1669-1676, 2006.
[161] K. S. Topp and B. S. Boyd, "Structure and biomechanics of peripheral nerves: nerve responses to physical stresses and implications for physical therapist practice," *Physical therapy,* vol. 86, no. 1, pp. 92-109, 2006.
[162] H. Millesi, G. Zöch, and R. Reihsner, "Mechanical properties of peripheral nerves," *Clinical orthopaedics and related research,* no. 314, pp. 76-83, 1995.
[163] S. Sunderland and K. Bradley, "Stress-strain phenomena in human spinal nerve roots," *Brain,* vol. 84, no. 1, pp. 120-124, 1961.
[164] M. Kwan, B. Rydevik, R. Myers, K. Triggs, S. Woo, and S. Garfin, "Biomechanical and histological assessment of human lumbosacral spinal nerve roots," *Trans Orthop Res Soc,* vol. 14, p. 348, 1989.

[165] S. Gracovetsky, "Stability or controlled instability," *Movement, Stability & Lumbopelvic Pain: Integration of research and therapy. Churchill Livingstone (Elsevier), Edinburgh,* pp. 279-293, 2007.
[166] D. Lucas and B. Bresley, "Stability of the ligamentous spine (Biomechanics lab report 40)," *San Francisco: University of California,* 1961.
[167] A. L. Nachemson and J. H. Evans, "Some mechanical properties of the third human lumbar interlaminar ligament (ligamentum flavum)," *Journal of biomechanics,* vol. 1, no. 3, pp. 211-220, 1968.
[168] J. Cholewicki, S. McGill, and R. Norman, "Lumbar spine loads during the lifting of extremely heavy weights," *Medicine and science in sports and exercise,* vol. 23, no. 10, pp. 1179-1186, 1991.
[169] A. Nachemson, "Lumbar spine instability. A critical update and symposium summary," *Spine,* vol. 10, no. 3, pp. 290-291, 1985.
[170] M. M. Panjabi and A. White, "Clinical biomechanics of the spine," 1990.
[171] W. H. KIRKALDY-WILLIS, "Presidential Symposium on Instability of the Lumbar Spine: Introduction," *Spine,* vol. 10, no. 3, p. 254, 1985. [Online]. Available: https://journals.lww.com/spinejournal/Fulltext/1985/04000/Presidential_Symposium_on_Instability_of_the.12.aspx.
[172] S. D. Boden and S. Wiesel, "Lumbosacral segmental motion in normal individuals. Have we been measuring instability properly?," *Spine,* vol. 15, no. 6, pp. 571-576, 1990.
[173] A. G. Patwardhan, R. M. Havey, K. P. Meade, B. Lee, and B. Dunlap, "A follower load increases the load-carrying capacity of the lumbar spine in compression," *Spine,* vol. 24, no. 10, pp. 1003-1009, 1999.
[174] S. Zahari, M. A. Latif, and M. A. Kadir, "The influence of preload application for vertebra segment in finite element modelling," in *2014 IEEE Conference on Biomedical Engineering and Sciences (IECBES)*, 2014: IEEE, pp. 198-203.
[175] C.-F. Du, N. Yang, J.-C. Guo, Y.-P. Huang, and C. Zhang, "Biomechanical response of lumbar facet joints under follower preload: a finite element study," *BMC musculoskeletal disorders,* vol. 17, no. 1, p. 126, 2016.
[176] L.-X. Guo and W. Fan, "Dynamic response of the lumbar spine to whole-body vibration under a compressive follower preload," *Spine,* vol. 43, no. 3, pp. E143-E153, 2018.
[177] K. Kim, Y. H. Kim, and S. Lee, "Increase of load-carrying capacity under follower load generated by trunk muscles in lumbar spine," *Proceedings of the Institution of Mechanical Engineers, Part H: Journal of Engineering in Medicine,* vol. 221, no. 3, pp. 229-235, 2007.
[178] K.-S. Han, A. Rohlmann, S.-J. Yang, B. S. Kim, and T.-H. Lim, "Spinal muscles can create compressive follower loads in the lumbar spine in a neutral standing posture," *Medical engineering & physics,* vol. 33, no. 4, pp. 472-478, 2011.
[179] T. Pitzen *et al.*, "A finite element model for predicting the biomechanical behaviour of the human lumbar spine," *Control Engineering Practice,* vol. 10, no. 1, pp. 83-90, 2002.
[180] A. Rohlmann *et al.*, "Activities of everyday life with high spinal loads," *PloS one,* vol. 9, no. 5, 2014.
[181] H. J. Wilke, P. Neef, M. Caimi, T. Hoogland, and L. E. Claes, "New in vivo measurements of pressures in the intervertebral disc in daily life," *Spine,* vol. 24, no. 8, pp. 755-762, 1999.
[182] J. M. Morris, D. B. Lucas, and B. Bresler, "Role of the trunk in stability of the spine," *JBJS,* vol. 43, no. 3, pp. 327-351, 1961.
[183] S. A. Keith, *Man's posture; its evolution and disorders*. 1923.
[184] D. Bartelink, "The role of abdominal pressure in relieving the pressure on the lumbar intervertebral discs," *The Journal of bone and joint surgery. British volume,* vol. 39, no. 4, pp. 718-725, 1957.
[185] R. Aspden, "Intra-abdominal pressure and its role in spinal mechanics," *Clinical Biomechanics,* vol. 2, no. 3, pp. 168-174, 1987.
[186] P. Davis, "Variations of the human intra-abdominal pressure during weight-lifting in different postures," *J Anat,* vol. 90, p. 601, 1956.
[187] H. Farfan, "Muscular mechanism of the lumbar spine and the position of power and efficiency," *Orth Clin North Am,* vol. 6, pp. 135-144, 1975.
[188] P. Davis, "Intratruncal pressure mechanisms," *Ergonomics,* vol. 28, no. 1, pp. 293-297, 1985.
[189] N. Arjmand and A. Shirazi-Adl, "Role of intra-abdominal pressure in the unloading and stabilization of the human spine during static lifting tasks," *European Spine Journal,* vol. 15, no. 8, pp. 1265-1275, 2006.
[190] J. Heyman, *The Mansonry Arch*. 1982.
[191] S. McGill and R. W. Norman, "Reassessment of the role of intra-abdominal pressure in spinal compression," *Ergonomics,* vol. 30, no. 11, pp. 1565-1588, 1987.

[192] S. M. McGill and R. W. Norman, "Low back biomechanics in industry: the prevention of injury through safer lifting," *Current issues in biomechanics,* pp. 69-120, 1993.
[193] S. Gracovetsky, H. Farfan, and C. Lamy, "The mechanism of the lumbar spine," *Spine,* vol. 6, no. 3, pp. 249-262, 1981.
[194] G. Meijer, "Development of a non-fusion scoliosis correction device. Numerical modelling of scoliosis correction," 2011.
[195] A. R. Blaser, M. Björck, B. De Keulenaer, and A. Regli, "Abdominal compliance: a bench-to-bedside review," *Journal of Trauma and Acute Care Surgery,* vol. 78, no. 5, pp. 1044-1053, 2015.
[196] M. M. Panjabi, "Clinical spinal instability and low back pain," *Journal of electromyography and kinesiology,* vol. 13, no. 4, pp. 371-379, 2003.
[197] J. Dvorak, M. Panjabi, D. Chang, R. Theiler, and D. Grob, "Functional radiographic diagnosis of the lumbar spine. Flexion-extension and lateral bending," *Spine,* vol. 16, no. 5, pp. 562-571, 1991.
[198] M. Pearcy, I. Portek, and J. Shepherd, "Three-dimensional x-ray analysis of normal movement in the lumbar spine," *Spine,* vol. 9, no. 3, pp. 294-297, 1984.
[199] I. Posner, A. A. WHITE III, W. T. EDWARDS, and W. C. HAYES, "A biomechanical analysis of the clinical stability of the lumbar and lumbosacral spine," *Spine,* vol. 7, no. 4, pp. 374-389, 1982.
[200] M. M. Panjabi, T. Oxland, I. Yamamoto, and J. J. Crisco, "Mechanical behavior of the human lumbar and lumbosacral spine as shown by three-dimensional load-displacement curves," *The Journal of bone and joint surgery. American volume,* vol. 76, no. 3, pp. 413-424, 1994.
[201] A. G. Rodriguez, A. E. Rodriguez-Soto, A. J. Burghardt, S. Berven, S. Majumdar, and J. C. Lotz, "Morphology of the human vertebral endplate," *Journal of orthopaedic research,* vol. 30, no. 2, pp. 280-287, 2012.
[202] J. Lotz, A. Fields, and E. Liebenberg, "The role of the vertebral end plate in low back pain," *Global spine journal,* vol. 3, no. 03, pp. 153-164, 2013.
[203] F. Kovacs *et al.*, "Vertebral endplate changes are not associated with chronic low back pain among Southern European subjects: a case control study," *American journal of neuroradiology,* vol. 33, no. 8, pp. 1519-1524, 2012.
[204] J. A. Hides, C. A. Richardson, and G. A. Jull, "Multifidus muscle recovery is not automatic after resolution of acute, first-episode low back pain," *Spine,* vol. 21, no. 23, pp. 2763-2769, 1996.
[205] K. He *et al.*, "The Implications of Paraspinal Muscle Atrophy in Low Back Pain, Thoracolumbar Pathology, and Clinical Outcomes After Spine Surgery: A Review of the Literature," *Global Spine Journal,* p. 2192568219879087, 2019.
[206] T. L. Wallwork, W. R. Stanton, M. Freke, and J. A. Hides, "The effect of chronic low back pain on size and contraction of the lumbar multifidus muscle," *Manual therapy,* vol. 14, no. 5, pp. 496-500, 2009.
[207] P. Ferreira, M. Ferreira, and P. Hodges, "Changes in recruitment of the abdominal muscles in people with low back pain: ultrasound measurement of muscle activity. Spine (Phila Pa 1976). 2004; 29 (22): 2560-6," ed.
[208] J. H. van Dieën, J. Cholewicki, and A. Radebold, "Trunk muscle recruitment patterns in patients with low back pain enhance the stability of the lumbar spine," *Spine,* vol. 28, no. 8, pp. 834-841, 2003.
[209] W. L. A. Lo, Q. Yu, Y. Mao, W. Li, C. Hu, and L. Li, "Lumbar muscles biomechanical characteristics in young people with chronic spinal pain," *BMC musculoskeletal disorders,* vol. 20, no. 1, pp. 1-9, 2019.
[210] P. Hodges, W. van den Hoorn, A. Dawson, and J. Cholewicki, "Changes in the mechanical properties of the trunk in low back pain may be associated with recurrence," *Journal of biomechanics,* vol. 42, no. 1, pp. 61-66, 2009.
[211] S. P. Silfies, D. Squillante, P. Maurer, S. Westcott, and A. R. Karduna, "Trunk muscle recruitment patterns in specific chronic low back pain populations," *Clinical biomechanics,* vol. 20, no. 5, pp. 465-473, 2005.
[212] J. Fairbank, J. P. O'Brien, and P. R. Davis, "Intraabdominal pressure rise during weight lifting as an objective measure of low-back pain," *Spine,* vol. 5, no. 2, pp. 179-184, 1980.
[213] M. M. El-Sayyad and I. Sabry, "Intra-abdominal pressure as a quantitative measure for spinal stresses," *Journal of Orthopaedic & Sports Physical Therapy,* vol. 9, no. 2, pp. 70-76, 1987.
[214] M. Hagins and E. M. Lamberg, "Individuals with low back pain breathe differently than healthy individuals during a lifting task," *journal of orthopaedic & sports physical therapy,* vol. 41, no. 3, pp. 141-148, 2011.
[215] R. Gunzburg *et al.*, "A cadaveric study comparing discography, magnetic resonance imaging, histology, and mechanical behavior of the human lumbar disc," *Spine,* vol. 17, no. 4, pp. 417-426, 1992.

[216] N. Inoue and A. A. E. Orías, "Biomechanics of intervertebral disk degeneration," *Orthopedic Clinics,* vol. 42, no. 4, pp. 487-499, 2011.
[217] H. A. L. Guerin and D. M. Elliott, "Degeneration affects the fiber reorientation of human annulus fibrosus under tensile load," *Journal of biomechanics,* vol. 39, no. 8, pp. 1410-1418, 2006.
[218] W. Yi *et al.*, "Influence of degenerative changes of intervertebral disc on its material properties and pathology," *Chinese Journal of Traumatology,* vol. 15, no. 2, pp. 67-76, 2012.
[219] M. Haefeli, F. Kalberer, D. Saegesser, A. G. Nerlich, N. Boos, and G. Paesold, "The course of macroscopic degeneration in the human lumbar intervertebral disc," *Spine,* vol. 31, no. 14, pp. 1522-1531, 2006.
[220] Y. E. Kim, V. K. Goel, J. N. Weinstein, and T. H. Lim, "Effect of disc degeneration at one level on the adjacent level in axial mode," *Spine,* vol. 16, no. 3, pp. 331-335, 1991.
[221] M. Adams, P. Dolan, W. Hutton, and R. Porter, "Diurnal changes in spinal mechanics and their clinical significance," *The Journal of bone and joint surgery. British volume,* vol. 72, no. 2, pp. 266-270, 1990.
[222] F. Postacchini, S. Gumina, G. Cinotti, D. Perugia, and C. DeMartino, "Ligamenta flava in lumbar disc herniation and spinal stenosis. Light and electron microscopic morphology," *Spine,* vol. 19, no. 8, pp. 917-922, 1994.
[223] J. J. Munns, H. S. An, A. A. E. Orías, G. B. Andersson, R. Takatori, and N. Inoue, "Ligamentum Flavum Hyperthropy Related to Disc Degeneration," *The Spine Journal,* vol. 10, no. 9, p. S76, 2010.
[224] S. Yan *et al.*, "Three-Dimensional Morphological Characteristics of Lower Lumbar Intervertebral Foramen with Age," *BioMed research international,* vol. 2018, 2018.
[225] W. H. Organization, "International classification of impairments, disabilities, and handicaps: a manual of classification relating to the consequences of disease, published in accordance with resolution WHA29. 35 of the Twenty-ninth World Health Assembly, May 1976," 1980.
[226] H. Merskey and N. Bogduk, "Classification of chronic pain, IASP Task Force on Taxonomy," *Seattle, WA: International Association for the Study of Pain Press (Also available online at www. iasp-painorg),* 1994.
[227] G. Waddell, *The back pain revolution*. Elsevier Health Sciences, 2004.
[228] J. Staal *et al.*, "KNGF Clinical Practice Guideline for Physical Therapy in patients with low back pain," *Royal Dutch Society for Physical Therapy [Koninklijk Nederlands Genootschap voor Fysiotherapie, KNGF],* 2014.
[229] T. R. Stanton, J. Latimer, C. G. Maher, and M. J. Hancock, "How do we define the condition 'recurrent low back pain'? A systematic review," *European Spine Journal,* vol. 19, no. 4, pp. 533-539, 2010.
[230] M. Rizk, E. Nader, C. Karam, and C. Ayoub, "Low back pain as perceived by the pain specialist," *Middle East J Anesthesiol,* vol. 21, pp. 463-82, 2012.
[231] R. Chou *et al.*, "Diagnosis and treatment of low back pain: a joint clinical practice guideline from the American College of Physicians and the American Pain Society," *Annals of internal medicine,* vol. 147, no. 7, pp. 478-491, 2007.
[232] B. A. Casazza, "Diagnosis and treatment of acute low back pain," *American family physician,* vol. 85, no. 4, pp. 343-350, 2012.
[233] M. Tominaga, M. Numazaki, T. Iida, and T. Tominaga, "Molecular mechanisms of nociception," *Nihon shinkei seishin yakurigaku zasshi= Japanese journal of psychopharmacology,* vol. 23, no. 3, pp. 139-147, 2003.
[234] R. Schleip, A. Zorn, and W. Klingler, "Biomechanical properties of fascial tissues and their role as pain generators," *Journal of musculoskeletal pain,* vol. 18, no. 4, pp. 393-395, 2010.
[235] H. Hall, "Effective spine triage: patterns of pain," *Ochsner Journal,* vol. 14, no. 1, pp. 88-95, 2014.
[236] J. S. Will, D. C. Bury, and J. A. Miller, "Mechanical low back pain," *American family physician,* vol. 98, no. 7, pp. 421-428, 2018.
[237] W. Kirkaldy-Willis, J. Wedge, K. Yong-Hing, and J. Reilly, "Pathology and pathogenesis of lumbar spondylosis and stenosis," *Spine,* vol. 3, no. 4, pp. 319-328, 1978.
[238] M. C. Battié, T. Videman, E. Levälahti, K. Gill, and J. Kaprio, "Genetic and environmental effects on disc degeneration by phenotype and spinal level: a multivariate twin study," *Spine,* vol. 33, no. 25, pp. 2801-2808, 2008.
[239] C. W. Pfirrmann, A. Metzdorf, M. Zanetti, J. Hodler, and N. Boos, "Magnetic resonance classification of lumbar intervertebral disc degeneration," *Spine,* vol. 26, no. 17, pp. 1873-1878, 2001.
[240] J. Nijs, A. Malfliet, K. Ickmans, I. Baert, and M. Meeus, "Treatment of central sensitization in patients with 'unexplained'chronic pain: an update," *Expert opinion on pharmacotherapy,* vol. 15, no. 12, pp. 1671-1683, 2014.

[241] M. J. Nasser, "How to approach the problem of low back pain: An overview," *Journal of family & community medicine,* vol. 12, no. 1, p. 3, 2005.
[242] S. M. Rapp, L. E. Miller, and J. E. Block, "AxiaLIF system: minimally invasive device for presacral lumbar interbody spinal fusion," *Medical Devices (Auckland, NZ),* vol. 4, p. 125, 2011.
[243] M. Nordin, F. Balague, and C. Cedraschi, "Nonspecific lower-back pain: surgical versus nonsurgical treatment," *Clinical Orthopaedics and Related Research®,* vol. 443, pp. 156-167, 2006.
[244] B. S. Blumberg and L. Sokoloff, "Coalescence of caudal vertebrae in the giant dinosaur Diplodocus," *Arthritis & Rheumatism: Official Journal of the American College of Rheumatology,* vol. 4, no. 6, pp. 592-601, 1961.
[245] E. C. Benzel, *Spine surgery: techniques, complication avoidance, and management*. Churchill Livingstone, 2005.
[246] D. Hoy, P. Brooks, F. Blyth, and R. Buchbinder, "The epidemiology of low back pain," *Best practice & research Clinical rheumatology,* vol. 24, no. 6, pp. 769-781, 2010.
[247] J. Obernauer, P. Kavakebi, S. Quirbach, and C. Thomé, "Pedicle-based non-fusion stabilization devices: a critical review and appraisal of current evidence," in *Advances and technical standards in neurosurgery*: Springer, 2014, pp. 131-142.
[248] R. J. Gala, G. S. Russo, and P. G. Whang, "Interspinous implants to treat spinal stenosis," *Current reviews in musculoskeletal medicine,* vol. 10, no. 2, pp. 182-188, 2017.
[249] J. Steadman, B. Catalani, C. Sharp, and L. Cooper, "Life-threatening perioperative anesthetic complications: major issues surrounding perioperative morbidity and mortality," *Trauma surgery & acute care open,* vol. 2, no. 1, p. e000113, 2017.
[250] S. Yin *et al.*, "Postoperative pulmonary complications following posterior spinal instrumentation and fusion for congenital scoliosis," *PloS one,* vol. 13, no. 11, 2018.
[251] J. A. Turner *et al.*, "Patient outcomes after lumbar spinal fusions," *Jama,* vol. 268, no. 7, pp. 907-911, 1992.
[252] H. Sari, T. O. Misirlioglu, U. Akarirmak, S. Hussain, and H. D. Kecebas, "The historical development and proof of lumbar traction used in physical therapy," *J Pharm Pharmacol,* vol. 2, pp. 87-94, 2014.
[253] D. H. Robinson and A. H. Toledo, "Historical development of modern anesthesia," *Journal of Investigative Surgery,* vol. 25, no. 3, pp. 141-149, 2012.
[254] J. Lister, "Antiseptic principle in the practice of surgery," *British medical journal,* vol. 2, no. 5543, p. 9, 1967.
[255] E. A. Underwood, "Wilhelm Conrad Röntgen (1845–1923) and the early development of radiology," ed: SAGE Publications, 1945.
[256] T. M. Daniel, "The history of tuberculosis," *Respiratory medicine,* vol. 100, no. 11, pp. 1862-1870, 2006.
[257] L. F. Peltier, *Orthopedics: a history and iconography* (no. 3). Norman Publishing, 1993.
[258] W. C. Campbell, "An operation for extra-articular fusion of the sacroiliac joint," *Surg Gynecol Obstet,* vol. 45, pp. 218-9, 1927.
[259] R. Hibbs, "Developmental abnormalities at the lumbosacral juncture causing pain and disability," *Surg Gynecol Obstet,* vol. 48, pp. 604-612, 1929.
[260] D. King, "Internal fixation for lumbosacral fusion," *JBJS,* vol. 30, no. 3, pp. 560-578, 1948.
[261] B. Burns, "An operation for spondylolisthesis," *Lancet,* vol. 1, p. 1233, 1933.
[262] H. Briggs and P. R. Milligan, "Chip fusion of the low back following exploration of the spinal canal," *JBJS,* vol. 26, no. 1, pp. 125-130, 1944.
[263] R. B. Cloward, "The treatment of ruptured lumbar intervertebral discs by vertebral body fusion: I. Indications, operative technique, after care," *Journal of neurosurgery,* vol. 10, no. 2, pp. 154-168, 1953.
[264] S. L. de Kunder, K. Rijkers, I. J. Caelers, R. A. de Bie, P. J. Koehler, and H. van Santbrink, "Lumbar interbody fusion: a historical overview and a future perspective," *Spine,* vol. 43, no. 16, pp. 1161-1168, 2018.
[265] I. O. Karikari and R. E. Isaacs, "Minimally invasive transforaminal lumbar interbody fusion: a review of techniques and outcomes," *Spine,* vol. 35, no. 26S, pp. S294-S301, 2010.
[266] J. Wang, Y. Zhou, Z. F. Zhang, C. Q. Li, W. J. Zheng, and J. Liu, "Comparison of one-level minimally invasive and open transforaminal lumbar interbody fusion in degenerative and isthmic spondylolisthesis grades 1 and 2," *European Spine Journal,* vol. 19, no. 10, pp. 1780-1784, 2010.
[267] B. Skovrlj, J. Gilligan, H. S. Cutler, and S. A. Qureshi, "Minimally invasive procedures on the lumbar spine," *World Journal of Clinical Cases: WJCC,* vol. 3, no. 1, p. 1, 2015.

[268] C. Faubert and W. Caspar, "Lumbar percutaneous discectomy," *Neuroradiology,* vol. 33, no. 5, pp. 407-410, 1991.
[269] T. Motosuneya, T. Asazuma, T. Tsuji, H. Watanabe, Y. Nakayama, and K. Nemoto, "Postoperative change of the cross-sectional area of back musculature after 5 surgical procedures as assessed by magnetic resonance imaging," *Clinical Spine Surgery,* vol. 19, no. 5, pp. 318-322, 2006.
[270] R. J. Mobbs, A. Lennox, Y.-T. Ho, K. Phan, and W. J. Choy, "L5/S1 anterior lumbar interbody fusion technique," *Journal of Spine Surgery,* vol. 3, no. 3, p. 429, 2017.
[271] R. J. Mobbs, K. Phan, G. Malham, K. Seex, and P. J. Rao, "Lumbar interbody fusion: techniques, indications and comparison of interbody fusion options including PLIF, TLIF, MI-TLIF, OLIF/ATP, LLIF and ALIF," *Journal of Spine Surgery,* vol. 1, no. 1, p. 2, 2015.
[272] W. S. Rosenberg and P. V. Mummaneni, "Transforaminal lumbar interbody fusion: technique, complications, and early results," *Neurosurgery,* vol. 48, no. 3, pp. 569-575, 2001.
[273] D. Serban, N. Calina, and G. Tender, "Standard versus minimally invasive transforaminal lumbar interbody fusion: a prospective randomized study," *BioMed research international,* vol. 2017, 2017.
[274] C. K. Lee, J. Y. Park, and H. Y. Zhang, "Minimally invasive transforaminal lumbar interbody fusion using a single interbody cage and a tubular retraction system: technical tips, and perioperative, radiologic and clinical outcomes," *Journal of Korean Neurosurgical Society,* vol. 48, no. 3, p. 219, 2010.
[275] B. M. Ozgur, H. E. Aryan, L. Pimenta, and W. R. Taylor, "Extreme Lateral Interbody Fusion (XLIF): a novel surgical technique for anterior lumbar interbody fusion," *The Spine Journal,* vol. 6, no. 4, pp. 435-443, 2006.
[276] S. Ohtori *et al.*, "Mini-open anterior retroperitoneal lumbar interbody fusion: oblique lateral interbody fusion for lumbar spinal degeneration disease," *Yonsei medical journal,* vol. 56, no. 4, pp. 1051-1059, 2015.
[277] H. Abbasi and A. Abbasi, "Oblique lateral lumbar interbody fusion (OLLIF): technical notes and early results of a single surgeon comparative study," *Cureus,* vol. 7, no. 10, 2015.
[278] M. Richter, M. Weidenfeld, and F. Uckmann, "Anterior lumbar interbody fusion. Indications, technique, advantages and disadvantages," *Der Orthopade,* vol. 44, no. 2, pp. 154-161, 2015.
[279] M. J. Winder and S. Gambhir, "Comparison of ALIF vs. XLIF for L4/5 interbody fusion: pros, cons, and literature review," *Journal of Spine Surgery,* vol. 2, no. 1, p. 2, 2016.
[280] I. Teng, J. Han, K. Phan, and R. Mobbs, "A meta-analysis comparing alif, plif, tlif and llif," *Journal of Clinical Neuroscience,* vol. 44, pp. 11-17, 2017.
[281] P. M. Udby and R. Bech-Azeddine, "Clinical outcome of stand-alone ALIF compared to posterior instrumentation for degenerative disc disease: a pilot study and a literature review," *Clinical neurology and neurosurgery,* vol. 133, pp. 64-69, 2015.
[282] R. E. Isaacs *et al.*, "Minimally invasive microendoscopy-assisted transforaminal lumbar interbody fusion with instrumentation," *Journal of Neurosurgery: Spine,* vol. 3, no. 2, pp. 98-105, 2005.
[283] W. A. Sulaiman and M. Singh, "Minimally invasive versus open transforaminal lumbar interbody fusion for degenerative spondylolisthesis grades 1-2: patient-reported clinical outcomes and cost-utility analysis," *Ochsner Journal,* vol. 14, no. 1, pp. 32-37, 2014.
[284] R. Hah and H. P. Kang, "Lateral and Oblique Lumbar Interbody Fusion—Current Concepts and a Review of Recent Literature," *Current reviews in musculoskeletal medicine,* vol. 12, no. 3, pp. 305-310, 2019.
[285] C. Mehren and A. Korge, "Minimally invasive anterior oblique lumbar interbody fusion (OLIF)," *European Spine Journal,* vol. 25, p. 471, 2016.
[286] J. G. DeVine, D. Gloystein, and N. Singh, "A novel alternative for removal of the AxiaLif (TranS1) in the setting of pseudarthrosis of L5–S1," *The Spine Journal,* vol. 9, no. 11, pp. 910-915, 2009.
[287] P. Kambin and L. Zhou, "Arthroscopic discectomy of the lumbar spine," *Clinical Orthopaedics and Related Research®,* vol. 337, pp. 49-57, 1997.
[288] J. W. Park, H. S. Nam, S. K. Cho, H. J. Jung, B. J. Lee, and Y. Park, "Kambin's triangle approach of lumbar transforaminal epidural injection with spinal stenosis," *Annals of rehabilitation medicine,* vol. 35, no. 6, p. 833, 2011.
[289] T. Alamin, F. Malek, E. Carragee, and M.-J. Kim, "The functional anaesthetic discogram: description of a novel diagnostic technique and report of 3 cases," *International Journal of Spine Surgery,* vol. 2, no. 2, pp. 107-113, 2008.
[290] R. Hoshide, E. Feldman, and W. Taylor, "Cadaveric analysis of the Kambin's triangle," *Cureus,* vol. 8, no. 2, 2016.

[291] M. Hardenbrook, S. Lombardo, M. C. Wilson, and A. E. Telfeian, "The anatomic rationale for transforaminal endoscopic interbody fusion: a cadaveric analysis," *Neurosurgical focus,* vol. 40, no. 2, p. E12, 2016.
[292] A. F. Ozer *et al.*, "Anatomic assessment of variations in Kambin's triangle: a surgical and cadaver study," *World neurosurgery,* vol. 100, pp. 498-503, 2017.
[293] H. Abbasi and C. M. Murphy, "Economic performance of oblique lateral lumbar interbody fusion (OLLIF) with a focus on hospital throughput efficiency," *Cureus,* vol. 7, no. 7, 2015.
[294] M. Sakane, "Anatomical relationship between Kambin's triangle and exiting nerve root," *Mini-Invasive Surg,* vol. 1, no. 1, pp. 99-102, 2017.
[295] K. Sairyo *et al.*, "State of the art: transforaminal approach for percutaneous endoscopic lumbar discectomy under local anesthesia," *The Journal of Medical Investigation,* vol. 61, no. 3.4, pp. 217-225, 2014.
[296] A. A. Limberg, *The planning of local plastic operations on the body surface: theory and practice*. Collamore Press, 1984.
[297] S. Das, "Urology in ancient India," *Indian journal of urology: IJU: journal of the Urological Society of India,* vol. 23, no. 1, p. 2, 2007.
[298] A. N. Bahsoun, S. Wheatstone, and E. Challacombe, "Simulation in historical perspective: the history of medical and surgical simulation," *Surgical Simulation,* p. 20, 2014.
[299] P. T. Scardino and J. Kelman, *Dr. Peter Scardino's Prostate Book, Revised Edition: The Complete Guide to Overcoming Prostate Cancer, Prostatitis, and BPH*. Penguin, 2010.
[300] S. K. Ghosh, "Human cadaveric dissection: a historical account from ancient Greece to the modern era," *Anatomy & cell biology,* vol. 48, no. 3, pp. 153-169, 2015.
[301] C. Jeon, "The virtual flier: The link trainer, flight simulation, and pilot identity," *Technology and culture,* vol. 56, no. 1, pp. 28-53, 2015.
[302] J. Ker and P. Bradley, "Simulation in medical education," *Understanding medical education: Evidence, theory and practice,* vol. 1, pp. 164-180, 2010.
[303] J. Cooper and V. Taqueti, "A brief history of the development of mannequin simulators for clinical education and training," *Postgraduate medical journal,* vol. 84, no. 997, pp. 563-570, 2008.
[304] P. Bradley, "The history of simulation in medical education and possible future directions," *Medical education,* vol. 40, no. 3, pp. 254-262, 2006.
[305] M. L. Heilig, "Sensorama simulator," ed: Google Patents, 1962.
[306] H. Q. Dinh, N. Walker, L. F. Hodges, C. Song, and A. Kobayashi, "Evaluating the importance of multi-sensory input on memory and the sense of presence in virtual environments," in *Proceedings IEEE Virtual Reality (Cat. No. 99CB36316)*, 1999: IEEE, pp. 222-228.
[307] S. L. Delp, J. P. Loan, M. G. Hoy, F. E. Zajac, E. L. Topp, and J. M. Rosen, "An interactive graphics-based model of the lower extremity to study orthopaedic surgical procedures," *IEEE Transactions on Biomedical engineering,* vol. 37, no. 8, pp. 757-767, 1990.
[308] N. E. Seymour *et al.*, "Virtual reality training improves operating room performance: results of a randomized, double-blinded study," *Annals of surgery,* vol. 236, no. 4, p. 458, 2002.
[309] J. Chikwe, A. C. de Souza, and J. R. Pepper, "No time to train the surgeons," ed: British Medical Journal Publishing Group, 2004.
[310] M. M. Hutter, K. C. Kellogg, C. M. Ferguson, W. M. Abbott, and A. L. Warshaw, "The impact of the 80-hour resident workweek on surgical residents and attending surgeons," *Annals of surgery,* vol. 243, no. 6, p. 864, 2006.
[311] M. Scerbo, "Medical virtual reality simulators: Have we missed an opportunity," *Human Factors and Ergonomics Society Bulletin,* vol. 48, no. 5, pp. 1-3, 2005.
[312] D. M. Gaba, "The future vision of simulation in healthcare," *Simulation in Healthcare,* vol. 2, no. 2, pp. 126-135, 2007.
[313] R. Valentine, V. Padhye, and P.-J. Wormald, "Simulation training for vascular emergencies in endoscopic sinus and skull base surgery," *Otolaryngologic Clinics of North America,* vol. 49, no. 3, pp. 877-887, 2016.
[314] M. W. Krueger, "Artificial reality II," 1991.
[315] R. M. Held and N. I. Durlach, "Telepresence," *Presence: Teleoperators & Virtual Environments,* vol. 1, no. 1, pp. 109-112, 1992.
[316] J. Steuer, "Defining virtual reality: Dimensions determining telepresence," *Journal of communication,* vol. 42, no. 4, pp. 73-93, 1992.

[317] W. R. Sherman and A. B. Craig, *Understanding virtual reality: Interface, application, and design*. Elsevier, 2002.
[318] M.-S. Yoh, "The reality of virtual reality," in *Proceedings Seventh International Conference on Virtual Systems and Multimedia*, 2001: IEEE, pp. 666-674.
[319] Z. Jianchao and Y. Zhihe, "Virtual reality technology and its application [M]," ed: Beijing: TsingHua University Press, 1996.
[320] S. Aukstakalnis and D. Blatner, *Silicon mirage; the art and science of virtual reality*. Peachpit Press, 1992.
[321] Z. Zhao, "Virtual reality technology: an overview," *Journal of Southeast University,* vol. 32, no. 2A, pp. 1-10, 2002.
[322] R. Gadh, "Virtual reality—a new technology for the mechanical engineer," 1998.
[323] C. H. Zhuang and P. Wang, " Virtual Reality Technology and Applications (in Chinese)," *Publishing House of Electronics Industry,* 2010.
[324] G. C. Burdea and P. Coiffet, *Virtual reality technology*. John Wiley & Sons, 2003.
[325] D. Van Krevelen and R. Poelman, "A survey of augmented reality technologies, applications and limitations," *International journal of virtual reality,* vol. 9, no. 2, pp. 1-20, 2010.
[326] M. O. Ward, G. Grinstein, and D. Keim, *Interactive data visualization: foundations, techniques, and applications*. CRC Press, 2010.
[327] M. Akay and A. Marsh, "Virtual Reality and the Vestibular System: A Brief Review," 2001.
[328] C. R. Sherman, "Motion sickness: review of causes and preventive strategies," *Journal of travel medicine,* vol. 9, no. 5, pp. 251-256, 2002.
[329] J. Taylor, "Proprioception," 2009.
[330] J. Han, G. Waddington, R. Adams, J. Anson, and Y. Liu, "Assessing proprioception: a critical review of methods," *Journal of Sport and Health Science,* vol. 5, no. 1, pp. 80-90, 2016.
[331] C. J. Price and C. Hooven, "Interoceptive awareness skills for emotion regulation: Theory and approach of mindful awareness in body-oriented therapy (MABT)," *Frontiers in psychology,* vol. 9, p. 798, 2018.
[332] M. A. Muhanna, "Virtual reality and the CAVE: Taxonomy, interaction challenges and research directions," *Journal of King Saud University-Computer and Information Sciences,* vol. 27, no. 3, pp. 344-361, 2015.
[333] S. Heim, *The resonant interface: HCI foundations for interaction design*. Addison-Wesley Longman Publishing Co., Inc., 2007.
[334] D. Allerton, "Flight Simulation-past, present and future," *The Aeronautical Journal,* vol. 104, no. 1042, pp. 651-663, 2000.
[335] M. SAMADBEIK, D. YAAGHOBI, P. BASTANI, S. ABHARI, R. REZAEE, and A. GARAVAND, "The applications of virtual reality technology in medical groups teaching," *Journal of Advances in Medical Education & Professionalism,* vol. 6, no. 3, p. 123, 2018.
[336] C. Anthes, R. J. García-Hernández, M. Wiedemann, and D. Kranzlmüller, "State of the art of virtual reality technology," in *2016 IEEE Aerospace Conference*, 2016: IEEE, pp. 1-19.
[337] T. Mazuryk and M. Gervautz, "Virtual reality-history, applications, technology and future," 1996.
[338] D. Escobar-Castillejos, J. Noguez, L. Neri, A. Magana, and B. Benes, "A review of simulators with haptic devices for medical training," *Journal of medical systems,* vol. 40, no. 4, p. 104, 2016.
[339] H. Culbertson, S. B. Schorr, and A. M. Okamura, "Haptics: The present and future of artificial touch sensation," *Annual Review of Control, Robotics, and Autonomous Systems,* vol. 1, pp. 385-409, 2018.
[340] M. Alaker, G. R. Wynn, and T. Arulampalam, "Virtual reality training in laparoscopic surgery: a systematic review & meta-analysis," *International Journal of Surgery,* vol. 29, pp. 85-94, 2016.
[341] T. H. Massie and J. K. Salisbury, "The phantom haptic interface: A device for probing virtual objects," in *Proceedings of the ASME winter annual meeting, symposium on haptic interfaces for virtual environment and teleoperator systems*, 1994, vol. 55, no. 1: Chicago, IL, pp. 295-300.
[342] A. Q. Keemink, H. van der Kooij, and A. H. Stienen, "Admittance control for physical human–robot interaction," *The International Journal of Robotics Research,* vol. 37, no. 11, pp. 1421-1444, 2018.
[343] S. N. Fry, N. Rohrseitz, A. D. Straw, and M. H. Dickinson, "TrackFly: virtual reality for a behavioral system analysis in free-flying fruit flies," *Journal of neuroscience methods,* vol. 171, no. 1, pp. 110-117, 2008.
[344] J. Brookes, M. Warburton, M. Alghadier, M. Mon-Williams, and F. Mushtaq, "Studying human behavior with virtual reality: The Unity Experiment Framework," *Behavior research methods,* pp. 1-9, 2019.

[345] M. Burt and C. Louw, "Virtual reality enhanced roller coasters and the future of entertainment–audience expectations," *World Leisure Journal,* vol. 61, no. 3, pp. 183-199, 2019.
[346] S. Gillner and H. Mallot, "Virtual reality and spatial cognition," 2001.
[347] W. I. Willaert, R. Aggarwal, I. Van Herzeele, N. J. Cheshire, and F. E. Vermassen, "Recent advancements in medical simulation: patient-specific virtual reality simulation," *World journal of surgery,* vol. 36, no. 7, pp. 1703-1712, 2012.
[348] H. R. Malone, O. N. Syed, M. S. Downes, A. L. D'Ambrosio, D. O. Quest, and M. G. Kaiser, "Simulation in neurosurgery: a review of computer-based simulation environments and their surgical applications," *Neurosurgery,* vol. 67, no. 4, pp. 1105-1116, 2010.
[349] G. Bashir, "Technology and medicine: the evolution of virtual reality simulation in laparoscopic training," *Medical teacher,* vol. 32, no. 7, pp. 558-561, 2010.
[350] S. K. Neequaye, R. Aggarwal, I. Van Herzeele, A. Darzi, and N. J. Cheshire, "Endovascular skills training and assessment," *Journal of vascular surgery,* vol. 46, no. 5, pp. 1055-1064, 2007.
[351] A. K. Sachdeva *et al.*, "A new paradigm for surgical procedural training," *Current problems in surgery,* vol. 48, no. 12, pp. 854-968, 2011.
[352] G. De Win *et al.*, "Laparoscopy training in surgical education: the utility of incorporating a structured preclinical laparoscopy course into the traditional apprenticeship method," *Journal of surgical education,* vol. 70, no. 5, pp. 596-605, 2013.
[353] N. E. Seymour, "VR to OR: a review of the evidence that virtual reality simulation improves operating room performance," *World journal of surgery,* vol. 32, no. 2, pp. 182-188, 2008.
[354] R. A. Chaer *et al.*, "Simulation improves resident performance in catheter-based intervention: results of a randomized, controlled study," *Annals of surgery,* vol. 244, no. 3, p. 343, 2006.
[355] P. Berger, M. Willems, J. Van Der Vliet, L. S. Kool, D. Bergqvist, and J. Blankensteijn, "Validation of the Simulator for Testing and Rating Endovascular SkillS (STRESS)-machine in a setting of competence testing," *Journal of Cardiovascular Surgery,* vol. 51, no. 2, p. 253, 2010.
[356] J. Pottle, "Virtual reality and the transformation of medical education," *Future healthcare journal,* vol. 6, no. 3, p. 181, 2019.
[357] S. Barry Issenberg, W. C. Mcgaghie, E. R. Petrusa, D. Lee Gordon, and R. J. Scalese, "Features and uses of high-fidelity medical simulations that lead to effective learning: a BEME systematic review," *Medical teacher,* vol. 27, no. 1, pp. 10-28, 2005.
[358] K. Walsh and P. Jaye, "Simulation-based medical education: cost measurement must be comprehensive," *Surgery,* vol. 153, no. 2, p. 302, 2013.
[359] C. McIntosh, A. Macario, B. Flanagan, and D. M. Gaba, "Simulation: what does it really cost?," *Simulation in Healthcare,* vol. 1, no. 2, p. 109, 2006.
[360] J. A. Iglesias-Vázquez, A. Rodríguez-Núñez, M. Penas-Penas, L. Sánchez-Santos, M. Cegarra-García, and M. V. Barreiro-Díaz, "Cost-efficiency assessment of Advanced Life Support (ALS) courses based on the comparison of advanced simulators with conventional manikins," *BMC emergency medicine,* vol. 7, no. 1, p. 18, 2007.
[361] S. Haque and S. Srinivasan, "A meta-analysis of the training effectiveness of virtual reality surgical simulators," *IEEE Transactions on Information Technology in Biomedicine,* vol. 10, no. 1, pp. 51-58, 2006.
[362] R. Aggarwal, J. Ward, I. Balasundaram, P. Sains, T. Athanasiou, and A. Darzi, "Proving the effectiveness of virtual reality simulation for training in laparoscopic surgery," *Annals of surgery,* vol. 246, no. 5, pp. 771-779, 2007.
[363] G. Ahlberg *et al.*, "Proficiency-based virtual reality training significantly reduces the error rate for residents during their first 10 laparoscopic cholecystectomies," *The American journal of surgery,* vol. 193, no. 6, pp. 797-804, 2007.
[364] T. P. Grantcharov, V. B. Kristiansen, J. Bendix, L. Bardram, J. Rosenberg, and P. Funch-Jensen, "Randomized clinical trial of virtual reality simulation for laparoscopic skills training," *Br J Surg,* vol. 91, no. 2, pp. 146-50, Feb 2004, doi: 10.1002/bjs.4407.
[365] K. R. Wanzel, S. J. Hamstra, M. F. Caminiti, D. J. Anastakis, E. D. Grober, and R. K. Reznick, "Visual-spatial ability correlates with efficiency of hand motion and successful surgical performance," *Surgery,* vol. 134, no. 5, pp. 750-757, 2003.
[366] P. E. Pelargos *et al.*, "Utilizing virtual and augmented reality for educational and clinical enhancements in neurosurgery," *Journal of Clinical Neuroscience,* vol. 35, pp. 1-4, 2017.

[367] F. E. Alotaibi, G. A. AlZhrani, A. J. Sabbagh, H. Azarnoush, A. Winkler-Schwartz, and R. F. Del Maestro, "Neurosurgical assessment of metrics including judgment and dexterity using the virtual reality simulator NeuroTouch (NAJD Metrics)," *Surgical innovation,* vol. 22, no. 6, pp. 636-642, 2015.
[368] L. Konge and L. Lonn, "Simulation-based training of surgical skills," *Perspectives on medical education,* vol. 5, no. 1, pp. 3-4, 2016.
[369] B. E. Sakakushev, B. I. Marinov, P. P. Stefanova, S. S. Kostianev, and E. K. Georgiou, "Striving for better medical education: the simulation approach," *Folia Medica,* vol. 59, no. 2, pp. 123-131, 2017.
[370] H. Miyata *et al.*, "Validity assessment of the laparoscopic radical nephrectomy module of the LapVision virtual reality simulator," *Surgery Open Science,* vol. 2, no. 1, pp. 51-56, 2020.
[371] P. Lamata *et al.*, "SINERGIA laparoscopic virtual reality simulator: Didactic design and technical development," *Computer methods and programs in biomedicine,* vol. 85, no. 3, pp. 273-283, 2007.
[372] A. Radetzky, M. Rudolph, S. Starkie, B. Davies, and L. M. Auer, "ROBO-SIM: a simulator for minimally invasive neurosurgery using an active manipulator," *Studies in health technology and informatics,* vol. 77, pp. 1165-1169, 2000.
[373] M. Baur, "EasyGuide Neuro: A New Approach to Image-Guided Surgery," in *Computer-Assisted Neurosurgery*: Springer, 1997, pp. 38-42.
[374] G. Coelho, S. Zymberg, M. Lyra, N. Zanon, and B. Warf, "New anatomical simulator for pediatric neuroendoscopic practice," *Child's Nervous System,* vol. 31, no. 2, pp. 213-219, 2015.
[375] M. Nakao *et al.*, "Haptic reproduction and interactive visualization of a beating heart for cardiovascular surgery simulation," *International journal of medical informatics,* vol. 68, no. 1-3, pp. 155-163, 2002.
[376] A. S. Sethi, W. J. Peine, Y. Mohammadi, and C. P. Sundaram, "Validation of a novel virtual reality robotic simulator," *Journal of endourology,* vol. 23, no. 3, pp. 503-508, 2009.
[377] H. Egi *et al.*, "Face, content and concurrent validity of the Mimic® dV-Trainer for robot-assisted endoscopic surgery: a prospective study," *European Surgical Research,* vol. 50, no. 3-4, pp. 292-300, 2013.
[378] J. Y. Lee, P. Mucksavage, D. C. Kerbl, V. B. Huynh, M. Etafy, and E. M. McDougall, "Validation study of a virtual reality robotic simulator—role as an assessment tool?," *The Journal of urology,* vol. 187, no. 3, pp. 998-1002, 2012.
[379] T. Alzahrani *et al.*, "Validation of the da Vinci Surgical Skill Simulator across three surgical disciplines: a pilot study," *Canadian Urological Association Journal,* vol. 7, no. 7-8, p. E520, 2013.
[380] A. J. Hung *et al.*, "Face, content and construct validity of a novel robotic surgery simulator," *The Journal of urology,* vol. 186, no. 3, pp. 1019-1025, 2011.
[381] D. G. Krishnan, A. V. Keloth, and S. Ubedulla, "Pros and cons of simulation in medical education: A review," *Education,* vol. 3, no. 6, pp. 84-87, 2017.
[382] Q. Zhao, "10 scientific problems in virtual reality," *Communications of the ACM,* vol. 54, no. 2, pp. 116-118, 2011.
[383] L. Li *et al.*, "Application of virtual reality technology in clinical medicine," *American journal of translational research,* vol. 9, no. 9, p. 3867, 2017.
[384] W. R. Mark, S. C. Randolph, M. Finch, J. M. Van Verth, and R. M. Taylor, "Adding force feedback to graphics systems: Issues and solutions," in *Proceedings of the 23rd annual conference on Computer graphics and interactive techniques*, 1996, pp. 447-452.
[385] H. Kolivand, B. Tomi, N. Zamri, and M. S. Sunar, "Virtual surgery, applications and limitations," in *Medical imaging technology*: Springer, 2015, pp. 169-195.
[386] M. Dragan and Z. Manfred, "Survey of Finite Element Method-Based Real-Time Simulations," *Applied Sciences*, vol. 9, no. 14, doi: 10.3390/app9142775.
[387] M. Garbey, B. L. Bass, and S. Berceli, "Multiscale mechanobiology modeling for surgery assessment," *Acta Mechanica Sinica,* vol. 28, no. 4, pp. 1186-1202, 2012.
[388] H. Delingette and N. Ayache, "Soft tissue modeling for surgery simulation," *Handbook of Numerical Analysis,* vol. 12, pp. 453-550, 2004.
[389] E. Cueto and F. Chinesta, "Real time simulation for computational surgery: a review," *Advanced Modeling and Simulation in Engineering Sciences,* vol. 1, no. 1, p. 11, 2014.
[390] B. E. Rapp, *Microfluidics: modeling, mechanics and mathematics*. William Andrew, 2016.
[391] R. Satava, "Medical virtual reality: The current status of the future," in *Medicine meets virtual reality*, 1996.
[392] D. Terzopoulos, J. Platt, A. Barr, and K. Fleischer, "Elastically deformable models," in *Proceedings of the 14th annual conference on Computer graphics and interactive techniques*, 1987, pp. 205-214.

[393] K. Waters, "Physical model of facial tissue and muscle articulation derived from computer tomography data," in *Visualization in Biomedical Computing'92*, 1992, vol. 1808: International Society for Optics and Photonics, pp. 574-583.
[394] J. C. Platt and A. H. Barr, "Constraints methods for flexible models," in *Proceedings of the 15th annual conference on Computer graphics and interactive techniques*, 1988, pp. 279-288.
[395] W. Mollemans, F. Schutyser, J. Van Cleynenbreugel, and P. Suetens, "Fast soft tissue deformation with tetrahedral mass spring model for maxillofacial surgery planning systems," in *International Conference on Medical Image Computing and Computer-Assisted Intervention*, 2004: Springer, pp. 371-379.
[396] P. Patete *et al.*, "A multi-tissue mass-spring model for computer assisted breast surgery," *Medical engineering & physics,* vol. 35, no. 1, pp. 47-53, 2013.
[397] L. P. Nedel and D. Thalmann, "Real time muscle deformations using mass-spring systems," in *Proceedings. Computer Graphics International (Cat. No. 98EX149)*, 1998: IEEE, pp. 156-165.
[398] A. V. Gelder, "Approximate simulation of elastic membranes by triangulated spring meshes," *Journal of graphics tools,* vol. 3, no. 2, pp. 21-41, 1998.
[399] F. Chen, L. Gu, P. Huang, J. Zhang, and J. Xu, "Soft tissue modeling using nonlinear mass spring and simplified medial representation," in *2007 29th Annual International Conference of the IEEE Engineering in Medicine and Biology Society*, 2007: IEEE, pp. 5083-5086.
[400] H. Delingette, "Biquadratic and quadratic springs for modeling St Venant Kirchhoff materials," in *International Symposium on Biomedical Simulation*, 2008: Springer, pp. 40-48.
[401] D. Bourguignon and M.-P. Cani, "Controlling anisotropy in mass-spring systems," in *Computer Animation and Simulation 2000*: Springer, 2000, pp. 113-123.
[402] S. F. Gibson, "3D chainmail: a fast algorithm for deforming volumetric objects," in *Proceedings of the 1997 symposium on Interactive 3D graphics*, 1997, pp. 149-ff.
[403] M. Harders, R. Hutter, A. Rutz, P. Niederer, and G. Székely, "Comparing a simplified FEM approach with the mass-spring model for surgery simulation," *Studies in health technology and informatics,* pp. 103-109, 2003.
[404] M. Zehn, "MBS and FEM: A Marriage-of-Convenience or a Love Story," *BENCHmark, International Magazine for Engineering Design & Analysis,* pp. 12-15, 2005.
[405] M. Busch and B. Schweizer, "Coupled simulation of multibody and finite element systems: an efficient and robust semi-implicit coupling approach," *Archive of Applied Mechanics,* vol. 82, no. 6, pp. 723-741, 2012.
[406] S. Cotin, H. Delingette, and N. Ayache, "A hybrid elastic model allowing real-time cutting, deformations and force-feedback for surgery training and simulation," 2000.
[407] J. Huang, S.-K. Ong, and A. Y. Nee, "Real-time finite element structural analysis in augmented reality," *Advances in Engineering Software,* vol. 87, pp. 43-56, 2015.
[408] M. Fiorentino, G. Monno, and A. Uva, "Interactive "touch and see" FEM Simulation using Augmented Reality," *Int. J. Eng. Educ,* vol. 25, no. 6, pp. 1124-1128, 2009.
[409] R. J. Guyan, "Reduction of stiffness and mass matrices," *AIAA journal,* vol. 3, no. 2, pp. 380-380, 1965.
[410] G. Picinbono, J. C. Lombardo, H. Delingette, and N. Ayache, "Improving realism of a surgery simulator: linear anisotropic elasticity, complex interactions and force extrapolation," *The Journal of Visualization and Computer Animation,* vol. 13, no. 3, pp. 147-167, 2002.
[411] D. Marinkovic and M. Zehn, "Co-rotational FEM for fast geometrically nonlinear static and dynamic algorithms," in *Research and Applications in Structural Engineering, Mechanics and Computation*: CRC Press, 2013, pp. 199-200.
[412] M. Müller and M. Gross, "Interactive virtual materials," in *Proceedings of Graphics Interface 2004*, 2004: Canadian Human-Computer Communications Society, pp. 239-246.
[413] K.-J. Bathe, *Finite element procedures*. Klaus-Jurgen Bathe, 2006.
[414] G. Székely, C. Brechbühler, R. Hutter, A. Rhomberg, N. Ironmonger, and P. Schmid, "Modelling of soft tissue deformation for laparoscopic surgery simulation," *Medical Image Analysis,* vol. 4, no. 1, pp. 57-66, 2000.
[415] J. Zhou, Z. Luo, C. Li, and M. Deng, "Real-time deformation of human soft tissues: A radial basis meshless 3D model based on Marquardt's algorithm," *Computer methods and programs in biomedicine,* vol. 153, pp. 237-252, 2018.
[416] G. Zhang, A. Wittek, G. Joldes, X. Jin, and K. Miller, "A three-dimensional nonlinear meshfree algorithm for simulating mechanical responses of soft tissue," *Engineering Analysis with Boundary Elements,* vol. 42, pp. 60-66, 2014.

[417] L. Jeřábková and T. Kuhlen, "Stable cutting of deformable objects in virtual environments using xfem," *IEEE computer graphics and applications,* vol. 29, no. 2, pp. 61-71, 2009.
[418] D. Bielser, V. A. Maiwald, and M. H. Gross, "Interactive cuts through 3-dimensional soft tissue," in *Computer Graphics Forum*, 1999, vol. 18, no. 3: Wiley Online Library, pp. 31-38.
[419] A. B. Mor and T. Kanade, "Modifying soft tissue models: Progressive cutting with minimal new element creation," in *International Conference on Medical Image Computing and Computer-Assisted Intervention*, 2000: Springer, pp. 598-607.
[420] H.-W. Nienhuys and A. F. van der Stappen, "Supporting cuts and finite element deformation in interactive surgery simulation," 2001.
[421] N. Molino, Z. Bao, and R. Fedkiw, "A virtual node algorithm for changing mesh topology during simulation," *ACM Transactions on Graphics (TOG),* vol. 23, no. 3, pp. 385-392, 2004.
[422] L. M. Vigneron, J. G. Verly, and S. K. Warfield, "On extended finite element method (xfem) for modelling of organ deformations associated with surgical cuts," in *International Symposium on Medical Simulation*, 2004: Springer, pp. 134-143.
[423] H. Courtecuisse, H. Jung, J. Allard, C. Duriez, D. Y. Lee, and S. Cotin, "GPU-based real-time soft tissue deformation with cutting and haptic feedback," *Progress in biophysics and molecular biology,* vol. 103, no. 2-3, pp. 159-168, 2010.
[424] R. Alterovitz, A. Lim, K. Goldberg, G. S. Chirikjian, and A. M. Okamura, "Steering flexible needles under Markov motion uncertainty," in *2005 IEEE/RSJ International Conference on Intelligent Robots and Systems*, 2005: IEEE, pp. 1570-1575.
[425] L. B. Ready, "American Society of Regional Anesthesia 1999 Gaston Labat Lecture--Acute pain: Lessons learned from 25,000 patients," *Regional anesthesia and pain medicine,* vol. 24, no. 6, p. 499, 1999.
[426] G. Ravali and M. Manivannan, "Haptic Feedback in Needle Insertion Modeling and Simulation," *IEEE reviews in biomedical engineering,* vol. 10, pp. 63-77, 2017, doi: 10.1109/RBME.2017.2706966.
[427] O. Goksel, E. Dehghan, and S. E. Salcudean, "Modeling and simulation of flexible needles," *Medical engineering & physics,* vol. 31, no. 9, pp. 1069-1078, 2009.
[428] H. Kataoka, T. Washio, M. Audette, and K. Mizuhara, "A model for relations between needle deflection, force, and thickness on needle penetration," in *International Conference on Medical Image Computing and Computer-Assisted Intervention*, 2001: Springer, pp. 966-974.
[429] T. Lehmann, M. Tavakoli, N. Usmani, and R. Sloboda, "Force-sensor-based estimation of needle tip deflection in brachytherapy," *Journal of Sensors,* vol. 2013, 2013.
[430] A. M. Okamura, C. Simone, and M. D. O'leary, "Force modeling for needle insertion into soft tissue," *IEEE transactions on biomedical engineering,* vol. 51, no. 10, pp. 1707-1716, 2004.
[431] S. Misra, K. B. Reed, B. W. Schafer, K. Ramesh, and A. M. Okamura, "Mechanics of flexible needles robotically steered through soft tissue," *The International journal of robotics research,* vol. 29, no. 13, pp. 1640-1660, 2010.
[432] M. Mahvash and P. E. Dupont, "Mechanics of dynamic needle insertion into a biological material," *IEEE transactions on bio-medical engineering,* vol. 57, no. 4, pp. 934-43, 2010, doi: 10.1109/TBME.2009.2036856.
[433] M. Färber, F. Hummel, C. Gerloff, and H. Handels, "Virtual reality simulator for the training of lumbar punctures," *Methods of information in medicine,* vol. 48, no. 05, pp. 493-501, 2009.
[434] K. Yan *et al.*, "Needle steering modeling and analysis using unconstrained modal analysis," in *The First IEEE/RAS-EMBS International Conference on Biomedical Robotics and Biomechatronics, 2006. BioRob 2006.*, 2006: IEEE, pp. 87-92.
[435] M. Torabi, K. Hauser, R. Alterovitz, V. Duindam, and K. Goldberg, "Guiding medical needles using single-point tissue manipulation," in *2009 IEEE International Conference on Robotics and Automation*, 2009: IEEE, pp. 2705-2710.
[436] A. Asadian, M. R. Kermani, and R. V. Patel, "A compact dynamic force model for needle-tissue interaction," in *2010 Annual International Conference of the IEEE Engineering in Medicine and Biology*, 2010: IEEE, pp. 2292-2295.
[437] J. T. Hing, A. D. Brooks, and J. P. Desai, "Reality-based needle insertion simulation for haptic feedback in prostate brachytherapy," in *Proceedings 2006 IEEE International Conference on Robotics and Automation, 2006. ICRA 2006.*, 2006: IEEE, pp. 619-624.

[438] P. N. Brett, T. Parker, A. J. Harrison, T. A. Thomas, and A. Carr, "Simulation of resistance forces acting on surgical needles," *Proceedings of the Institution of Mechanical Engineers, Part H: Journal of Engineering in Medicine,* vol. 211, no. 4, pp. 335-347, 1997.
[439] B. Querleux, *Computational Biophysics of the Skin*. Jenny Stanford Publishing, 2016.
[440] S. P. DiMaio and S. E. Salcudean, "Needle insertion modeling and simulation," *IEEE Transactions on robotics and automation,* vol. 19, no. 5, pp. 864-875, 2003.
[441] D. Glozman and M. Shoham, "Flexible needle steering for percutaneous therapies," *Computer Aided Surgery,* vol. 11, no. 4, pp. 194-201, 2006.
[442] J. Xu, L. Wang, K. C. Wong, and P. Shi, "A meshless framework for bevel-tip flexible needle insertion through soft tissue," in *2010 3rd IEEE RAS & EMBS International Conference on Biomedical Robotics and Biomechatronics*, 2010: IEEE, pp. 753-758.
[443] C. Simone and A. M. Okamura, "Modeling of needle insertion forces for robot-assisted percutaneous therapy," in *Proceedings 2002 IEEE International Conference on Robotics and Automation (Cat. No. 02CH37292)*, 2002, vol. 2: IEEE, pp. 2085-2091.
[444] L. Barbé, B. Bayle, M. de Mathelin, and A. Gangi, "Needle insertions modeling: Identifiability and limitations," *Biomedical signal processing and control,* vol. 2, no. 3, pp. 191-198, 2007.
[445] R. Kikuuwe, Y. Kobayashi, and H. Fujimoto, "Coulomb-friction-based needle insertion/withdrawal model and its discrete-time implementation," in *Proc. EuroHaptics*, 2006, pp. 207-212.
[446] N. Mitsuhashi, K. Fujieda, T. Tamura, S. Kawamoto, T. Takagi, and K. Okubo, "BodyParts3D: 3D structure database for anatomical concepts," *Nucleic acids research,* vol. 37, no. suppl_1, pp. D782-D785, 2009.
[447] D. Moratal, *Finite Element Analysis: From Biomedical Applications to Industrial Developments*. BoD–Books on Demand, 2012.
[448] K. Sato, S. Kikuchi, and T. Yonezawa, "In Vivo Intradiscal Pressure Measurement in Healthy Individuals and in Patients With Ongoing Back Problems," *Spine,* vol. 24, no. 23, p. 2468, 1999. [Online]. Available: https://journals.lww.com/spinejournal/Fulltext/1999/12010/In_Vivo_Intradiscal_Pressure_Measurement_in.8.aspx.
[449] H.-J. Wilke and A. Rohlmann, "Forces on the spine," in *Biomaterials for Spinal Surgery*: Elsevier, 2012, pp. 114-143.
[450] S. Naserkhaki and M. El-Rich, "Sensitivity of lumbar spine response to follower load and flexion moment: finite element study," *Computer methods in biomechanics and biomedical engineering,* vol. 20, no. 5, pp. 550-557, 2017.
[451] S. Konno, S. Kikuchi, and Y. Nagaosa, "The relationship between intramuscular pressure of the paraspinal muscles and low back pain," *Spine,* vol. 19, no. 19, pp. 2186-2189, 1994.
[452] E. Kim *et al.*, "Comparison of intra-abdominal pressure among 3 prone positional apparatuses after changing from the supine to the prone position and applying positive end-expiratory pressure in healthy euvolemic patients: a prospective observational study," *Journal of neurosurgical anesthesiology,* vol. 29, no. 1, pp. 14-20, 2017.
[453] A. Rohlmann, S. Neller, L. Claes, G. Bergmann, and H.-J. Wilke, "Influence of a follower load on intradiscal pressure and intersegmental rotation of the lumbar spine," *Spine,* vol. 26, no. 24, pp. E557-E561, 2001.
[454] H. L. Sis *et al.*, "Effect of follower load on motion and stiffness of the human thoracic spine with intact rib cage," *Journal of biomechanics,* vol. 49, no. 14, pp. 3252-3259, 2016.
[455] C. Våpenstad *et al.*, "Lack of transfer of skills after virtual reality simulator training with haptic feedback," *Minimally Invasive Therapy & Allied Technologies,* vol. 26, no. 6, pp. 346-354, 2017.
[456] A. C. Klop, M. E. Vester, K. L. Colman, J. M. Ruijter, R. R. Van Rijn, and R. J. Oostra, "The effect of repeated freeze-thaw cycles on human muscle tissue visualized by postmortem computed tomography (PMCT)," *Clinical Anatomy,* vol. 30, no. 6, pp. 799-804, 2017.
[457] N. Newell, J. Little, A. Christou, M. Adams, C. Adam, and S. Masouros, "Biomechanics of the human intervertebral disc: A review of testing techniques and results," *Journal of the mechanical behavior of biomedical materials,* vol. 69, pp. 420-434, 2017.
[458] Y. Nakanishi and V. Nethery, "Anthropometric comparison between Japanese and Caucasian American male university students," *Applied Human Science,* vol. 18, no. 1, pp. 9-11, 1999.
[459] G. D. O'Connell, E. J. Vresilovic, and D. M. Elliott, "Comparison of animals used in disc research to human lumbar disc geometry," *Spine,* vol. 32, no. 3, pp. 328-333, 2007.

[460] P. Brinckmann and H. Grootenboer, "Change of disc height, radial disc bulge, and intradiscal pressure from discectomy. An in vitro investigation on human lumbar discs," *Spine,* vol. 16, no. 6, pp. 641-646, 1991.
[461] J. Brown, S. Sorkin, J.-C. Latombe, K. Montgomery, and M. Stephanides, "Algorithmic tools for real-time microsurgery simulation," *Medical image analysis,* vol. 6, no. 3, pp. 289-300, 2002.
[462] C. Monserrat, U. Meier, M. Alcaniz, F. Chinesta, and M. C. Juan, "A new approach for the real-time simulation of tissue deformations in surgery simulation," *Computer Methods and Programs in Biomedicine,* vol. 64, no. 2, pp. 77-85, 2001.
[463] M. Bro-Nielsen, "Surgery simulation using fast finite elements," in *International Conference on Visualization in Biomedical Computing*, 1996: Springer, pp. 529-534.
[464] D. Koschier, S. Lipponer, and J. Bender, "Adaptive tetrahedral meshes for brittle fracture simulation," in *Proceedings of the ACM SIGGRAPH/eurographics symposium on computer animation*, 2014: Eurographics Association, pp. 57-66.
[465] Q. Cheng, P. X. Liu, P. Lai, Y. Zou, C. Li, and L. Hu, "Modelling of soft tissue cutting in virtual surgery simulation: A literature review," *International Journal of Robotics and Automation,* vol. 32, no. 3, pp. 243-255, 2017.
[466] I. Peterlik, M. Sedef, C. Basdogan, and L. Matyska, "Real-time visio-haptic interaction with static soft tissue models having geometric and material nonlinearity," *Computers & Graphics,* vol. 34, no. 1, pp. 43-54, 2010.
[467] N. Sharma and L. M. Aggarwal, "Automated medical image segmentation techniques," *Journal of medical physics/Association of Medical Physicists of India,* vol. 35, no. 1, p. 3, 2010.
[468] I. Gibson and G. Zhan, "Finite element simulation of the spine with haptic interface," in *Proceedings of the 2nd International Convention on Rehabilitation Engineering & Assistive Technology*, 2008, pp. 20-25.
[469] K. T. Huynh, Z. Gao, I. Gibson, and W. F. Lu, "Haptically integrated simulation of a finite element model of thoracolumbar spine combining offline biomechanical response analysis of intervertebral discs," *Computer-Aided Design,* vol. 42, no. 12, pp. 1151-1166, 2010.
[470] C. M. Norris, "Spinal stabilisation: 3. Stabilisation mechanisms of the lumbar spine," *Physiotherapy,* vol. 81, no. 2, pp. 72-79, 1995.
[471] Y.-J. Lim, D. Deo, T. P. Singh, D. B. Jones, and S. De, "In situ measurement and modeling of biomechanical response of human cadaveric soft tissues for physics-based surgical simulation," *Surgical endoscopy,* vol. 23, no. 6, p. 1298, 2009.
[472] Y. Lin, H. Chen, D. Yu, Y. Zhang, and W. Yuan, "A predictive bone drilling force model for haptic rendering with experimental validation using fresh cadaveric bone," *International journal of computer assisted radiology and surgery,* vol. 12, no. 1, pp. 91-98, 2017.
[473] L. Pelliccia *et al.*, "A cadaver-based biomechanical model of acetabulum reaming for surgical virtual reality training simulators," *Scientific Reports,* vol. 10, no. 1, pp. 1-12, 2020.
[474] D. F. Pepley, M. A. Yovanoff, K. A. Mirkin, S. R. Miller, D. C. Han, and J. Z. Moore, "Integrating Cadaver Needle Forces Into a Haptic Robotic Simulator," *Journal of medical devices,* vol. 12, no. 1, pp. 0145011-145015, 2018, doi: 10.1115/1.4038562.
[475] F. Li *et al.*, "Real-time needle force modeling for VR-based renal biopsy training with respiratory motion using direct clinical data," *Applied Bionics and Biomechanics,* vol. 2019, 2019.
[476] C. R. Carignan and K. R. Cleary, "Closed-loop force control for haptic simulation of virtual environments," 2000.